Numerical and experimental studies on single point diamond turning of brittle and ductile materials

A Thesis

Submitted in partial fulfillment of the requirements for the degree

of

DOCTOR OF PHILOSOPHY

by

Borad M Barkachary

(Roll No. 10610325)

Department of Mechanical Engineering
Indian Institute of Technology Guwahati,
Guwahati, Assam, India
2019

Indian Institute of Technology Guwahati
Department of Mechanical Engineering
Guwahati – 781 039

STATEMENT

The present thesis entitled, **"Numerical and experimental studies on single point diamond turning of brittle and ductile materials"** has been carried out by me under the supervision of Dr. Shrikrishna N. Joshi, Department of Mechanical Engineering, Indian Institute of Technology Guwahati. This work has not been submitted elsewhere for the award of any degree.

Date: 9 May, 2019

(Borad M Barkachary)
Roll No. 10610325
Department of Mechanical Engineering,
Indian Institute of Technology Guwahati,
Guwahati – 781039, India

Indian Institute of Technology Guwahati
Department of Mechanical Engineering
Guwahati – 781 039

CERTIFICATE

It is certified that the work described in this thesis, entitled **"Numerical and experimental studies on single point diamond turning of brittle and ductile materials"**, done by **Mr. Borad M Barkachary** (Roll No. 10610325), a Ph.D. student in the Department of Mechanical Engineering, Indian Institute of Technology Guwahati, for the award of degree of **Doctor of Philosophy** has been carried out under my supervision. This work has not been submitted elsewhere for the award of any degree.

Date: 9 May, 2019

Dr. Shrikrishna N. Joshi
Associate Professor
Department of Mechanical Engineering
Indian Institute of Technology Guwahati
Guwahati – 781 039, India

THESIS APPROVAL SHEET

This thesis entitled

Numerical and Experimental Studies on Single Point Diamond Turning of Brittle and Ductile Materials

by

Borad M. Barkachary
(Roll No. 10610325)

is approved for the degree of

DOCTOR OF PHILOSOPHY

Examiners

[Prof. G. L. Samuel]

[Dr. S. S. Gautam]

[Prof. K. D. Singh]

Supervisor

[Dr. Shrikrishna N. Joshi]

Chairman

[Prof. P. S. Robi]

Date: May 09, 2019
Place: Indian Institute of Technology Guwahati

Dedicated to

My family

Abstract

Silicon and silicon carbide materials are widely used materials in semiconductor industries, defence, aerospace and biomedical due to their excellent mechanical, chemical and thermal properties. However, mechanical processing of these materials is very much difficult because of their brittleness. Single point diamond turning (SPDT) successfully produces optical finish surfaces on these materials; however, it causes severe tool wear to the diamond tool. SPDT comprises of complex interaction of its process factors. Analytical modeling of these parameters is difficult. Numerical simulations are therefore becoming imperative to study the nanometric cutting processes. At present, molecular dynamic (MD) simulation is regarded as the high-end numerical simulator. However, MD simulation considers a very limited work-domain, i.e., a nano-portion of the cutting process. Moreover, it requires substantial computing time. An alternate way to this problem is to employ finite element method (FEM). FEM is capable of obtaining insight into the effects of the cutting process that are sometimes not possible to visualize through experiments.

After an extensive literature review on various aspects of SPDT process such as analytical, experimental and numerical studies on various process parameters, tool geometry, and material aspects, it was found that scant literature is available on numerical simulation of silicon and silicon carbide. Moreover, there is hardly any comprehensive and systematic study reported on the influence of critical machining parameters such as speed, feed, depth of cut, tool geometry parameters viz. rake angle, cutting edge radius on the performance measures, i.e., cutting forces and surface roughness. Thus, a need was identified to understand the effects of various process parameters, tool geometry, workpiece material, working condition on process output and product quality. This motivated to carry out the present research work.

In this research work, a finite element method based two-dimensional numerical model of nanoindentation and plunge cutting process is developed to determine the ductile to brittle transition (DBT) thickness and to understand the ductile regime machining (DRM) of silicon and silicon carbide. This thesis aims to provide an understanding of the ductile regime machining by identifying the critical depth of transition and thereby predicting the machining force and surface roughness to optimize the process conditions for the improvement of process efficiency and product quality. Arbitrary Lagrangian Eulerian (ALE) formulation with an explicit solution scheme was employed to simulate the interaction between the diamond indenter and the workpiece. The diamond indenters and the silicon carbide in the model are defined as homogeneous and isotropic elastic materials. Drucker-Prager material model is

used to model the material behavior of silicon carbide along with elastic material properties. Experimental validations of load-displacement (P-h) plots were carried out by using published experimental data and found that the calculated Young's modulus and hardness from the numerical simulations are in good agreement. It was observed that the maximum von-Mises stress reaches to 16 GPa and 38 GPa when the indenter's depth was around 91 nm and 375 nm just before the formation of crack/fracture for silicon and silicon carbide respectively. These pressures are higher than the hardness of the workpiece (12 GPa and 26 GPa) that felicitate to change the phase of silicon and silicon carbide. Thus, the critical depth of indentation, i.e., ductile to brittle transition was found to be 91 nm and 375 nm for silicon and SiC respectively.

Plunge cutting simulations were carried out by using a diamond tool having rake angles of 0º, −25º and −30º, the clearance angle of 10º. To achieve an inclined motion of the tool, i.e., continuously varying depth of cut from 0 to 600 nm, tool has given simultaneous speeds along *x* and *y*-axis directions. To identify the DBT depth or critical depth of cut (CDC), three methods were employed, i.e., visual inspection of surface profile, variation of machining force and specific cutting energy. A comparative analysis of performance of three methods has also been presented. The CDCs obtained from the force analysis were 78 nm, 84 nm and 108 nm for 0º, –25º and –30º rake angle tool respectively. The critical depths of cut for SiC were found to be around 65 nm. These values are found to be close to the experimental CDCs.

A two-dimensional numerical model of SPDT process of silicon and silicon carbide using FEM was developed to predict the machining force values. The results predicted by the numerical model and developed integrated approach were validated with available published experimental results. Prediction using two different material models viz. Johnson-Cook (JC) and Drucker-Prager (DP) were compared. A study on the chip formation while performing the nanometric cutting simulation of SPDT of SiC was presented. Parametric studies were also carried out using full factorial and response surface methodology based set of numerical experiments and the behavior of SPDT of silicon and silicon carbide was studied. The confirmation simulations showed mean prediction error of below 8.5% for silicon carbide and 5% for silicon.

An integrated finite element method-image processing technique (FEM-IPT) based model for the prediction of surface roughness during SPDT of Al6061−T6 is presented. The present technique is found to be simple and economical. It very well predicts the surface roughness values before the actual machining runs. The comparison between experimental roughness and numerically predicted roughness shows that the prediction error during SPDT

of Al601-T6 was varied between 2.19−20.41% and the overall mean prediction error was found to be 8.71%.

In view of limited availability of SPDT machine to carry out experimental studies, very limited numbers of experiments were carried out on available Al6061-T6. Results were used to validate the developed FEM-IPT model and to investigate the effect of process parameters such as speed, feed, and depth of cut on the surface roughness. Mixed level full factorial experiments were carried out. Experimental results showed that minimum surface roughness value of Ra = 6.5 nm was successfully obtained for a combination of speed of 1.309 m/s, feed of 3 μm/rev and depth of cut of 10 μm whereas maximum surface roughness value of Ra=13.03 nm was obtained for speed 2.356 m/s, feed 10 μm/rev and depth of cut 20 μm. The results of regression analysis reveal that the mathematical model developed using factorial analysis allows prediction of surface roughness within 7.3% prediction error. It is felt that the developed integrated approach will be useful to predict the surface roughness at shop floor before carrying out the actual machining runs. This will certainly help the process engineers to apply proper process parameters to obtain the desired process performance. The information and knowledge generated during numerical and the experimental studies presented in this thesis will be useful to the researchers and engineers as important guidelines. Overall, it is found that the numerical approach developed in this work can be thought to be simple, easy and economical alternatives to costly, tedious and time-consuming physical experiments.

भारतीय प्रौद्योगिकी संस्थान गुवाहाटी
Indian Institute of Technology Guwahati

Acknowledgements

It has been a great experience for me during the entire span of my research work. Many people have inspired, motivated and helped me during the entire course of this work and it is my heartfelt desire to acknowledge their immense goodwill and valuable support.

I wish to express my sincere and deep appreciation to Dr. Shrikrishna N. Joshi for his encouragement, insightful guidance, all the patience, support, and enthusiastic support throughout my studies, including the writing of this dissertation. I must acknowledge him for providing the unconditional freedom to work, think and express on whatever I have done in my research work by having faith in my capabilities. I am also thankful to my supervisor for providing me the opportunity to work on this research project.

I am highly thankful to my doctoral committee members, Prof. P. S. Robi, Prof. S. Senthilvelan, Prof. Praveen Kumar and Dr. Bimlesh Kumar for their continuous academic guidance and checking my work progress and seminars during my Ph.D. Their valuable discussions and suggestions were truly encouraging for me. I would like to express my sincere gratitude to Prof. Santosha K. Dwivedy, Prof. Anoop K. Dass, Prof. Pinakeswar Mahanta and Prof. Debabrata Chakraborty, present and former Heads, Department of Mechanical Engineering, Indian Institute of Technology Guwahati, for providing various laboratory facilities and sanctioning funds without which completion of the work would not have been possible. I am also grateful to all the faculty members of the Mechanical Engineering department.

I would also like to thank Ministry of Human Resource and Development (MHRD), Government of India and Science and Engineering Research Board (SERB), Government of India for providing financial support. I sincerely thank Indian Institute of Technology Guwahati for providing all sort of infrastructural facilities to carry out this doctoral research work. I would also like to acknowledge Advanced Manufacturing Laboratory, and Central Workshop of Indian Institute of Technology Guwahati and all scientific officers and staff members for providing instruments and helping me to carry out the research work.

I would also like acknowledge Prof. Ravindra Kumar Sinha, present Director, Dr. Vinod Karar, Chief Scientist, Central Scientific Instruments Organization (CSIO), Chandigarh (India), for providing experimental facilities to conduct experimental study without which completion of the work would not have been possible. I am also grateful to all the scientists (Neha Khatri, Vinod Mishra) and project staffs (Rohit Sharma, Ajay Rana, Rakesh Panwar) of

Optical Devices and Systems, CSIO Chandigarh (India) for helping me to carry out experiments at their facility.

I deeply acknowledge the unabated support and counselling provided by my colleagues and friends, Dr. Ravikant, Dr. Gururaj Bholar, Mr. Sanasam Sunderlal Singh, Ms. Ngangkham Devarani, Ms. Sanghamitra Das and Ms. Upasana Sarma throughout my studies. I also highly appreciate the technical cooperation given by Mr. Jiten Basumatary, and Mr. Argha Das.

My most sincere gratitude and appreciation go to my parents Mr. Madan Chandra Barkachary, Mrs. Nilima Bala Gayary, my grandmother Mrs. Dewali Barkachary, my sisters, Mrs. Belshree Barkachary and Ms. Minishree Barkachary, my brother-in-laws Mr. Rajib Basumatary, Mr. Akon Chandra Baro, my niece Mr. Pritom R. Basumatary, Mr. David R. Basumatary, my in-laws Mr. Dharanidhar Baro and Mrs. Rohini Baro and finally my dear wife Mrs Karabi Baro and my lovely son Mr. Aumlin B. Barkachary for their patience, continuous encouragement and moral support over the period of PhD work. I am deeply indebted to all the other members of my family who gave me continuous support and encouragement throughout my life.

Borad M Barkachary

Date: 9 May, 2019 (Roll No. 10610325)

Table of Contents

	Page No
Abstract	i
Acknowledgements	v
Table of Contents	vii
List of Figures	xiii
List of Tables	xvii
List of Abbreviations	xix
List of Symbols	xxi
1 INTRODUCTION	
1.0 Single Point Diamond Turning (SPDT)	1
1.1 SPDT of Brittle Materials	2
1.2 Motivation for the Present Research Work	5
1.3 Scope of the Present Research Work	7
1.4 Organization of the Thesis	8
2 LITERATURE REVIEW ON SINGLE POINT DIAMOND TURNING, NANOINDENTATION AND PLUNGE CUTTING	
2.0 Scope	11
2.1 Conventional Machining of Brittle Materials	11
2.2 Single Point Diamond Turning (SPDT)	12
2.3 Process Parameters of SPDT	13
2.3.1 Machining Parameters	14
2.3.2 Cutting Tool Geometry	16
2.4 Ductile Regime Machining of Brittle Materials	19
2.4.1 Ductile to Brittle Transition (DBT)	20
2.4.2 Nanoindentation	22
2.4.3 Plunge Cut	25
2.5 Performance Parameters	29
2.5.1 Machining Forces	29
2.5.2 Surface Finish	32
2.6 Numerical Modeling and Simulation of SPDT Process	35
2.7 Discussion	40
2.8 Objectives of the Present Research Work	42
3 A STUDY ON DUCTILE REGIME MACHINING USING NUMERICAL SIMULATIONS OF NANOINDENTATION	
3.0 Scope	45
3.1 Motivation and Objectives of Present Work	45
3.2 Overview of the Present Work	48
3.3 Nanoindentation and Computation of Mechanical Properties	49
3.4 Numerical Simulation of Nanoindentation for the Determination of Mechanical Properties	51
3.4.1 Selection of Solution Methodology	51
3.4.2 Development of FEM Based Nanoindentation Model	53
A. *Assumptions*	54
B. *Governing Equations*	54
C. *Geometric Modeling of Process Continuum*	58

D. *Material Model and Properties* 59
E. *Damage and Failure Models of Silicon Carbide* 60
F. *Damage and Failure Models of Silicon* 62
G. *Element and Meshing* 62
H. *Modeling of Surface Contact* 64
I. *Boundary Conditions* 65
J. *FEM Solver Methodology* 65
3.5 Computation of Young's Modulus and Hardness from Load-Displacement Plot 67
3.5.1 Computation of Elastic Modulus 67
3.5.2 Computation of Hardness 69
3.5.3 A Case Study 69
A. *Elastic Modulus* 70
B. *Hardness* 72
3.6 Experimental Validation of FEM based Nanoindentation Simulation 72
3.6.1 Experimental Validation of Nanoindentation of Silicon Carbide 72
3.6.2 Experimental Validation of Nanoindentation of Silicon 74
3.7 Study of Ductile to Brittle Transition (DBT) using Nanoindentation 76
3.7.1 Determination of DBT 76
3.7.2 Validation of DBT with Published Experimental Results 79
3.8 *In-situ* Study of Phase Changing Pressure 80
3.9 Numerical Study on the Effect of Residual Stress on DBT during Repetitive Indentation 82
3.10 Summary 85

4 A STUDY ON DUCTILE REGIME MACHINING USING NUMERICAL SIMULATIONS OF PLUNGE CUTTING

4.0 Scope 87
4.1 The Need 87
4.2 Overview of the Present Work 88
4.3 Overview of the Process Model Development 89
4.4 Numerical Simulation of Plunge Cutting Process of Silicon 90
4.4.1 Assumptions 91
4.4.2 Governing Equations 91
4.4.3 Geometric Modeling 94
4.4.4 Material Model and Properties 95
4.4.5 Damage and Failure Models 95
4.4.6 Chip Separation Criterion 95
4.4.7 Finite element and Meshing 96
4.4.8 Arbitrary Lagrangian Eulerian (ALE) Method 97
4.4.9 Contact Algorithm 98
4.4.10 Boundary Conditions 99
4.4.11 Solution Methodology 100
4.4.12 Post Processing 100
4.5 Results and Discussion 100
4.5.1 Determination of Critical Depth of Cut 100
4.5.1.1 *Visual Inspection of Surface Profile* 101
4.5.1.2 *Analysis of Machining Forces* 102
4.5.1.3 *Specific Cutting Energy* 105
4.5.2 Comparison of Methods used to Determine Critical Depth of Cut during Plunge Cutting Simulation 108
4.6 Numerical Simulation of Plunge Cutting of Silicon Carbide 109
4.7 Summary 111

5 NUMERICAL MODELING AND SIMULATION OF CUTTING FORCES DURING SINGLE POINT DIAMOND TURNING PROCESS

5.0 Scope 115
5.1 The Need 115
5.2 Overview of the Process Model Development 116
5.3 Development of Numerical Model for SPDT of Silicon using Finite Element Method 118
5.3.1 Model Definition and Assumptions 119
5.3.2 Geometric Modeling 120
5.3.3 Material Models and Properties 121
5.3.3.1 *Drucker-Prager Material Model* 121
5.3.3.2 *Johnson-Cook Material Model* 121
5.3.3.3 *Chip Separation Criterion and Failure Models* 122
5.3.4 Governing Equations 123
5.3.5 Element and Meshing 123
5.3.6 Contact Algorithms 124
5.3.7 Boundary Condition 124
5.3.8 Solver Selection 125
5.3.9 Post Processing 125
5.4 Results Analysis 126
5.5 Numerical Simulation and Experimental Validation of SPDT of Silicon Carbide 126
5.5.1 Selection of Suitable Material Model 127
5.5.2 Study on Quantitative Crack Propagation using JC and DP Material Models 131
5.5.3 Parametric Analysis of SPDT of Silicon Carbide using Full Factorial Analysis 136
5.5.4 Full Factorial Design 136
5.5.5 Selection of Machining Parameters and their Importance 137
5.5.6 Analysis of Results and Discussion 138
5.5.6.1 *ANOVA Analysis of Cutting Force* 138
5.5.6.2 *Model Fitness Check* 140
5.5.6.3 *Regression Analysis* 142
5.5.6.4 *Parametric Influence on Cutting Force* 142
5.5.6.5 *ANOVA Analysis of Thrust Force* 144
5.5.6.6 *Model Fitness Check* 145
5.5.6.7 *Regression Analysis* 146
5.5.6.8 *Parametric Influence on Thrust Force* 146
5.5.7 Confirmation Simulations 148
5.5.8 Multi-Objective Optimization of Machining Forces using FFA 150
5.6 Numerical Simulation and Experimental Validation of SPDT of Silicon 152
5.6.1 Experimental Validation of Machining Simulation of Silicon 152
5.6.2 Formation of Chip during SPDT of Silicon 153
5.6.3 Ploughing/Rubbing 154
5.6.4 Parametric Analysis of SPDT of Silicon using Response Surface Methodology 155
5.6.5 Response Surface Methodology 155
5.6.6 Parametric Analysis of SPDT of Si using FEM and RSM 156
5.6.7 Selection of Machining Parameters and their Importance 157
5.6.8 Analysis of Results and Discussion 158
5.6.8.1 *ANOVA Analysis of Cutting Force* 158
5.6.8.2 *Model Fitness Check* 159
5.6.8.3 *Regression Analysis* 160

5.6.8.4 *Parametric Influence on Cutting Force* 161
5.6.8.5 *ANOVA Analysis of Thrust Force* 164
5.6.8.5 *Model Fitness Check* 165
5.6.8.6 *Regression Analysis* 166
5.6.8.7 *Parametric Influence on Thrust Force* 166
5.6.8.8 *Confirmation Simulations* 168
5.8.9 Multi-Objective Optimization of Machining Forces using RSM 171
5.7 Summary 172

6 NUMERICAL PREDICTION OF SURFACE ROUGHNESS DURING SINGLE POINT DIAMOND TURNING

6.0 Scope 175
6.1 The Need 175
6.2 Overview of the Present Work 176
6.3 Selection of Workpiece Material 177
6.4 Selection of Modeling Domain 177
6.5 2D Finite Element Simulation of SPDT of Al6061-T6 179
6.6 Numerical Simulations using the Developed Model 182
6.7 Calculation of Surface Roughness using FEM-IPT Technique 183
6.7.1 Edge Detection 184
6.7.2 Digitization 184
6.7.3 Roughness Calculation 185
6.8 Experimental Validation of the Developed Integrated FEM-IPT Model 186
6.9 Summary 187

7 EXPERIMENTAL STUDIES ON SINGLE POINT DIAMOND TURNING PROCESS

7.0 Scope 189
7.1 The Need 189
7.2 Experimental Procedure 189
7.3 Experimental Setup 190
7.3.1 Workpiece 191
7.3.2 Cutting Tool 192
7.4 Measurement of Process Responses 193
7.5 Selection of Machining Parameters and their Levels 193
7.6 Experimental Study based on Mixed Level Full Factorial Design 194
7.7 Results and Discussion 195
7.8 Parametric Study 198
7.8.1 ANOVA Analysis 199
7.8.2 Model Fitness Check 200
7.8.3 Regression Analysis 201
7.8.4 Parametric Influence on Surface Roughness 202
7.8.5 Regression Modeling of Surface Roughness using Factorial Analysis 205
7.12 Summary 206

8 CONCLUSIONS AND FUTURE WORK

8.0 Overview 209
8.1 Conclusions and Research Contributions 209
8.1.1 A Study on Ductile Regime Machining using Numerical Simulations of Nanoindentation 209
8.1.2 A Study on Ductile Regime Machining using Numerical Simulations 212

of Plunge Cutting
8.1.3 Numerical Modeling and Simulation of Cutting Forces during Single Point Diamond Turning Process 213
8.1.4 Numerical Prediction of Surface Roughness during Single Point Diamond Turning 215
8.1.5 Experimental Studies on Single Point Diamond Turning Process 216
8.2 Recommendations for Future Work 216

References 217
Appendices 230
List of Publications 244

List of Figures

Figure No.	Figure Title	Page No.
1.1	Components and products made by using SPDT	1
1.2	Schematic of ductile regime machining	4
2.1	Schematic of Single Point Diamond Turning Machine	12
2.2	Inputs and output parameters during SPDT process	13
2.3	Process parameters in SPDT process	14
2.4	Schematic of the tool geometry of single point diamond tool	16
2.5	Schematic representations of positive, negative and zero rake angles of a tool	16
2.6	Schematic diagram for calculating the effective rake angle	17
2.7	(a) Ductile-regime machining model using a round nose cutting tool (b) Analytical model of ductile-regime machining	21
2.8	(a) Schematic of typical nanoindentation tester, (b) Force actuator, (c) Capacitive displacement gauge	23
2.9	Sectional front view and top view of plunge cut showing different zones of material removal with critical depth of cut	26
2.10	Schematic of an inclined angle plunge cut	27
2.11	Influence of depth of cut and feed rate on ductile-brittle transition	27
2.12	Photograph of an inclined plunge-cut groove shows clearly ductile (Ld) and semi-ductile (Ls) areas.	28
2.13	Dimensional comparisons of macro, FEM and MD simulations	36
2.14	Schematic of the model used in the MD simulation of nanometric cutting of single crystal aluminum	36
2.15	Schematic of MD simulation	37
2.16	FEM simulation results of SPDT of SiC for 0º rake, 5º clearance	39
2.17	SPH simulations with or without SDM	39
2.18	Overview of the present research work	43
3.1	Overview of the work carried out in this chapter	48
3.2	Schematic of (a) indentation process and (b) load-displacement plot	49
3.3	Schematic of (a) indenter and specimen surface geometry at full load and full unload condition (b) load versus displacement graph with various indentation parameters	50
3.4	Schematic of developed numerical model	52
3.5	Schematic of Berkovich indenter showing front and top views	53
3.6	Schematic of 2D axisymmetric indentation simulation model	58
3.7	Workpiece and indenter meshing	62
3.8	Comparison of load-displacement plot with no of elements in indentation zone	64
3.9	Schematic of the boundary conditions applied	65
3.10	von-Mises plot at maximum loading depth of 5 nm	66
3.11	Load-displacement plot	70
3.12	Fitting of the unloading curve and finding the slope	70
3.13	Load vs. displacement: numerical and experimental results for SiC	73
3.14	Load vs. displacement: numerical and experimental results for Si	75
3.15	Indentation depth (a) before fracture and (b) after fracture for silicon carbide	77
3.16	Average stress (nodes 1 to 6) vs. indentation depth	78
3.17	Indentation depth (a) before fracture and (b) after fracture for silicon	78
3.18	Average stress generated at the selected nodes vs. indentation depth	79

3.19	Different pressure zones (a) before failure at 372.97 nm depth and (b) after failure at 400 nm depth for silicon carbide	80
3.20	Different pressure zones after (a) Loading and (b) Unloading during nanoindentation on silicon	81
3.21	Spherical nanoindentation of SiC showing irregular stress field	82
3.22	Repetitive nanoindentation using spherical indenter with depths 10, 20, 50, 100, 200 nm	83
3.23	P-h plot for cyclic nanoindentation of silicon carbide with spherical indenter	84
4.1	Overview of the work carried out to obtain DBT thickness	88
4.2	Schematic of developed numerical model of plunge cutting	89
4.3	Schematic of Plunge cut showing different zones	91
4.4	Schematic of FEM formulation to solve an engineering problem	92
4.5	Schematic of finite difference method (central difference method)	93
4.6	Tool and workpiece geometry and dimensions	94
4.7	Mesh model of workpiece and tool	96
4.8	Comparison of motion of mesh and material with Lagrangian, Eulerian and ALE formulation	98
4.9	Schematic illustration of sliding and sticking zones at the chip-tool interface	98
4.10	Schematic of the boundary conditions applied to the tool and workpiece	99
4.11	Plunge cut with 0° rake angle	101
4.12	Plunge cut with −25° rake angle	101
4.13	Plunge cut with −30° rake angle	101
4.14	Variations of the cutting and thrust forces during a single plunge cut using 0º rake angle tool for continuously varying depth of cut	103
4.15	Variations of principal and thrust cutting forces during a single plunge cut using −25º rake angle tool	104
4.16	Variations of principal and thrust cutting forces during a single plunge cut using −30º rake angle tool	104
4.17	Schematic for the determination of chip area	105
4.18	Variation of specific cutting energy for 0º, −25º and −30º rake angle tools	106
4.19	Determination of critical depth of cut from simulated specific cutting energy for (a) 0° rake angle, (b) −25° rake angle and (c) −30° rake angle tools	108
4.20	Variations of the principal and thrust cutting forces during a single plunge cut using 0º rake angle tool	110
4.21	Variations of the principal and thrust cutting forces during a single plunge cut using –25º rake angle tool	110
4.22	Variations of the principal and thrust cutting forces during a single plunge cut using –30º rake angle tool	111
5.1	3D and 2D process continuums in numerical simulation of SPDT	116
5.2	Overview of the work carried out in this chapter	117
5.3	Input and output parameters from finite element simulation of machining	119
5.4	Comparison of SPDT machining and plunge cutting	120
5.5	Finite element method based numerical model for SPDT of silicon	121
5.6	Boundary conditions during SPDT of silicon carbide	125
5.7	Comparison of cutting force for JC and DP model for set 1	128
5.8	Comparison of cutting force for JC and DP model for set 2	129
5.9	Comparison of cutting force for JC and DP model for set 3	129

5.10	Comparison of thrust force for JC and DP model for set 1	130
5.11	Comparison of thrust force for JC and DP model for set 3	130
5.12	Crack propagation of silicon carbide with Drucker-Prager material model at (a) 1.5μs, (b) 1.95 μs, (c) 1.99 μs and (d) 2.0 μs	131
5.13	Crack propagation of silicon carbide with Johnson-Cook material model at (a) 1.5 μs, (b) 2.19 μs, (c) 2.4 μs and (d) 2.77 μs	132
5.14	Contour plot of equivalent von-Mises stress with the formation of a ductile chip (0° rake angle, 5° clearance angle and 100 nm depth of cut)	133
5.15	Contour plot of equivalent von-Mises stress with the formation of a brittle chip (0° rake angle, 5° clearance angle and 100 nm depth of cut)	133
5.16	Optical microscopic image of the ductile chip during experimental cutting of SiC	134
5.17	Five essential stages in the brittle material removal	134
5.18	Stages of chip formation during SPDT machining of SiC	135
5.19	Parametric analysis of SPDT of silicon using FEM and full factorial	136
5.20	Normal plot of residuals for cutting force	141
5.21	Plot of actual vs. predicted response of cutting force	141
5.22	Residuals versus fitted value plot of cutting force	141
5.23	Main effect plot of cutting force	142
5.24	Interaction plot for cutting force	143
5.25	Normal plot of residuals for thrust force	145
5.26	Plot of actual vs. predicted response of thrust force	145
5.27	Residuals versus fitted value plot of thrust force	146
5.28	Main effect plots of thrust force	146
5.29	Interaction plot for thrust force	147
5.30	Numerically determined and predicted values of cutting and thrust force	150
5.31	Optimization of cutting and thrust forces	151
5.32	Comparison of experimental and numerical results of silicon	153
5.33	Formation of ductile chips with stress zones during SPDT of silicon	153
5.34	Rolling/ploughing action during machining (5nm depth of cut)	154
5.35	Parametric analysis of SPDT of silicon using FEM and RSM	156
5.36	Normal plot of residuals for cutting force	160
5.37	Plot of actual vs. predicted response of cutting force	160
5.38	Main effect plots for cutting force	161
5.39	Contour plot for cutting force	162
5.40	Normal plot of residuals for thrust force	165
5.41	Plot of actual vs. predicted response of thrust force	165
5.42	Main effect plots of thrust force	166
5.43	Contour plots for thrust force	167
5.44	Numerically measured and predicted values of (a) cutting force and (b) thrust force	170
5.45	Response optimizations for cutting and thrust forces	171
6.1	Overview of the work carried out in this chapter	176
6.2	Cross section of undeformed chip geometry	178
6.3	Geometries of 3D turning simulation and boundary condition	178

6.4	Process continuums in numerical simulation of SPDT of Al6061-T6 for (a) 3D and (b) 2D numerical models	179
6.5	Element type and mesh model of 2D orthogonal cutting simulation	181
6.6	Boundary conditions	182
6.7	2D turning with formation of chips showing von-Mises stress	182
6.8	Overview of the integrated MATLAB code of FEM-IPT technique	183
6.9	(a) Image of the simulated machined workpiece including chip, (b) Edge of the simulated machined workpiece including chip	184
6.10	(a) Simulated machined workpiece with detected edge, (b) Adding of scale the workpiece and digitization	185
6.11	Schematic of surface roughness measurement using arithmetic average method	185
6.12	Measured surface roughness showing mean and arithmetic average roughness	186
6.13	Roughness profile from numerical simulation for process conditions	186
7.1	Experimental setup of SPDT	190
7.2	Preparation of sample for facing operation on SPDT	191
7.3	(a) Fixing of the samples to a large aluminum plate, (b) Samples after removing the wedge, (c) Fixture to hold the sample and (d) Sample with fixture	192
7.4	Single point diamond tool from Contour Fine Tooling	193
7.5	Taylor Hobson 2D Profilometer	193
7.6	Measurement of surface roughness using 2D profilometer	194
7.7	Roughness profile for least Ra = 6.5 nm (Process condition: Cutting speed=1.309 m/s, feed rate=3 μm and depth of cut=10 μm)	196
7.8	Roughness profile for largest Ra =13.03 nm (Process condition: Cutting speed=2.356 m/s, feed rate=10 μm and depth of cut=20 μm	196
7.9	Effect of depth of cut on surface roughness (speed =1.309 m/s)	197
7.10	Effect of depth of cut on surface roughness (speed = 2.356 m/s)	197
7.11	Mirror like surface obtained from SPDT of Al6061 alloy	198
7.12	Normal plot of residuals for surface roughness	200
7.13	Plot of actual vs. predicted response of surface roughness	201
7.14	Residuals versus fitted value plot of surface roughness	201
7.15	Main effect plot of surface roughness	202
7.16	Schematic of effect of feed rate on surface roughness	203
7.17	Schematic of material recovery and swelling during ductile material cutting	204
7.18	Interaction plot for surface roughness	205
7.19	Measured Vs. Predicted surface roughness plot	205

List of Tables

Table No	Table Title	Page No.
3.1	Material properties of Diamond, Silicon and Silicon Carbide	60
3.2	Constants for Drucker-Prager constitutive model for Si and SiC	60
3.3	Ductile damage parameters for SiC based on triaxiality test	61
3.4	Mesh sensitivity analysis result for indentation zone	63
3.5	List of indenter parameters for spherical indenter	68
3.6	Indentation parameters (fixed and variable parameters)	71
3.7	Comparison of experimental and simulated Young's modulus and hardness at different indentation depth for SiC	74
3.8	Comparison of experimental and simulated Young's modulus and hardness at different indentation depth for Si	76
3.9	Young's modulus and hardness with and without residual stress	84
4.1	Critical depth of cut for 0º, −25º and −30º rake angle from visual inspection	102
4.2	Critical depth of cut obtained from three methods for 0º, −25º and −30° rake angle	109
5.1	Constants for Johnson-Cook constitutive model for Si and SiC	122
5.2	Mesh convergence simulation	124
5.3	Process conditions for simulations	127
5.4	Process variables and their levels	137
5.5	Numerical matrix and results for the SPDT performance characteristics	138
5.6	Analysis of variance (ANOVA) results for cutting force	139
5.7	ANOVA table for thrust force	144
5.8	Confirmation tests and their comparison with the results	148
5.9	FEM simulated and FFA predicted values of cutting and thrust forces	149
5.10	Response optimizations for cutting force and thrust force parameters	151
5.11	Cutting tool geometry during machining of silicon	152
5.12	Process variables and their levels	157
5.13	Experimental matrix and results for the SPDT performance characteristics	157
5.14	Model summary statistics of cutting force (CF)	158
5.15	ANOVA table for cutting force (before elimination)	159
5.16	Observations on the effect of process parameters on cutting forces	163
5.17	ANOVA table for thrust force (before elimination)	164
5.18	Observations on the effect of process parameters on the thrust force	168
5.19	Confirmation tests and their comparison with the results	169
5.17	FEM simulated and RSM predicted values of cutting and thrust forces	169

5.18	Response optimizations for cutting force and thrust force parameters	171
6.1	JC material parameters values for Al6061-T6	180
6.2	Material properties of Al6061-T6	180
6.3	Johnson– Cook failure parameters for Al6061-T6	181
6.4	Comparison of experimental, numerical and theoretical roughness values	187
7.1	Chemical composition of Al6061-T6 Al alloy	191
7.2	Machining parameters and their levels	194
7.3	Measured surface roughness for all the set of process combinations	195
7.4	Analysis of variance (ANOVA) results	199
7.5	Analysis of variance (ANOVA) results after eliminating insignificant terms	200
7.6	Measured and predicted surface roughness for all the set of process combinations	206

List of Abbreviations

2D	Two dimensional
3D	Three dimensional
2FI	Two factorial interaction
AFM	Atomic force microscopy
ALE	Arbitrary Lagrangian-Eulerian
ANOVA	Analysis of variance
a-Si	Amorphous silicon
BUE	Build up edge
CAE	Computer aided engineering
CDC	Critical depth of cut
CNC	Computer numerical control
CPU	Central processing unit
c-Si	Crystalline silicon
CSIO	Central Scientific Instruments Organization
CSIR	Council of Scientific and Industrial Research
CUCT	Critical undeformed chip thickness
CVD	Chemical vapor deposition
DBT	Ductile to brittle transition
DF	Degree of freedom
DOE	Design of experiment
DP	Drucker-Prager
DRM	Ductile regime machining
FEM	Finite element method
FFA	Full factorial analysis
FVM	Finite volume method
HPPT	High pressure phase transformation
IPT	Image processing technique
JC	Johnson-Cook
LLNL	Lawrence Livermore National Lab
MD	Molecular dynamic
μ-LAM	Micro-laser assisted machining
MS	Mean square
ODB	Output database
PMMA	Poly-methyl methacrylate

RF	Reaction force
RGB	Red green blue
RMD	Renormalized molecular dynamics
RP	Reference point
RPM	Revolution per minute
RSM	Response surface methodology
SCE	Specific cutting energy
SDM	Surface defect machining
Si	Silicon
SiC	Silicon carbide
SHPB	Split Hopkinson pressure bar
SPDT	Single Point Diamond Turning
SPH	Smooth particle hydrodynamics
SS	Sum of square
UPM	Ultra-precision machining

List of Symbols

d	Depth of cut
r	Cutting edge radius
α_e	Effective rake rangle
f	Feed rate
y_c	Average surface damage depth
R	Tool nose radius
W_d	Distance from the tool centre to the fracture-pit transition on the uncut shoulder
α	Nominal rake angle
ϕ	Shear angle
β	Friction angle
F_c	Cutting force
F_t	Thrust force
F_f	Feed force
F_s	Shear force
F	Frictional force
F_n	Normal shear force
N	Normal frictional force
F_r	Resultant force
A_p	Projected area
A_s	Surface area of contact
h_c	Contact depth
P	Indentation load
h	Displacement of indenter tip
h_{max}	Maximum depth of penetration at peak load
P_{max}	Peak load
h_f	Final residual depth after unloading
h_f	Depth elastically recovered after unloading
σ_{Mises}	von-Mises stress
$\sigma_1, \sigma_2\ \sigma_3$	Principal stresses
σ_Y	Yield strength of material
$\vec{U}$	Vector of displacements
N	Matrix of shape function
$\vec{Q}^{(e)}$	Vector of nodal displacements

t	Time
L	Lagrangian function
K	Kinetic energy
P	Potential energy
R	Dissipation function
Q	Nodal displacement
$\dot{Q}$	Nodal velocity
σ_e	Equivalent stress
σ_m	Mean stress
a, b	Material constant
I_1	First invariant of the stress tensor
J_2	Second invariant of the deviatoric stress tensor
α	Pressure-sensitivity coefficient
κ	Material constant
σ_c	Yield stress in compression
σ_t	Yield stress in tension
ρ	Density
E	Young's modulus
G	Shear modulus
υ	Poison's ratio
K_c	Fracture toughness
k	Thermal conductivity
η	Stress triaxiality
$\bar{\varepsilon}_D^{pl}$	Critical equivalent plastic strain
$\dot{\bar{\varepsilon}}^{pl}$	Plastic strain rate
G_f	Hillerborg's fracture energy
$\bar{\varepsilon}_{0i}$	Plastic strain at damage initiation
$\bar{\varepsilon}_f$	Equivalent plastic strain at failure
$\bar{\varepsilon}$	Equivalent plastic strain
$\bar{u}$	Equivalent plastic displacement
$\bar{u}_f$	equivalent plastic displacement at failure
L	Characteristic length of the element

INTRODUCTION

1.0 Single Point Diamond Turning (SPDT)

Single Point Diamond Turning (SPDT), is an ultra-precision machining process. It employs ultra-sharp poly or single crystal diamond tools to produce components with the surface finish in the order of Aº [Davis *et al.* (2009)]. Generally, the cutting edge radius of these ultra-sharp tools varies between 20 to 100 nm. According to Davies *et al.* (2003), the experiments on single crystal diamond turning was first reported by Jesse Ramsden in 1779. A diamond was used to cut a hardened steel screw for dividing engines. Based on this, the ultra-precision machining technology was first introduced in 1960s to fabricate super finished surfaces with sub-micrometric form accuracy and surface waviness [Ikawa *et al.* (1991)]. The SPDT process was then commercialized in late 1970s. After that it has become an indispensible process in the precision manufacturing of infrared imaging systems; spherical, aspherical, and freeform optics; precision moulds; metal mirrors and reflectors; lenses required for camera, binoculars, projectors and human visions. Figure 1.1 shows some of the components that are manufactured by using SPDT.

Figure 1.1 Components and products made by using SPDT [Courtesy: Optics and Allied Engg. Pvt. Ltd., India, http://www.opticsindia.com/products/ir-optics-and-spdt/spdt-applications-areas/ as seen on 10-01-2019]

SPDT has important applications in the field of optics, instrumentation, electronics, military, medical, and space. These are listed as follows [Yu *et al.* (2011), Sumipro (2018), Chiu and Lee (1997), Goel (2013)]:

- Reflective mirrors in copper, gold, electroless nickel and aluminium alloys.
- Precision mould inserts and cores in electroless-plated brass, ferrous and non-ferrous metals for plastic lenses of camera, binoculars and projectors.
- Astronomical telescopic metal mirrors.
- Lenslet arrays, spherical and aspherical optical lenses such as diffractive lenses, Fresnel lenses, toric lenses and free form optics from crystals, metals, acrylic, and other materials.
- Medical instrumentation, optics for human vision (contact lenses, scleral lens) and implants
- High power machining laser optics and
- Infra-red hybrid lenses for thermal imaging, missile guidance systems for defense sector.

1.1 SPDT of Brittle Materials

During mechanical machining of materials, the material removal is achieved mainly by two mechanisms: ductile-mode and brittle mode. In the ductile mode, the chip formation takes place through the continuous plastic flow of material in front of the cutting edge of the tool when the resultant shear stress exceeds the critical value of material-dependent shear strength [John (2003), Mir (2016)]. Unlike the ductile materials, which have much larger fracture strains; brittle material exhibit extremely small fracture strain than its yield strength. As a result, the tensile and compressive stresses exerted by the tool develop small cracks in the workpiece. The initiated crack quickly propagates through the minimum resistance path to produce discontinuous chips. The brittle material fails to resist the load before its yield point and the chips are formed by the initiation and evolution of cracks.

Mechanical cutting of brittle materials is difficult due to the occurrence of fracture without significant plastic deformation. During this process, brittle material produces discontinuous chips which significantly affect the surface integrity of the part being machined. Thus, precision manufacturing of aspheric lenses from silicon or silicon carbide is quite difficult and challenging. In general, conventional grinding and polishing operations are employed to super finish the surfaces, but these processes are time consuming, tedious and highly skill dependent. During the last four decades, researchers worldwide noticed that the

brittle material has a critical layer or thickness of few nanometres that is called the "ductile-regime" under which brittle material behaves like ductile material. The brittle material can be deformed plastically to form continuous ductile chips under following conditions:

i) Machining below critical depth of cut [Leung *et al.* (1998)]
ii) Using extreme negative rake angle tool [Patten and Gao (2001)]
iii) Applying external hydrostatic pressure [Yan *et al*. (2001), Yoshino *et al.* (2001)].

To improve the surface finish of brittle materials, researchers worldwide tried to understand the phenomenon of **ductile regime machining**. In this process, the brittle material is removed by plastic flow, which produces crack-free surface. Initially, King and Tabor reported an investigation on ductile regime machining (DRM) on rock salt and proposed that high hydrostatic pressure plays a crucial role in the ductile removal of brittle material during the frictional wear [King and Tabor (1954)]. By using the same principle, the SPDT process carries out ductile mode machining of silicon, silicon carbide and other brittle materials at nanometric scale. However, application of controlled parameters viz. cutting speed, feed rate, rake angle, depth of cut and type of coolant is essential [Leung *et al.* (1998)].

Ductile regime machining can be understood from the well-known machining model proposed by Blake and Scattergood (1990). A schematic of the model is shown in Figure 1.2. It depicts the projection of the tool which is perpendicular to the cutting direction. R is the tool nose radius and f is the feed rate. Due to the round nose tool, the chip thickness varies from zero (at the tool tip centre) to a maximum (at the top of the uncut shoulder of the workpiece). All brittle materials exhibit an average surface damage depth which varies with the depth of deformation [Ohta *et al.* (2007), Lakhdari *et al.* (2019)]. With increase in the feed rate, the depth of deformation increases and it enhances the damage depth. The increased damage depth penetrates the cut surface and remains in the finished surface even after subsequent machining operation that leads to rough surface with fracture and cracks. Therefore, it is necessary to keep the depth of deformation as low as possible so that damage depth does not penetrate the cut surface. The maximum depth of deformation with which the material can be machined without the penetration of damage into the cut surface is termed as critical depth of cut and machining in this regime is termed as ductile regime machining.

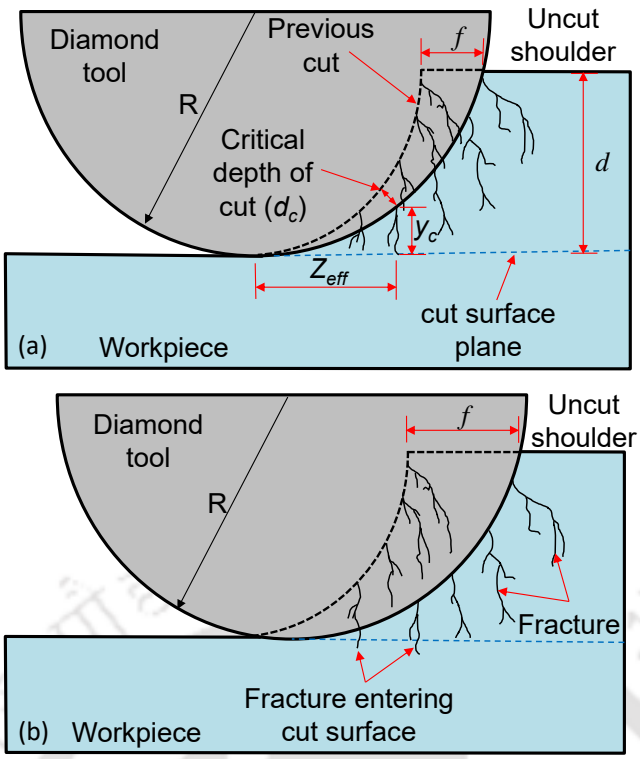

Figure 1.2 Schematic of ductile regime machining [Redrawn from Blake and Scattergood (1989)]

The literature ascertained that the brittle material can be machined in ductile mode by suppressing the propagation of cracks in the material. The propagation of cracks can be suppressed by applying compressive stress on the workpiece by the tool. Nakasuji *et al.* (1990) described the ductile transition and plastic deformation based on density of defects present in the materials. Brittle materials exhibit very small density of defects, which acts as the nuclei of fracture in brittle materials. Thus, if the stress field exerted by the tool is small, it minimizes, sometimes ceases the nucleation of the fracture. That means, when the depth of cut is kept small, the stress field generated at the cutting region is also small and thus, the initiation of fracture at the defects can be avoided. It was stated that all brittle materials exhibit a critical layer or thickness of few nanometres beyond that it behaves as ductile mode. As the depth of cut increases, the stress field also increases and cracks are initiated from the defects. Thus, material removal mechanism changes from ductile to brittle mode. The critical layer or thickness at which this transition occurs varies from material to material.

Researchers carried out both experimental and numerical studies to understand ductile regime machining process such as nanoindentation, plunge cutting and nano cutting. In general, nanoindentation is used for the measurement of mechanical properties such as hardness and Young's modulus. In this test, sample surface is deformed by an indenter having higher hardness than the sample material. The applied load and the displacement of the

workpiece due to the applied load data are then employed in the analytical model developed by Oliver and Pharr (1992, 2004) to obtain the mechanical properties. Lawn *et al.* (1994) observed ductile behavior of brittle materials during Hertzian indentation test. From then, researchers attempted a number of eminent works to find out phase transition, crack length and fracture toughness of brittle materials by using nanoindentation test.

Literature reports plunge cutting experiments to determine the critical depth of cut of brittle materials. In plunge cutting process, the cutting tool is moved along a path inclined to the workpiece surface. The depth of cut is varied from zero to few hundreds of nanometers, generally above the critical depth of cut of the material. The machined surface and cutting force values obtained from plunge cutting operation are then studied to understand the ductile to brittle transition. Reported research revealed that, damage free smooth surface was obtained up to few nanometers of depth of cut. When the depth of cut is increased further, surface roughness increases. This transition from smooth to rough surface provides useful information about ductile to brittle transition thickness of the material.

1.2 Motivation for the Present Research Work

Silicon and silicon carbide materials are widely used in semiconductor, defence, aerospace and biomedical applications due to their excellent mechanical, chemical and thermal properties. However, processing of these materials with conventional material removal process is very much difficult because of their brittleness. SPDT can easily produce optical finish surfaces on these materials; however, it causes severe tool wear. SPDT is a complex process as it involves formation of highly localized stresses, strains and temperature. The surface generation in SPDT comprises of burnishing, elastic recovery, plastic deformation, and materials swelling [Kong *et al.* (2006)]. Literature reports important research on analytical or numerical modeling of SPDT to mimic the complex physical phenomenon. Various numerical methods based simulations viz. molecular dynamics (MD) simulation and finite element method (FEM) simulation have been reported to study the SPDT process. MD simulation is regarded as the high-end numerical simulator which can simulate nanometric cutting conditions. It can simulate at an atomic scale and has the ability to describe the microstructural evolution of the material being processed. However, MD based simulations have a very limited application due to its nanometric level of process continuum. The molecular dynamic simulation requires huge computing time and abundant memory. FEM is capable of modeling complex physical phenomena which are sometimes not possible to visualize through experiments, and it cover a wide range of process continuum, i.e., from macro to nanometric scale.

Understanding of the effect of process parameters of SPDT on its performance parameters such as machining forces and surface roughness is important for improving the product quality and process efficiency. However, the SPDT process is slow due to nanometric level material removal. SPDT machining of hard and brittle material results in rapid tool wear which affects the productivity and product quality. Machining of ferrous materials causes high tool wear because of the chemical affinity of diamond with the carbon. Silicon (Si) is extremely difficult to diamond machine, primarily due to its hardness. Because of high temperature and friction generated during machining, diamond reacts with carbon particles to form SiC bond and causes rapid tool wear. SiC is hard, but it is regarded as brittle because of its low fracture toughness. Therefore it is prone to fracture and subsurface damage during SPDT operation. On the other hand, machining of soft and ductile materials using diamond tool also quite difficult due to the formation of built up edge (BUE).

After an extensive literature review on various aspects of SPDT process such as analytical, experimental and numerical studies on various process parameters, tool geometry and material aspects, it was found that very scant literature is available on numerical simulation of silicon and silicon carbide. Also, none of the research has reported on the parametric study of the process to optimize the process conditions to improve the efficiency and product quality. A need thus was identified to develop a finite element model to understand the physics of SPDT process and to mimic the practical phenomena of chip formation during nanometric cutting of brittle and ductile material using a diamond tool.

Very few attempts have been reported on optimization of SPDT of brittle materials to improve the process productivity and product quality. There is hardly any comprehensive and systematic study reported in the literature on the influence of critical machining parameters such as speed, feed, depth of cut, tool geometry parameters viz. rake angle, cutting edge radius on the performance measures, i.e., cutting forces and surface roughness. Conducting experiments to understand the effects of various process parameters, tool geometry, workpiece material, working condition on process output and product quality is important; however these are tedious; time consuming and costly. This provided the motivation to carry out the present research work on understanding the ductile regime machining phenomenon (DRM) of brittle material and ductile materials by using FEM based simulations of nanoindentation, plunge cutting, the SPDT operation of Si, SiC and Al; and to find out the optimum process conditions for desired productivity and product quality.

1.3 Scope of the Present Research Work

The present research work focuses upon understanding of DRM of brittle materials such as silicon, silicon carbide (difficult to machine) and machining of ductile material like Al6061-T6 (difficult to polish). Silicon (Si) is a vital substrate material used in the manufacture of refractive lenses, solar cells, electronic devices and infrared optics [Yan *et al.* (2012)]. Silicon carbide (SiC) is now being used in the manufacture of space-based optical imaging systems [Robichaud *et al.* (2008)], critical parts of automobiles, biomedical implants, electronics systems, fiber optics communication systems [Pulliam *et al.* (2000)]. SiC is hard, chemically stable, wear and corrosion resistant material. It exhibits good electrical and thermal insulation characteristics. Aluminium 6061-T6 alloy is highly ductile and mostly used in the construction of aircraft structures, yacht, automotive parts, optical mold inserts for plastic lens and most importantly aluminum mirrors (with aspheric surfaces) for optical industries [Dashwood and Grimes (2010)].

The present work primarily focuses on the development of a two-dimensional (2D) numerical modeling of single point diamond turning process using FEM. Initially, finite element method based two-dimensional numerical model of nanoindentation and plunge cutting process is developed to determine the ductile to brittle transition (DBT) thickness and to understand the ductile regime machining (DRM) of silicon and silicon carbide. This thesis aims at understanding of the ductile regime machining by identifying the critical depth of transition and thereby predicting the machining force and surface roughness to optimize the process conditions for the improvement of process efficiency and product quality.

Initially, a two-dimensional numerical model of actual SPDT process of silicon and silicon carbide using FEM is developed and then the experimental validation of predicted machining force values has been carried out. During the study, the effect of employing two different material models viz. Johnson-Cook (JC) and Drucker-Prager (DP) on the chip formation was studied. Further, parametric studies were carried out by the developed numerical model to study the effect of process parameters viz. speed, rake angle, depth of cut, cutting edge radius on the performance parameters viz. components of machining force.

An integrated finite element method-image processing technique (FEM-IPT) based methodology has been developed for the prediction of surface roughness during SPDT of Al6061−T6. Due to limited availability of SPDT machine and related resources for experiments; in the present work experimental studies were only carried out on Al6061-T6. The results were used to validate the developed FEM-IPT model. Further, the model was used

to investigate the influence of process parameters such as speed, feed and depth of cut on the surface roughness. Mixed level full factorial experiments were designed and carried out.

It is to be noted that the study on the effect of crystal orientation, tool wear, thermal and vibrations are out of the scope of this study. The work is primarily intended to determine the ductile to brittle transition zones and to obtain the required optical surface finish during the nanometric cutting of brittle as well as ductile materials. It is envisaged that the knowledge obtained from the present numerical and experimental studies will be useful to the researchers and industrial engineers to carry out efficient and quality SPDT operations.

1.4 Organization of the Thesis

The organization of chapters in this thesis in detail is as follows:

Chapter 1 presented an overview of the single point diamond turning process in terms of its mechanism, advantages and limitations, and applications. The motivation for carrying out research in the area of single point diamond turning of silicon, silicon carbide and aluminium has been brought out at the end of the chapter.

Chapter 2 presents an extensive literature review in the area of single point diamond turning process and outlines the objectives. The chapter highlights various challenges associated with the ductile-regime machining of hard and brittle materials. The status of research work on various aspects of SPDT process, such as ductile regime machining, nanoindentation, plunge cutting, numerical modeling, experimental investigations and parametric analysis is presented. The approaches toward the numerical modeling of SPDT process as well as experimental studies are critically studied. The chapter concludes by summarizing important observations from the literature review, and stating the research objectives.

Chapter 3 presents, in detail, modeling and simulation studies carried out on nanoindentation process to study the ductile to brittle transition. Details regarding the finite element modeling and the associated procedures are presented. The mechanical properties evaluated from the numerical study are compared with available experimental results from the literature. The deformations of silicon and silicon carbide have discussed with the help of nanoindentation simulations.

Chapter 4 presents finite element method based numerical simulations of plunge cutting of silicon and silicon carbide to study the ductile to brittle transition. Various output parameters such as surface topography and machining force were thoroughly analyzed and discussed. Three methods were employed, i.e., visual inspection of surface profile, variation of

machining force and specific cutting energy. A comparative analysis of these methods has also been presented. Moreover numerical simulations for an industrially important material i.e. silicon carbide have been presented and finally the validation of numerical predictions is presented. .

Chapter 5 presents, in detail, the development of nanometric cutting simulation of SPDT of silicon and silicon carbide using finite element method. The governing equations, boundary conditions and solution methodology for the analysis are explained at length. The model is validated in terms of force values with previously published experimental results. Chip morphology, material model, crack propagation and elastic recovery were studied in detail. Studies on the effects of various input process parameters viz. speed, rake angle, depth of cut and cutting edge radius on the performance parameters viz. machining forces of SPDT of silicon and silicon carbide have been presented in detail.

Chapter 6 reports, in detail, the development of surface roughness prediction model by integrating finite element method and image processing technique (FEM-IPT). The modules of the developed approach such as edge detection, digitization and surface roughness (Ra) calculation are presented in detail. Then simulations have been carried out on Al6061-T6 workpiece material to compare the surface roughness obtained from FEM-IPT technique with that of experimental results.

Chapter 7 presents, in detail, the experimental investigations on SPDT of Al6061. The objectives of this work were to validate the results of developed FEM-IPT technique and to determine the most influencing process parameters. Experimental details in terms of machine tools, fixtures, and measurement of responses are presented. A study on the influence of process parameters such as speed, feed and depth of cut on the surface roughness has been presented. Based on the study, recommendations for practical applications have been suggested.

Chapter 8 presents the important assessment and conclusions from the present research work. The scope for carrying out future work in this area is presented at the end of the chapter.

भारतीय प्रौद्योगिकी संस्थान गुवाहाटी
Indian Institute of Technology Guwahati

LITERATURE REVIEW ON SINGLE POINT DIAMOND TURNING, NANOINDENTATION AND PLUNGE CUTTING

2.0 Scope

This chapter presents a detailed literature review in the area of process modeling and simulation of single point diamond turning (SPDT). Initially, the details of the SPDT process in terms of mechanism, principle of working, machining parameters; and the challenges in machining of brittle materials are presented. Various modeling approaches such as analytical, numerical, and mathematical have been critically studied. Nanoindentation and plunge cutting techniques in the context of understanding the ductile regime machining (DRM) during SPDT have been critically studied. Published literature on experimental investigations into the influence of process parameters, cutting tool geometry, material properties of workpiece and tool on various response parameters, viz. force, roughness, stress, chip morphology are covered extensively. The chapter concludes by summarizing essential observations from the literature survey, identification of research gaps and stating the research objectives.

2.1 Conventional Machining of Brittle Materials

Mechanical processing of brittle material is characterized by the occurrence of fracture without significant plastic behavior. Brittle material produces discontinuous chips owing to brittle failure at the shear plane before any actual plastic flow occurs. The brittle fracture during machining significantly influences the surface integrity and dimensional accuracy of the part being machined. Thus, traditional machining is generally not recommended to produce precision components and high quality surface on brittle materials. Finishing operations such as grinding and polishing operations can produce mirror finished surfaces, but these are expensive, time-consuming and have low productivity [Fang *et al.* (2013)]. Literature reveals that brittle materials can be machined in ductile mode if the employed depth of cut is below the critical depth (nm). Due to nanometric depth, a number of issues arise during micro-nano machining. These are as follows:

- The cutting tool cannot be considered as perfectly sharp.
- The uncut chip thickness becomes equal or smaller than the cutting edge radius of the tool and hence the effective rake angle becomes highly negative.
- Material removal takes place through ploughing, rubbing or slipping phenomenon rather than shearing.

- Handling and transportation of micro components.
- The materials cannot be treated as isotropic and homogeneous.

2.2 Single Point Diamond Turning (SPDT)

Single point diamond turning (SPDT) is an ultra-precision machining process. The basic difference between a standard lathe and a SPDT machine is that the SPDT machine uses a sharp diamond tipped bit for its machining and it is equipped with hydrostatic/aerostatic bearings for the table and spindle; granite bed for vibration isolation and feedback system of sub-nanometer resolution. A schematic of the single point diamond turning machine is shown in Figure 2.1.

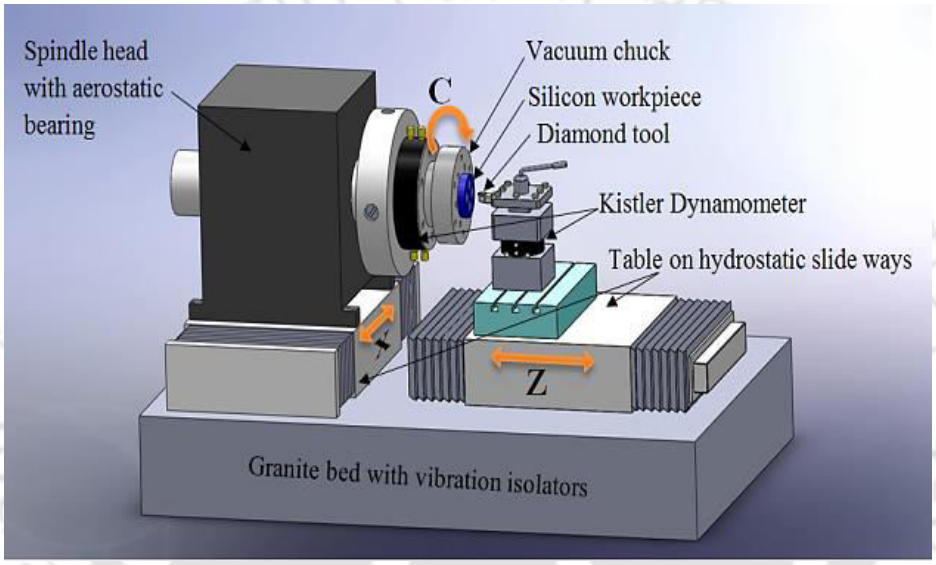

Figure 2.1 Schematic of Single Point Diamond Turning Machine

The first ever use of diamond turning can be traced back to the 1930s when the jewelry industry began diamond turning for manufacturing of watch dial components [Krauskopf (1984)]. However, the SPDT of metals such as aluminum and beryllium copper with the use of mono-crystal diamond tools was dated back to 1966 [Chiu and Lee (1997)]. Then the researchers started working on diamond turning in USA government labs such as Lawrence Livermore National Lab (LLNL) and Oak Ridge Y-12 National Lab. In the late 1970s, the SPDT machine was commercialized. Then it was started being employed in energy, optics, computers, electronics, space, and defense applications [Ikawa *et al.* (1991)]. In the eighties, this technique was used in the manufacturing of aluminum substrate drums in photocopiers, aluminum scanner mirrors and aluminum substrates for memory disks.

Initially, SPDT was reported to be used for machining of non-ferrous metals such as aluminum [Ding and Rahman (2012), Fang *et al.* (2014), Kushendarsyah and Sathyan (2013)], copper [Luo *et al.* (2014), Mahajan *et al.* (2010), Zong *et al.* (2014)], PMMA [Zhou

et al. (2010)], nickel [Lin *et al.* (2007)], brass [Yu *et al.* (2012), Wang and To (2011)] for the manufacturing of critical parts of telescopes, video projectors, lasers and imaging systems [Mishra *et al.* (2019)]. Processing of brittle materials viz. glass, ceramics, and crystals has become of greater interest to the researchers and engineers due to their growing demand in industries. Eminent efforts have been made by the worldwide researchers to understand the machining mechanics, especially ductile regime machining of brittle materials such as silicon, silicon carbide, germanium and glass to achieve crack-free optical finish surfaces. To achieve the crack-free surface, the brittle material is to be processed in ductile mode. The transition from ductile cutting mode to brittle cutting is influenced by parameters such as critical undeformed chip thickness (CUCT), hydrostatic pressure, cutting edge radius and tool rake angle. Later, researchers found a way to successfully machine the brittle material without any surface cracks and fracture. This was possible due to the discovery of "ductile regime machining" technique, wherein the material removal is accompanied by plastic deformation [Blake and Scattergood (1990)]. After this, SPDT has extensively been used for machining of brittle materials such as silicon [Fang (1998), Fang *et al.* (2007), Yan *et al.* (2003), Leung *et al.* (1998), Patten and Gao, (2001), Goel *et al.* (2013a), Singh *et al.* (2013)], silicon carbide [Patten and Jacob (2008), Patten *et al.* (2005), Ravindra *et al.* (2009), Luo *et al.* (2012), Goel *et al.* (2013b, c)], germanium [Patten (1996), Blackley and Scattergood (1989), Pawase *et al.* (2014), Yan *et al.* (2006a), Gupta *et al.* (2016)], and glass [Fang and Zhang (2004), Fang *et al.* (2003), Bhagwat *et al.* (2012)] in the ductile mode by controlling the process parameters, viz. depth of cut, speed and feed precisely.

2.3 Process Parameters of SPDT

Figure 2.2 shows the parameters that affect the machining precision of SPDT process.

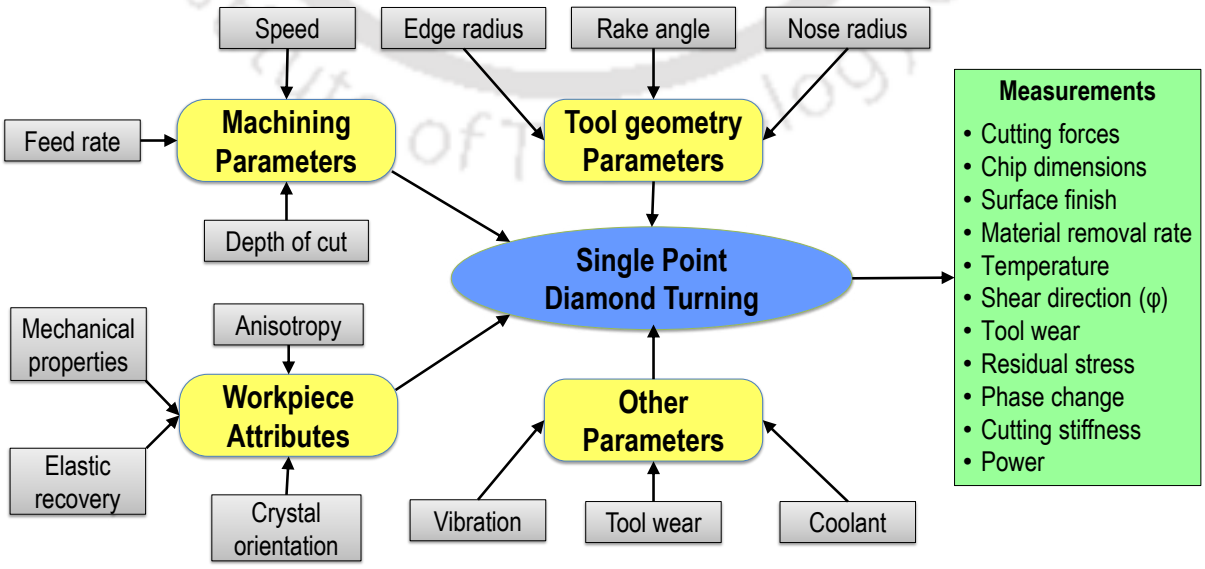

Figure 2.2 Inputs and output parameters during SPDT process

There are many parameters that influence the product quality and process performance of the SPDT process. These include process parameters, cutting tool geometry, workpiece and tool material properties (microstructure and crystal orientation), machine tool conditions, and machining conditions. These parameters can be broadly divided into four categories, namely machining parameters, tool geometry parameters, material properties, and other parameters. An extensive literature review has been carried out to understand the effects of these parameters on the SPDT performance parameters such as phase change, machining (cutting and thrust) forces, chip morphology, surface roughness, and tool wear. Details about the reported experimental and numerical works are discussed in the following sections.

2.3.1 Machining Parameters

Figure 2.3 shows the parameters that are generally employed in the machining of brittle and ductile material using SPDT process. Cutting speed also called surface speed or simply speed is the speed difference (relative velocity) between the cutting tool and the surface of the workpiece it is operating on. It is expressed in units of distance along the workpiece surface per unit of time, typically micrometers per minute (μm/min). Spindle speed (n_s) is the frequency of rotation of the spindle, measured in revolutions per minute (r/min or more commonly RPM). The depth of cut (d) is the immersion length of the cutting tool inside the workpiece along the axial direction of the tool. Feed rate (f) is the velocity at which the tool is fed to the workpiece. It is generally expressed either in units of distance per unit time (typically micrometer per minute (μm/min)) or in unit of distance per revolution (μm/rev) of the workpiece.

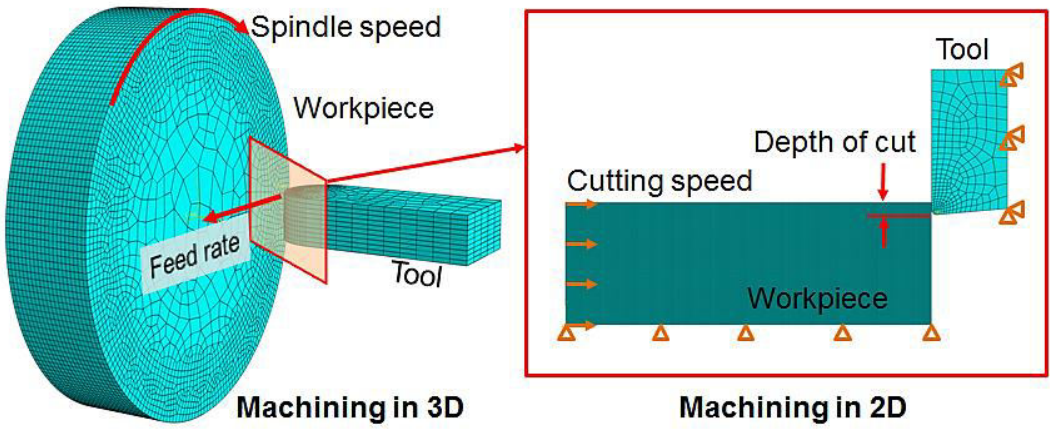

Figure 2.3 Process parameters in SPDT process

Researchers have extensively studied the influence of process parameters on surface finish, profile accuracy, and tool wear. Leung *et al.* (1998) reported that to obtain a high

quality surface using SPDT, the machining process should be in the ductile regime and the chip thickness must be of the order of a few micrometers and less than its critical value.

Leung *et al.* (1998) carried out diamond turning experiments on single crystal silicon by varying machining parameters such as feed rate, depth of cut, tool rake angles, cutting lubricants and crystallographic orientation of the crystal being cut. It was reported that proper selection of machining condition is essential for obtaining high quality surface on silicon. Born & Goodman (2001) conducted a series of experiments to study the influence of machining parameters on tool wear during ductile regime diamond turning of large single-crystal silicon optics. The machining parameters under investigation were depth-of-cut, feed rate, surface cutting speed, tool radius, tool rake angle and side rake angle, and cutting fluid. It was reported that the tool wear can be minimized if feed rate of 6.35 mm/rev, depth of cut of 1.016 mm, cutting speed of 228.6 m/min, rake angle of −60º and tool nose radius of 5.08 mm are used. Khatri *et al.* (2015) investigated the effect of spindle speed, tool feed rate and depth of cut on surface roughness in diamond turning of silicon optics. It was observed that a fine surface finish value of 31.6 nm can be obtained on Si at tool feed rate of 2.5 μm/rev, depth of cut of 1.5 μm and spindle speed of 1500 rpm.

Yan *et al.* (2002) proposed a method for ductile regime turning of silicon using a straight–nosed diamond tool. This method enabled thinning of undeformed chip thickness and at the same time allows to use large tool feed. It was reported that a surface finish of roughness 7.3 nm can be achieved when a process condition of 40 μm feed rate, 0° rake angle, 6° clearance angle and 1500 rpm of speed is applied. Khan *et al.* (2003) investigated the effect of feed rate on the surface finish of Al6061 alloy by varying the feed rate values from 0.3 μm/rev to 30 μm/rev. Results showed a roughness value of 13.55 nm for machining condition of feed rate of 6 μm/rev, spindle speed of 3000 rpm, depth of cut of 2 μm and diamond tool parameters of nose radius of 0.5 mm, rake angle of 0°. Patten *et al.* (2005) and Patten and Jacob (2008) carried out experimental and numerical studies on the ductile regime machining of SiC using SPDT. Authors studied the effect of rake angle and depth of cut on ductile behavior of single crystal SiC and demonstrated that ductile regime machining can be achieved when the depth of cut is less than 500 nm. Mahajan *et al.* (2010) investigated the quantitative effect of process parameters such as spindle speed, feed, depth of cut and tool nose radius on the surface roughness of copper. It was found that the tool nose radius is the most influencing parameter amongst the all considered parameters. A surface roughness value of 5.8 nm was achieved with the spindle speed of 3000 rpm, feed rate of 4 μm/rev, depth of cut of 6 μm and tool nose radius of 1.03 mm.

2.3.2 Cutting Tool Geometry

Figure 2.4 shows the tool geometry parameters employed in the machining of brittle and ductile material using SPDT process. These are rake angle, nose radius and cutting edge radius. Rake angle is the angle of inclination of rake surface from the reference plane. The rake angle can be of negative, neutral (zero) and positive value. A tool is said to have a negative rake angle when the wedge angle and clearance angle together makes an obtuse angle (Figure 2.5 (a). If both wedge angle and clearance angle together makes 90º, it will have zero rake angle (see Figure 2.5 (b)). When the wedge angle and clearance angle together makes an acute angle, the tool is said to have a positive rake angle (Figure 2.5 (c)). The cutting edge radius is the roundness of the corner made by rake face and clearance face. No tool can be made perfectly sharp as there will be always some bluntness at the cutting edge. Nose radius is the curvature of the tooltip measured in the top rake plane of a cutting tool.

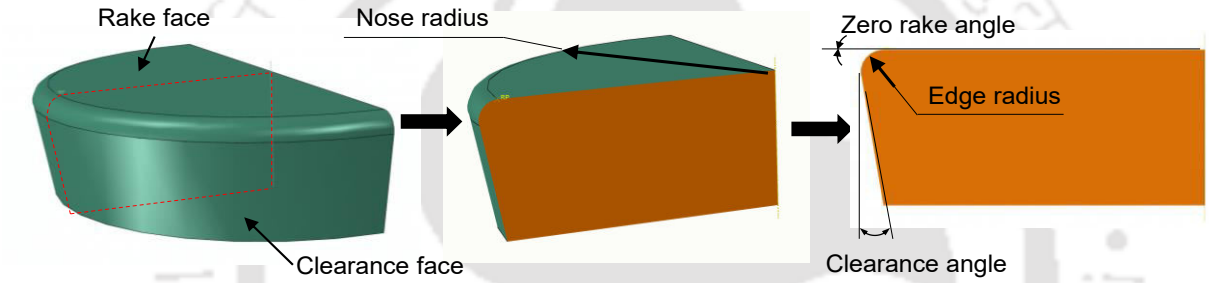

Figure 2.4 Schematic of the tool geometry of single point diamond tool

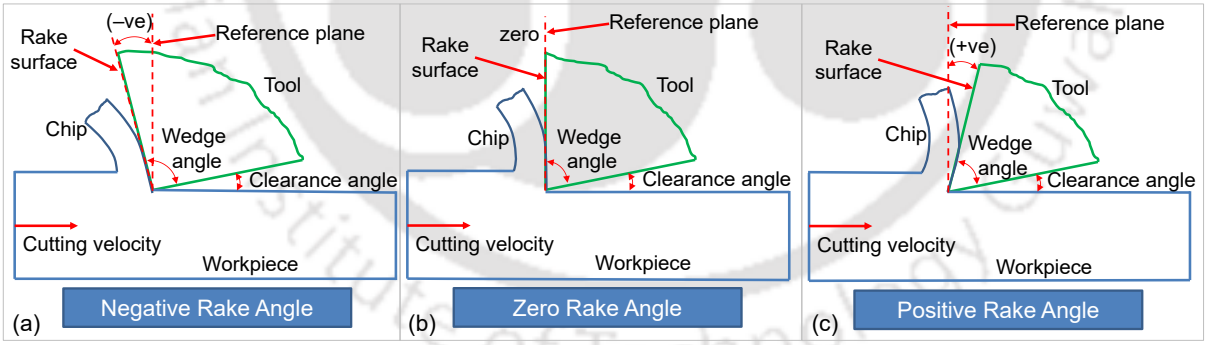

Figure 2.5 Schematic representations of positive, negative and zero rake angles of a tool

Reported studies have shown that the cutting tool geometry has a significant effect on the machining of brittle materials. It affects the performance parameters such as ductile to brittle transition, machining force, and surface quality. Komanduri *et al.* (1998) shown that the high negative rake angle and large edge radius (relative to the depth of cut) of the tool provide necessary hydrostatic pressure beneath the tool for the formation of plastic deformation by suppressing the initiation of brittle fracture. Blackley and Scattergood (1991) performed cutting tests on silicon and germanium with 0º, −10º and −30º tools and found that

the necessary critical depth of cut for ductile machining increases with the increase in negative rake angle. Patten and Gao (2001) used both the rake face (–45°) and the clearance face (–85°) as rake angle for machining of silicon and found that a smooth ductile cut with no evidence of fracture. It was reported that hydrostatic pressure plays an important role in minimizing fracture and producing smooth surfaces. It was also observed that the negative rake angle tool produces high hydrostatic pressure in comparison to that of positive and zero rake angle tools. However, Fang and Venkatesh (1998) claimed that a zero degree rake angle tool perform better in producing high quality surface finish than –25° negative rake angle tools during cutting of silicon.

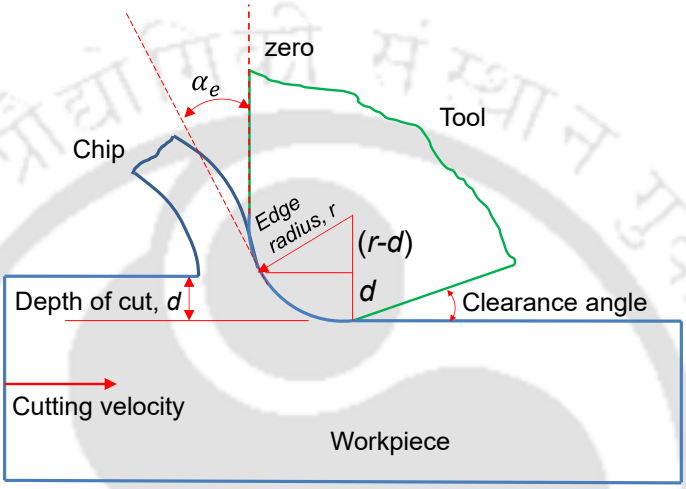

Figure 2.6 Schematic diagram for calculating the effective rake angle

The effective rake angle can be calculated with the help of tool geometry parameters as shown in Figure 2.6. It is given by equation (2.1) as suggested by Lai *et al.* (2012):

$$\sin \alpha_e = \frac{r-d}{r} = 1 - \frac{d}{r} \tag{2.1}$$

where r is the cutting edge radius, d is the depth of cut and α_e is the effective rake angle.

In addition to the rake angle, the cutting edge of the tool also plays an important role in ductile mode cutting of brittle materials. The relationship between the cutting edge radius of the tool and the undeformed chip thickness is instrumental in achieving ductile mode cutting of brittle materials. Studies by Fang and Zhang (2003) and Yan *et al.* (2002, 2009) suggested that the cutting tool of 0º rake angle can be negative if the cutting edge radius is more than the undeformed chip thickness. This negative effective rake angle helps in achieving ductile cutting of brittle material by providing the required hydrostatic pressure for the plastic deformation to occur. Asai and Kobayashi (1990) reported that during ultra-precision machining, to obtain a mirror-like surface, the undeformed chip thickness must be

equal to or smaller than the cutting edge radius of the tool. Yan *et al.* (2002), Leung *et al.* (1998), and Patten and Gao (2001) also reported the effect of cutting edge radius on the ductile cutting of brittle material. Leung *et al.* (1998) emphasized on the proper selection of negative rake angle to avoid the occurrence of extensive tensile cracking during diamond turning of brittle materials. Shibata *et al.* (1996) employed a diamond for turning of single crystal silicon with both –20º and –40º rake angle tools. Very fine surface finish was obtained when –40º rake tool at 100 nm depth of cut was employed.

Patten *et al.* (2005) performed experiments on 6H-SiC workpiece with a unique method of varying the tool rake angle by adjusting the center line of the tool cutting edge. This created an effective negative rake angle between 0º to 90º. It was observed that the ductile cutting is more favorable when the rake angle is changed from 0 to –45º and the depth of cut is below 100 nm. Moreover, it was noted that the cutting mechanism changes from ductile to brittle as the depth of cut increases from 100 nm to 500 nm.

Fang *et al.* (2007) reported that the cutting edge radius (r) has significant influence on the ductile to brittle transition (DBT). If the depth of cut is less than the edge radius then an effective rake is created and the chips are formed via extrusion like phenomenon. In this situation, 0º rake produces a negative rake and a negative rake produces a more negative rake angle. Based on the experimental work by Arefin *et al.* (2007) and a molecular dynamics simulation by Cai *et al.* (2007a), it was reported that in order to obtain ductile-regime machining of silicon, the cutting edge radius must be below 807 nm and higher than maximum undeformed chip thickness.

A number of researchers [Yan *et al.* (2003), Li *et al.* (2005), Goel *et al.* (2013a), Singh *et al.* (2013)] attempted to investigate wear of diamond tools and reported that flank wear dominates the wear of diamond tool during machining of silicon. Goel *et al.* (2011, 2013a) reported the formation of silicon carbide at the tool-work interface during machining of silicon. This phenomenon provided information regarding the initiation of wear of the diamond tool. Further, they described the tribochemistry involved in the process which leads to diamond tool wear.

Observations:

In SPDT process, the influencing parameters can be classified into four groups namely process parameters, tool geometry parameters, workpiece–tool properties and machining condition. Understanding of the effect of these process parameters of SPDT on its performance parameters such as machining forces and surface roughness is important for

improving the product quality and process efficiency. Literature reports significant research work on experimental studies of SPDT process on various materials. Most of these works have studied individual process parameters. Literature also reports some experimental studies on the effect of machining parameters on diamond tool wear. High capital and operating costs limit the extensive experimental studies of SPDT. After an extensive literature review on various aspects of SPDT process, it was found that very scant literature is available on numerical simulation of silicon and silicon carbide. Also, very scant research has been reported on the parametric study of the process to optimize the process conditions to improve the process efficiency and product quality.

2.4 Ductile Regime Machining of Brittle Materials

The optical quality surfaces are generally produced on brittle materials by employing DRM mode of cutting. The machining of brittle material where the chips are generated through plastic deformation rather than fracture is known as **ductile-regime machining**. King *et al.* (1954) made the first investigation on ductile regime machining (DRM) through plastic deformation on rock salt and proposed that high hydrostatic pressure plays a crucial role in the ductile removal of brittle material during the frictional wear. Brittle materials exhibit very low fracture toughness due to which they normally fracture with little or no plastic deformation. Thus, these materials are difficult to machine using conventional machining process. However, brittle materials can be machined using appropriate machining parameters at a very fine scale of the order of several nanometers. Blake and Scattergood (1989) stated that it is possible to machine brittle materials without introducing subsurface fracture damage when high stiffness, high precision machine are used. Further, the authors conducted precision machining of germanium and silicon using SPDT to investigate the ductile regime machining [Blake and Scattergood (1990)]. Similarly, Yan *et al.* (2001), Bridgeman and Šimon (1953) shown that high hydrostatic pressure can felicitate plastic flow in brittle materials such as silicon and glass at room temperatures. Hence, under the influence of large hydrostatic stresses, brittle materials including diamond can be deformed plastically even at room temperature. Kovalchenko (2012) provided an exhaustive review on ductile regime machining of semiconductors, ceramics, and glass.

The ductile-mode machining of brittle materials has emerged from the process of nanoindentation of brittle materials. Researchers noted that, indentation of brittle material with a very small depth of indentation by a sharp pointed diamond indenter leaves some irreversible deformation zone without any fracture [Lawn and Wilshaw (1975), Lawn and Evans (1977), Lawn *et al.* (1980), Marshall and Lawn, (1986)]. Lawn and Wilshaw (1975)

carried out nanoindentation tests on glass and observed ductile behavior of glass which led to the identification of the elastic-plastic transition. Studies by Huerta and Malkin (1976) and Moore and King (1980) also reported the plastic deformation of brittle materials such as glass and SiC at various process conditions.

Morris *et al.* (1995) stated that the ductile behavior, i.e., plastic flow of brittle material has its origin attributed to the phase transformation induced by high value of hydrostatic pressure/stress. On similar grounds, Yan *et al.* (2001) and Yoshino *et al.* (2001) carried out machining experiments on silicon under a high external hydrostatic pressure (more than 400 MPa). It was noted that ductile machining of silicon yielded continuous chips with smooth work surfaces. Yan *et al.* (2002) evaluated the feasibility of ductile-regime machining of silicon using large tool feeds of the order of 20 μm/rev. Fang and Zhang (2003) studied the effect of variation in tool edge radius on the performance of cutting of single crystal silicon. The results showed that ductile regime cutting can be achieved even by 0º rake angle tool if the undeformed chip thickness is less than a critical value, which consequently varies the effective rake angle.

2.4.1 Ductile to Brittle Transition (DBT)

The reported literature on ductile regime machining demonstrated that during machining of brittle materials, there is a transition from brittle mode to ductile mode when the depth of cut decreases to very small (usually < 1 μm) for ceramics [Toh and McPherson (1986)] and other materials such as glasses, semiconductor materials and crystals [Blackley and Scattergood (1994), Fang and Venkatesh (1998), Moriwaki *et al.* (1992)].

Literature reveals eminent research works on understanding of brittle-ductile transition phenomenon through indentation [Yan *et al.* (2006b), Rao *et al.* (2007), Goel *et al.* (2014a, b)], scratching [Meng *et al.* (2015)], taper turning [(Arif *et al.* (2013), Xiao *et al.* (2018), Yan *et al.* (2012), Fang *et al.* (2005), Fang and Zhang (2003)], scribing [Wu and Melkote (2012)], grinding [Yin *et al.* (2003), Yuan *et al.* (2012), Zhu *et al.* (2014)] and machining [Blakely and Scattergood (1994), Beltrao *et al.* (1999), Ngoi and Sreejith (2000), Patten *et al.* (2005), Yan *et al.* (2009a, b), Goel *et al.* (2013a, b)].

Blake and Scattergood (1990) suggested that, during nano-scratching and nano-indentation process, the critical chip thickness defines the regime of plastic deformation. Accordingly, a new machining model was proposed to explain the ductile regime machining of brittle materials as shown in Figure 2.7 (a).

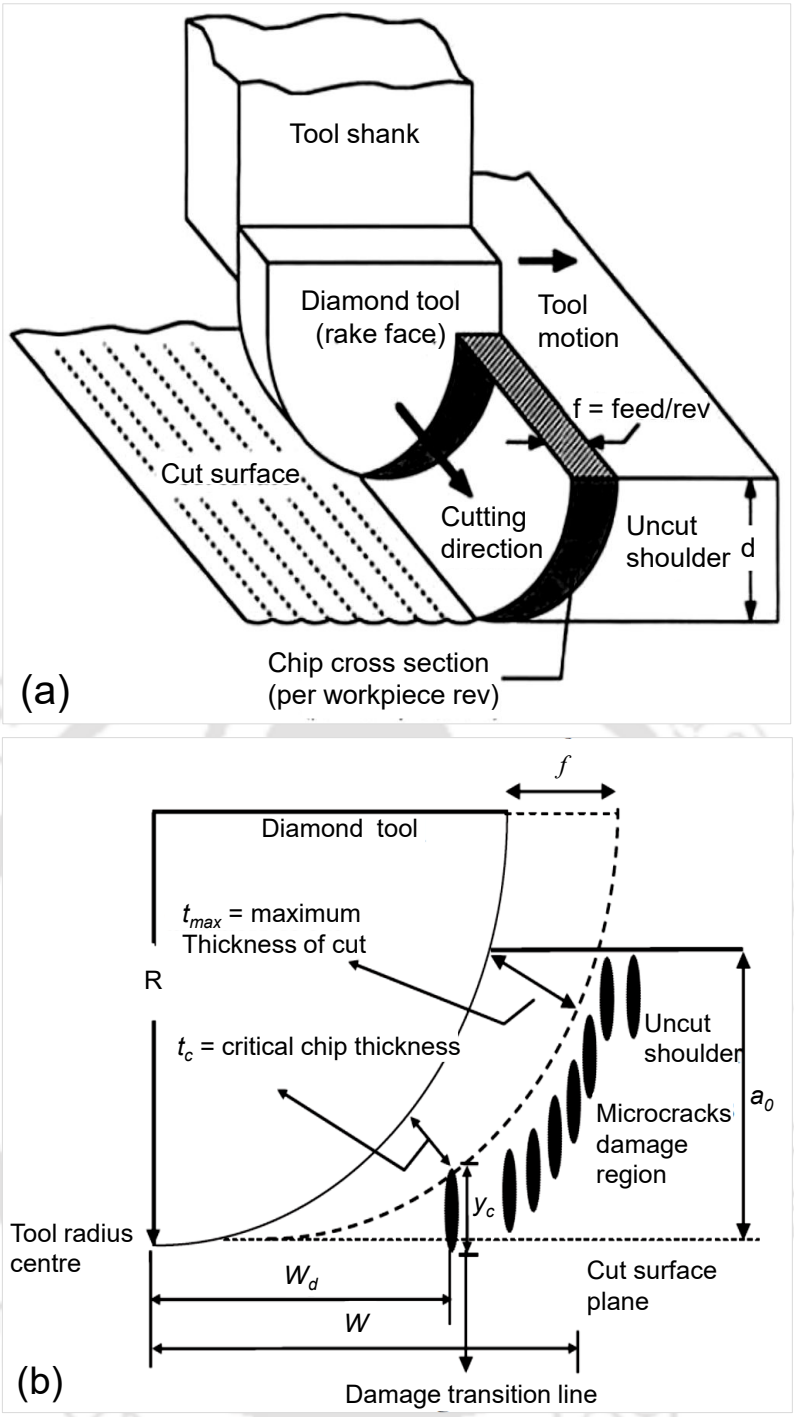

Figure 2.7 (a) Ductile-regime machining model using a round nose cutting tool [Blake and Scattergood (1990)], (b) Analytical model of ductile-regime machining [Blackley and Scattergood (1991)]

This theoretical machining model has widely been used as the machining mechanism of all brittle materials. Figure 2.7 (b) shows the brittle-ductile transition model proposed by Blackley and Scattergood (1991) for the cutting of brittle materials. It depicts a projection of the tool, perpendicular to the cutting direction, where f is the feed rate, y_c the average surface damage depth and W_d the distance from the tool centre to the fracture-pit transition on the uncut shoulder. Authors suggested that to achieve ductile regime machining of brittle

material, feed rate, depth of cut and tool nose radius should be chosen wisely so that average damage depth does not penetrate into the finished cut surface.

Shimada *et al.* (1995) proposed a generalized hypothesis for brittle-to-ductile transition in micro-machining and micro-indentation of Si and $LiNbO_3$. It was suggest that any material, in spite of their ductility, can be machined in ductile mode under the sufficiently small scale of machining, i.e., nanometric level depth of cut. Fang and Venkatesh (1998) demonstrated the diamond cutting of silicon to achieve surface finish of the order of tens of nanometers. A critical depth of cut of 236 nm was obtained for single crystal silicon where the ductile-brittle transition occurs. Patten *et al.* (2007), Ravindra and Patten (2007) and Bhattacharya *et al.* (2006) examined the critical depth of cut at which the ductile to brittle transition (DBT) occurs for the polytypes of SiC and found that the DBTs are 70 nm, 820 nm and 550 nm for 6H-SiC, 4H-SiC and CVD 3C-SiC respectively. Similarly, Young *et al.* (2007) found the DBT for silicon as 20-40 nm. Gao *et al.* (2000) and Patten and Gao (2001) carried out nano-cutting on silicon and demonstrated the ductile response of silicon. In what follows, the nanoindentation and plunge cutting method are explained in details in the following subsections.

2.4.2 Nanoindentation

Since past few decades, the hardness measurement techniques have been improved with sophisticated instruments. Numerous methods and instruments have been developed to determine the mechanical properties of a material, e.g. tensile/compressive, shear, triaxial, scratch test, nanoindentation etc. For brittle materials such as Si and SiC, tensile/compressive testing is not suitable as it is difficult to obtain sufficient amount of strain before the material specimen fails.

Nanoindentation test is used to measure mechanical properties of materials such as hardness and Young's modulus. In this test the softer material of interest (specimen) is deformed by a harder material (indenter) whose properties are known. Indentation techniques can also be used to obtain the strain-hardening exponent, creep, fracture toughness, viscoelastic properties and stress-strain data. Nanoindentation is similar to the conventional hardness testing method in which the scale of the penetration is measured in nanometers rather than in micron or millimeters. It is also considered as nondestructive characterization technique as only a small area scale is considered for deformation. Literature reveals that the hypothesis of ductile-mode machining has emerged from the indentation of brittle materials. Nanoindentation helps in understanding of ductile to brittle transition and evaluation of plastic deformation of brittle materials. Many researchers [Rao *et al.* (2007), Yan *et al.* (2005a,

2005b, 2006b, 2010), Goel *et al.* (2014a, b)] worked on nanoindentation of brittle materials and suggested that under a specified hydrostatic pressure or below a certain thickness (in the range of few nanometers to submicron), brittle materials behave as ductile material even at ambient temperature. This concept is especially useful in the machining of brittle materials, since this ductile phase transition due to hydrostatic pressure can be used as a guideline to remove the material in ductile mode. Moreover, it is possible to extract strain-strain data for brittle material, which is not possible through conventional tensile/compressive testing as it is difficult to obtain sufficient amount of strain before it fails during tensile loading.

In general, two types of nanoindentation systems are used for indentation purpose, i.e., MTS NANO Indenter XP (MTS Corporation, Nano Instruments Innovation Center, TN, USA) and a micro-force tester (Instron Corporation, Norwood, MA, USA) [Zhang (2007)]. A typical nanoindentation instrument consists of three basic components: (a) an indenter mounted onto a rigid column or load frame, (b) an actuator for applying the force and (c) a sensor for measuring the indenter displacements. The indenter (generally Berkovich indenter) is attached to the holder using a rigid metal-bonding process. Diamond is mostly preferred in making of the indenters because it has high hardness and elastic modulus. Moreover, it minimizes the deformation of the indenter during indentation as compared to other less-stiff materials in which the elastic displacements of the indenter must be considered.

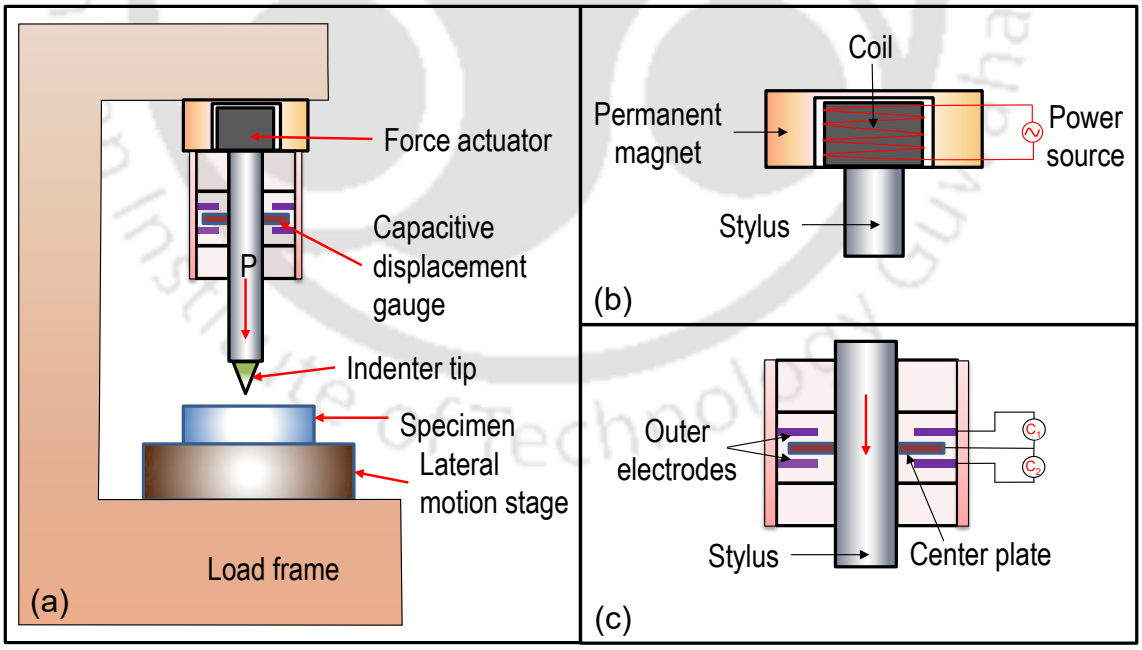

Figure 2.8 (a) Schematic of typical nanoindentation tester, (b) Force actuator, (c) Capacitive displacement gauge [Nair *et al.* (2014), Sun *et al.* (2018)]

Figure 2.8 (a) shows the schematic of a typical nanoindentation tester with a force actuator and a capacitive displacement sensor. Small forces are generated either (a)

electromagnetically with a coil and magnet assembly or (b) electrostatically using a capacitor with fixed and moving plates or (c) piezoelectric actuators. The force actuator with coil and permanent magnet assembly is shown in Figure 2.8 (b). The most common and earliest means of applying force is to insert a coil inside a permanent magnet. The magnetic field is generated by varying the current inside the coil. This generated field interacts with the field of the permanent magnet, which generates the necessary force to push the holder with indenter onto the sample. However, the current that is used to actuate the magnet produces joule heating effect that leads to thermal drift in the instrument. In case of electrostatic force actuation, the voltage is applied between the middle and upper/lower plate, and the generated force is proportional to the square of the voltage. The advantage of the electrostatic force actuation lies in its temperature stability and good control over thermal drift. The vertical displacement is measured using a capacitance technique, i.e., by measuring the downward displacement of the plate at the center with respect to those of the two outer plates (Figure 2.8 (c)).

For brittle materials, nanoindentation finds a very important and useful technique as it is capable of finding physical parameters which are difficult to obtain from general tensile/compression tests. It is capable of providing nanometric displacement to the tip of the indenter and recording of a very small load value in the range of mN with high degree of precision. The capital cost involved in nanoindentation instrument is very high in comparison to that of conventional micro hardness testing instruments. Lawn *et al.* (1994) observed distributed irreversible deformation in brittle ceramics during Hertzian indentation tests. It was concluded that brittle material shows an effective ductility behavior in the indentation stress-strain response. A model was developed to quantitatively represent the relationship of the radial crack size and the fracture toughness of the material. Later, Oliver and Pharr (1992, 2004) taken up the model and derived an analytical model to determine mechanical properties such as Young's modulus and hardness from the nanoindentation simulation.

Yan *et al.* (2005a, 2005b, 2006b) and Pandey *et al.* (2011) investigated the phase change and amorphization of silicon by carrying out nanoindentation tests before and after the diamond machining. Transmission electron microscopic observation confirmed the formation of amorphous phase during diamond turning that affects the surface function of the machined part. It was observed that the machining-induced amorphous silicon is softer than diamond-cubic silicon. Rao *et al.* (2007) studied the phase transformation in both crystalline silicon (c-Si) and relaxed amorphous silicon (a-Si) during nanoindentation using sharp Berkovich tip. It was found that relaxed a-Si matrix is more prone to high pressure phase transformation (HPPT) compared to c-Si. Similar observations were reported by Goel *et al.* (2014a) during

experimental and numerical studies on nanoindentation on polysilicon and single crystal silicon. It was reported that the HPPT was observed to occur more preferentially along the grain boundaries than across the grain boundaries. In the subsequent work, Goel *et al.* (2014b) presented extensive experimental work on nanoindentation tests on 4H-SiC. Authors observed yielding or incipient plasticity in 4H-SiC typically at a shear stress of about 21 GPa (an indentation depth of 33.8 nm) through a pop-in event. Recently, Yao *et al.* (2018) reported phase transformation of SiC from 4H to 3C in the vicinity of a crack during nanoindentation.

Observations:

Nanoindentation is found to be a very useful tool to obtain various mechanical properties such as Young's modulus, hardness, strain-hardening exponent, creep, fracture toughness, viscoelastic properties, and stress-strain data. However, it is very difficult to obtain the *in-situ* information about the stress and pressure developed, temperature profile, and displacement underneath the indenter during physical experiments. Therefore, the use of numerical techniques such as MD and FEM can thought to be simple, easy and economical alternatives to costly, tedious and time-consuming physical experiments. Literature reports experimental studies on nanoindentation of silicon and silicon carbide to understand the phase transition during the nanoindentation test. Scant literature has been reported on MD simulation of nanoindentation process; whilst, very scant literature has been reported on FEM simulation of nanoindentation of silicon and silicon carbide. Moreover, none of the literature has attempted to determine the ductile to brittle transition thickness.

2.4.3 Plunge Cut

A taper cut or inclined plunge cut is a machining concept which is used to determine the ductile to brittle transition zones. This helps in identifying the critical depth of cut so that crack-free surface can be obtained during machining of brittle materials. In this concept, material removal is carried out on an inclined surface. This allows varying the chip thickness from zero to a few nanometers. Figure 2.9 shows the schematic of a plunge-cut made on a brittle material as described by Brinksmeier *et al.* (1995) and Leung *et al.* (1998). Initially, as the depth of cut starts from zero to few nanometers which is much smaller than the cutting edge radius, elastic recovery is experienced, this is called elastic zone. As the depth increases, the material experiences the elastic to elastic-plastic zone. In this zone as well, there is no material removal occurs and only ploughing phenomenon occurs. In this zone, the depth of cut is still much lesser than the cutting edge radius and can also be correlated to nanoindentation where slight residual depth can be found after the unloading step.

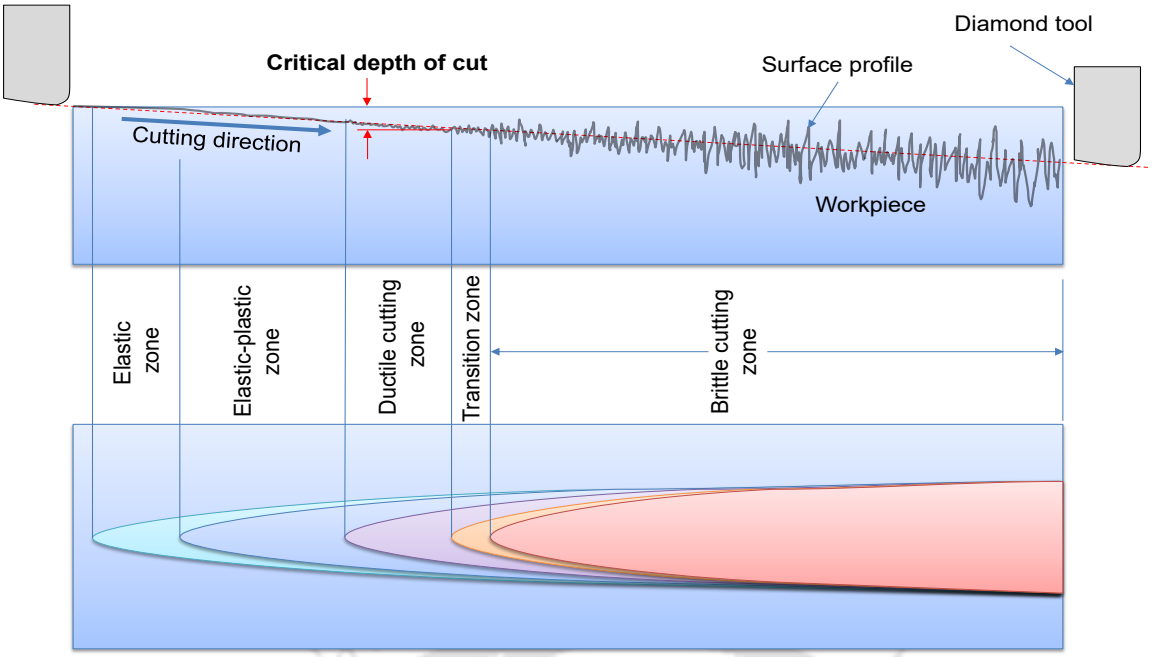

Figure 2.9 Sectional front view and top view of plunge cut showing different zones of material removal with critical depth of cut [Redrawn from Brinksmeier *et al.* (1995) and Leung *et al.* (1998)]

After the elastic-plastic zone, the depth of cut slowly becomes comparable to the cutting edge radius and the material starts flowing along the rake face of the tool. Here, the thrust force continues to increase without visible change in surface topography, i.e., any trace of surface damage. As the depth of cut increases further, brittle micro fractures starts appearing which leads to lower the thrust force and it becomes equal to the cutting force. This zone is termed as ductile-to-brittle transition zone. Beyond transition point, the thrust force becomes lower than the cutting force because material undergoes brittle fracture and the thrust force per unit volume of material removed decreases as compared to the cutting force. In this zone, damage and fracture occur on the surface. As per Arif *et al.* (2013) and Fang and Zhang (2003), if the undeformed chip thickness is very small, plastic deformation serves as the dominant mode of material removal. This is because, the energy required to extend pre-existing flaws in the microstructure of brittle material exceeds the energy required to mobilize the micro-structural dislocations [Arif *et al.* (2013)]. Hence, machining energy, also known as specific cutting energy is a viable parameter to characterize the modes of material removal while machining a brittle material.

Brinksmeier *et al.* (1995) carried out plunge cutting experiments on an inclined surface in monocrystalline brittle materials such as silicon and germanium. The inclined cut permits the study of varying depths of cut along the tool path. Figure 2.10 shows an inclined angle plunge cut. The experiments clearly showed the presence of a critical depth. Above the critical depth, brittle material removal occurs and below it, the ductile mode of removal was

observed. A small zone of elastic deformation involving rubbing or friction was also observed. This technique is now widely used by researchers to determine the ductile mode cutting conditions for several materials.

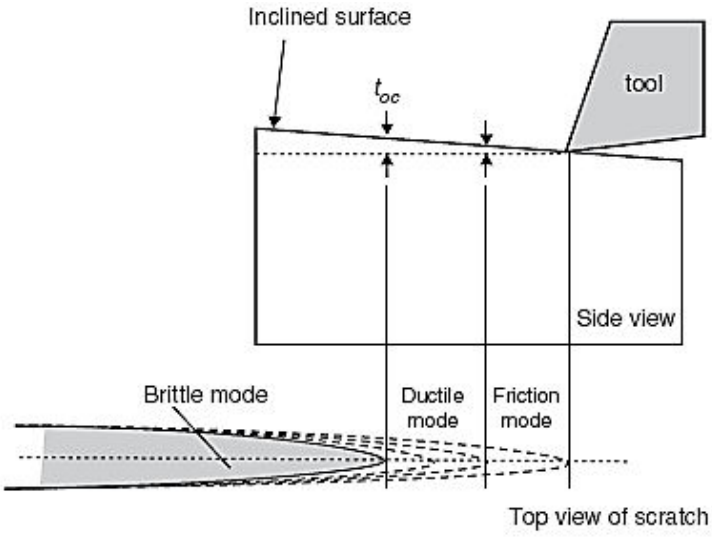

Figure 2.10 Schematic of an inclined angle plunge cut [Brinksmeier et al (1995)]

Leung *et al.* (1998) investigated experimentally the influence of depth of cut during nanometric cutting of silicon by varying depths of cut, and found three distinct regimes: viz., elastic, ductile and brittle. These regimes are schematically shown in Figure 2.11.

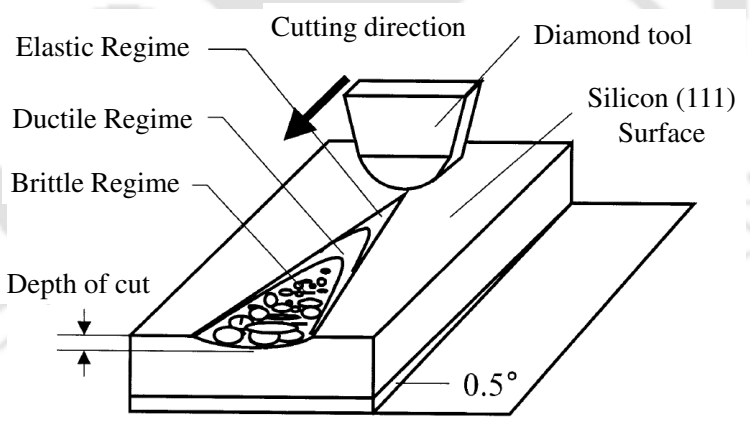

Figure 2.11 Influence of depth of cut and feed rate on ductile-brittle transition [Leung *et al.* (1998)]

Fang and Venkatesh (1998) carried out taper cutting (inclined plunge cutting) experiments with increasing depth of cut on single crystal silicon. Figure 2.12 shows the topographic details studied by using Atomic Force Microscopy (AFM). The use of 0º rake diamond tool results in better surface finish than with −25º rake tool at the same speed. It was concluded that 0º rake tool can be used at 90 m/min to obtain 1 nm finish, whereas with −25º rake the speed has to be 9 m/min**.** An *et al.* (2015) carried out experimental studies on

nanometric plunge cutting of BK7 and fused silica glasses to investigate machined surface morphology, surface roughness, cutting force and specific cutting energy. The results revealed that the critical undeformed chip thickness for BK7 was found as 320 nm and for fused silica as 30 nm.

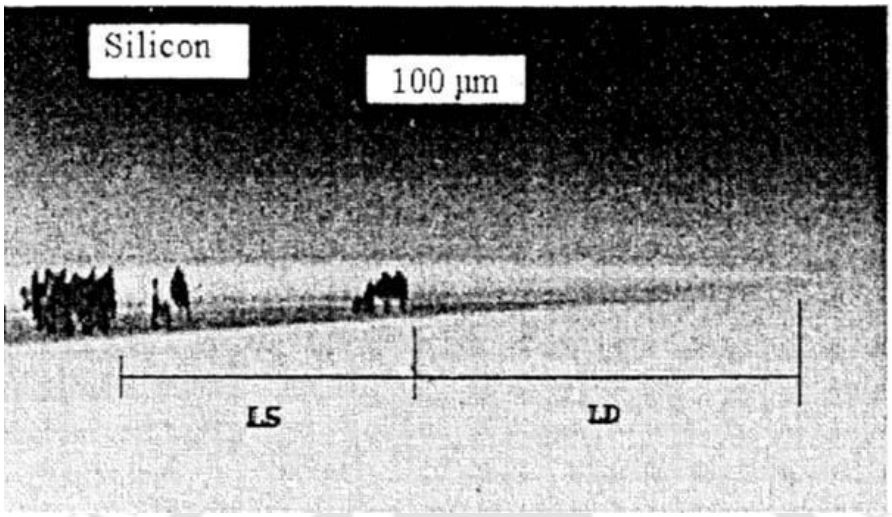

Figure 2.12 Photograph of an inclined plunge-cut groove shows clearly ductile and semi-ductile areas [Fang and Venkatesh (1998)]

Chao *et al.* (2002) used face turning experiments with a slightly tilted workpiece to determine the DBT by using the analysis of surface roughness. Results showed that a critical depth of cut of 0.2 μm to 1 μm was obtained when a round-nose tool was used. Fang and Zhang (2003, 2004) performed taper cutting experiments with increasing depth of cut on single crystal silicon and BK7 glass with the inclination ratio of 1:10000. The tool edge radius was estimated to be 110 nm. Taper cutting with a cutting tool of −80º rake was conducted by moving the 0º rake tool backward. It was observed that when the depth of cut was less than a threshold value, the plunge-cut surface was fairly rough and poorer than the surface before machining due to plowing and sliding action. Yan *et al.* (2009b) conducted plunge-cutting experiments on single crystalline silicon using diamond tools at a low speed. The results showed that the thickness of the machining-induced amorphous layer strongly depends on the tool rake angle and depth of cut, and varies synchronously with surface waviness. Authors proposed a subsurface damage model by considering the phase transformation and dislocation behavior of silicon under high-pressure conditions. Subsequently, Yan *et al.* (2012) carried out plunge cutting experiments along different cutting direction on single crystal silicon using different tool rake angles. It was found that amorphization, poly-crystallization, dislocation and internal microcracking were occurred depending on the cutting direction. In the recent study, Xiao *et al.* (2018) investigated the mechanism of brittle-ductile cutting mode transition from the perspective of mechanics in the cutting zone. FEM modeling and experimental study

was conducted on SiC to verify the analysis of the mechanics, and to estimate the critical undeformed chip thickness according to the proposed mechanics.

Observations:

From the literature review, it was learned that taper or plunge cutting can be used to study the ductile regime machining of brittle materials. This helps in determining the ductile to brittle transition zones thereby identifying the critical depth of cut. This is further helpful in producing crack free surface during machining of brittle materials. In a plunge cutting process, the depth of cut is varied from zero to few hundreds of nm, normally above the critical depth of cut of the workpiece material. A significant literature has been reported on experimental study of plunge cutting of silicon and silicon carbide. However, very scant literature is available on numerical simulation of plunge cutting simulation to determine the ductile to brittle transition of silicon and silicon carbide. A need thus exist to develop a numerical model for quicker and accurate prediction of ductile to brittle transition of silicon and silicon carbide.

2.5 Performance Parameters

Researchers studied various output parameters such as machining forces, surface finish, ductile to brittle transition, phase change, chip morphology, and specific cutting energy during SPDT of various materials. These are briefly discussed in the following sections.

2.5.1 Machining Forces

Over the years, cutting forces have been extensively investigated to gain a pivotal understanding of mechanics of chip formation and tool wear during a material removal process. High cutting forces influence surface integrity; increase the power consumption and cause the tool failure. Analysis of cutting forces is important in determining the machinability, ductile to brittle transition and optimization of process parameters. The principal cutting force components in machining include tangential cutting force which is in the direction of cutting velocity, feed force in the direction of feed and thrust force normal to the cutting velocity. During the past few decades, various models have been developed for the determination of forces in cutting operations and well documented in the literature. The well-known Merchant's force model [Merchant (1945a, b)] is based on orthogonal cutting assumed perfectly sharp tool and derived an analytical relationship for various parameters such as cutting and thrust forces, shear angle, tool rake angle, and friction angle. This model also provides relationships of various forces such as cutting force, thrust force, shear force, normal

shear force, friction force and normal force component. In the late eighties, Oxley (1989) developed a slip-line theory based model to predict various machining parameters such as chip thickness and tool-chip contact length involved in the metal cutting process.

However, the primary assumption of sharp tool used in Merchant and Oxley's models cannot be used in SPDT machining [Liu *et al.* (2004)]. As the depth of cut approaches to nanometric scale, the bluntness associated with the tool tip creates a 'ploughing' action rather than shearing, which is the primary mode of chip formation in SPDT process. Therefore, these models cannot be directly applied to determine the machining parameters during SPDT process. This led to the development of newer theories. Researchers have reported various analytical models to predict the machining parameters. Lo-A-Foe *et al.* (1988) proposed a analytical model based on the model introduced by Dautzenberg and his team to estimate the cutting force and surface profile while machining aluminum and brass using single point diamond turning. Patten *et al.* (2007) presented an analytical model by extending the existing Lee and Shaffer's second model to predict the chip thickness, cutting force and thrust force. Authors validated the developed model for nanometric machining of silicon carbide for the experimental condition of –45º rake angle tool and 50 nm and 250 nm depth of cut.

Literature reports eminent articles on experimental studies on the influence of process parameters on cutting force. Lucca *et al.* (1991) studied the effect of depth of cut on principal and thrust forces. It was concluded that the principal force becomes small and the thrust force increases as the depth of cut decreases. In case of very low depth of cut (smaller than the cutting edge radius), the effective rake angle changes to negative. Therefore, the material is forced to flow downward below the tool tip due to the edge radius. This causes the thrust force to increase and eventually cross over the cutting force. When the depth of cut increases above the cutting edge radius, shearing of material takes place, and then the thrust force decreases and cutting force increases.

Patten *et al.* (2005) carried out experimental studies on single crystal 6H-SiC by varying rake angles and depth of cut. Authors observed the ductile removal of SiC when the depth of cut is below 500 nm. This ductile behavior has been confirmed by production of smooth surfaces, formation of ductile chips and phase transformation to metallic state. Bhattacharya *et al.* (2005) carried out orthogonal ductile machining on polycrystalline SiC (6H) with three different diamond tools (one poly-crystal and two single crystal diamond tools from different manufacturer) having −45º rake angle and 5º clearance angle. Authors studied variation of cutting force and surface roughness with the depth of cut and type of diamond tool. It was reported that ductile regime machining of polycrystalline SiC is possible at depths of cut of 10

and 25 nm. In the subsequent work, Patten *et al.* (2007) and Patten and Jacob (2008) conducted FEM based 2D numerical simulations using pressure sensitive Drucker-Prager yield criterion. The generated cutting and thrust forces were compared with the experimental results. The results were in good agreement for smaller depths of cut (below the critical depth of cut). However, the simulations were not able to predict the forces where the experiments revealed brittle machining conditions as the model did not include a fracture criterion or brittle material removal mechanisms. Venkatachalam *et al.* (2009) proposed a predictive model to determine the undeformed chip thickness in micro-machining of single crystal silicon (1 1 1) materials. The comprehensive model includes a force model considering the rounded tool edge radius effect and ploughing. Yan *et al.* (2009a) carried out submicron-level orthogonal cutting simulation of silicon by using finite element approach. Authors investigated the effects of tool edge radius on cutting force, cutting stress, temperature and chip formation. It was observed that increase in the tool edge radius and a decrease in chip thickness causes a significant increase in the thrust force. The hydrostatic pressure generated in the cutting region also revealed the phase transformations in silicon.

Arif *et al.* (2013) developed an analytical model to predict the critical undeformed chip thickness for ductile–brittle transition in nano-machining of brittle materials based on specific cutting energy. The results were validated by carrying out the experimental study on silicon and BK7 Glass. The model was used to identify three distinct zones of machining, i.e., ductile-mode, transitional-mode and brittle-mode. Venkatachalam *et al.* (2015) studied the effect of microstructure on cutting forces and flow stresses in ultraprecision machining of polycrystalline SiC. MD simulations were performed to explore the effect of grain size, grain boundary and crystallographic orientation and found that both cutting force and thrust force increase with the increase in grain size. Goel *et al.* (2016) carried out MD simulations to study the mechanisms of plasticity during cutting of mono crystalline and polycrystalline silicon using polycrystalline and single crystal diamond tool. It was reported that the direct amorphisation from the pristine crystalline phase, in contrast to HPPT, is the root cause of plasticity in silicon. Moreover, the plasticity in silicon is triggered by large deviatoric stresses rather than the high temperature in the cutting zone. Similarly, Mir *et al.* (2017) presented numerical studies on surface defect machining (SDM) method in the fabrication of silicon using smooth particle hydrodynamics (SPH) simulation approach. An inverse parametric analysis was carried out to determine the Drucker- Prager (DP) constitutive model parameters of silicon from indentation test simulations. Cutting forces and steady-state chip formation in different defect type simulations were studied. It was revealed that SDM can be effectively

exploited to attain better surface finish and reduced tool wear in single point diamond turning process.

Observations:

Analysis of machining forces is important in view of the computation of power consumption, machinability study, and prediction of tool failure. Till date, significant experimental works have been reported on understanding of the cutting mechanism and chip formation during machining of silicon and silicon carbide. However, as the machining scale enters from micro to nano regime, it becomes complicated and challenging to study the force, pressure, stress, and roughness during the cutting process. Important numerical research works on SPDT process using molecular dynamics (MD) have been reported to study the insight of the machining process by analyzing stress, chips formation, temperature, and phase change during the machining process. However, experimental validation of MD based results is still difficult due to its very small, i.e., atomic level study domain. Few attempts have been reported on numerical simulations using finite element method. Very scant literature is reported on the influence of various material models on the process performance during numerical simulation of SPDT process of brittle material. Selection of proper material model is essential in obtaining accurate results. Researchers have reported use of various material models such as Johnson-Cook, Johson-Homilquist and Drucker-Prager for modeling of ceramic materials. However, there is no comparative study amongst these material models for machining of Si and SiC is reported till date. Also, scant research work is reported on systematic parametric study based on the numerical simulation of SPDT of Si and SiC.

2.5.2 Surface Finish

Production of required surface finish is essentially an important aspect of SPDT to generate high quality optical surfaces such as mirrors, reflectors, and lenses used for optical systems. During the process of material removal, the tool wears out, and surface quality degrades. Measuring the surface roughness *in-situ* is difficult. During the SPDT process, the factors that affect the surface roughness are feed, depth of cut, speed, tool geometry, material properties, machine tool errors, tool wear, and chatter/vibrations. Under ideal conditions, the surface roughness profile can easily be computed by using the tooltip profile and feed per revolution. Surface roughness also depends on the material properties. To achieve the nanometer level surface roughness and sub-micrometer level form accuracy, extremely high precision measuring instruments are needed to inspect the quality of the machined surfaces [Ali (2012), Qian and Takacs (2012)].

It is reported that, to achieve good surface finish, the brittle material should be machined in ductile mode. Many research works have been reported on experimental studies on SPDT of silicon and silicon carbide to study the ductile regime machining. Blake and Scattergood (1989, 1990) experimentally investigated the formation of ductile chips during machining of silicon and germanium. It was observed that ductile chips can be obtained if the depth of cut is maintained below 200 nm for germanium and 250 nm for silicon while using −10º and −30º rake angle tool respectively. However, this thickness is affected by the tool rake angle. Lucca *et al.* (1994) studied the aspects of surface generation in orthogonal ultra-precision machining of copper using single point diamond tools. It was found that depth of damage was unaffected by cutting velocity, feed rate and nominal depth of cut whereas crystal orientation was seen to have largest affect. Leung *et al.* (1998) experimentally demonstrated the possibility of ductile-regime machining of single crystal silicon under different cutting conditions such as feed rate, depth of cut, tool rake angles, cutting lubricants and crystallographic orientation of the crystal being cut. It was reported that a surface finish in the order of 2.86 nm can be obtained at the process condition of speed of 10000 rpm, depth of cut of 1 μm, feed rate of 1 μm/rev, rake angle of −25º, clearance angle of 10º, tool nose radius of 0.637 mm and alcohol as cutting fluid. Cheung and Lee (2000) presented a model-based simulation system for the analysis of surface roughness generation in ultra-precision diamond turning. Later, Cheung and Lee (2001) presented parametric analysis of nano surface generation of aluminum alloy. It was found that the tool feed, tool geometry, spindle error motions and relative vibration between the tool, materials swelling and tool interference are the important factors that contribute to the surface generation in SPDT. Chan *et al.* (2001) investigated the surface generation in ultra-precision diamond turning of Al6061/15SiC_p metal-matrix composites based on different analytical approaches which include parametric analysis, cutting mechanic analysis, finite element method (FEM) analysis and power spectrum analysis. Parametric analysis was performed to explore the *in-situ* inter-relationships between the process parameters and the surface roughness. Khan *et al.* (2003) presented experimental study on Al6061 alloy to investigate the effect of feed rate on surface figure and surface finish keeping all other parameters constant. An empirical formula was derived from the practical surface finish versus the tool feed rate and observed that better quality surface finish can be obtained when a very low feed rate is employed. Bhattacharya *et al.* (2006) carried out scratching experiments of CVD coated silicon carbide using diamond styli and tool to study the ductile response and to determine the DBT depth. Results showed a surface roughness of less than 20 nm can be achieved with cutting speed of 0.001 mm/s, feed rate of 1μm/rev and estimated depth of cut of 500 nm and tool having 3 mm nose radius, −45º rake

angle and 5º clearance angle. Lee *et al.* (2007) developed a multiscale simulation model that comprises of a microplasticity model, a dynamic model and enhanced surface topography model. The model generates a 3D nanosurface and the simulated roughness values were found to agree well with the experimental ones. Arefin *et al.* (2007) conducted experiments on silicon to determine the upper bound of cutting edge radius. It was stated that for brittle material to be cut in ductile mode, the undeformed chip thickness must be smaller than the tool edge radius. However, in order to increase the productivity, the undeformed chip thickness is expected to be as large as possible. Therefore, the tool edge radius is expected to be as large as possible. The upper bound value reported in this work for cutting of silicon wafer material with a single crystal diamond tool was found to be between 700 to 800 nm. Mohammadi *et al.* (2015) carried out diamond cutting of single crystal silicon coupled with micro-laser assisted machining (μ-LAM). A laser was used to heat and thermally soften the work piece material before carrying out the cutting process. Authors investigated the effect of laser heating and tool rake angle on the surface roughness. It was found that laser heating improves the surface roughness by 80% and −25º rake angle tool gives better surface finish than −45º rake angle tool.

Literature also reports eminent articles on prediction of surface roughness by developing mathematical expressions by using design of experiment (DOE) study of silicon [Krulewich (1996), Born and Goodman (2001)], silicon carbide [Patten and Jacob (2008), Ravindra and Patten (2008), Venkatachalam (2007)] and Al6061 [He *et al.* (2015), Khan *et al.* (2003), Mishra *et al.* (2014)]. Yan *et al.* (2003) developed a ductile machining system based on the straight line enveloping method to fabricate convex axisymmetric aspheric surfaces on brittle materials. A surface was generated on single crystal silicon using a straight nosed diamond tool and average roughness value of 16 nm was successfully obtained. Chen and Zhao (2015) presented a surface roughness predicting model for Al7075 and evaluated the influence of relative tool-work vibration, machine tool error, cutting force, material property and cutting parameters on the surface roughness. He *et al.* (2015) presented a coupled theoretical and empirical method to predict the surface roughness achieved by single point diamond turning of hardening aluminum alloy. As per this method, the surface roughness was considered to be composed of both certain and uncertain parts. Radial basis function neural network and particle swarm optimization algorithm were employed to the experimental data to find out the optimal cutting parameters to achieve the best surface roughness. Similarly, Khatri *et al.* (2015) conducted SPDT machining experiments on silicon by varying tool feed rate, spindle speed and depth of cut and studied the effect of machining parameters on the surface roughness by using response surface methodology (RSM). A prediction model

was developed by using experimental data to predict the surface roughness. It was found that best surface roughness can be obtained on silicon was 31.6 nm at feed rate of 2.5 μm/rev, depth of cut of 1.5 μm and spindle speed of 1500 rpm.

Observations:

Surface roughness, an important product quality parameter affects several functional attributes of SPDT products viz. friction, wear, lubrication, light reflection/refraction, corrosion resistance. Theoretically, in case of the cutting process (turning or facing), the surface finish mainly depends on the tool nose radius and the feed rate. However, in reality, it depends upon the process parameters, tool geometry, workpiece and cutting tool interaction, workpiece and tool material properties, tool wear, cutting environment. As the surface roughness is measured after the completion of the machining operation, it is time-consuming and labor-intensive. Moreover, the SPDT process is slow as the volume of material removal is in micron or nanometric scale. Thus, carrying out extensive trials to optimize the process to obtain the desired surface finish is time-consuming. Literature reports that most of the works have been used either experimental or theoretical way to investigate the surface quality for SPDT process. There is hardly any attempt reported on modeling of surface roughness by using FEM simulations of SPDT process.

2.6 Numerical Modeling and Simulation of SPDT Process

With the improvement of computer systems, numerical analysis has emerged as a powerful tool to investigate the machining processes and provide a rational insight into machining response behavior of materials. Numerical simulations can predict the material behavior from conventional to micro to nanoscale machining process.

Literature reports that researchers employed particularly finite element method (FEM) and molecular dynamics (MD) methods for process modeling and simulation of the ultra-precision machining process. FEM works by applying the principle of continuum mechanics whereas MD uses discrete mechanics that considers inter-atomic bonding of atoms. Figure 2.13 shows the dimensional comparisons of macro, FEM and MD simulations. In FEM, the working dimension may vary from macro to nano scale whereas in MD simulation the maximum dimension that can be considered is up to few nanometers. The initial work on molecular dynamics (MD) simulation was reported by Alder and Wainwright in the late 1950s [Alder and Wainwright (1957)]. Later, it was adapted to simulate ultra-precision machining during the 1980s at Lawrence Livermore National Laboratories (LLNL), USA [Belak and Stowers (1990)]. Since then, several studies were carried out in different aspects of

nanometric machining. These include crystallographic orientation effects on plastic deformation, tool edge radius and minimum depth of cut effects on the chip formation mechanism, phase transition, effects of defect structure in the workpiece material, and diamond tool wear.

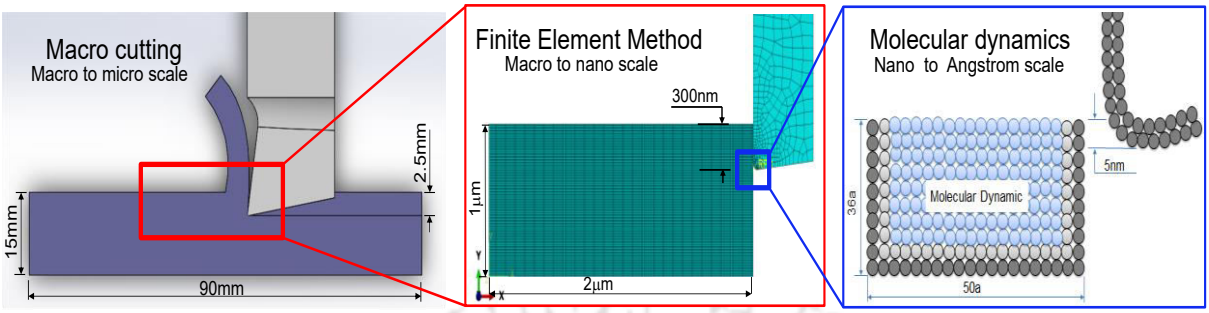

Figure 2.13 Dimensional comparisons of macro, FEM and MD simulations

Shimada and Ikawa (1992) presented MD simulations of nanometric chip removal process in micro-cutting of copper. In this study, the chip morphologies, cutting forces and specific energy were predicted and found in good agreement with experiments. Komanduri *et al.* (2000) studied the effects of crystal orientation, cutting direction and positive rake angle on nanometric cutting of single crystal aluminum. It was observed that the cutting forces vary cyclically with the orientation of the crystal and the direction of cutting. It was also noted that the cutting force decreases with the increase in the rake angle. Figure 2.14 shows the MD model used to simulate ultra-precision cutting of single crystal aluminum.

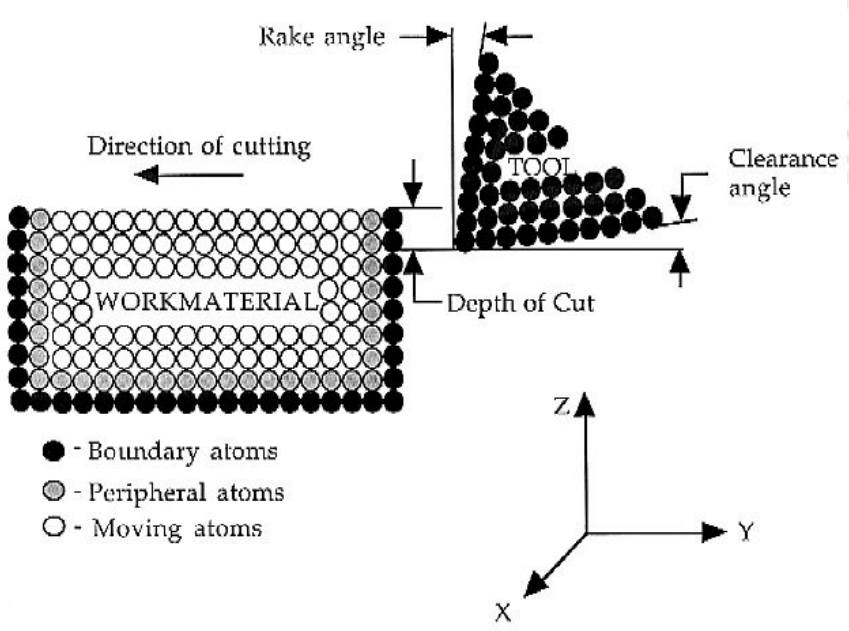

Figure 2.14 Schematic of the model used in the MD simulation of nanometric cutting of single crystal aluminum [Komanduri *et al.* (2000)]

Further, Komanduri *et al.* (2001) carried out MD simulation on silicon using the Tersoff potential by varying the rake angle, width of cut, depth of cut and clearance angle and studied the nature of material removal and surface generation in ultra-precision machining and grinding. During the study, it was observed that four different material removal mechanisms exist viz. compression of the work material ahead of the tool; chip formation akin to an extrusion-like process; side flow; and subsurface deformation in the machined surface. Inamura *et al.* (1997) presented computer simulations of machining of silicon by using renormalized molecular dynamics (RMD) to investigate the crack initiation process. The results showed that silicon can be machined in ductile mode under absolute vacuum medium; however it exhibits brittle-ductile transition depending on the scale of machining under normal atmosphere. Cai *et al.* (2007a) conducted physical experiments as well as MD simulations of nanometric machining of silicon wafer to study the mechanism of ductile chip formation. It was concluded that the plastic deformation occurred due to phase transformation rather than atomic dislocation. Similarly, Komanduri and Raff (2001), Oluwajobi (2012), Goel *et al.* (2015), Guo *et al.* (2016) and Abdulkadir *et al.* (2018) contributed significant knowledge by carrying out molecular dynamics (MD) based simulations and have laid a sound foundation for the study of nanometric cutting processes using MD simulation. Goel and his team reported extensive work on numerical simulations of nanometric machining of silicon and silicon carbide using MD simulation. Authors studied atomistic aspects of ductile response of SiC [Goel *et al.* (2011)], effect of temperature and crystal orientation on tool wear [Goel *et al.* (2012a, 2012b, 2013a)], brittle to ductile transition of SiC [Goel *et al.* (2013b)] and effect of the microstructure on cutting behavior of silicon [Goel *et al.* (2016)]. Figure 2.15 shows the typical MD model developed by Goel *et al.* (2011) to simulate the SPDT process.

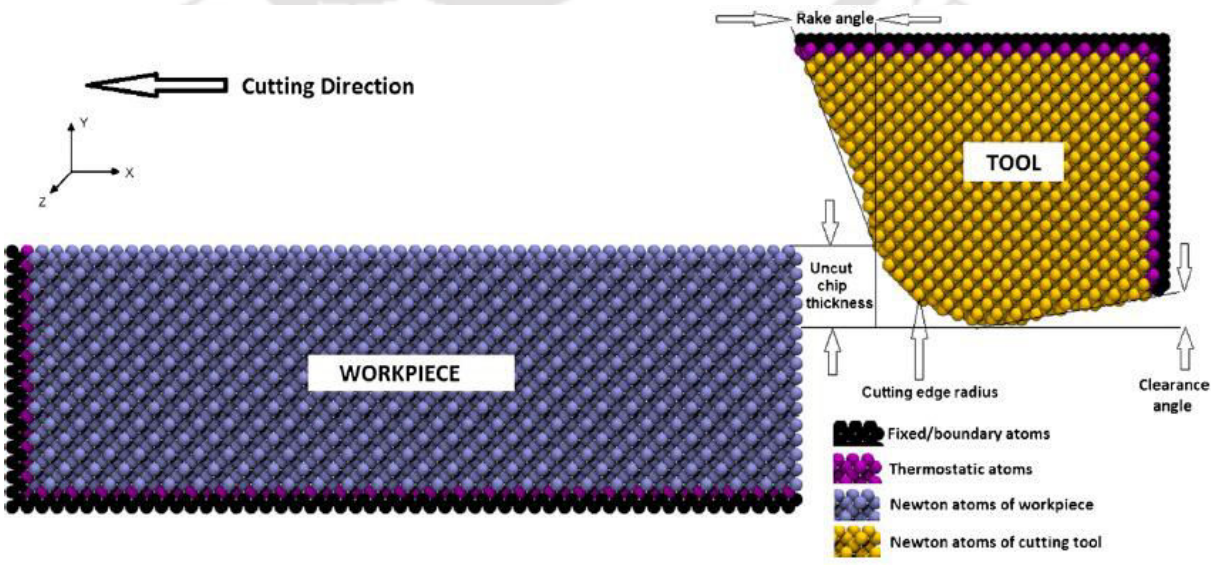

Figure 2.15 Schematic of MD simulation [Goel *et al.* (2011)]

It was seen that the MD method successfully simulate the mechanism of nano cutting of brittle materials. However, the method has a limitation that it can be applied to a very small size of process continuum, i.e., several millions of atoms or even less. The time scales are in the order of picoseconds. As the results are available at atomistic scale, these are difficult to compare with the experimental data [Goel *et al.* (2017)] and apply in general, real-life process conditions of SPDT.

FEM is very widely used to model and simulate the machining processes from macro to nano level. It predicts the cutting forces, stresses, strains and temperatures. During FEM based modeling, the effects of large deformation; strain rate effect; tool-chip contacts and friction; local heating and temperature effect can easily be incorporated. In this method, various boundary and loading conditions such as thermal, structural, electrical, magnetic can be defined and complex physical interaction of tool and workpiece can be simulated. Literature reports eminent studies on analysis of chip morphologies, cutting forces, temperature, stresses and strains and other output variables. Literature reports tremendous works on finite element based macro-micro cutting simulations of metals [Davim *et al.* (2008, 2009), Jagadesh & Samuel (2015, 2017)]. Yan *et al.* (2007) studied the effect of hydrostatic pressure and temperature in ductile machining of silicon using finite element simulation. It was demonstrated that the high pressure is the dominant reason for ductile machining of silicon rather than the high temperature. Subsequently, Yan *et al.* (2009a) simulated SPDT of silicon using FEM method and demonstrated that increase in the cutting edge radius causes decrease in the cut chip thickness and a corresponding increase in the thrust force. Lowering the cutting edge radius (below 200 nm) shifts the high temperature zone from the tool rake face to the tool flank face resulting in the transition of the wear pattern from crater to flank wear. Similarly, Patten *et al.* (2005, 2007, 2008) and Patten and Jacob (2008) simulated SPDT of single crystal 6H-SiC by employing a Drucker-Prager (pressure sensitive) yield criterion in a commercially available FEM package. Authors investigated the effect of rake angle and depth of cut on machining forces to study the ductile to brittle transition. It was found that the cutting forces agreed well with experimental results only under ductile-regime machining conditions. It is because the model did not include fracture criterion or brittle material removal mechanisms. Figure 2.16 depicts the FEM simulation model of SiC showing pressure developed at the cutting region.

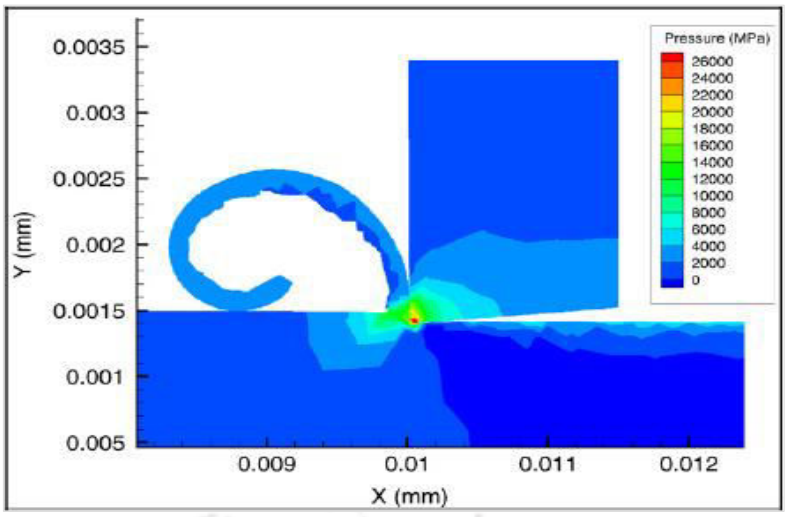

Figure 2.16 FEM simulation results of SPDT of SiC for 0º rake, 5º clearance [Patten and Jacob (2008)]

Mir *et al.* (2017) carried out numerical simulation of surface defect machining (SDM) of silicon using Smooth particle hydrodynamics (SPH). Pressure sensitive Drucker-Prager yield criterion was employed to model the material behavior of silicon. It was found that SDM approach offers reduction in the cutting resistance of the material and thus reduces the requirement of cutting energy. Consequently, it reduces the diamond tool wear and improves the surface finish. Figure 2.17 depicts the SPH model employed to simulate SDM of silicon. The von-Mises stress developed during SDM is slightly lower than that without incorporating SDM.

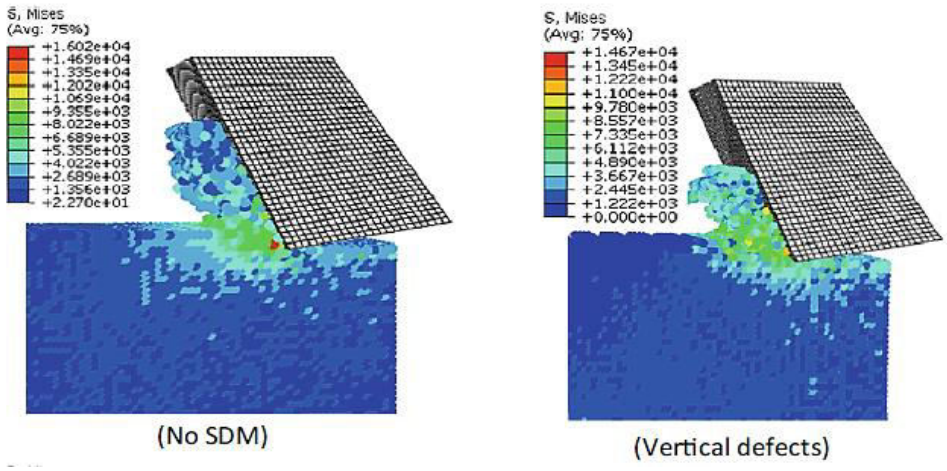

Figure 2.17 SPH simulations with or without SDM [Mir *et al.* (2017)]

Observations:

Analysis of machining forces and surface roughness is important in view of the analysis of process efficiency and product quality of ultra-precision machining process. Till date, significant experimental works have been reported on understanding of the cutting

mechanism and chip formation during machining of silicon and silicon carbide. However, as the machining scale enters from micro to nano regime, it is interesting to study the force, pressure, stress, and roughness during the cutting process. Numerical simulation regarded as a simple, efficient and computationally inexpensive method to study the complex nanometric cutting process of brittle materials. Significant numerical studies have been reported on molecular dynamics (MD) based simulations of SPDT. These were focused on the study of stress, chips formation, temperature, crystallographic effect, phase transformation during the ultra-precision cutting operation. However, experimental validation of these studies is difficult due to its very small, i.e., atomic level study domain. Few attempts have been reported on numerical simulations using finite element method. To the best knowledge; no literature has been reported on the study of the influence of material model during numerical simulation of SPDT process of brittle material. Selection of proper material model is essential in obtaining accurate results.

2.7 Discussions

In the present work, an extensive literature review has been carried out on the numerical as well as experimental studies on SPDT of silicon and silicon carbide materials. The reported investigations provide very useful insights into SPDT of brittle materials in ductile mode. Literature also reports research on various aspects of SPDT process such as nanoindentation, plunge cutting, DRM, DBT, critical depth of cut, high pressure phase transformation, process parameters, tool geometry, cutting force, surface roughness, MD and FEM simulations. In the past few decades, numerous studies on the ductile-brittle transition process and the mechanism of brittle material machining have been carried out. Many researchers investigated and demonstrated different methods to distinguish the transition zone between brittle mode and ductile mode machining of brittle material. From the extensive literature review, the following research gaps have been identified.

- Researchers noted that nanoindentation of brittle material leaves some irreversible deformation zone without any fracture. Also, it is a very important and useful technique in finding the physical parameters of brittle materials which are difficult to obtain from general tensile/compression tests. Thus, it would be worthy and interesting to develop a numerical model of nanoindentation of brittle material to determine the mechanical properties and as well as ductile to brittle transition thickness of silicon and silicon carbide by using *in situ* measurement and analysis of contact pressures in the nanoindentation process.

- From the extensive literature review, it was learned that taper or plunge cutting can be used to study the ductile regime machining of brittle materials. It helps in determining the ductile to brittle transition zones thereby helps in identifying the critical depth of cut. Significant literature have been reported on experimental study of plunge cutting of silicon and silicon carbide, However, very scant literature is available on numerical simulation of plunge cutting simulation to determine the ductile to brittle transition of silicon and silicon carbide. A need thus exists to develop an efficient and alternate numerical model for quicker and accurate prediction of ductile to brittle transition of silicon and silicon carbide.
- Analysis of machining forces is important in view of computation of power consumption, analysis of machinability of the workpiece, determination of optimal levels of process parameters and analysis and prediction of tool failure. Till date, significant experimental works have been reported on understanding of the cutting mechanism and chip formation during machining of silicon and silicon carbide. Though, many numerical studies on SPDT process using molecular dynamics (MD) have been reported to study the insight of the machining process by analyzing stress, chips formation, temperature, phase change during the machining process; experimental validation of these results is difficult due to its very small, i.e., atomic level study domain. Very scant literature has been reported on numerical simulations using finite element method. To the best knowledge; no literature has been reported on the study of the influence of material model during numerical simulation of SPDT process of brittle material. Selection and use of a proper material model are essential in obtaining accurate results.
- Surface roughness is an important criterion to characterize the quality of the product that is manufactured by a machining process. It affects several functional attributes viz. friction, wear, lubrication, light reflection/refraction, corrosion resistant, etc. of the components. Theoretically, in case of the cutting process (turning or facing), the surface finish mainly depends on the tool nose radius and the feed rate. However, in reality, it depends on various factors such as process parameters, tool geometry, the interaction between the workpiece and cutting tool, workpiece and tool material properties, tool wear, cutting environment and the type of machine tool used. Surface roughness measurement is a post-machining operation. Thus, it is time-consuming and labor-intensive. Literature reports that most of the works have been used either experimental or theoretical way to describe the surface quality. There is very limited literature available on modeling of surface roughness by using FEM simulations of SPDT process. Therefore, it would be worthy to develop a finite element based prediction system by

integrating finite element method with image processing technique to predict the surface roughness.

- The numerical investigations of SPDT process help in understanding the mechanism of the process such as complex interaction between cutting tool and workpiece, material behavior (transition), etc. Based on the simulations, the machining forces, ductile to brittle transition thickness, chip morphology, and surface roughness can be successfully obtained. However, it is difficult to incorporate the effect of uncontrollable parameters such as imperfections in machine tool and cutting tool structures, errors in the setting of cutting tools, deformations, and vibrations in the structure of machine tools such as spindle, workpiece fixtures, and material inhomogeneity.

2.8 Objectives of the Present Research Work

Based on the research gaps identified during the literature review on various aspects of SPDT process, the objectives of present research have been derived. The overall objective of the proposed research work is to improve the surface quality and process efficiency during single point diamond turning of the brittle and ductile materials by carrying out systematic numerical and experimental investigations. The specific objectives of the proposed work are as follows:

1. To study the physics of nanometric cutting of hard, brittle materials such as Si and SiC and to determine the ductile to brittle transition thickness by carrying out finite element method (FEM) based simulations of nanoindentation and plunge cutting. To study the ductile regime machining phenomenon during single point diamond turning of brittle materials by using FEM based modeling and simulation approach.
2. To analyze the machining forces generated in SPDT process by developing a realistic numerical process model. To investigate the effects of process parameters such as cutting speed, feed rate, depth of cut, materials properties, tool geometry, etc. on machining forces, chip morphology and crack propagation.
3. To develop an integrated methodology using FEM and image processing technique for accurate and quick prediction of surface roughness during machining of Al6061-T6.
4. To carry out comprehensive experimental investigations on SPDT of Al6061-T6 for validation of the research outcomes of developed FEM-IPT model and to investigate the influence of process parameters such as speed, feed, and depth of cut on the surface roughness.

To achieve the above stated objectives, in this present work, extensive numerical and experimental work were planned and then systematically performed. Figure 2.18 shows an overview of various stages of the present research work.

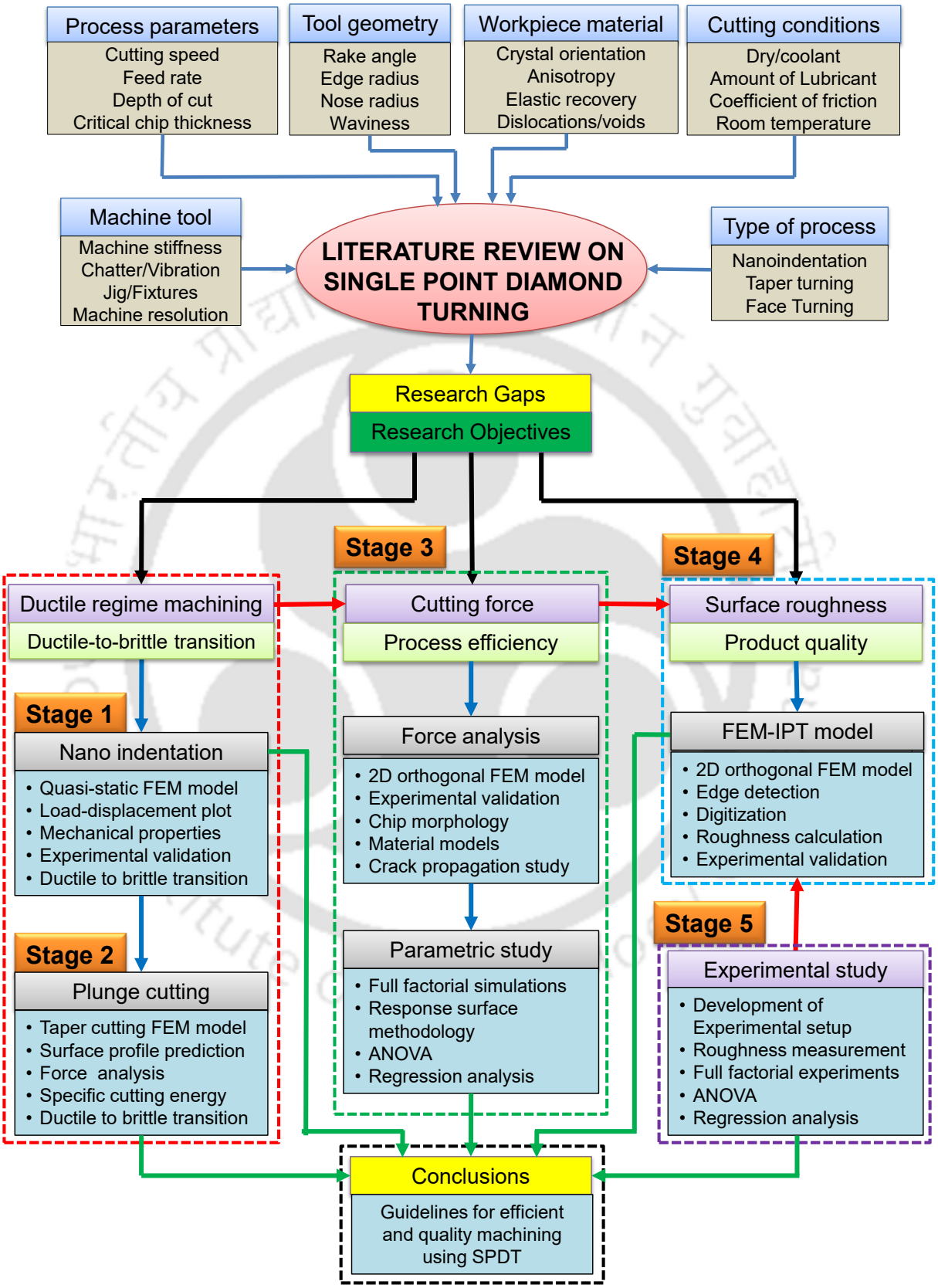

Figure 2.18 Overview of the present research work

The stages of the work are as follows.

- **Stage 1**: Development of a finite element based two-dimensional non-linear dynamic explicit numerical model of nanoindentation to determine the ductile to brittle transition (DBT) thickness and to understand the ductile regime machining (DRM) of brittle materials.
- **Stage 2**: Development of a finite element based two-dimensional non-linear dynamic explicit plane strain numerical model of plunge cutting process to determine the ductile to brittle transition (DBT) thickness and a detailed study on the results obtained from the nanoindentation simulations.
- **Stage 3**: Development of two-dimensional non-linear dynamic explicit, plane strain numerical model of SPDT process of silicon and silicon carbide using FEM to predict the cutting forces. Experimental validation of the developed numerical model.
- **Stage 4**: Development of an integrated finite element method-image processing technique (FEM-IPT) based model for the prediction of surface roughness during SPDT of Al6061-T6 and silicon.
- **Stage 5**: Experimental studies of SPDT on Al6061-T6 to validate the developed FEM-IPT model and to investigate the influencing parameters such as speed, feed and depth of cut on surface roughness.

The details of these stages are presented in the next chapters.

A STUDY ON DUCTILE REGIME MACHINING USING NUMERICAL SIMULATIONS OF NANOINDENTATION

3.0 Scope

This chapter primarily focuses upon the study of ductile regime machining of brittle materials during single point diamond turning with the help of finite element simulation of nanoindentation. Initially, an overview of the work carried out in this chapter is presented. A study on ductile behavior and transition from ductile to brittle regions that occur during the nanoindentation process of brittle materials viz. silicon (Si) and silicon carbide (SiC) has been carried out. Details of the development of the finite element based model of nanoindentation in terms of assumptions, governing equations, model geometry, material behavior modeling, damage model, meshing, surface contact modeling, boundary conditions, and solution methodologies are presented. After the development, a comparison with published experimental results is presented. Effects of various process conditions and parameters on responses are studied and presented in detail.

3.1 Motivation and Objectives of Present Work

During mechanical processing of hard and brittle materials, the material removal is mainly dependent upon the strength of the material (deform or fracture), size and density of defects, flaws, cracks and size of the stress field in the material. Since brittle materials are very sensitive to localized brittle micro-fractures; the material removal mechanism in machining of hard and brittle materials is achieved by micro-cracks and generation of chip fragments [Bifano *et al.* (1991), Ravindra *et al.* (2009)].

In the past few decades, numerous studies on the ductile-brittle transition process and the mechanism of hard-brittle material machining have been carried out. Researchers investigated and demonstrated various methods to distinguish the transition zones between brittle mode and ductile mode machining of brittle material. However, the transition from ductile to brittle regime is dependent on the method of implementation and process conditions applied. Researchers used several techniques viz. nanoindentation, fly cutting, taper cutting, plunge cutting, scratching to determine the transition point as described in previous Chapter 2. By using these techniques, important aspects such as pressure phase transition, intensity of electrical conductivity change at the indentation/cutting zone, variation of acoustic sound during machining, surface texture/profile after machining using the optical measuring

instrument, fluctuation of machining force and specific cutting energy during unit removal of material can be studied.

Ductility of a material can be defined as the extent to which materials can be deformed permanently without fracture. All materials exhibit the property of ductility, no matter how brittle they are. Glass exhibits perfectly brittle at macroscale whilst it undergoes plastic deformation at the micro scale [Xi *et al.* (2005)]. Over the past two decades, extensive and eminent research works have been carried out on the evaluation of plastic deformation of hard and brittle materials like glass and ceramics through indentation, scratching, scribing, grinding and machining. The hypothesis of ductile-mode machining of brittle materials has emerged from the indentation of brittle materials. Researchers noted that indentation of brittle material with a very small depth of indentation by a sharply pointed diamond indenter leaves some irreversible deformation zone without any fracture [Lawn and Evans (1977, 1980), Marshall and Lawn, (1986)]. It was also reported that if the brittle material is processed with cutting condition below a critical depth of cut, plastic flow occurs and a crack free machined surface can be obtained [Puttick *et al.* (1989)]. Brittle materials such as silicon and silicon carbide may behave like ductile materials at ambient conditions if sufficient contact pressures are applied, i.e., above 9-16 GPa for silicon [Cheong and Zhang (2000), Domnich *et al.* (2000), Domnich and Gogotsi (2001), Cai *et al.* (2007b)] and 30-60 GPa for silicon carbide [Chang and Cohen (1987), Patten *et al.* (2005), Patten and Jacob (2008)]. These findings may be useful in smoother and crack-free machining of brittle materials. Significant literature is reported on measurement and analysis of residual stresses in the indentation zone [Scattergood and Blake (1990), Bifano *et al.* (1991), Blackley and Scattergood (1991), Leung et *al.* (1998), Patten and Jacob (2005)]; however, very scant literature is available on *in-situ* measurement of contact pressures. Thus, it was found to be worthy and interesting research direction on understanding the ductile regime machining mechanism by using *in-situ* measurement and analysis of contact pressures in the nanoindentation process.

The main objective of this chapter is to understand; study and investigate the ductile-to-brittle transition, i.e., to identify the critical depth where the transition from ductile to brittle occurs by carrying out finite element simulations of nanoindentation. For brittle materials, nanoindentation finds a very important and useful technique as it is capable of finding physical parameters which are difficult to obtain from general tensile/compression tests. It provides nanometric displacement to the tip of the indenter and records a very small load value (of the order of mN) with a high degree of precision. The capital cost involved in nanoindentation instrument is very high in comparison to that of conventional micro hardness testing instruments.

Although the experimental study is regarded as defining methodology to study and analyze any problem, it is very difficult to obtain the *in-situ* information about the stress and pressure developed, temperature profile, and displacement underneath the indenter during physical experiments. Therefore, use of numerical techniques such as finite element method (FEM), finite volume method (FVM) can be thought to be simple, easy and economical alternatives to costly, tedious and time-consuming physical experiments. By using numerical techniques, one can carry out simulations of nanoindentation process by mimicking and analyzing the actual process while performing the indentation. Thus, it was thought worthy to develop a numerical model for two-dimensional nonlinear dynamic explicit analysis of nanoindentation of brittle materials for various sets of process conditions.

In this work, FEM-based simulations of nanoindentation of silicon and silicon carbide have been carried out by using spherical indenter. In the case of nanometric machining, the depth of cut is very small, the tool becomes blunt, and the workpiece is compressed underneath the tool edge. This phenomenon can be characterized as a loading process of the indentation process. Due to the compressive force experienced by the workpiece, the brittle material changes its phase from brittle to ductile. Thus, the main interest of this work is to study the occurrence of ductile onset of brittle material by carrying out finite element based numerical simulations of nanoindentation and plunge cut simulations. The present study has been carried out to achieve the following objectives.

- To explore nano-mechanical responses during static nanoindentation of brittle materials such as silicon (Si) and silicon carbide (SiC).
- To assess the feasibility of modeling and simulation of a hardness test using the finite element method.
- To derive basic mechanical properties of Si and SiC from the FEM based model and simulated results.
- To validate the results predicted by the proposed methodology by using the published experimental load-displacement graphs.
- To examine the occurrence of ductile onset of brittle material by measuring the *in-situ* contact pressures.
- To obtain the critical transition depth of cut and to study the insights of ultra-precision machining of SiC.

3.2 Overview of the Present Work

This section presents an overview of the current research work carried out to study the ductile regime machining (Figure 3.1). It comprises of development of a two dimensional, nonlinear numerical model for nanoindentation simulations of Si and SiC using finite element method. The results predicted by the model such as hardness and Young's modulus along with load-displacement plot have been validated.

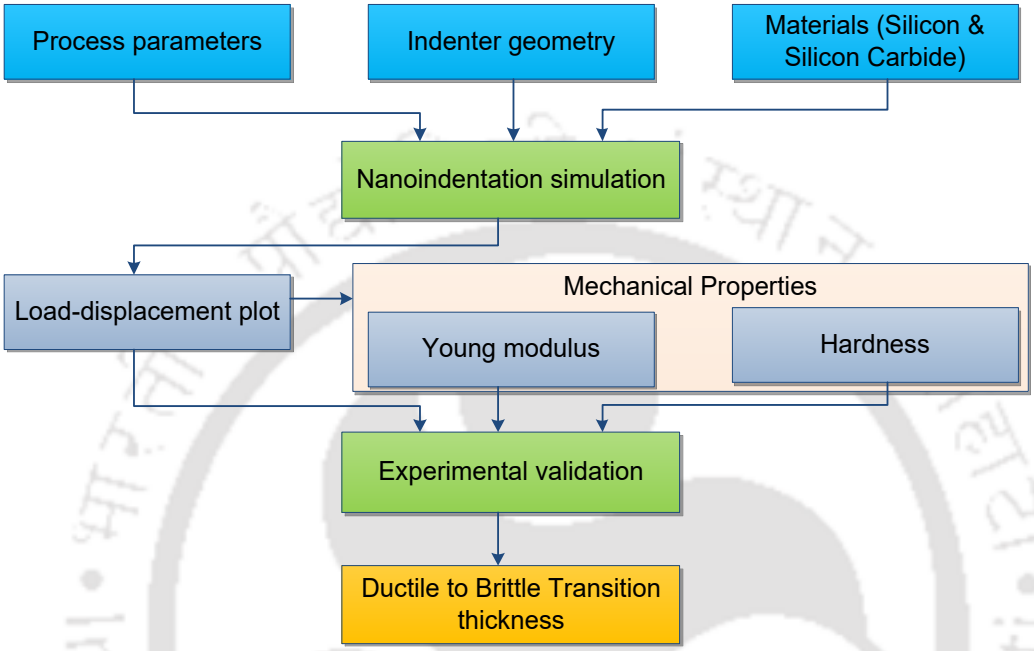

Figure 3.1 Overview of the work carried out in this chapter

In the present work, the process of nanoindentation using finite element method and its capability to demonstrate the ductile to brittle transition has been studied. Further, using the developed numerical model, a detail study has been carried out to understand the ductile regime machining of brittle material during single point diamond turning.

Various stages of the present work are presented in the following order.

- Selection of suitable FEM model for nanoindentation simulation by considering the effect of various influencing parameters viz. element type, indenter tip geometry, loading speed to minimize the error between numerical and experiment.
- Development of two-dimensional non-linear dynamic explicit FEM based numerical model of quasi-static nanoindentation process.
- Extraction of load-displacement (P-h) plots from the developed numerical model and validation of the same with the results published in literature.
- Computation of hardness and Young's modulus values from the P-h plots using Oliver-Pharr analytical method and their experimental validation.

- Study and analysis of *in-situ* phase changing pressure and critical indentation depth (depth before element failure) to evaluate the DBT thickness for silicon and silicon carbide.
- Comparison of predicted DBT values with experimental values.

3.3 Nanoindentation and Computation of Mechanical Properties

Figure 3.2 shows schematic of indentation process and load displacement plot. During the nanoindentation process, the indenter is pressed into the material due to which both the elastic and plastic deformations occur. This produces an impression with a projected area, A_p. The surface area of contact, A_s depends on the shape of the indenter to a contact depth, h_c. Basically, the nanoindentation process includes a loading and unloading cycle, which may be with or without dwell cycle. Figure 3.2 (b) shows indentation load (P) plotted against the displacement of indenter tip (h) with respect to top of the surface (before deformation) for one complete indentation cycle. The important parameters are the maximum depth of penetration at peak load (h_{max}), the peak load (P_{max}) and the final residual depth after unloading (h_f). The slope S, is known as the contact stiffness. It is determined by drawing a tangent to the upper $1/3^{th}$ portion of the unloading curve. The contact stiffness, hardness and elastic modulus are determined by using Oliver-Pharr method [Oliver and Pharr (1992, 2004)] as described in ISO 14577 and ASTM E2546.

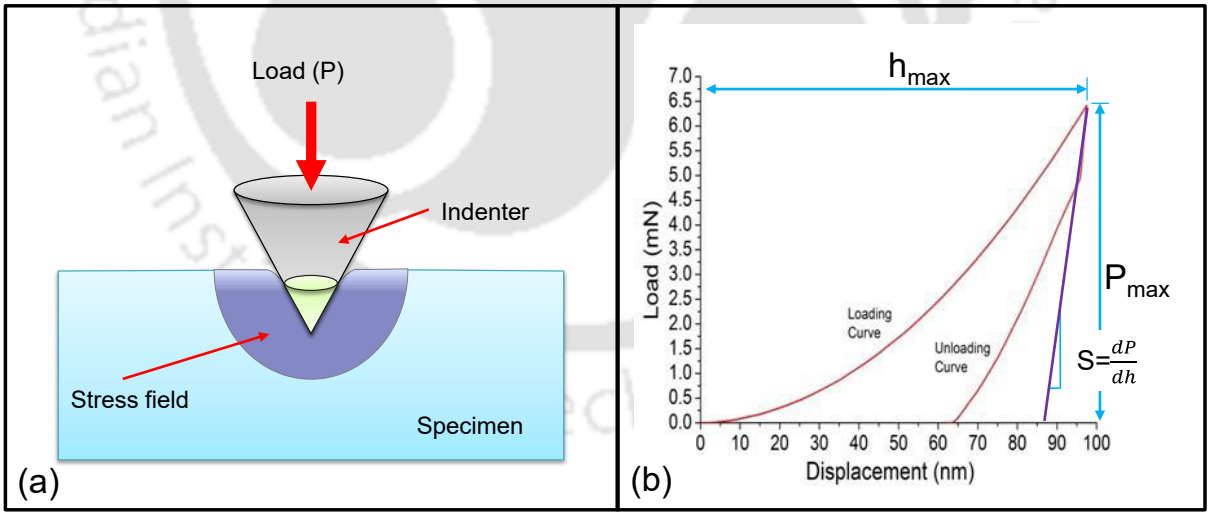

Figure 3.2 Schematic of (a) indentation process and (b) load-displacement plot

Elastic modulus and hardness can be easily be obtained by using nanoindentation testing. In nanoindentation, the depth of penetration of a diamond indenter is measured along the direction of application of prescribed load (Figure 3.3 (a)). The resulting load-displacement response typically shows an elastic-plastic loading followed by an elastic unloading as shown in Figure 3.3 (b).

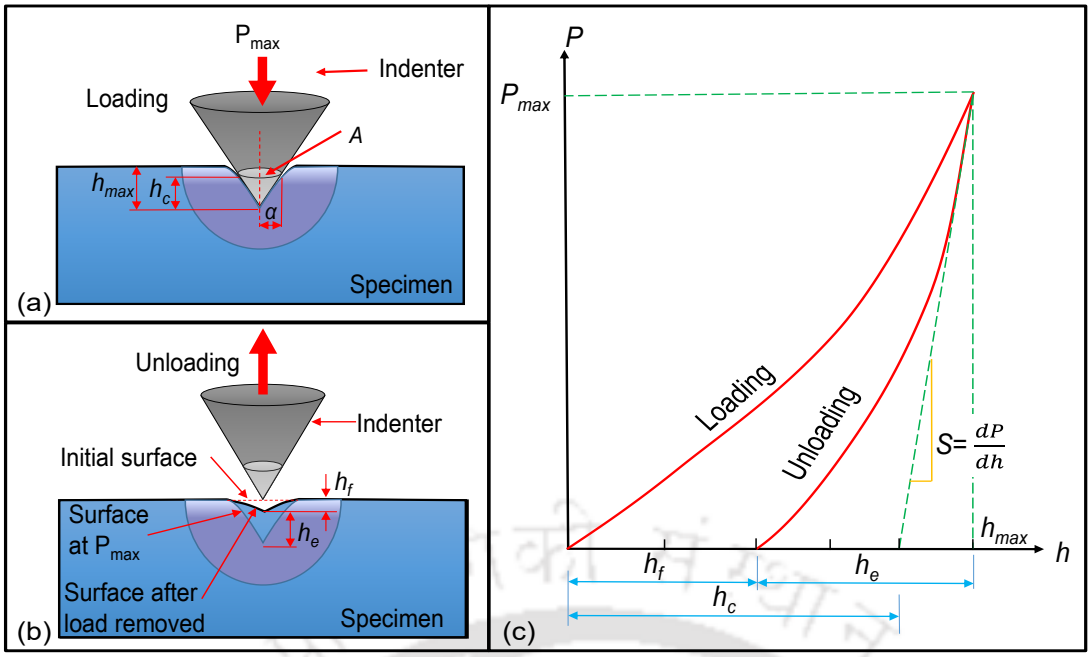

Figure 3.3 Schematic of (a) indenter and specimen surface geometry at full load and full unload condition (b) load versus displacement graph with various indentation parameters

Utilizing the unloading data and max load-displacement values along with the elastic equations of contact, the elastic modulus and hardness of the specimen material can be computed. To determine the hardness and Young's modulus by using the nanoindentation load-displacement graphs, three analytical models viz. Doerner-Nix Model [Doerner and Nix (1986)], Field and Swain model [Field and Swain (1993)], and Oliver and Pharr are commonly used in the practice. Out of the three models, Oliver and Pharr method proposed by Oliver and Pharr [Oliver and Pharr (1992, 2004)] has been established as the standard procedure since 1992 for determining the hardness and elastic modulus from load-displacement plot obtained from the indentation process. Therefore, in the present work, the Oliver and Pharr model has been used and it will be discussed in detail. To compute the elastic modulus and hardness by using this method, some assumptions are to be made for computational simplicity. These assumptions are proposed by Bulychev *et al.* (1975) and later taken up by Oliver and Pharr (1992, 2004). These assumptions are as follows.

- Deformation upon unloading is purely elastic.
- The compliance of the sample and indenter tip is combined as springs in series.
- The contact between a rigid indenter of defined shape with a homogeneous, isotropic and elastic workpiece is modeled using an analytical model for the determination of contact surface area.
- For the calculation of Modulus of elasticity (based on the unloading curve), indenter and work sample are assumed to be linear and isotropic materials.

The analytical method to determine the elastic modulus and hardness from the experimental and numerical load-displacement plot are elaborated and presented with a case study of nanoindentation of SiC in section 3.5.

3.4 Numerical Simulation of Nanoindentation for the Determination of Mechanical Properties

3.4.1 Selection of Solution Methodology

Today high-speed processers and user-friendly solvers have increased the computational efficiency during numerical simulations. Numerical simulations are mainly used to understand the physics of manufacturing processes. During the literature study, it is learnt that molecular dynamic (MD) simulation is well capable of simulating various mechanical problems at atomic level to get the insight of the material micro-structure and grain boundaries. However, the correlation of the results obtained from MD simulation with actual experimental result is still lagging due to its limitation of requirement of huge computational time and length scales [Goel *et al.* (2014)]. High computational time and memory requirement during MD simulation do not permit the scaling of simulation parameters to the experimental scale. The length scales of process continuum are restricted to few nanometers (or few millions of atoms) and the cutting and indentation velocities should be in the range of 50 m/s in order to reduce the computation time, whereas, in actual experiment, these values are around 1 m/s for machining and 0.1–10 μm/s for nanoindentation. Because of these variations in values, it might cause unexpected spurious effects during the result analysis [Goel *et al.* (2014)].

Finite element method (FEM) is mostly used in mechanical analysis for the determination of stresses and displacements. However, nowadays with the development of high end computers, FEM can also be used in the analysis of many disciplines such as heat transfer, contact mechanics, fluid dynamics, and electromagnetism [Zienkiewicz and Taylor (1977)]. In the present work, the nanoindentation simulations have been carried out using a commercial finite element (FE) package Abaqus™. Quasi-static nanoindentation simulations were carried out on silicon and silicon carbide by using spherical indenter tip. Quasi-static nanoindentation permits systematic examination of the load displacement plot to enable better understanding of deformation mechanisms, evaluation of mechanical properties, and aspects of plasticity of brittle materials such as Si and SiC [Goel *et al.* (2014)]. Since, it is a very slow process, a minute variation in the load or displacement can easily be captured. These variations occur due to pop-in and pop-out events which are associated with the plastic deformation of the material. Generally, the hardness of a material can be determined by static indentation. Thus, in the present work, load-displacement graphs are extracted from the

simulation results, and by using these results, Young's modulus and hardness values have been calculated using Oliver and Pharr analytical model. The methodology developed and the input, output parameters used in the present work are shown in Figure 3.4.

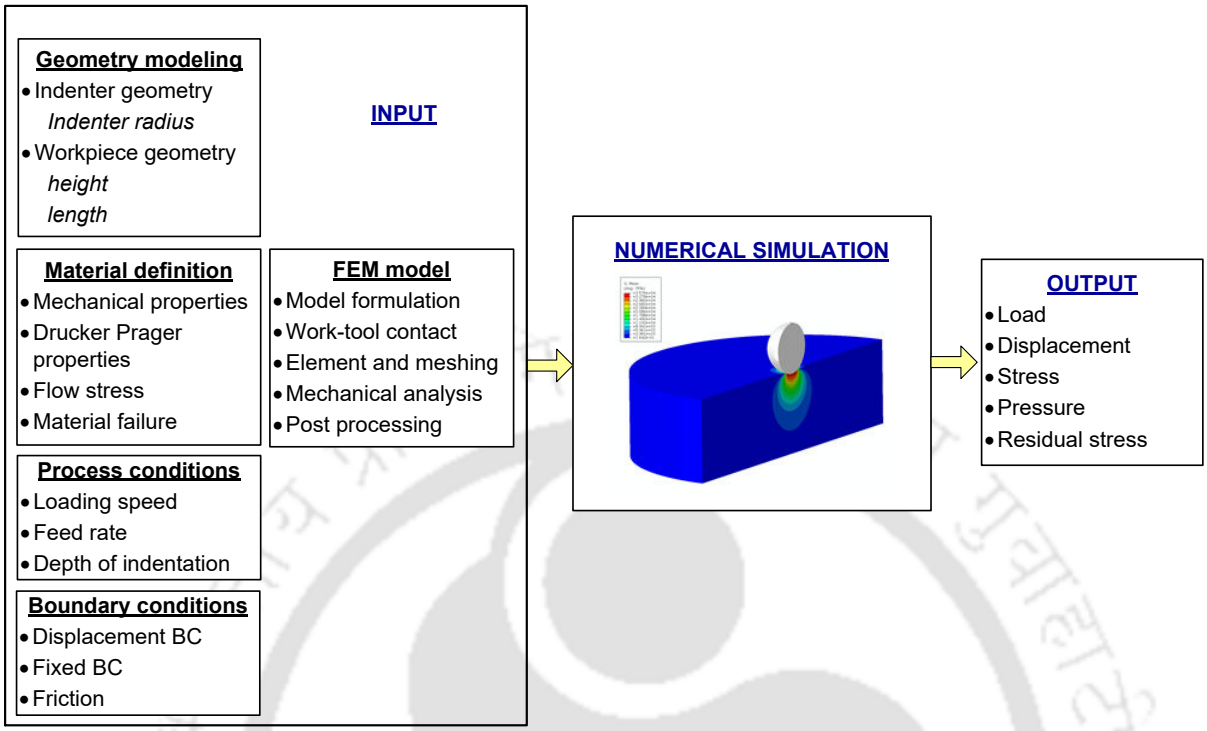

Figure 3.4 Schematic of developed numerical model

The step–by–step procedure followed in the FEM based modeling and simulation is outlined below.

- Geometric modeling of workpiece and diamond indenter. Details are given in Section 3.4.2 (C).
- Material properties were assigned to the workpiece and the indenter. Details are given in Section 3.4.2 (D).
- Workpiece geometry was discretized with 4-node axisymmetric, bilinear plane strain reduced integration elements, CAX4R. Then, the mesh sensitivity analysis has been carried out to fine tune the FEM output parameters such as load and displacement. The objective was to reduce the computation time and to enhance the prediction accuracy. Details of the discretization and mesh sensitivity analysis are given in Section 3.4.2 (E).
- Initial boundary conditions such as mechanical constraints 'encastre'-a fixed boundary condition to keep the workpiece fixed, symmetric boundary condition to two sides of the workpiece, velocity of the indenter. Details are given in Section 3.4.2 (I).

- Dynamic explicit solution has been carried out. The solution scheme is presented in Section 3.4.2 (J) in detail.
- Solver computed the stress, pressure, force and displacement at each node of domain at the end of the analysis. The node outputs were used to analyze the process. A case study to demonstrate the simulation by using the developed model is presented in Section 3.5.

These steps are discussed at length in the following sections.

3.4.2 Development of FEM based Nanoindentation Model

During the nanoindentation process, the material is pressed using a diamond indenter. Three faced pyramid shaped Berkovich indenter is the most commonly used diamond indenter in the nanoindentation process. The tip of the Berkovich indenter has three sides and has spherical shape of few nanometers radius at the joint of edges. Figure 3.5 shows the schematic of three faced pyramid shaped Berkovich diamond indenter.

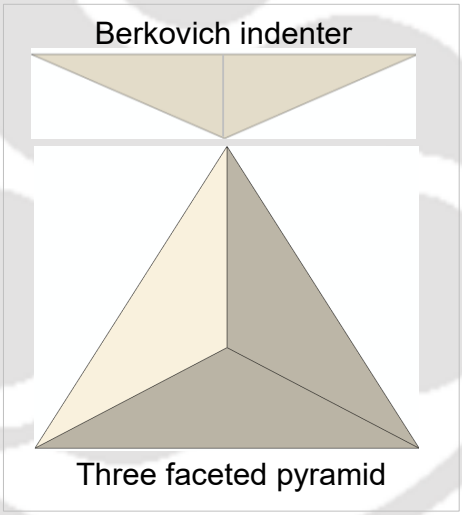

Figure 3.5 Schematic of Berkovich indenter showing front and top views

The nanoindentation process involves frictional interaction between the workpiece and indenter along with the elastic-plastic deformation. In this work, quasi-static nanoindentation simulations were carried out on silicon and silicon carbide by using spherical indenter tip. Quasi-static nanoindentation permits systematic examination of the load displacement plot that would be useful for study of deformation mechanisms, plasticity of brittle materials and evaluation of mechanical properties [Goel *et al.* (2014a, b)]. Quasi-static simulation enables simulation for a very small step. Therefore, in this work, only mechanical analysis of nanoindentation process has been attempted.

A. Assumptions

In the present work following assumptions have been considered for the development of numerical model of quasi-static nanoindentation process.

- Workpiece and diamond indenter materials are assumed to be homogeneous and isotropic in nature.
- The diamond indenter is assumed to be perfectly rigid.
- To induce the plastic deformation in brittle materials such as silicon and silicon carbide without defining independent slip system, von-Mises criterion is used for the plastic yielding [Lu and Bogy (1995), Bhattacharya and Nix (1988a, b), Zhang and Mahdi (1996)].
- The workpiece is considered as flat and free of initial residual stresses.
- The contact between the indenter and top surface of the work material is assumed to be frictionless. It is because the effect of friction between the indenter tip and the surfaces of the work material in nanoindentation process is negligible as size of the process continuum is very small (in nm) [Bhattacharya and Nix (1988a, b), Lu and Bogy (1995)].
- The tip movement is maintained at 0.1 mm/s to meet the quasi-static condition.
- As the indentation process is carried out in a very slow loading speed (0.01 to 0.1 mm/s). The temperature effect in the process can be ignored.

B. Governing Equations

In this work, a commercial finite element (FE) software Abaqus™ is used to simulate the nanoindentation process. However a detail theoretical study of the plastic deformation has been carried out. Moreover, the essential step to obtain the field variable using FEM has been studied. These are presented as follows.

During the process of nanoindentation, the tip of the indenter applies compressive forces on the workpiece. The stress generated during plastic deformation can be computed using von-Mises criterion which is given by

$$\sigma_{Mises} = \sqrt{\frac{(\sigma_1-\sigma_2)^2+(\sigma_2-\sigma_3)^2+(\sigma_3-\sigma_1)^2}{2}} \tag{3.1}$$

where σ_1, σ_2 and σ_3 are the three principle stresses. When the σ_{Mises} reaches the yield strength of material (σ_Y), the specimen starts to deform plastically. In this present simulation, von-Mises stress is used to measure the pressure and residual stresses obtained in the

numerical simulation. It is to be noted that, after indentation process, the surface of the workpiece material (i.e., place of interest) is free from the hydrostatic stresses. Thus, it is convenient to use von-Mises stress to determine the various stresses and pressures from the nanoindentation simulation, because it also does not include hydrostatic stresses. Also, it is worth to mention that, the onset pressure at the interface of indenter and workpiece is determined which is still not possible to determine during the actual (physical) experiments. The calculated pressures are compared with the workpiece material's hardness (relative to a possible HPPT or stress induced amorphization).

In dynamic problems, the field variables such as displacements, velocities, strains, stresses and load are all time-dependent. The procedure involved in deriving the finite element equations of a dynamic nanoindentation problem can be carried out by the following steps [Wang (2007)]:

Step 1: Idealize the body into 'e' finite elements.

Step 2: Assume the displacement model of an element 'e' as

$$\vec{U}(x,y,z,t) = \begin{Bmatrix} u(x,y,z,t) \\ v(x,y,z,t) \\ w(x,y,z,t) \end{Bmatrix} = [N(x,y,z,t)]\vec{Q}^{(e)}(t) \tag{3.2}$$

where, $\vec{U}$ is the vector of displacements, $[N]$ is the matrix of shape functions and $\vec{Q}^{(e)}$ is the vector of nodal displacements which is assumed to be a function of time *t*.

Step 3: Derive the element characteristic (stiffness and mass) matrices and characteristic (load) vector. The strain can be expressed as

$$\vec{\varepsilon} = [B]\vec{Q}^{(e)} \tag{3.3}$$

Accordingly the stress can be written as

$$\vec{\sigma} = [D]\vec{\varepsilon} = [D][B]\vec{Q}^{(e)} \tag{3.4}$$

where, $[B]$ is the strain-nodal displacement matrix and $[D]$ is matrix of elastic constants.

By differentiating equation (3.1) with respect to time, the velocity field can be obtained as

$$\vec{U}(x,y,z,t) = [\dot{N}(x,y,z)]\dot{\vec{Q}}^{(e)}(t) \tag{3.5}$$

where, $\dot{\vec{Q}}^{(e)}$ is the vector of nodal velocities. To derive the dynamic equations of motion of a structure, we can use either Lagrange equations. The Lagrange equations are given by

$$\frac{d}{dt}\left\{\frac{\partial L}{\partial \dot{Q}}\right\} - \left\{\frac{\partial L}{\partial Q}\right\} + \left\{\frac{\partial R}{\partial \dot{Q}}\right\} = \{0\} \tag{3.6}$$

where, $L = K_E - P_E$ (3.7)

L is called the Lagrangian function, K is the kinetic energy, P is the potential energy, R is the dissipation function, Q is the nodal displacement and $\dot{Q}$ is the nodal velocity. The kinetic and potential energies of an element 'e' can be expressed as

$$K_E{}^{(e)} = \frac{1}{2}\iiint_{V^{(e)}} \rho \dot{\vec{U}}^T \dot{\vec{U}} dV \tag{3.8}$$

and

$$P^{(e)} = \frac{1}{2}\iiint_{V^{(e)}} \varepsilon^T \vec{\sigma} dV - \iint_{S_1^{(e)}} \vec{U}^T \overrightarrow{\overrightarrow{\Phi}} dS_1 - \iiint_{V^{(e)}} \vec{U}^T \overrightarrow{\overrightarrow{\phi}} dV \tag{3.9}$$

where, $V^{(e)}$ is the volume, ρ is the density and $\dot{\vec{U}}$ is the vector of velocities of element e. By assuming the existence of dissipative forces proportional to the relative velocities, the dissipation function of the element e can be expressed as

$$R^{(e)} = \frac{1}{2}\iiint_{V^{(e)}} \mu \dot{\vec{U}}^T \dot{\vec{U}} dV \tag{3.10}$$

where, μ can be called the damping coefficient. In equation (3.8) to (3.10), the volume integral has to be taken over the volume of the element and in equation (3.10), the surface integral has to be taken over that portion of the surface of the element on which distributed surface forces are prescribed. By using equation (3.2) to (3.4), the expression for K, P and R can be written as:

$$K = \sum_{e=1}^{E} K^{(e)} = \frac{1}{2}\dot{\vec{Q}}^T \left[\sum_{e=1}^{E} \iiint_{V^{(e)}} \rho [N]^T [N]\, dV\right] \dot{\vec{Q}} \tag{3.11}$$

$$P = \sum_{e=1}^{E} P^{(e)} = \frac{1}{2}\vec{Q}^T \left[\sum_{e=1}^{E} \iiint_{V^{(e)}} [B]^T [D][B]\, dV\right] \vec{Q} - \vec{Q}^T \left(\sum_{e=1}^{E} \iint_{S_1^{(e)}} [N]^T \overrightarrow{\overrightarrow{\Phi}}(t) dS_1 + \iiint_{V^{(e)}} [N]^T \overrightarrow{\overrightarrow{\phi}}(t) dV\right) - \vec{Q}^T \vec{P}_c(t) \tag{3.12}$$

$$R = \sum_{e=1}^{E} R^{(e)} = \frac{1}{2}\dot{\vec{Q}}^T \left[\sum_{e=1}^{E} \iiint_{V^{(e)}} \mu\, [N]^T [N] dV\right] \dot{\vec{Q}} \tag{3.13}$$

where, $\vec{Q}$ is the global nodal displacement vector, $\dot{\vec{Q}}$ is the global ndodal velocity vector, and $\vec{P}_c(t)$ is the vector of concentrated nodal forces of the structure of body. By defining the matrices involving the integrals as

$$\left[M^{(e)}\right] = \text{element mass matrix} = \iiint_{V^{(e)}} \rho[N]^T[N]dV \tag{3.14}$$

$$\left[K^{(e)}\right] = \text{element stiffness matrix} = \iiint_{V^{(e)}} [B]^T[D][B]dV \tag{3.15}$$

$$\left[C^{(e)}\right] = \text{element damping matrix} = \iiint_{V^{(e)}} \mu[N]^T[N]dV \tag{3.16}$$

$$\vec{P}_s^{(e)} = \text{vector of element nodal forces produced by surface forces} = \iiint_{S_1^{(e)}} [N]^T \overrightarrow{\overrightarrow{\Phi}} \cdot dS_1 \tag{3.17}$$

$$\vec{P}_b^{(e)} = \text{vector of element nodal forces produced by body forces} = \iiint_{V^{(e)}} [N]^T \overrightarrow{\overrightarrow{\emptyset}} \cdot dS_1 \tag{3.18}$$

Step 4: Assemble the element matrices and vectors. Derive the overall system of equations of motion. Equation (3.11) to (3.13) can be written as

$$K_E = \frac{1}{2}\dot{\vec{Q}}^T[M]\dot{\vec{Q}} \tag{3.19}$$

$$P_E = \frac{1}{2}\vec{Q}^T[K]\vec{Q} - \vec{Q}^T\vec{P}_E \tag{3.20}$$

$$R = \frac{1}{2}\dot{\vec{Q}}^T[C]\dot{\vec{Q}} \tag{3.21}$$

where

$$[M] = \text{master mass matrix of the structure} = \sum_{e=1}^{E}\left[M^{(e)}\right] \tag{3.22}$$

$$[K] = \text{master stiffness matrix of the structure} = \sum_{e=1}^{E} [K^{(e)}] \tag{3.23}$$

$$[C] = \text{master damping matrix of the structure} = \sum_{e=1}^{E} [C^{(e)}] \tag{3.24}$$

$$\vec{P}(t) = \text{total load vector} = \sum_{e=1}^{E} \left[P_s^{(e)}(t) + P_b^{(e)}(t) \right] + \vec{P}_c(t) \tag{3.25}$$

By substituting equations (3.19) to (3.21) into equation (3.7), we can obtain the dynamic equations of motion of the structure or body as

$$[M]\ddot{\vec{Q}}(t) + [C]\dot{\vec{Q}}(t) + [K]\vec{Q}(t) = \vec{P}(t) \tag{3.26}$$

where, $\ddot{\vec{Q}}$ is the vector of nodal accelerations in the global system. If damping is neglected, the equation of motion can be written as

$$[M]\ddot{\vec{Q}}(t) + [K]\vec{Q}(t) = \vec{P}(t) \tag{3.27}$$

Steps 5 and 6: Solve the equations of motion by applying the boundary and initial conditions. Equation (3.26 or 3.27) can be solved by using the techniques of a set of simultaneous linear differential equations for propagation problems. Once the time history of nodal displacements $\vec{Q}(t)$ is known, the time histories of stresses and strains in the elements can be found as in the case of static problems.

C. Geometric Modeling of Process Continuum

Initially, the geometric models of spherical diamond indenter and workpiece have been developed. Figure 3.6 shows the workpiece, spherical indenter, and relevant geometric parameters.

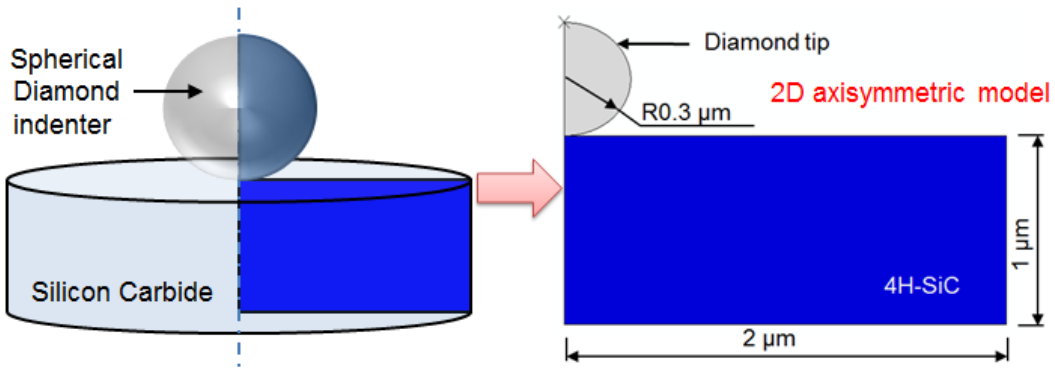

Figure 3.6 Schematic of 2D axisymmetric indentation simulation model

The spherical indenter has a diameter of 600 nm. Semi-spherical geometry of the indenter was created and positioned at the left side of the workpiece continuum. The work was considered to be axisymmetric rectangular block of 2 μm × 1 μm. These dimensions were thought to be sufficient enough to simulate a semi-infinite half space to simulate the indentation with a maximum depth of 50 nm.

D. Material Model and Properties

In this present simulation, a nanoindentation problem is considered to be based on continuum mechanics where quasi-static loading of the indenter is applied. The diamond indenters and the silicon carbide in the model are defined as homogeneous and isotropic elastic materials. Drucker-Prager material model is used to model the material behavior of silicon carbide along with elastic material properties. The Drucker–Prager yield criterion given by [Drucker and Prager (1952)] is a pressure-dependent model for determining whether a material has failed or undergone plastic yielding. It is basically derived from the Morh-Coulomb yield surface. The Mohr–Coulomb yield surface is a cone with a hexagonal cross section in deviatoric stress space. The criterion was originally introduced to deal with the plastic deformation of soils. The Drucker–Prager criterion can be expressed in terms of the equivalent stress (or von-Mises stress) and the hydrostatic (or mean) stress as

$$\sigma_e = a + b\sigma_m \tag{3.28}$$

where, σ_e is the equivalent stress, σ_m is the mean stress, and *a, b* are material constants. The material model is adopted for the understanding of elastic-plastic as well as brittle fracture during the pressure sensitive loading and unloading process. The Drucker–Prager yield criterion can also be described as a simple modification of the von-Mises criterion, in which the hydrostatic stress component is also included to introduce pressure-sensitivity [Drucker and Prager (1952), Ajjarapu *et al.* (2004)]. The Drucker-Prager yield criterion is given by:

$$\sqrt{3.J_2} + I_1.\alpha - \kappa = 0 \tag{3.29}$$

where I_1 is the first invariant of the stress tensor, J_2 is the second invariant of the deviatoric stress tensor, α is the pressure-sensitivity coefficient, and κ is a material constant.

The quantity J_2 is given by the following:

$$J_2 = \frac{1}{6}[(\sigma_1 - \sigma_2)^2 + (\sigma_2 - \sigma_3)^2 + (\sigma_3 - \sigma_1)^2] \tag{3.30}$$

where α_i are the principal stresses. The quantity κ is given by the following equation. It is equal to the yield stress when $\sigma_c = \sigma_t$, that means, it is not pressure dependent.

$$\kappa = \frac{2\sigma_c\sigma_t}{\sigma_c+\sigma_t} \tag{3.31}$$

where σ_c and σ_t are the yield stresses in tension and compression, respectively.

In Abaqus, the Drucker Prager model constants are redefined by dilation angle (ψ), friction angle (β) and flow stress ratio (K). These material constants for the Drucker-Prager model are generally obtained by fitting tri-axial compression and tension data. But, tri-axial test data are not readily available. Therefore, material parameters are calculated indirectly by matching the Mohr-Coulomb yield surface with the Drucker-Prager yield surface. The details of the geometric interpolation of the matching of Mohr-Coulomb and Drucker-Prager surfaces to obtain Drucker-Prager material parameters can be found in Chen and Han (1988). The material properties for diamond, silicon and silicon carbide materials are listed in Table 3.1. The constants for Drucker-Prager material model of silicon and silicon carbide are listed in Table 3.2.

Table 3.1 Material properties of Diamond [Mariayyah (2007), Goel *et al.* (2016)], Silicon [Venkatachalam (2007)] and Silicon Carbide [Mariayyah (2007), Goel (2014)]

Parameters	Unit	Diamond	Silicon	Silicon Carbide
Density (ρ)	[kg/m^3]	3350	2328	3211
Young's Modulus (E)	[GPa]	1141	135	411
Shear modulus (G)	[GPa]	512	79.9	193
Poison's ratio (υ)		0.07	0.27	0.231
Fracture toughness (K_c)	[MPa.m$^{1/2}$]	5.3 to 8	0.9	1.9
Thermal Conductivity (k)	W/m.K]	700	150	155.76
Specific Heat (c)	[J/kg.K]	520	700	800

Table 3.2 Constants for Drucker-Prager constitutive model for Si [Mir *et al.* (2016)] and SiC [Mariayyah (2007)]

Parameters	Angle of friction [°]	Flow stress ratio	Dilation angle [°]	Yield stress [MPa]
SiC	13	0.92	−5	0.01625
Si	26	0.82	−20	0.015867

E. Damage and Failure Models of Silicon Carbide

To investigate the ductile to brittle transition during nanoindentation process, it is essential to simulate the damage and fracture of the material under the action of applied loads. The material is said to be failed when it loses its load carrying capacity. In this work, the objective is to obtain both ductile and brittle failure of silicon and silicon carbide materials with high strain, strain rate effects. Ductile damage criterion obtained from triaxial test [Abaqus 6.11 Documentation] is used along with other mechanical properties to model the element failure. For elements where the material has reached its failure, i.e. when it no longer

has any load carrying capacity, a deletion criterion can be imposed. This means that failed elements are deleted from the simulation.

In the ductile damage initiation criterion, the onset of damage is met when the following criterion is satisfied [Mabrouki *et al.* (2008)]:

$$\omega_D = \int \frac{1}{\bar{\varepsilon}_D^{pl}\left(\eta, \dot{\bar{\varepsilon}}^{pl}\right)} d\bar{\varepsilon}^{pl} = 1 \tag{3.32}$$

where $\omega_D$is a monotonically increasing state variable, the critical equivalent plastic strain, $\bar{\varepsilon}_D^{pl}$, is a function of stress triaxiality, η, and plastic strain rate, $\dot{\bar{\varepsilon}}^{pl}$. Thus, the ductile damage initiation criterion can be specified with $\bar{\varepsilon}_D^{pl}(\eta, \dot{\bar{\varepsilon}}^{pl})$. The ductile damage parameters for SiC obtained from triaxiality test is listed Table 3.3 at strain rate value of zero.

Table 3.3 Ductile damage parameters for SiC based on triaxiality test [Abaqus 6.11 Documentation]

Fracture strain	Stress triaxiality
3.86958	−0.89667
3.01956	−0.8237
2.28835	−0.74727
1.67109	−0.66639
1.16251	−0.57945
0.756814	−0.48361
0.447555	−0.37326
0.227363	−0.23509
0.087533	−0.02697

The damage evolution can be computed by using Hillerborg's fracture energy G_f that is required to open a unit area of crack is defined as:

$$G_f = \int_{\bar{\varepsilon}_{0i}}^{\bar{\varepsilon}_f} L\bar{\sigma}_Y \mathrm{d}\bar{\varepsilon} = \int_0^{\bar{u}_f} \bar{\sigma}_Y \mathrm{d}\bar{u} \tag{3.33}$$

where $\bar{\varepsilon}_{0i}$ is the plastic strain at damage initiation, $\bar{\varepsilon}_f$ is the equivalent plastic strain at failure, $\bar{\varepsilon}$ is the equivalent plastic strain, $\bar{u}$ is the equivalent plastic displacement, $\bar{u}_f$ is the equivalent plastic displacement at failure and L is the characteristic length of the element. The damage evolution parameter is defined in the form of a scalar stiffness degradation parameter ω_s as given by:

$$\omega_s = \frac{L\bar{\varepsilon}}{\bar{u}_f} = \frac{\bar{u}}{\bar{u}_f} \tag{3.34}$$

The equivalent plastic displacement at failure is expressed by:

$$\bar{u}_f = \frac{2G_f}{\sigma_y} \tag{3.35}$$

where σ_y is the yield stress of the material and G_f is fracture energy dissipation which can be determined by:

$$G_f = \left[\frac{1-\nu^2}{E}\right] K_c^2 \tag{3.36}$$

where K_c is the fracture toughness of the material.

F. Damage and Failure Models of Silicon

For the damage model of silicon, compressive yield stress values with plastic strain values have been used. These yield stress values are taken from Split Hopkinson pressure bar (SHPB) test presented in Mir Amir's dissertation. The details of SHPB test can be referred elsewhere in [Mir (2016)]. It is well known fact that, the strain rates involved in machining are high and the yield stress values at higher strain rates are necessary in order to characterize the behavior of the workpiece material during machining. The yield stress and plastic strains values of silicon are listed in Appendix 3.1.

G. Element and Meshing

Figure 3.7 shows the meshed geometries of indenter and workpiece.

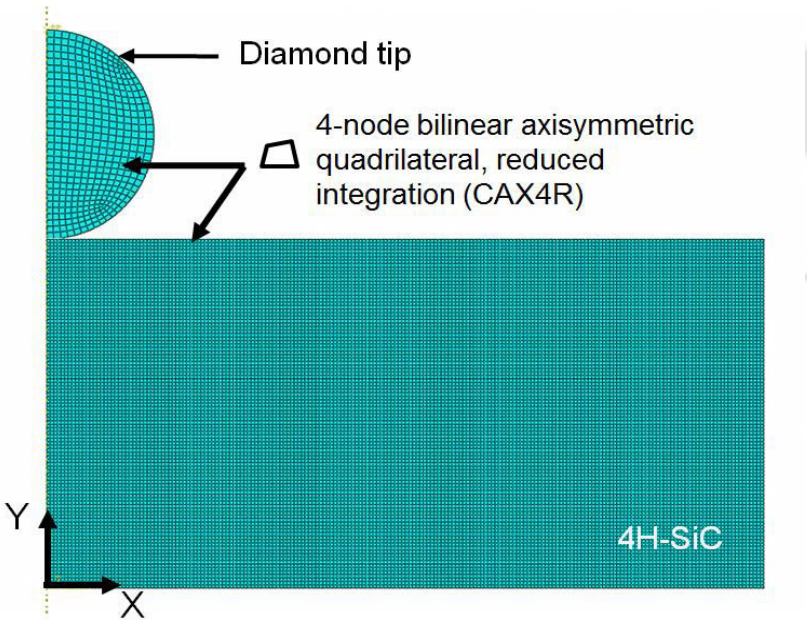

Figure 3.7 Workpiece and indenter meshing

In the present work, two-dimensional, 4-node quadrilateral CAX4R elements are employed. The process continuum is axisymmetric. The element type is 4-node quadrilateral, reduced integration and "hourglass control" element. For complicated finite element

problems, using high order elements, it becomes necessary to use numerical integration to calculate the stiffness matrix. The chosen element type consumes less computation time; easily model non-linear constitutive behavior. The SiC block was discretized uniformly to get uniform element density throughout the block. After the discretization of process continuum mesh refinement was carried out. In general, there are four methods of mesh refinement, viz. *h*-refinement, *p*-refinement, *hp*-refinement and *r*-method [Dixit (2009)]. In the present simulation, *h*-refinement is used. In this method, the size of the element is reduced by increasing the number of elements in order to get more accurate results. The *h*-method improves results by using a finer mesh of the same type of element. This method refers to decreasing the characteristic length (*h*) of elements, dividing each existing element into two or more elements without changing the type of elements used. Consequently, the number of elements in a domain increases. If a part is modeled with a very course mesh, then the stress distribution across the part will be very inaccurate. In order to increase the accuracy of the solution, more elements must be added. This means creating a finer mesh using mesh refinement method.

The mesh sensitivity analysis has been carried out for a typical process condition – indenter tip radius of 300 nm, max loading depth of 5 nm, loading speed of 0.1 mm/s. This process conditions is similar to the experimental conditions mentioned in the published literature by Goel *et al.* (2014b). Extensive numerical trials have been carried out to find out optimum sizes of elements. Table 3.4 shows various sizes of element used to discretize the indentation zone along with respective computation time and maximum load to displacement values.

Table 3.4 Mesh sensitivity analysis result for indentation zone

S. No.	No. of elements	Element size (mm)	Max displacement (nm)	Max load (μN)	CPU time (s)
Experiment			**5.55**	**103.26**	
1	50	0.0002	5.0	190.40	14
2	105	0.000135	5.0	122.88	13
3	153	0.000115	5.0	104.88	15
4	200	0.0001	5.0	88.79	16
5	406	0.00007	5.0	60.05	20
6	800	0.00005	5.0	85.26	38
7	20000	0.00001	5.0	121.94	3276

It can be seen that as the element sizes vary from 0.0002 mm to 0.00001 mm, the number of elements increases from 50 to 20000 elements for discretization of the same size of process continuum. The respective simulation time also increases from 14 s to 3276 s. Figure 3.8 shows the plots of load-displacement curves for various sizes of elements. It also shows the comparison of numerical results with the experimental results given by Goel *et al.* (2014b).

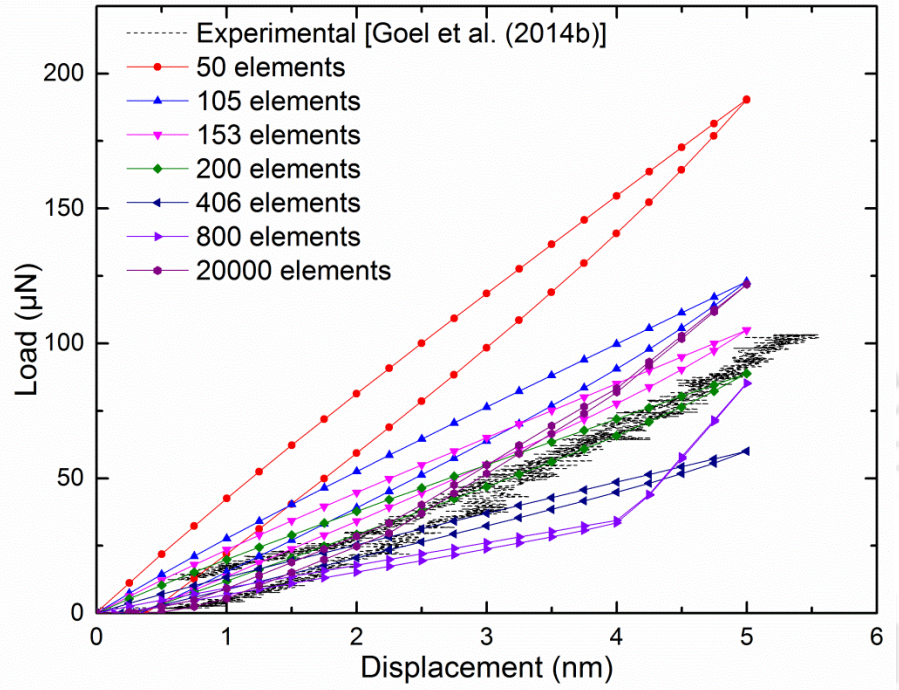

Figure 3.8 Comparison of load-displacement plot with no of elements in indentation zone

It is known fact that, the fine mesh refinement with higher number of elements produces accurate results, however, it requires high computation time and cost. It can be seen that the load-displacement plots at 153, 200 and 20000 elements were closer to the experimental results [Goel *et al.* (2014b)] in comparison with those obtained for remaining cases. The trend of variation of load-displacement for 0.00001 mm element size was found to be fairly matching with the experimental results. Therefore, in the present work it was chosen for further FE based analysis of nanoindentation process.

H. Modeling of Surface Contact

The bottom surface of the indenter and the top surface of work materials formed a contact pair in the present numerical model. General contact and surface to surface contact has been assigned between the contact pairs. Based on the suggestion from literature [Bhattacharya and Nix (1988a, b), Lu and Bogy (1995), Panich (2004)], frictionless contact property is enabled between the two contact surfaces. The effect of friction between the

indenter tip and the surfaces of the work material in nanoindentation process can be assumed as negligible because only a small portion of the indenter contact the surface of the workpiece.

I. Boundary Conditions

Figure 3.9 shows the boundary conditions applied on the indenter and workpiece geometric models. The work material or substrate base surface was constrained by fixed boundary conditions. The nodes on the base cannot move in any directions. *X*-symmetry boundary condition was applied to the vertical surface of the workpiece as shown in Figure 3.9.

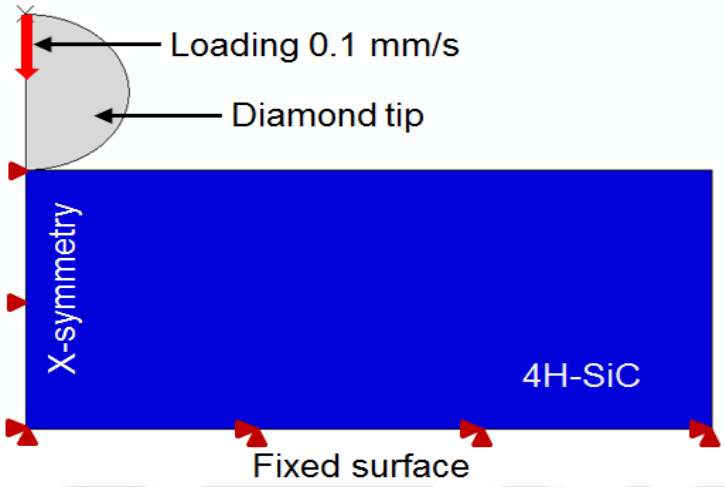

Figure 3.9 Schematic of the boundary conditions applied

It means that, the workpiece geometry and diamond tip is symmetric along the symmetry line and both form a revolving 3D geometry around the x-axis. Since, the rigidity of diamond indenter is significantly larger than that of workpiece; the rigid body constraint was applied to the diamond indenter at the reference point. First, it was restrained in *x* direction along with all the rotational degrees of freedom. As the process carries out at very low speed (of the order of 0.1 mm/s), quasi-static loading condition was assumed. A speed of 0.1 mm/s was applied to the reference point of the diamond tip. As the contact area is very small and loading speed is very slow, the effects of variation in temperature were not considered in the current simulation.

J. FEM Solver Methodology

The numerical simulation of nano-indentation has been carried out in two steps, i.e., loading and unloading. Both the steps have been analyzed by following the non-linear dynamic explicit solution step method with automatic (self-adaptive) time step algorithm. It maintains the constant time increment in each step. In dynamic explicit automatic time step

algorithm, the time increment is adjusted automatically to meet the corresponding convergence rate. The loading behavior of nanoindentation was simulated by increasing the indenter displacement in small increments. During the loading steps, the indenter was moved in negative Y direction, i.e., downward direction with velocity of 0.1 mm/s and indents the work material to the maximum indentation depth. During the unloading step, the indenter returns to its original position incrementally. For each loading and unloading steps, 20 frames have been generated to reduce the data size.

The FEM solver utilizes the equations of motion (governing equations), boundary conditions and input process conditions to simulate the nanoindentation process. It considers one element at a time and solves the equations for field output (such as stress, strain, temperature, displacement, force etc.) and applies it to next surrounding element. In general, FEM solves the equations based to time function by evaluating stiffness matrix at each iteration of definite time step. In this fashion, the equations are solved for the entire geometry within the defined step time period. Abaqus™ stores all the output data in to a file with .ODB file extension. After the completion of the simulation, it was post processed to extract required outputs. In the present case, force, displacement, stress values were extracted from the ODB field output file.

Figure 3.10 shows the FEM simulation results of nanoindentation of silicon carbide using spherical indenter. It shows the distribution of von-Mises stress on the workpiece surface at maximum loading depth of 5 nm.

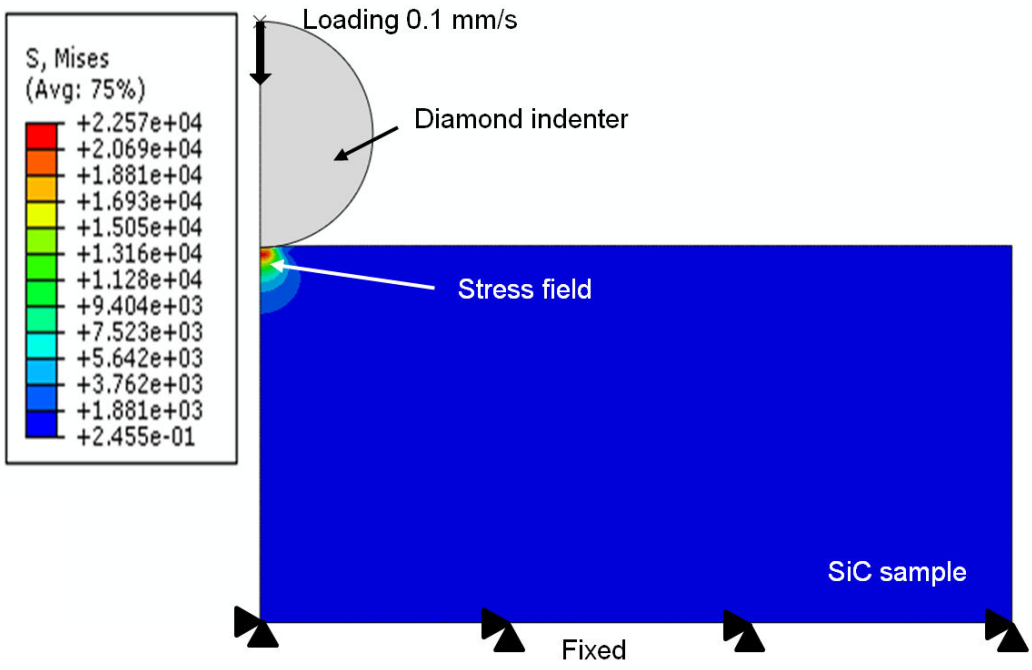

Figure 3.10 von-Mises plot at maximum loading depth of 5 nm

As the load is applied, the indenter leaves a mark on the surface of SiC. Compressive stresses are generated as a result of impression during the loading stage which are shown in the Figure 3.10 and marked as stress field. The intensities of stresses are shown in the legend. The corresponding reaction forces generated at the reference point of the indenter were recorded with respect to the displacement of the workpiece. The displacement is measured from the node at the corner of the workpiece where the indenter is making contact with the workpiece. This corner node also helps in extracting the final residual depth left after unloading. These parameters are very much important for the calculation of elastic modulus and hardness.

3.5 Computation of Young's Modulus and Hardness from Load-Displacement Plot

This section presents the methodology to compute the Young's modulus and hardness from the load-displacement plots that were extracted from nanoindentation process. To calculate Young's modulus and hardness, Oliver and Pharr [Oliver and Pharr (1992)] analytical method has been used. It is described as follows.

3.5.1 Computation of Elastic Modulus

During the nanoindentation method, a small indentation in the specimen is made and the indentation load P, and displacement h, during one complete cycle of loading and unloading are recorded. It is important to determine the stiffness of the contact between the indenter and the material being tested to obtain the mechanical properties of interest. Assuming the case of the elastic contact for a cone and a flat specimen, the force and the indenter displacement are given by Sneddon's equations [Sneddon (1948, 1965)]:

$$P = \frac{2}{\pi} E_r \tan\alpha \, h^2 \tag{3.37}$$

where, E_r is the reduced modulus, α is the indenter cone half-angle (Figure 3.3 (a)). Taking the derivative of P w.r.t. h to obtain:

$$\frac{dP}{dh} = 2\left[\frac{2}{\pi} E_r \tan\alpha\right] h \tag{3.38}$$

where, dP/dh is defined as the contact stiffness (S), which is a very important quantity in the analysis of nanoindentation test data. Substituting the term $\left[\frac{2}{\pi} E_r \tan\alpha\right]$ back to the equation (3.37), we can write

$$P = \frac{1}{2}\frac{dP}{dh} h \tag{3.39}$$

From the Figure 3.6 (a), the displacement h of the indenter and the radius of the circle of the contact 'a' is related by:

$$h = \frac{\pi}{2} a \cot \alpha \tag{3.40}$$

Substituting the value of h in equation (3.38), we get

$$\frac{dP}{dh} = 2\left[\frac{2}{\pi} E_r \tan \alpha\right] \times \left[\frac{\pi}{2} a \cot \alpha\right]$$

$$\Rightarrow \frac{dP}{dh} = 2E_r a \tag{3.41}$$

The projected contact area, $A = \pi a^2$. Thus, from equation (3.38), we get

$$E_r = \frac{1}{2} \frac{dP}{dh} \frac{\sqrt{\pi}}{\sqrt{A}} \tag{3.42}$$

The equation (3.42) applies to the elastic contact of any axis-symmetric indenter (such as a sphere, cone) and can be used to calculate the combined elastic modulus of the indenter and the specimen. The contact stiffness $S = dP/dh$ can be measured from the initial slope of the unloading curve. The contact radius can be found from the depth of the circle of contact h_c and the geometry of the indenter. Once the stiffness S is measured, reduced modulus E_r, which accounts for the measured elastic displacement contributing from both the sample and the indenter tip can be computed by:

$$E_r = \frac{1}{2} \frac{S}{\beta} \frac{\sqrt{\pi}}{\sqrt{A}} \tag{3.43}$$

where, β is a constant that depends on the geometry of the indenter. It is used to determine the elastic modulus and hardness values accurately as it affects contact stiffness and projected area which are important for calculating elastic modulus and hardness respectively. The standard values of β suggested by Oliver and Pharr and other researchers are listed in Table 3.5.

Table 3.5 List of indenter parameters for spherical indenter [Králík and Němeček (2014)]

Indenter type	Projected area (A)	Intercept factor (k)	Geometry correction factor (β)
Sphere	πa^2	0.75	1

The reduced modulus can be used to calculate the actual modulus of the sample, which is given by:

$$\frac{1}{E_r} = \frac{1-\upsilon_i^2}{E_i} + \frac{1-\upsilon_s^2}{E_s} \tag{3.44}$$

where E_i = 1141 GPa and υ_i= 0.07 are the elastic modulus and Poisson's ratio respectively for diamond indenter as per Goel *et al.* (2014b) and Nawaz *et al.* (2017). From this equation we can calculate the E_{sample} (elastic modulus) for the given sample.

3.5.2 Computation of Hardness

Hardness is the property of material which shows the resistance to the plastic deformation. It is given by the ratio of the applied force (P_{max}) to the corresponding area of contact (A):

$$\text{Hardness, } H = \frac{Applied\ load}{Contact\ area} = \frac{P_{max}}{A} \tag{3.45}$$

where P_{max} is the maximum load and A is the projected area of contact or hardness impression. The effect of indentation depth on hardness measurement has been a real area of concern. When low loads are applied, the resultant area of contact might be very small or sometimes it recovers elastically with no residual impression left behind, due to which, the contact area of impression approaches to zero. This gives an exaggerated hardness value as the contact area becomes nearly zero in equation (3.45). The most common method to determine the hardness of a material is by static indentation.

3.5.3 A Case Study

After the development of the numerical model, simulations were carried out. For a typical process condition of 5 nm depth of indentation with 300 nm radius spherical indenter and 0.1 mm/s loading speed, a case study on computing elastic modulus and hardness is presented below.

A. Elastic Modulus

Figure 3.11 shows the load-displacement plot that was extracted from ODB field output. The step by step procedure to compute the elastic modulus is as follows.

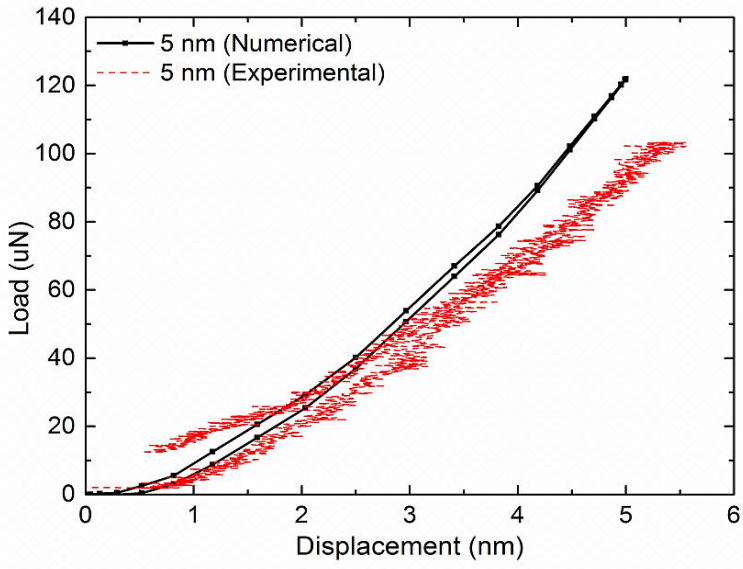

Figure 3.11 Load-displacement plot

- From the extracted load-displacement plot, maximum load, corresponding maximum displacement and final displacement after the unloading are recorded. In the present case, maximum load was 121.89 μN for the maximum displacement of 5 nm. The displacement after unloading was 0.28 nm.
- From the unloading curve, 1/3rd data points (7 points) of the total unloading data points (21 points) are linearly fitted. Usually between 25% and 100% of the unload curve data are commonly used for the fitting function depending on the quality of the unloading data [Oliver & Pharr (2004), Shuman *et al.* (2006)]. In the present case we have found that 1/3th of the data points give good results while calculating Young's modulus and hardness. The fitted line is extended to meet the x-axis for the ease of finding the slops from the linearly fitted line as shown in Figure 3.12.

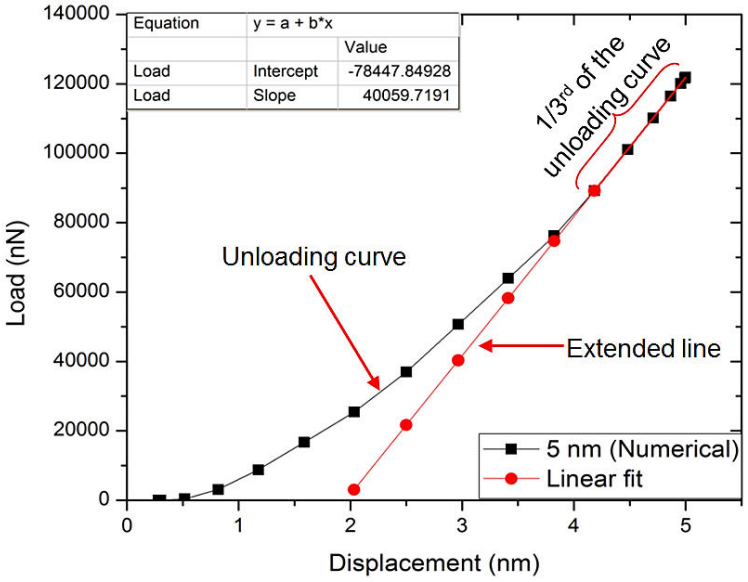

Figure 3.12 Fitting the unloading curve and finding the slope

- From the linearly fitted line, the slope is calculated. This is regarded as the stiffness,

  S = 40059.72 N/m^2.

- From the P-h plot, the fixed and variable parameters for indentation parameters were obtained and listed in Table 3.6.

Table 3.6 Indentation parameters (fixed and variable parameters)

Parameters	Value	Unit
Indentation depth at max load (h)	4.9993×10^{-8}	m
Indentation load at max load (P_{max})	0.000122	N
Unloading displacement	4.72×10^{-8}	m

- Depending on the indenter tip used, the contact radius was calculated. For spherical indenter, the contact radius was computed as

  Contact radius, $a = \sqrt{R^2 - (R-h)^2} = \sqrt{h(D-h)}$

  $=\sqrt{4.9993(600 - 4.9993)}$

  $=54.54$ nm (3.46)

  where, R is the radius of the indenter, D is the diameter of the spherical indenter, and h is the max depth at max load.

- Corresponding contact area between the indenter tip and workpiece at maximum displacement was calculated as

  Contact area, $A = \pi a^2 = 9.34879 \times 10^{-15}$ m^2 (3.47)

- After finding out the stiffness (S), contact area (A) and taking indenter geometry correction factor $\beta = 1$, the reduced modulus (E_r) was calculated as

  $$S = \beta \frac{2\sqrt{A}}{\sqrt{\pi}} E_r$$

  $$E_r = \frac{1}{2\beta} \frac{\sqrt{\pi}\times 40059.72}{\sqrt{9.34879\times 10^{-15}}}$$

  $E_r = 3.67253 \times 10^{11}$ N/m^2 (3.48)

- In the present simulation, the diamond indenter was considered as perfectly rigid body. However, in the physical experiments, there may be a slight deformation in the nanometric tip which might have absorbed some load. Therefore, it is quite appropriate to assume an

infinite value of Young's modulus for the diamond as well. Thus, the second term in the Equation (3.44) will become zero [Yu *et al.* (2003)]. Then by using Equation (3.44), the elastic modulus of SiC sample was computed as

$$\frac{1}{E_r} = \frac{1-\upsilon_i{}^2}{E_i} + \frac{1-\upsilon_s{}^2}{E_s}$$

$$\Rightarrow \frac{1}{3.67253\times10^{11}} = 0 + \frac{1-(0.23)^2}{E_s}$$

$$\Rightarrow E_s = 348 \text{ GPa} \tag{3.49}$$

Thus, the Young's modulus (E_s) for the silicon carbide sample is found as 348 GPa.

B. Hardness

The hardness value of silicon carbide can be calculated by using Equation (3.45). It is given as,

$$\text{Hardness, } H = \frac{P_{max}}{A} = \frac{0.000122}{9.34879\times10^{-15}} = 13.04\ GPa \tag{3.50}$$

After determining the required output parameters, the results were validated with the published experimental results. These are presented in the following section.

3.6 Experimental Validation of FEM based Nanoindentation Simulation

After the development of numerical model, the experimental validation of the responses predicted by the numerical model was carried out. The validation was carried out for silicon and silicon carbide materials. These are presented in the following sections.

3.6.1 Experimental Validation of Nanoindentation of Silicon Carbide

The predictions of our numerical model have been validated with the experimental results of Goel *et al.* (2014b). Figure 3.13 shows the computed and experimental results of load vs. displacement plots. For this comparison, similar process conditions were employed. Spherical indenter tip with diameter of 600 nm has been modeled. The material model, workpiece geometry, boundary conditions, element type and mesh model used in this simulation are already described in section 3.4.2. Accordingly, numerical simulations of nanoindentation of SiC have been carried out and results were extracted. Plots of computed and experimental results in terms of load vs. displacement for indentation depths of 5 nm, 10 nm, 12 nm, 25 nm and 50 nm are shown in Figure 3.13. It shows the comparison of load-

displacement plots of experimental results and numerical simulations for 5, 10, 12, 20, 25 and 50 nm depth indentations. From the figure, it is observed that numerical results fairly match with the experimental results. With these encouraging results, further comparisons have been carried out by using Oliver and Pharr analytical procedure as explained in section 3.5.

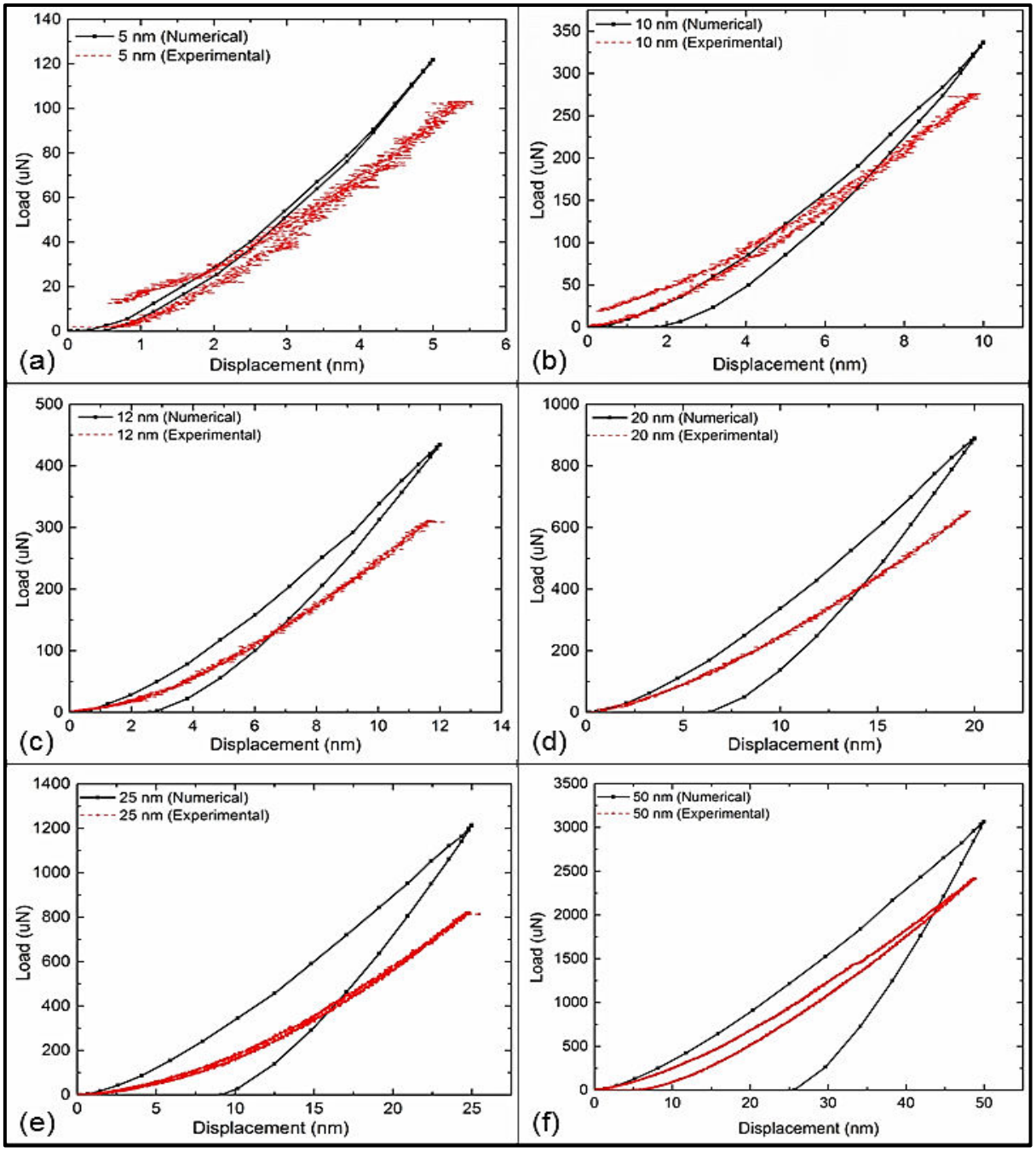

Figure 3.13 Load vs. displacement: numerical and experimental results for SiC

The computed values of Young's modulus and hardness values are listed in Table 3.7. It also shows peak loads, projected area, calculated Young's modulus and hardness for various levels of indentation depth. From the table, it is observed that, peak loads predicted in simulations are slightly higher than that of experimental peak loads. This is possibly due to consideration of various assumptions such as diamond indenter was considered as perfectly

rigid body and spherical and workpiece and indenter both assumed to be isotropic and homogeneous. The simulations were found to be predicting well with overall prediction error of **19.9%** considering all responses together. Also, the computed values of projected area are found to be similar with experimental results with maximum prediction error of **2.63%.** The numerical model is capable of predicting the Young's modulus and hardness with 32% and 24.7% of absolute prediction error respectively.

Table 3.7 Comparison of experimental and simulated Young's modulus and hardness at different indentation depth for SiC

Peak displacement	Peak Load (μN)			Projected area (nm^2)			Young's Modulus (GPa)			Hardness (GPa)		
	Experiment	Simulation	Prediction error (%)	Experiment	Simulation	Prediction error (%)	Experiment	Simulation	Prediction error (%)	Experiment	Simulation	Prediction error (%)
5 nm	103.3	121.9	15.3	9978.2	9348.8	−6.7	233	348	33.1	10	13	23.0
10 nm	276.2	336.9	18.0	18055.9	18541.7	2.6	275	358	23.1	15	18	15.8
12 nm	312.2	434.5	28.2	22422.1	22174.6	−1.1	270	351	23.0	14	20	29.7
20 nm	654.1	889.5	26.5	35791.4	36455.9	1.8	246	376	34.7	18	24	25.8
25 nm	821.8	1215.1	32.4	45967.9	45177.4	−1.7	255	397	35.7	18	27	34.2
50 nm	2415.2	3065.9	21.2	84811.4	86427.8	1.9	265	459	42.4	28	35	19.8
Average prediction error			**23.6**			**2.63**			**32.0**			**24.7**

3.6.2 Experimental Validation of Nanoindentation of Silicon

Nanoindentation simulations were also carried out for silicon as the workpiece. To validate the developed finite element based nanoindentation model, the experimental results given by Rao *et al*. (2007) were considered. All the process conditions in the simulation were set similar to that of experimental studies carried out by Rao *et al*. (2007). The workpiece geometry, boundary condition, element type and mesh model used in the present simulation were similar to that for SiC (section 3.4.2) except the material model and process conditions. Numerical simulations were carried out and results were extracted in terms of load vs. displacement values. Figure 3.14 shows the plots of experimental and numerical simulation results for indentation depths 45 nm, 75 nm, 95 nm, 115 nm, 130 nm and 140 nm. It can be seen that the numerical results are in well agreement with the experimental results.

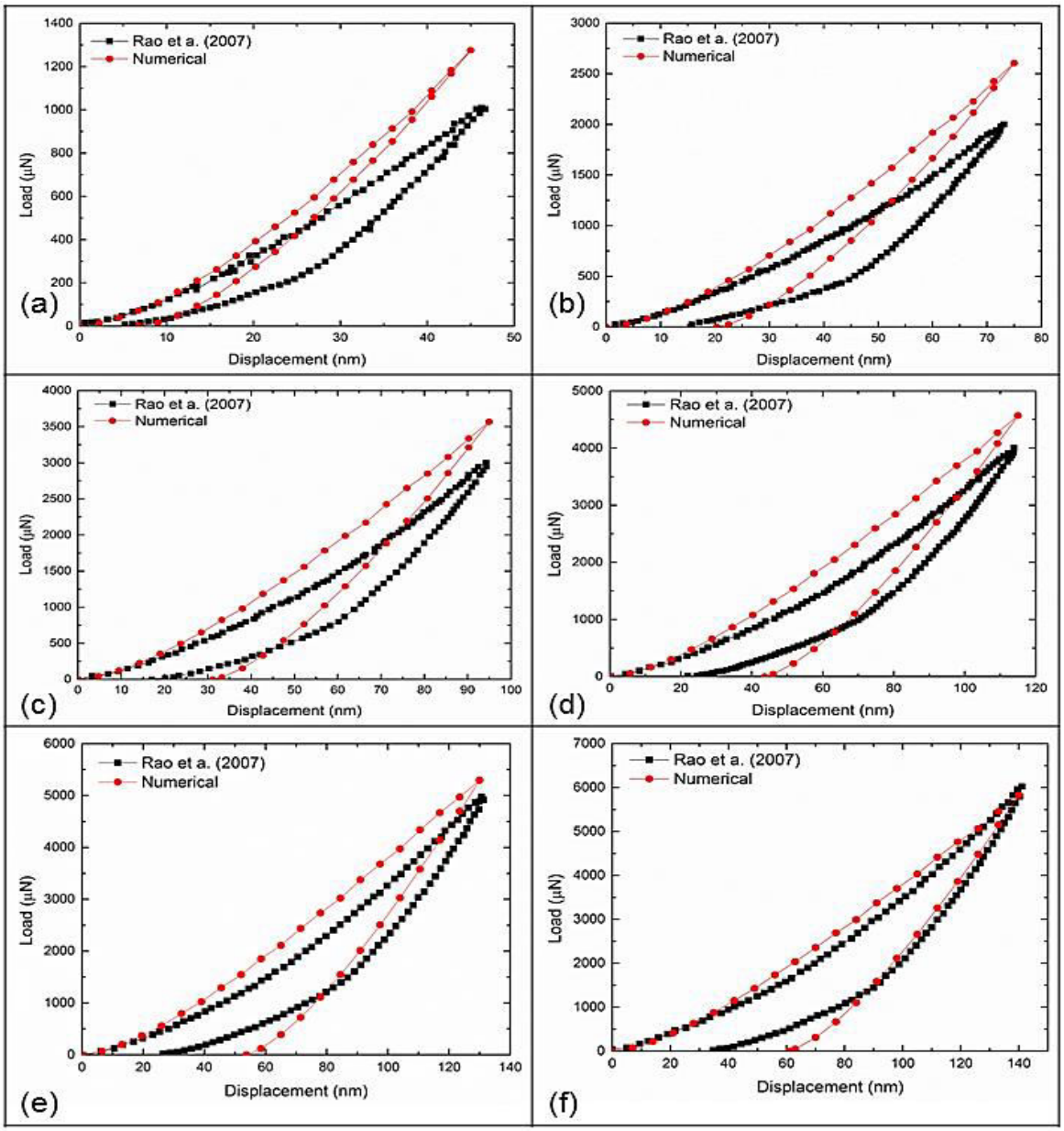

Figure 3.14 Load vs. displacement: numerical and experimental results for Si

After the numerical simulations, using Oliver and Pharr analytical procedure explained in section 3.5, the Young's modulus and hardness values were calculated. These are listed in Table 3.8. It also depicts the comparison of experimental results with the numerical results in terms of peak loads, projected area, calculated Young's modulus and hardness for various levels of indentation depths. It can be observed that, the peak load for simulations are higher than the experimental peak load. However, computations of projected area, Young's modulus and hardness were found to be agreeing very well with the experimental results with the overall prediction error of **10.9%.** Computation of projected area is found to be quite accurate with **1.3%** as average prediction error. The average prediction errors for Young's modulus and hardness were noted to be **9.2%** and **16.5%** respectively.

From the Figure 3.14, it is also noticed that the peak loads are higher for simulation results at lower depths and gradually become lower at higher depth (140 nm) as compared to that of experimental results. Furthermore it is to be noted that the our results are found to be in-line with the established values of Young's modulus and hardness values for silicon 190 GPa and 12 GPa respectively [Reddy (2008)]. The variations in the results between experimental results and numerical simulations may be due to the consideration of indenter as rigid body and employing the work material as isotropic and homogeneous.

Table 3.8 Comparison of experimental and simulated Young's modulus and hardness at different indentation depth for Si

Peak displacement	Peak Load (μN)			Projected area (nm2)			Young's Modulus (GPa)			Hardness (GPa)		
	Experiment	Simulation	Prediction error (%)	Experiment	Simulation	Prediction error (%)	Experiment	Simulation	Prediction error (%)	Experiment	Simulation	Prediction error (%)
45 nm	1004.2	1275.2	27	81157.7	78492.9	−3	139	155	11	12	16	31
75 nm	2000.4	2604.4	30	121056.3	123750.0	2	176	169	−4	17	21	27
95 nm	3000.0	3566.8	19	149824.4	150778.6	1	196	179	−9	20	24	18
115 nm	4001.7	4568.5	14	173974.9	175292.9	1	193	188	−3	23	26	13
130 nm	4975.3	5296.1	6.4	192637.2	192028.6	−0	211	193	−9	26	28	7
140 nm	6026.0	5826.6	−3	203447.6	202400.0	−1	243	198	−18	30	29	−3
Average prediction error			**16.6**			**1.3**			**9.2**			**16.5**

After successful validation of the present numerical model for Si and SiC, it was thought appropriate to carry out a detail study on understanding of ductile to brittle transition (DBT) of brittle materials using the developed numerical model. In what follows the study on the DBT is presented in the next section.

3.7 Study of Ductile to Brittle Transition (DBT) using Nanoindentation

The detail study of ductile to brittle transition of brittle material using nanoindentation simulation is described in the following subsections.

3.7.1 Determination of DBT

The objective of this section is to determine the ductile-to-brittle (DBT) thickness by using nanoindentation simulation. In this work, a spherical indenter of 500 nm radius was used to achieve indentation depth from 0 to 500 nm. The indenter, workpiece geometries, meshing, and boundary conditions were kept similar to those presented in section 3.4.2.

Simulations were carried out on silicon and silicon carbide materials using rigid diamond indenter. Diamond indenter was given the downward movement with velocity of 0.1 mm/s. The indentation pressure below the indenter tip was observed closely until the failure occurs. The indentation depth and pressure were recorded for the comparison with the experimental ductile to brittle transition depths.

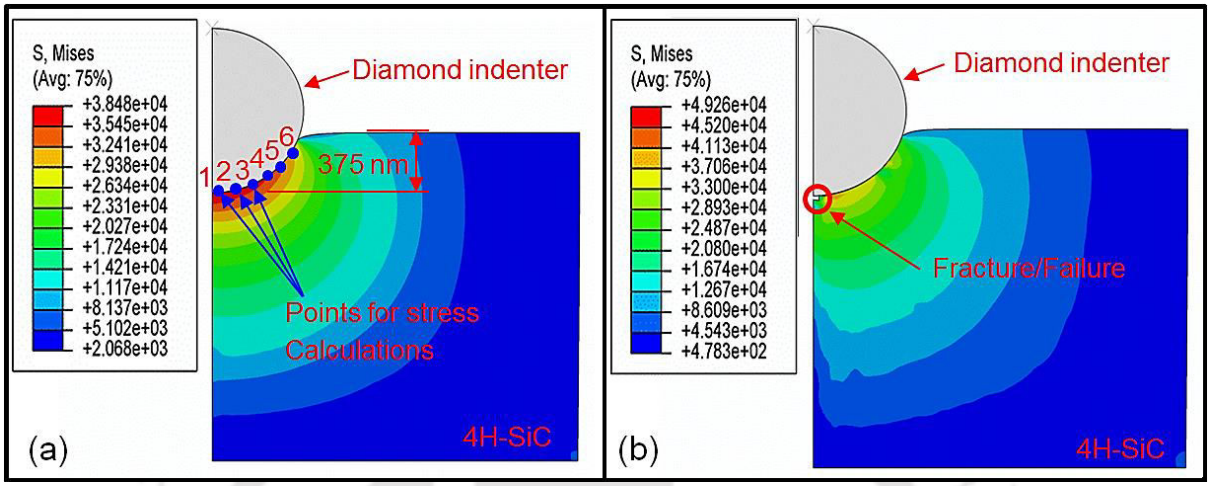

Figure 3.15 Indentation depth (a) before fracture and (b) after fracture for silicon carbide

Figure 3.15 shows the von-Mises stress field for 4H-SiC specimen before and after the occurrence of fracture. From Figure 3.15 (a), it can be noted that a maximum von-Mises stress of about 38 GPa occurs when the indenter's depth is 375 nm. This value is noted when the step time is 375 μs and ODB frame is 15. This pressure (~38 GPa) is sufficient to change the phase (> hardness of SiC, i.e., 25–35 GPa [Noreyan *et al.* (2005), Reddy (2008), Patten and Jacob (2008)]) of the material and the depth can be comparable to the ductile to brittle transition depth [Patten *et al.* (2005)]. Just after the 15th ODB frame, i.e. at 16th frame and step time 400 μs, there appeared a crack/fracture (Figure 3.15 (b)) marked with red circle. The von-Mises stress also suddenly increased to 49 GPa from 38 GPa. The average stress was calculated along the contact surface between indenter and specimen (shown with blue dots in Figure 3.15 (a)). It is to be noted that von-Mises stresses plotted in the Figure 3.16 are the average values of stresses generated at nodes 1 to 6 as shown in Figure 3.15 (a).

Figure 3.16 shows the plot of average stress versus indentation depth. It reveals that the stress increases linearly up to some depth (~120nm) and when the pressure/stress reaches the threshold value for dislocation initiation, micro-cracks start forming underneath the tip. Because of the movement of dislocations, the stresses are absorbed to some extent which is depicted in the Figure 3.16. When all the dislocation movements are completed, a linear stress of 30-35 GPa is obtained which is near to the phase changing pressure. Similar observations have also been presented by Szlufarska *et al.* (2004, 2005) and Mishra and Szlufarska (2009)

on their nanoindentation simulation using molecular dynamics. Just after the fracture (375 nm depth), stresses of the selected nodes were drastically reduced.

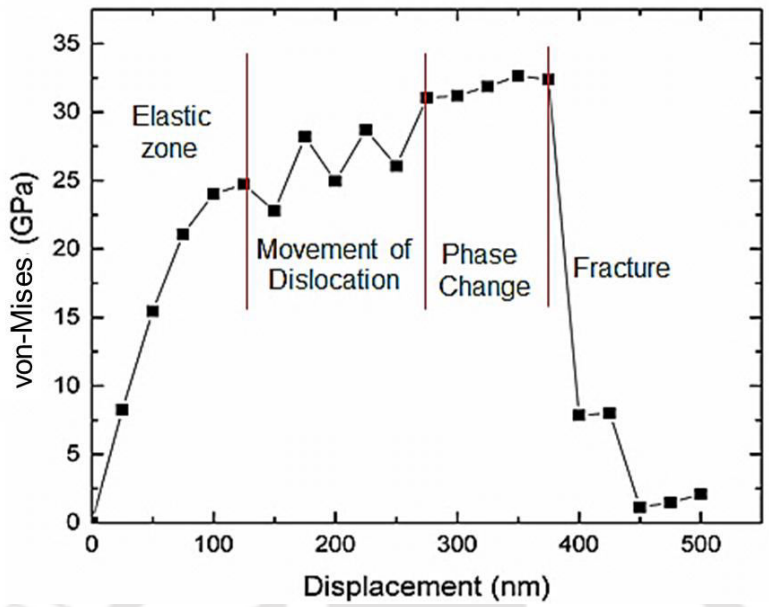

Figure 3.16 Average stress (nodes 1 to 6) vs. indentation depth

Similar to the numerical simulation of SiC, simulations were carried out to determine the DBT for silicon (isotropic) sample. It was found out that the fracture occurs at ~16.6 GPa, where the cubic diamond structure of silicon transforms to metallic β-silicon (Figure 3.17 (b)). Here, the peak displacement was noted as ~ 91 nm. During silicon cutting, generally, the machining pressure in the ductile regime is higher than 10 GPa, which is sufficiently high for phase transformation of silicon [Yan *et al.* (2009a)].

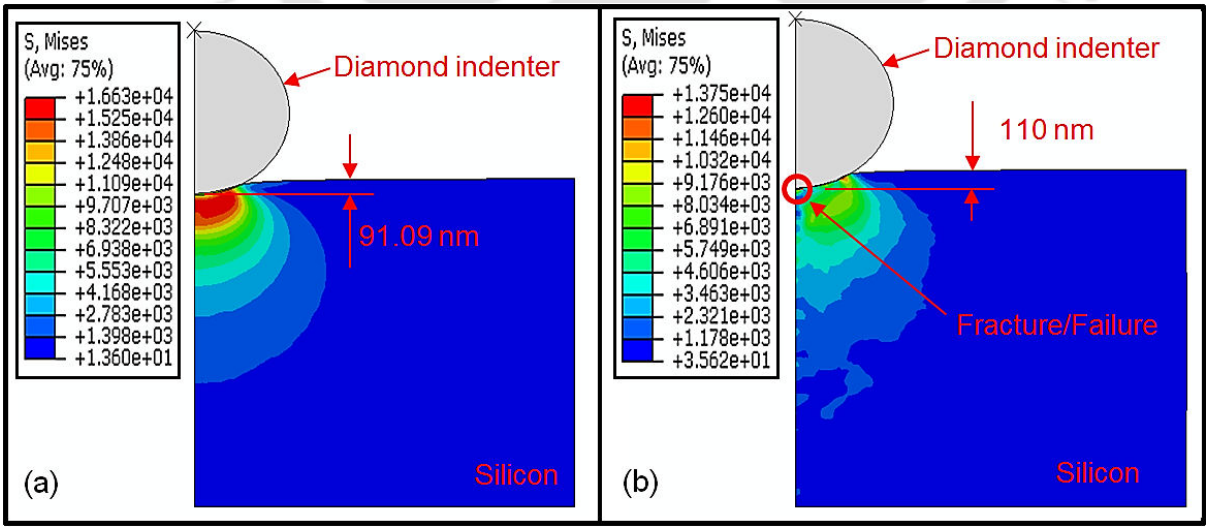

Figure 3.17 Indentation depth (a) before fracture and (b) after fracture for silicon

According to Yan *et al.* (2005b), dislocation phenomenon of silicon is still not fully understood. Literature suggests that dislocations do not move during conventional mechanical

testing at temperatures below 450˚C [Alexander and Haasen (1969), Ray *et al.* (1971)]. Under extreme conditions such as indentation loading, where localized stresses can approach the theoretical shear strength of the material, dislocation structures have been observed in silicon. pure edge dislocations generally do not form in silicon because, at room temperature, the dislocations are relatively immobile in silicon [Yan *et al.* (2009b)]. From the Figure 3.18, it is observed that the movements of dislocations are not clearly identifiable. Only a small portion of stresses has been absorbed at room temperature during the indentation process.

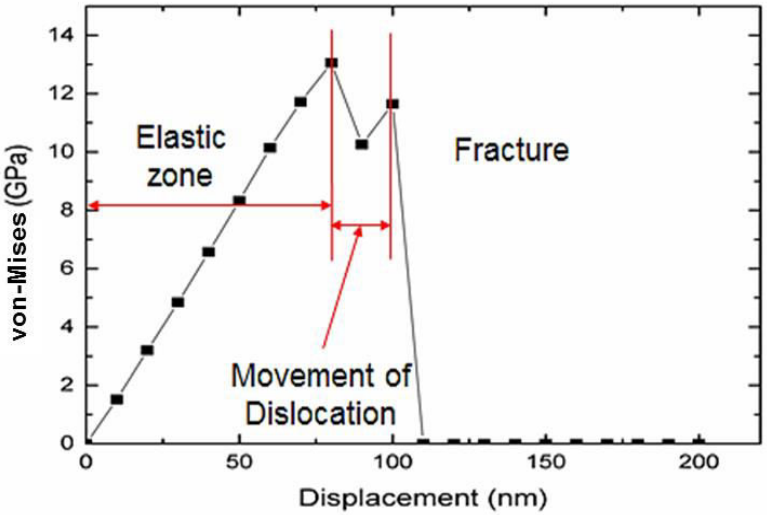

Figure 3.18 Average stress generated at the selected nodes vs. indentation depth

From the above two analyses, the DBT values for SiC and Si were found to be around **375 nm** (Figure 3.16) and **91 nm** (Figure 3.18) respectively. These are the values at which the first micro crack initiates in the workpiece. The validation of these findings is presented in the following section.

3.7.2 Validation of DBT with Published Experimental Results

Literature reports significant experimental works on obtaining DBT for silicon and silicon carbide through plunge cut/taper turning, fly cutting, scratch test and machining. The published literature Yan *et al.* (2001, 2003, 2005a), Yan (2004), Venkatachalam *et al.* (2009), Fang and Venkatesh (1998), Fang and Zhang (2003) and Arif *et al.* (2013) show the DBT for silicon varies between 50 to 200 nm. The computed DBT for silicon using the present model is well within this range. Similarly, for silicon carbide, the experimental DBT is reported to be in the range of 300 to 500 nm [Patten *et al.* (2005), Ravindra and Patten (2008)]. The numerical value of DBT (~375 nm) for silicon carbide using our numerical model is found to be very well in the range of experimentally reported DBT value.

3.8 *In-situ* Study of Phase Changing Pressure

In general, brittle materials undergo phase change when they applied with compressive hydrostatic stress [Strössner *et al.* (1987), Yoshida *et al.* (1993), Lu *et al.* (2008)**].** In case of 3C-SiC, the material undergoes a phase transition into the Rocksalt (RS)-type structure at 60-100 GPa or higher accompanied by a volume reduction of 20.3%. Upon pressure release, the RS-structured SiC transformed back to 3C-SiC phase below 35.0 GPa. 6H-SiC polytype remained stable up to about 90.0 GPa with an indication of a phase transition above this pressure [Yoshida *et al.* (1993)]. Sekine and Kobayashi's shock compression experiments on 6H-SiC demonstrated a first-order phase transition with a volume reduction of about 15% into a six fold coordinated structure around 105 GPa [Sekine and Kobayashi (1997)].

Silicon material exhibits different transition phases during the application of pressure. Published literature have demonstrated that silicon undergoes plastic deformation and phase transformation under the existence of high hydrostatic pressure [Zhao *et al.* (1986), Hu and Spain (1984), Yan (2004), Cai *et al.* (2007b), Needs and Mujica (1995), Minomura and Drickamer (1962), Clarke *et al.* (1988)]. Initially, the silicon will be in cubic (diamond) structure (α-silicon) in the pressure range of 0 −11.3 GPa. A transition to the β-Sn structure (II) and amorphous phase initiates at 11.2 ± 0.2 GPa and two phases (I + II) coexist at 12.5 ± 0.2 GPa. However, during unloading stage, this metallic phase is not stable at low pressure (~4 GPa) and changes to an amorphous phase or other metastable phases. At 13.2 ± 0.2 GPa a new phase (V) initiates, and the transition completes at 16.4 ± 0.5 GPa. This hexagonal phase continues to exist from 25 GPa to 40 GPa. Beyond this, metastable phases (VIII and IX) can be found. On release of pressure, the phase sequence is V → (V + II) (14.5 – 11.0 GPa) → II → (II + III) (10.8 – 8.5 GPa) → III, the last phase persisting to room pressure. The simulation results indicate a pressure of about 38 GPa at the peak displacement. This is greater than the hardness of the material, i.e. 26 GPa [Patten *et al.* (2007)], as shown in Figure 3.19.

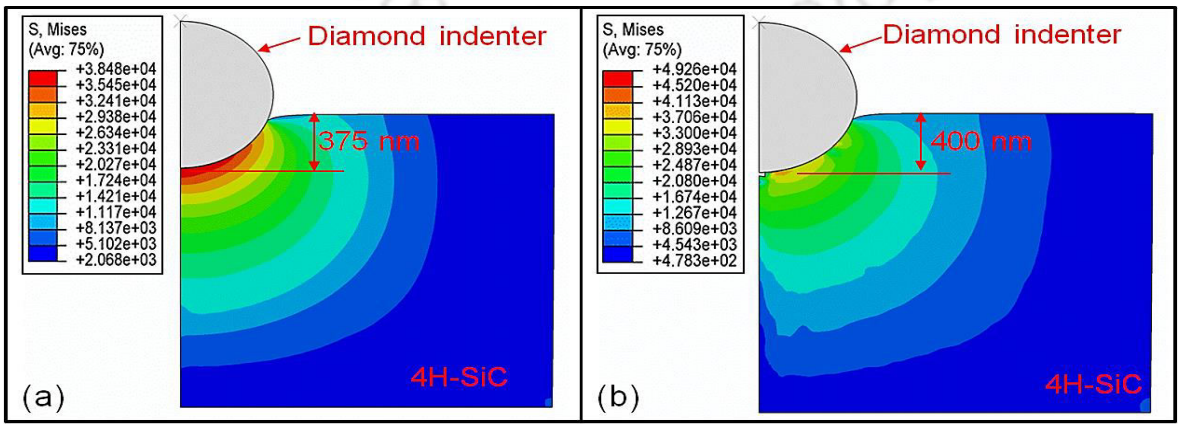

Figure 3.19 Different pressure zones (a) before failure at 372.97 nm depth and (b) after failure at 400 nm depth for silicon carbide

In case of numerical simulation for silicon nanoindentation, the von-Mises stress of ~16 GPa was noted during the deepest indentation which is larger than the transition pressure for silicon from cubic (diamond) to β-Sn metallic phase. This finding is found to be in line with the published results of hardness 10.79 GPa by Cai *et al.* (2007b), Zhang and Tanaka (1999) and Cheong and Zhang (2000). As per our simulations, the residual stresses on the surface were found to be 0.37 to 0.7 GPa for silicon. This is also in line with experimental findings of 0.3 to 1.5 GPa reported by Juliano and Penrose (2002). The different pressure zones appeared during nanoindentation process during loading and after unloading and their corresponding phases are shown in Figure 3.20.

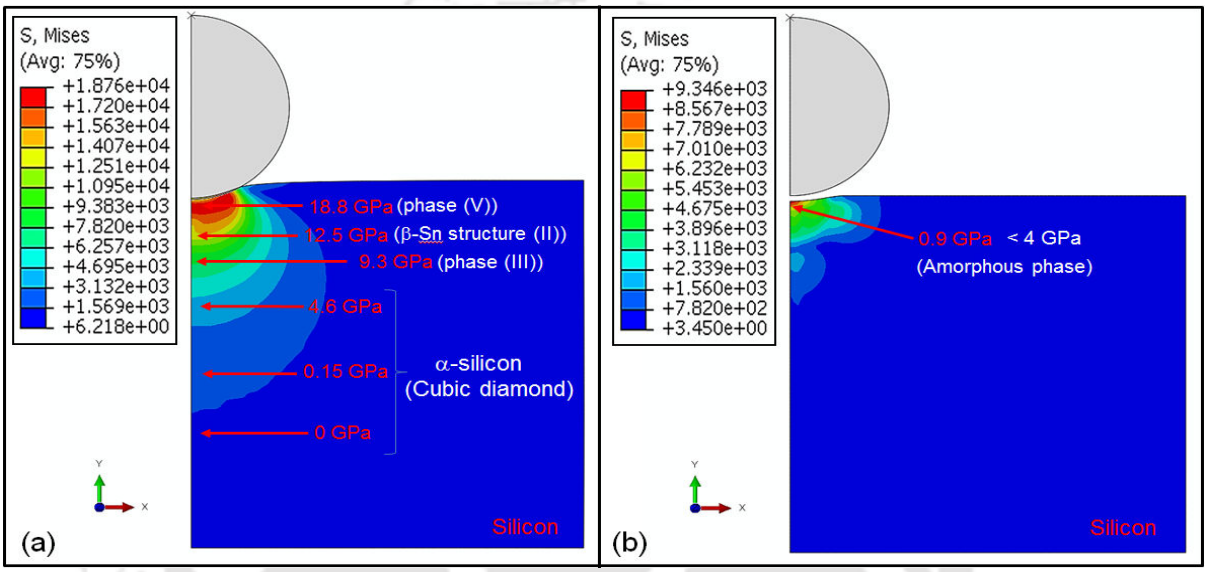

Figure 3.20 Different pressure zones after (a) Loading and (b) Unloading during nanoindentation on silicon

During our numerical simulations, some irregular stress fields were observed along the element layer (considering a plane along the center of the indenter and perpendicular to workpiece surface). These stress fields are unusual, as no anisotropic properties and crystal orientations were considered in the model. The reason behind this fact may be that, just under the indenter tip, there exists an amorphous layer of few nanometers thickness. Under the amorphous layer, dislocations are present which trigger the plastic deformation of the workpiece. Although the amorphous layer cannot be clearly differentiated, the dislocations can be identified by the stress field as shown in red colored circles in Figure 3.21. Similar observations have been made by Jasinevicius *et al.* (2005), Nix and Gao (1998) in their experimental works. Nix and Gao (1998) mentioned that during indentation with rigid cone, geometrically necessary dislocations beneath the indenter are required to account for the permanent shape change at the surface. Jasinevicius *et al.* (2005) described the dislocations and subsurface micro-cracks beneath the amorphous layer during pyramidal micro indentation

and diamond turning. Overall the present work indicates the presented numerical modeling using FEM can be successfully utilized to predict the micro-cracks as well

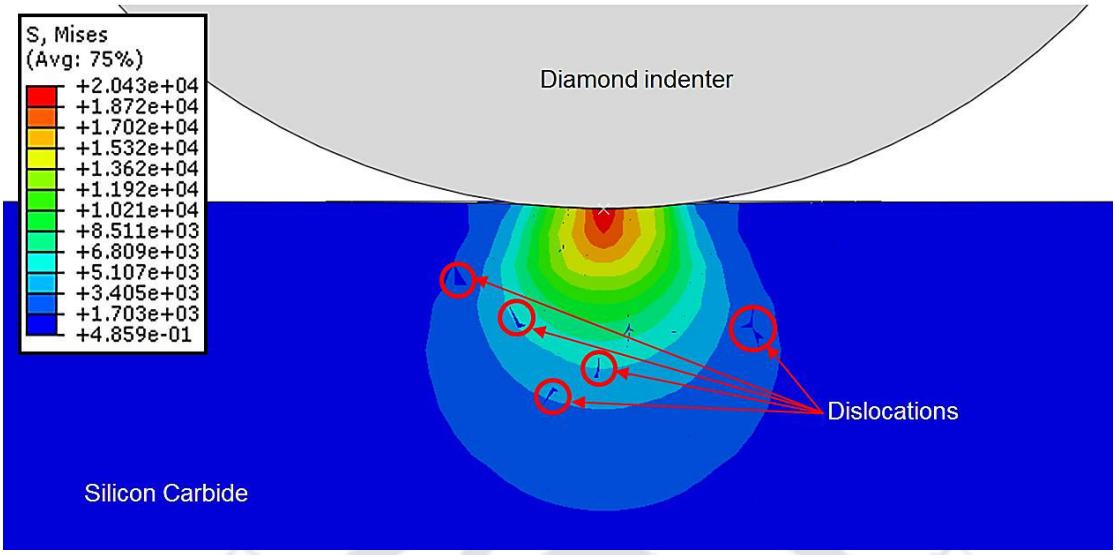

Figure 3.21 Spherical nanoindentation of SiC showing irregular stress field

3.9 Numerical Study on the Effect of Residual Stress on DBT during Repetitive Indentation

In general, the surfaces of workpieces on which hardness to be measured are either mechanically or chemically processed. These processing generate some sort of residual stresses on the surface of the workpiece. Thus, it was thought worthy to carry out numerical simulation to check the effect of residual stress on P-h plot, Young's modulus and hardness. To obtain these results, simulation of repetitive nanoindentation cycles have been carried out at the same location with the indentation depths of 10, 20 and 50 nm, so that the successive indentations will leave some stress on the workpiece. For this purpose, a 2D axisymmetric spherical nanoindentation FEM model was developed. The model geometry, material model, element type, and meshing employed in this simulation are similar to that of described in section 3.4.2. Total ten steps were created to simulate the ten cyclic loading-unloading indention boundary conditions. The repetitive nanoindentation simulation was carried out at various indentation depths of 10, 20 and 50 nm. These depths were chosen in such a way that it includes at least two indentation depths (20 and 50 nm) which matches with the experimental depths so that it can be compared with their corresponding P-h plots, Young's modulus and hardness. The step corresponding to 20 nm depth of indentation will have the residual stresses generated due to earlier 10 nm depth loading-unloading process. Similarly, 50 nm indentation depth will have residual stress generated due to its prior 20 nm indentation depth. However, in this method, both 20 and 50 and later indentation depths will have some initial depth due to which their indentation will not start from the origin or zero. Figure 3.22

shows FEM simulation results of indentation of silicon carbide using spherical indenter. It shows the maximum stress field at peak load and residual stresses left after each indentation i.e. 10, 20 and 50 nm indentation depths after the complete unloading state in each case.

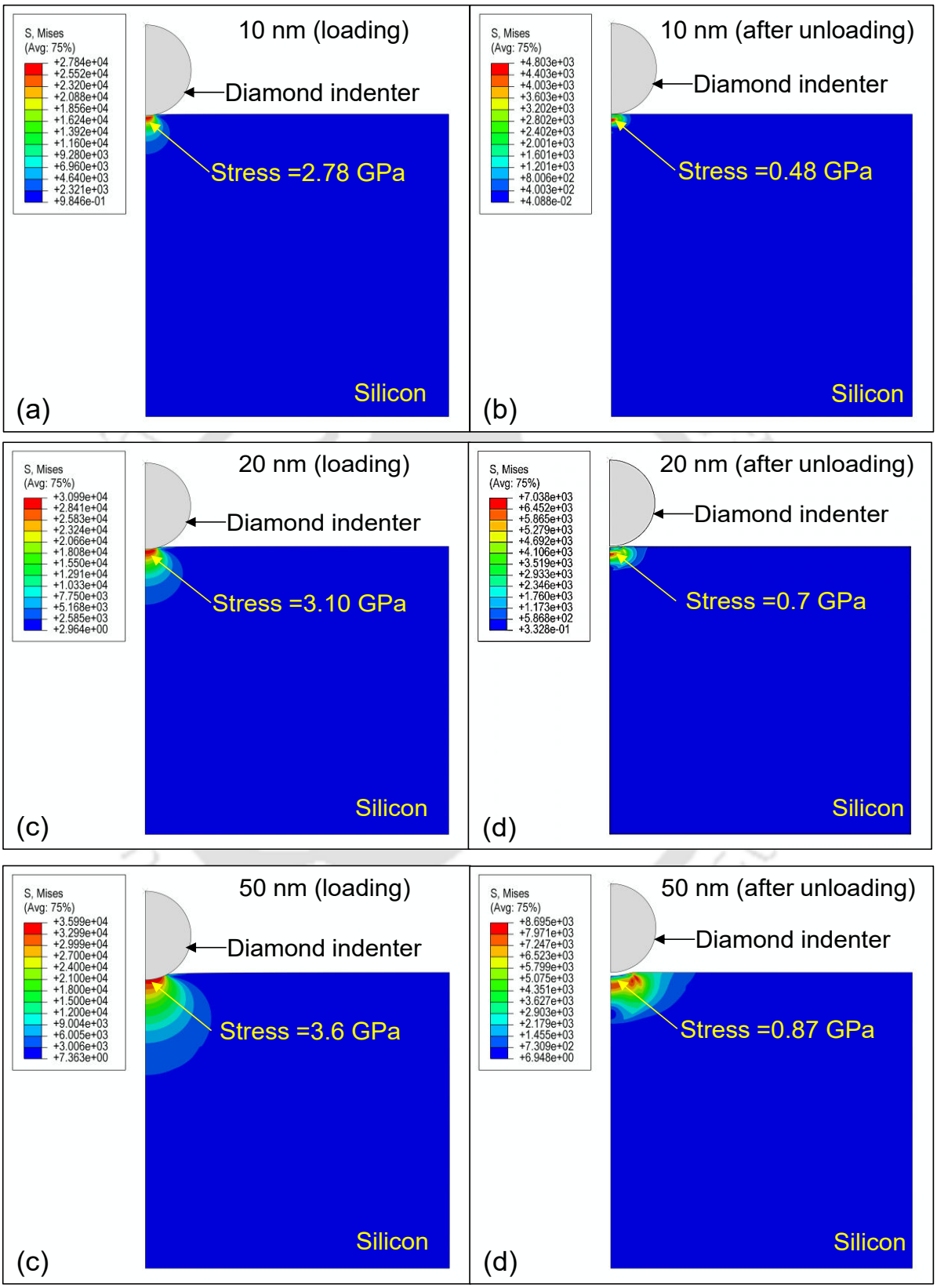

Figure 3.22 Repetitive nanoindentations using spherical indenter with depths 10 nm, 20 nm and 50 nm

Load-displacement plots were extracted from the simulation for 10, 20 and 50 nm and are shown in Figure 3.23. Linear fitting lines were drawn for each unloading curves as described in section 3.5.3 (A) and Figure 3.12. Then the corresponding slope/stiffness values were determined. Young's modulus and hardness values were calculated for 20 nm and 50 nm depth of indentation and listed in Table 3.9.

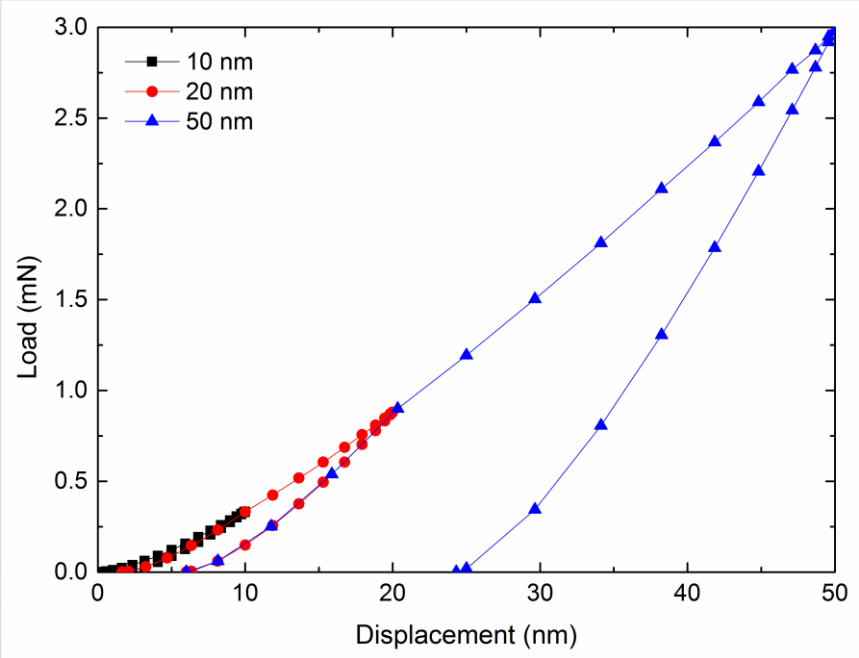

Figure 3.23 P-h plot for cyclic nanoindentation of silicon carbide with spherical indenter

Table 3.9 Young's modulus and hardness with and without residual stress

Displacement (nm)	Young's modulus (GPa) (cyclic)	Young's modulus (GPa) (original)	Hardness (GPa) (cyclic)	Hardness (GPa) (original)
20	370.38	375.99	24.14	24.4
50	421.22	459.31	34.51	35.47

Generally, in case of metals, Young's modulus and hardness values increase with increase in indentation depths due to strain hardening. Moreover, in multiple indentations, due to the repetitive loading, stiffness of the workpiece increases which also increases the hardness and Young's modulus. Table 3.9 shows a comparison between computed values of Young's modulus and hardness for indentation depth 20 and 50 nm with the experimental values. It was found that Young's modulus and hardness values of repetitive indentation were lesser than the residual stress free indentation. This is because, in the initial 10 nm of loading, silicon undergoes phase change and a layer of amorphous silicon is formed when the indenter is removed and pressure is reduced to below 4 GPa. Because of the amorphous layer, the hardness and Young's modulus value decrease. This phenomenon is well explained by Yan

and his team [Yan *et al.* (2005b)] by conducting indentations on the workpiece before and after cutting.

3.10 Summary

In this present work, displacement controlled quasi-static 2D-axisymmetric nanoindentation simulations were performed on Si and SiC specimen using a spherical indenter. Quasi-static nanoindentation simulation in particular permits systematic examination to enable a better understanding of deformation mechanisms, evaluation of mechanical properties, and aspects of the plasticity of brittle materials such as Si and SiC. More importantly, it permits to investigate onset pressure, stress, and temperature at the indentation zone. Experimental validations of P-h plots were carried out based on the available published experimental data. Using Oliver and Pharr analytical procedure, Young's modulus and hardness values were found out and also compared with experimental values for verification.

- It is found that the calculated Young's modulus and hardness from the numerical simulations were slightly higher than the experimental value. This may be due to the assumption of rigid indenter, the geometry of the indenter, residual stress and material properties incorporated in the model. However, they are agreeing well.
- The numerical simulations of nanoindentation of SiC and Si were found to be predicting well with an overall prediction error of 15.4% respectively.
- After the validation of the model, critical depth of indentation, i.e., ductile to brittle transition and phase changing pressures were analyzed. It is observed that von-Mises stress is higher than the hardness of the workpiece and sufficient to change the phase.
- During the analysis of stress versus indentation depth, it is observed that stress increases linearly up to some depth (~120nm) when the pressure/stress reaches the threshold pressure for dislocation initiation. Because of the movement of dislocations, some of the stresses are absorbed for which non-linear variation of stress has been observed. After all the dislocation movements are completed, linear stress of 30-35 GPa was obtained which is near to the phase changing pressure. Fracture occurs at indentation depth of 375 nm which can be considered as the critical depth of indentation or ductile to brittle transition thickness. This thickness is found to be consistent with the previously published experimental results.
- A similar trend is also found in case of silicon material with lower stress; however distinct dislocation zone is not available in case of silicon material.

Overall, the present work provided a realistic, simple, efficient integrated approach for

the prediction of load-displacement, mechanical properties and ductile to brittle transition during nanoindentation of brittle materials. Based on the results obtained, it is felt that the developed FEM model can be applied with confidence in practice for quick and accurate computation of mechanical properties and ductile to brittle transition. Even though the proposed model is able to determine mechanical properties and ductile to brittle transition, however, the proposed model does not provide the information about the machining, quality of surface machined and chip morphology which is vital in deciding the machining parameters to obtain the desired process performance during SPDT process. In view of this, it was thought appropriate to carry out another study on ductile to brittle transition using a plunge cut to add more emphasis to the results predicted using nanoindentation simulation. The details of the same are provided in the next chapter.

A STUDY ON DUCTILE REGIME MACHINING USING NUMERICAL SIMULATIONS OF PLUNGE CUTTING

4.0 Scope

This chapter presents finite element method based numerical simulations of plunge cutting of silicon and silicon carbide to study the ductile to brittle transition. The objective of this chapter is to identify the ductile to brittle transition of silicon and silicon carbide. At first, the need for carrying out a numerical simulation of plunge cutting is defined. Then, an overview of the proposed approach for modeling plunge cutting using FEM is presented. A 2D dynamic explicit numerical model of plunge cutting is developed using *x* and *y* directions speeds to achieve a continuously varying depth of cut from 0 to 600 nm. Details of the modeling and development of the finite element model of plunge cut in terms of assumptions, governing equations, geometry, mesh model, boundary condition and solutions methodologies are presented. To identify the critical depth of cut, i.e., ductile to brittle transition, various output parameters are thoroughly analyzed and discussed. Three methods were employed, i.e., visual inspection of surface profile, variation of machining force and specific cutting energy. A comparative analysis of the three methods employed has also been presented. Further, the work was extended by carrying out simulations for silicon carbide and the critical depth of cut was determined. The simulated results were validated with the published experimental results.

4.1 The Need

From the reported literature, it was learned that to obtain a crack-free surface on brittle material by using SPDT process; it is necessary to know the ductile to brittle transition thickness of the material. The previous chapter presented a finite element based two-dimensional numerical model of the nanoindentation process. By using the developed model, mechanical properties such as Young's modulus and hardness were computed successfully. The model also provided a close value of ductile to brittle transition thickness of silicon and silicon carbide. However, it did not provide the information about the machining, quality of surface machined and chip morphology which is vital in deciding the machining parameters to obtain the desired process performance during the single point diamond turning (SPDT) process. In view of this, a literature review was carried out and it was learned that taper or plunge cutting can be an alternate and easy method to study the ductile regime machining of brittle materials. In a plunge cutting process, the depth of cut is varied from zero to few hundreds of nm (above the critical depth of cut) and various response variables such as

machined surface profile, cutting force and specific cutting energy are analyzed. Based on this, the critical depth of cut for precision machining can be obtained.

Significant literature has been reported on experimental study of plunge cutting of silicon [Fang and Venkatesh (1998), Fang and Zhang (2003), Yan *et al.* (2009b, 2012)] and silicon carbide [Xiao *et al.* (2015a, b), Jacob *et al.* (2005)]. However, very scant literature is reported on numerical simulations of plunge cutting to determine the ductile to brittle transition of silicon and silicon carbide. Thus, a need was identified to develop a numerical model for quicker and accurate prediction of ductile to brittle transition of silicon and silicon carbide. A research work in this direction has been carried out in the present work with the following objectives:

- To simulate the plunge cut during single point diamond turning (SPDT) using FEM.
- To study the variation of stresses in the cutting zone during the plunge cutting.
- To estimate the critical depth of cut, i.e., ductile to brittle transition thickness and phase transformation pressure by analyzing the machined surface, cutting force and specific cutting energy.
- To assess the performance of various methods to estimate the critical depth of cut.

In what follows, the details of the model development are provided in the following sections.

4.2 Overview of the Present Work

This section presents an overview of the present research work carried out on understanding of ductile regime machining. Figure 4.1 shows the various stages of finite element based simulation of plunge cut.

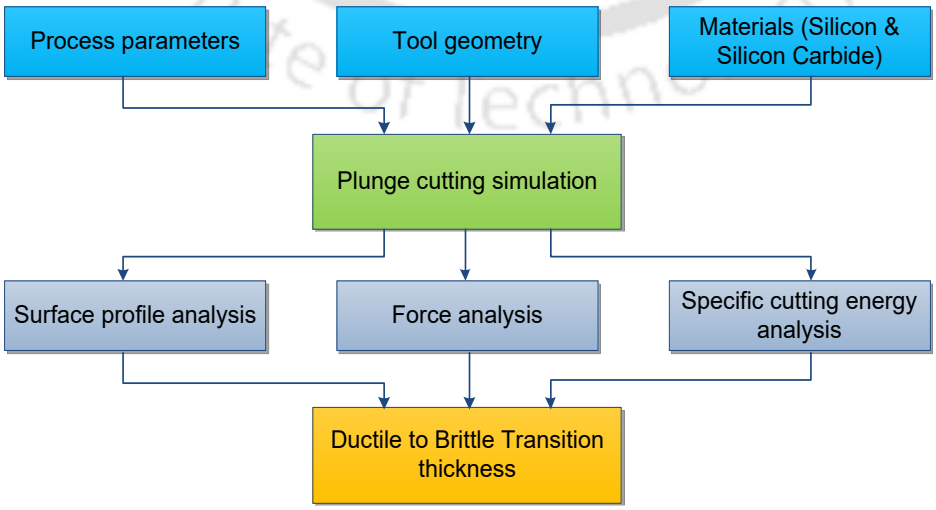

Figure 4.1 Overview of the work carried out to obtain DBT thickness

It comprises of development of a two dimensional, nonlinear dynamic explicit numerical model of plunge cutting of silicon and silicon carbide. Three different approaches have been employed to obtain the DBT thickness of silicon and silicon carbide. The predicted values of DBT thickness are compared with the established experimental results and the best method to estimate the critical depth of cut (DBT thickness) is suggested.

The various stages of the work carried out as follows.

1. Development of a two-dimensional (2D) non-linear dynamic explicit finite element method (FEM) based numerical model of plunge cutting operation.
2. Analysis of simulated machined surface for the first visible micro cracks.
3. Analysis of machining forces (cutting and thrust force).
4. Calculation of specific cutting energy from the cutting force and chip area for the estimation of ductile to brittle transition thickness for silicon and silicon carbide.
5. Comparison of predicted DBT thickness with already established DBT thickness from the experiments.

The next section presents the details of model development.

4.3 Overview of the Process Model Development

In the present work, finite element based numerical model has been developed to simulate the process of plunge cutting. Figure 4.2 shows the various details of the process model development.

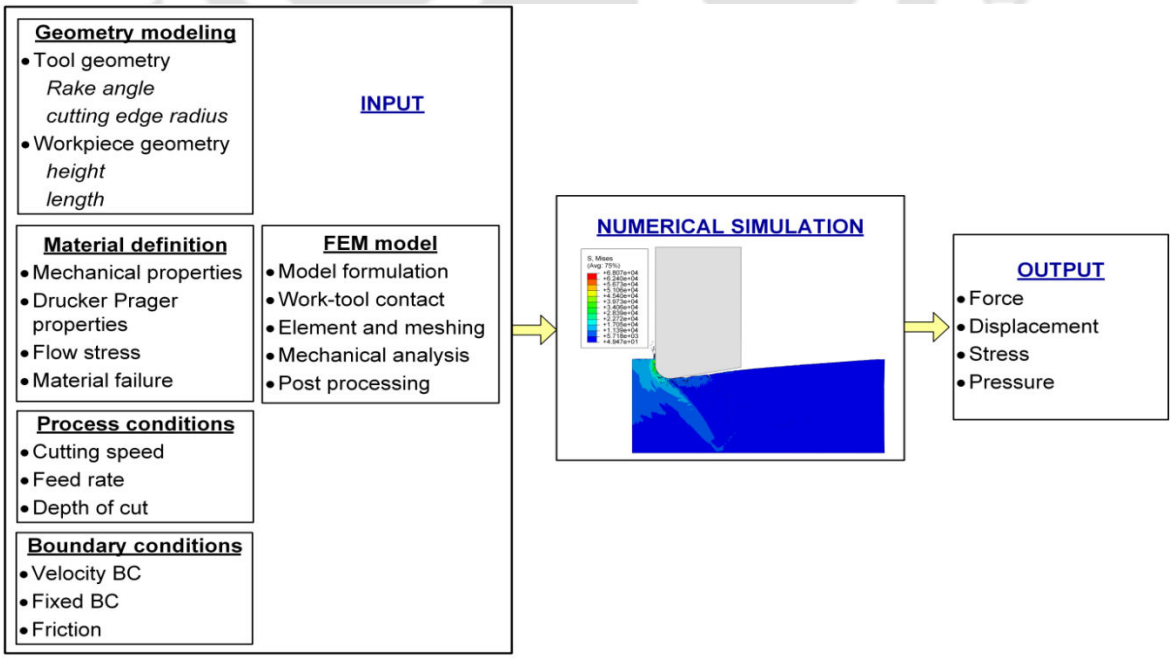

Figure 4.2 Schematic of developed numerical model of plunge cutting

The step– by–step procedure followed in the present FEM based modeling and simulation is outlined below.

- Development of geometric models of workpiece and diamond tool.
- Applying material properties to the workpiece.
- Discretization of a workpiece geometry using 4-node quadrilateral, bilinear plane strain reduced integration elements, CPE4R.
- Application of boundary conditions such as mechanical constraints 'encastre'–a fixed boundary condition to keep the workpiece fixed, symmetric boundary condition, velocity of the diamond tool.
- Dynamic explicit solution of the developed model.
- Determination of stress, pressure, force and displacement at the end of the analysis and computation of response parameters such as surface profile, machining force and specific cutting energy to determine ductile to brittle transition.
- Validation of computed responses with the published experimental results.
- Comparison of different approaches used to estimate the critical depth of cut.

In what follows these steps are discussed at length in the following sections.

4.4 Numerical Simulation of Plunge Cutting Process of Silicon

During single point diamond turning (SPDT) process, brittle material undergoes transition from brittle to ductile as the undeformed chip thickness reduces below the threshold of submicron scale [Fang and Zhang (2003), Arif *et al*. (2013)]. It is postulated by the researchers that if the undeformed chip thickness is very small, plastic deformation becomes dominant mode of material removal. In plunge cutting operation, the depth of cut is gradually increases from zero to few hundreds of nanometers, that is, above the critical depth of cut. This is commonly used to determine the ductile to brittle transition zones so that crack free surface can be obtained during machining of brittle materials using SPDT process.

Figure 4.3 shows schematic of a plunge-cut made on a brittle material. It shows three distinct zones of material response viz. ductile zone, transition zone and brittle zone. As the depth of cut increases, the tool approaches the ductile-to-brittle transition zone. At a point, the thrust force and cutting force become equal; this is called the transition point. Beyond this point, the rate of increase of cutting force becomes higher than that of thrust force. In the brittle zone, the thrust force per unit volume of material removed decreases with random variations in the force caused by the fracture process as material undergo brittle fracture. This phenomenon is very important to be studied. Therefore, in the present work, a 2D finite

element method based numerical model of plunge cut has been developed. The details of model development and the results are presented in the following sections.

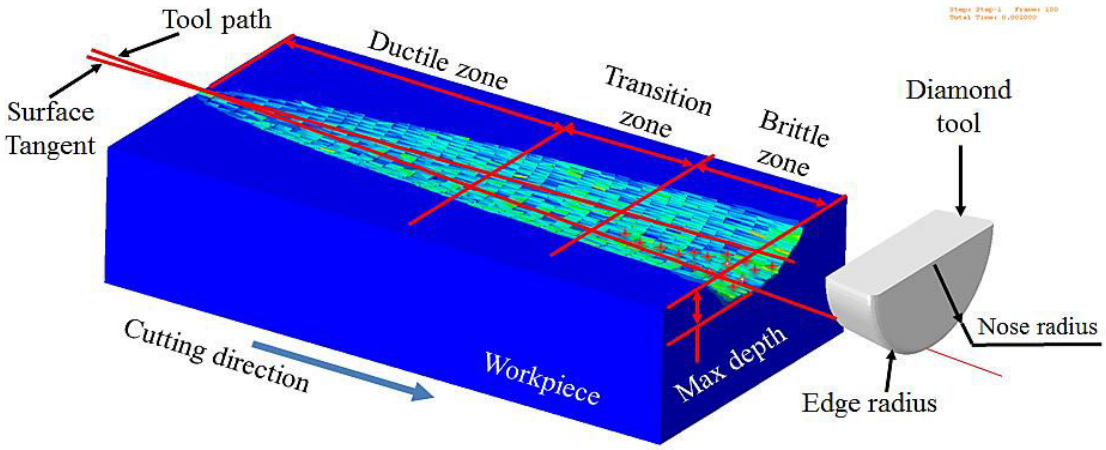

Figure 4.3 Schematic of Plunge cut showing different zones

4.4.1 Assumptions

In this work, the determination critical depth of cut, i.e. ductile to brittle transition thickness under different cutting conditions is considered to be the main objective. Numerical modelling and simulation of plunge cutting process involves complex interaction between the tool and workpiece, contact modelling, material properties and material failure. Following assumptions were made during the numerical simulations.

- Workpiece material is isotropic and homogeneous in nature.
- The workpiece is flat and free of initial residual stresses.
- As the hardness of diamond tool is significantly larger than that of the silicon, the diamond tool is assumed as rigid body and tool wear is neglected in this study.
- As per Blake and Scattergood (1990), Wang and Liao (2008), for the cutting speed range of 0.8–8.2 m/s, there is no remarkable effect of temperature on the generated surface of the silicon material. Therefore, the effects of temperature are not considered in the present simulations.
- Cutting is considered as perfectly orthogonal.
- Cutting occurs in dry-mode.
- The cutting is chatter free. There are no tool and work vibrations due to external media.

4.4.2 Governing Equations

The basic idea of FEM is to break up the geometry of the body into finite, simple shaped elements, thus the problem becomes solvable. In any finite element method, the

structure of interest or domain is divided into finite pieces (called elements) and each element is connected with nodes that hold elements together. Then, based on boundary conditions, governing equations are applied to the nodes to obtain an algebraic equation. All the algebraic equations from each element are approximated by the FEA software to find the global algebraic equation for the domain. Then the unknown variables are calculated from the obtained algebraic equation. These steps are presented in Figure 4.4.

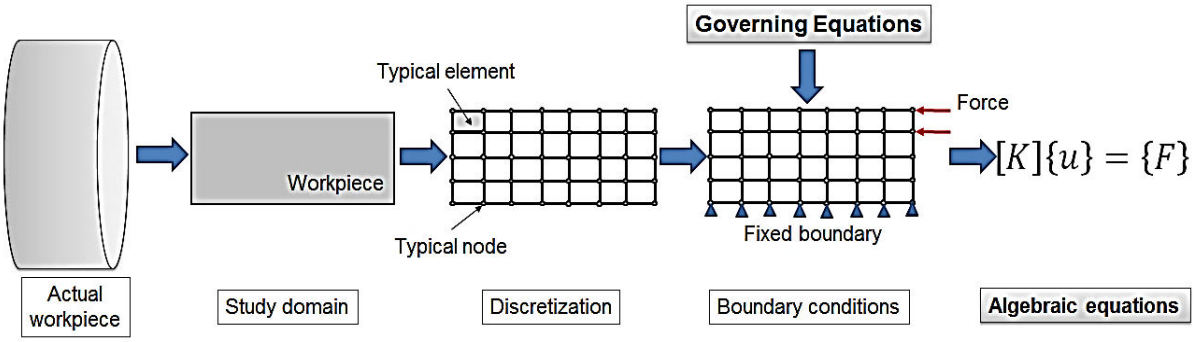

Figure 4.4 Schematic of FEM formulation to solve an engineering problem

where K is the property, u is the behavior and F is the action. In the current mechanical analysis, K is the stiffness matrix, u are the displacements of the nodes and F is the external force applied. The differential equation of motion that governs the mechanical response of a system of finite elements can be written as:

$$m\ddot{u} + c\dot{u} + ku = F \tag{4.1}$$

where m is the mass, c is the damping coefficient, k is the stiffness coefficient. Equation (4.1) is rewritten in matrix form as:

$$[M]\ddot{u} + [C]\dot{u} + [K]u = [F] \tag{4.2}$$

where $[M]$ is the mass matrix, $[C]$ is the viscous damping matrix, $[K]$ is the stiffness matrix, F is the external force vector and $\ddot{u}$, $\dot{u}$ and u are the nodal acceleration, velocity and displacement vectors, respectively. Nodal acceleration at the beginning of time increment i can be obtained by rewriting Equation (4.2) as:

$$\ddot{u}_i = M^{-1}(F - C\dot{u}_i - Ku_i) \tag{4.3}$$

The explicit dynamic analysis procedure is based on using very small time steps. In explicit formulation, central difference scheme has been used to discretize the equations. In central difference method, both forward and backward method are combinedly used to evaluate the velocity and acceleration at a given point by making use of one step forward and one step backward.

Figure 4.5 shows the schematic of finite difference method. If the equilibrium equation (4.2) is regarded as a system of ordinary differential equations with constant coefficients, any convenient finite different method can be employed to approximate the accelerations and velocities in terms of displacements used.

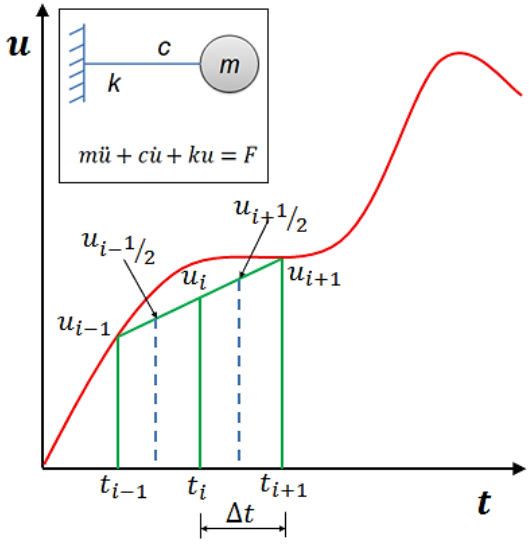

Figure 4.5 Schematic of finite difference method (central difference method)

An effective procedure used in Abaqus™ is the central difference method, and the accelerations at the beginning of the current time increment *t*, is given by

$$\ddot{u}_i = \frac{\dot{u}_{i+1/2} - \dot{u}_{i-1/2}}{\Delta t} = \frac{\left(\frac{u_{i+1}-u_i}{\Delta t}\right) - \left(\frac{u_i - u_{i-1}}{\Delta t}\right)}{\Delta t} = \frac{u_{i+1} - 2u_i + u_{i-1}}{(\Delta t)^2} \tag{4.4}$$

Here Δt is the time step, u_{i-1} and u_{i+1} are the displacements at the beginning of the previous increment and the end of the current time increment respectively. Also the velocities at the beginning of the current time increment *t* can be obtained from equation (4.5) and is given by

$$\dot{u}_i = \frac{u_{i+1} - u_{i-1}}{2\Delta t} \tag{4.5}$$

The displacement solution at the end of the current time increment $i + 1$ is obtained by considering (4.2) at time *t*, and is given by equation (4.6):

$$M\ddot{u}_i + C\dot{u}_i + Ku_i = F \tag{4.6}$$

Substituting the relations for accelerations and velocities in 4.4 and 4.5 in to 4.6 we obtain the following relation:

$$M\left(\frac{u_{i+1} - 2u_i + u_{i-1}}{(\Delta t)^2}\right) + C\left(\frac{u_{i+1} - u_{i-1}}{2\Delta t}\right) + Ku_i = F$$

$$\left(\frac{M}{\Delta t^2}+\frac{C}{2\Delta t}\right)u_{i+1}=F-\left(\frac{M}{\Delta t^2}-\frac{C}{2\Delta t}\right)u_{i-1}-\left(K-\frac{2M}{\Delta t^2}\right)u_i \tag{4.7}$$

Equation (4.7) gives the values of the displacements at the end of the current time increment $i+1$. The solution of u_{i+1} is based only on the equilibrium conditions at time t. For this particular reason the integration procedure is called an explicit integration method. Also in the central difference method, the calculation of u_{i+1} involves u_i and u_{i-1}. Therefore to calculate the solution at time Δt a special procedure must be used. Since u_0 is known (an initial condition), $\ddot{u}_o$ can be calculated using equation (4.2) at time 0; Also the relations shown in equations (4.4) and (4.5) can be used to obtain u_{-1}. This method is effective only when a small step size, and therefore, a large number of time steps are used. For this reason, this method is mainly applied when a lumped mass matrix can be assumed and a velocity-dependent damping can be neglected; then equation (4.7) becomes

$$\left(\frac{M}{\Delta t^2}\right)u_{i+1}=F-\left(\frac{M}{\Delta t^2}\right)u_{i-1}-\left(K-\frac{2M}{\Delta t^2}\right)u_i \tag{4.8}$$

Therefore, if the mass matrix is diagonal, the system of equations in (4.2) can be solved without inverting the matrix equations i.e., only matrix multiplications are required to obtain the displacement components, and this reduces the computational cost greatly when compared to an implicit method. In the present work, the FEM based problem is formulated and solved by using explicit method. For this purpose commercial Abaqus^{TM} was used.

4.4.3 Geometric Modeling

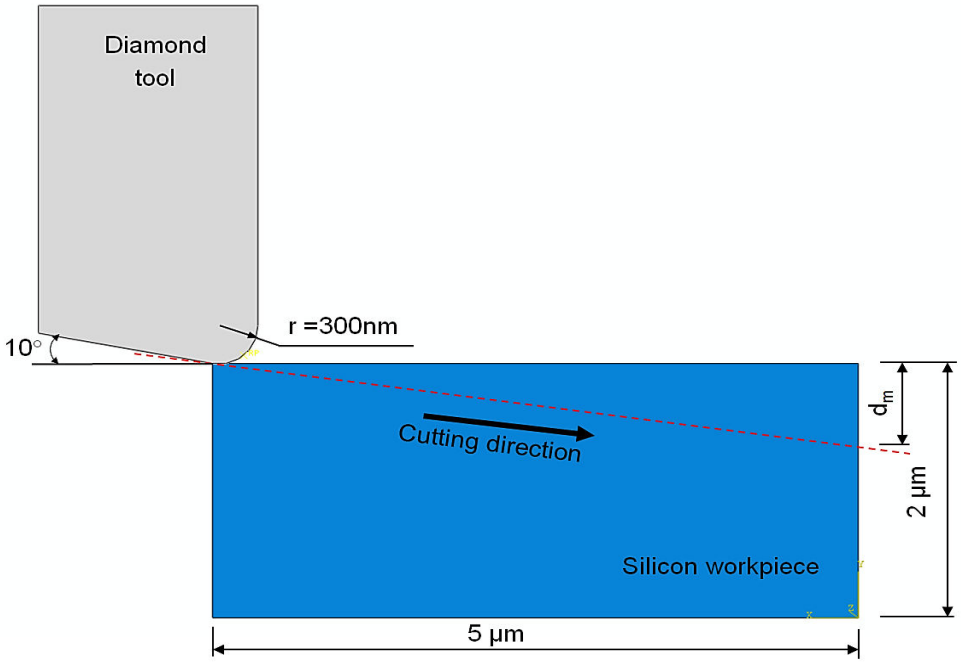

Figure 4.6 Tool and workpiece geometry and dimensions

Initially, the geometric models of cutting tool and workpiece have been developed. Figure 4.6 shows the developed 2D geometric models of the workpiece, cutting tool, and relevant geometric parameters used in the plunge cut simulation. The workpiece geometry is modeled as of rectangular shape with dimensions 5 µm × 2 µm. The diamond tool has rake angle of 0°, –25° and –30° and clearance angle of 10° and the cutting edge radius of 300 nm similar to that of blunt diamond indenter tip. The maximum depth of cut (600 nm) is chosen based on the data available in literature.

4.4.4 Material Model and Properties

For the simulation of plunge cutting of silicon using diamond, the diamond tool and the silicon are considered as homogeneous and isotropic. The diamond tool is considered as rigid. Drucker-Prager material model is used to model the material behavior of silicon along with elastic material properties. The details of the Drucker-Prager material model are already presented in the section 3.4.2 (D) of Chapter 3. Also, for the materials properties of diamond, silicon and silicon carbide, Table 3.1 in the section 3.4.2 (D) can be referred. For Drucker-Prager material properties of silicon and silicon carbide, Table 3.2 can be referred.

4.4.5 Damage and Failure Models

In the plunge cutting, the chips are formed as a result of excessive (large) material deformation of workpiece at the tool-workpiece interface under the action of applied force. Therefore, the prediction and control of the material failure is a critical issue. In order to investigate the surface finish and integrity of the produced parts, it is essential to simulate the damage and fracture of the material under the action of applied loads. The damage and failure model and the associated parameters employed are same as that presented in earlier section 3.4.2 (E) of Chapter 3.

4.4.6 Chip Separation Criterion

According to Wedberg (2013), the chip formation process, which starts in the primary deformation zone, is described as a crack that moves ahead of the tool tip splitting the material like in splitting of wood. In the beginning of the cutting process, when the tool moves towards the workpiece, tool compresses the workpiece and a stress concentration is built up in front of the tool tip. When these stresses reach a certain limit, i.e., yield strength of the material, then the separation of the chip from the workpiece begins. For the present simulation, the damage calculated for each element in the finite element model was given by the equation (4.9)

$$D = \sum \frac{\Delta \bar{\varepsilon}^p}{\bar{\varepsilon}^{pf}} \tag{4.9}$$

Fracture is allowed to occur when D = 1.0 and the concerned elements are removed from the computational domain. In fact, they still exist, in order to keep the nodal and elemental connectivity intact during the simulation. However, the deviatoric stresses of the corresponding elements were set to zero and remain zero for the rest of the analysis. In Abaqus™, the user can keep the damaged elements either as the part of the analysis or can remove them from the analysis. The material model and properties for silicon are already listed in Table 3.1 and 3.2 of Chapter 3.

4.4.7 Finite Element and Meshing

Plunge cutting involves large deformations and element distortions. These factors are to be dealt with during the modelling. In this present work, the workpiece is meshed with the 2D solid element CPE4R. It is a quadrilateral plane strain solid element. It provides bilinear displacement, reduced integration with hourglass control and element deletion (for workpiece). It allows the deletion of the material from the geometry in case of any element failure.

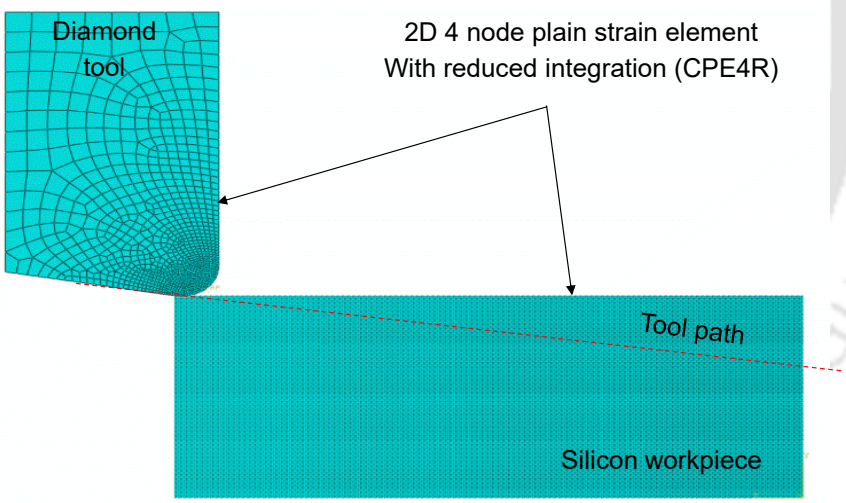

Figure 4.7 Mesh model of workpiece and tool

As shown in Figure 4.7, the entire geometry is discretized into very small finite elements. Mesh sensitivity analysis was carried out to obtain the refined results (machining force) for a chosen process condition. It can be seen that, in case of work material, the element sizes were kept uniform whereas in case of tool, bias mesh discretization was applied to get the higher mesh density at the cutting region where the tool and workpiece interaction takes place. Uniform mesh in the workpiece will help to locate the initiation of brittle fracture on the surface profile. The detail analysis is presented in Appendix 4.1. For this particular

case, the optimal number of elements for the tool and the workpiece were found to be 902 and 204204 elements respectively.

4.4.8 Arbitrary Lagrangian Eulerian (ALE) Method

In finite element method, the motion or the displacement is described by using two classical mathematical formulations. These are Lagrangian method and Eulerian method. In Lagrangian method, the mesh moves with the material, and in the Eulerian method, the mesh is fixed in space and the material moves with respect to the grid. In case of Lagrangian formulation, no material passes between the elements and boundary nodes remain on the boundary. The Lagrangian formulation is used to analyze transient problems which undergo large deformations. It is widely used due to its ability to simulate the formation of chips and to determine the chip geometry as a function of cutting parameters, plastic deformation process and material properties. However, during the Lagrangian formulation, mesh distortion occurs because the mesh deforms with the material. In the Eulerian formulation, the finite element mesh is fixed in the space and the material flows through the mesh that eliminates the possibility of element distortion during the process. It reduces the computation time as fewer elements required for the analysis. The models do not need separation criteria for simulating the material failure. However, the major drawback of the Eulerian formulation is that it needs a prior knowledge of the chip geometry, chip-tool contact length, chip thickness, and contact conditions to simulate the chip formation. Moreover in this approach, the boundary nodes and the material boundary may not coincide. Therefore, the boundary conditions and interface conditions are difficult to apply. This limits the application of the Eulerian formulation for metal cutting simulations.

In machining simulation, there are large deformations of the elements due to the plastic deformation. The excessive element distortion causes the abortion of simulation. To handle this problem, researchers have developed an iterative procedure called arbitrary Lagrangian-Eulerian (ALE) approach which combines the features of Lagrangian and Eulerian formulations [Zetterberg (2014)]. In this approach, the mesh follows the material flow and the problem is solved for displacement calculation using the steps of Lagrangian formulation. For velocity, the mesh is repositioned and the problem is solved using Eulerian steps. The combined formulation avoids the severe element deformation which is a typical problem often associated with the Lagrangian approach. Figure 4.8 shows the explanatory demonstration of the differences between Eulerian, Lagrangian and ALE formulations.

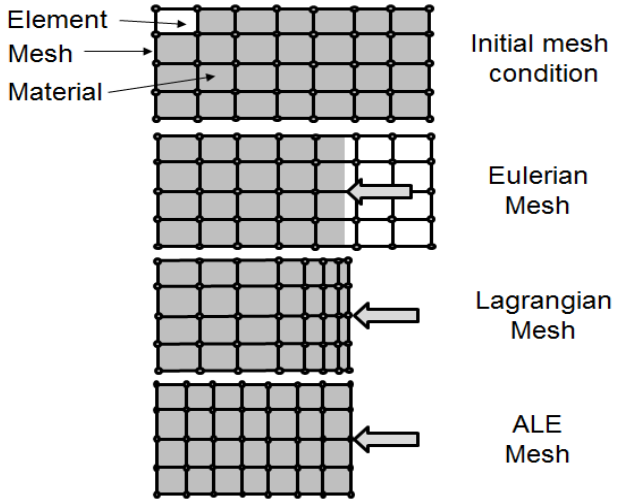

Figure 4.8 Comparison of motion of mesh and material with Lagrangian, Eulerian and ALE formulation

4.4.9 Contact Algorithm

The friction condition at the tool and workpiece interface influences the cutting forces, temperature, machining quality and tool wear. During plunge cutting process, there exists a contact between two contact zones: the first one between the tool rake face and the chip, and the second one between the machined surface and the tool clearance face. In Abaqus™ explicit formulation, the contact between the cutting tool and the workpiece is defined using modified Coulomb friction model where it can be divided into two regions, namely the sliding region and the sticking region (see Figure 4.9) [Zetterberg (2014)].

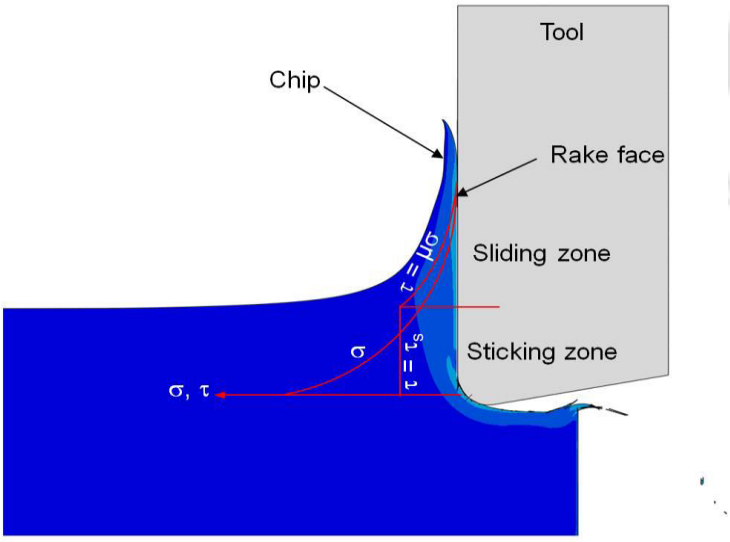

Figure 4.9 Schematic illustration of sliding and sticking zones at the chip-tool interface

Figure 4.9 shows a schematic of sliding and sticking zones at the chip-tool interface that occurs during a metal cutting operation. Sticking friction occurs near to the cutting edge which is in contact with the workpiece and the sliding friction occurs far away from the

contact area. The sliding region obeys the Coulomb friction law. In the sticking region, the frictional stress τ_f is equal to the critical frictional stress τ_{crit}. The model can be expressed by the following formulations:

$$\tau_f = k_{chip} \text{ when } \mu\sigma_n > k_{chip} \text{ (Sticking region)} \quad (4.10)$$

$$\tau_f = \mu\sigma \text{ when } \mu_n\sigma < k_{chip} \text{ (Sliding region)} \quad (4.11)$$

where τ is the frictional stress, σ_n is the normal stress and k_{chip} is the shear flow stress of the material. In the present work, the coefficient of friction μ is considered as 0.2 [Mir *et al.* (2017)]. The advantage of using the modified Coulomb friction model is that the solver determines the friction state automatically according to the contact stress value during the simulation process [Wu and Zhang (2014)].

4.4.10 Boundary Conditions

Figure 4.10 depicts a schematic of the boundary conditions applied to the tool and workpiece. The workpiece is constrained at the bottom with encastre, i.e. fixed boundary condition to imitate the clamping action during the plunge cutting. This means that, all the nodes of the base cannot move in any directions. The diamond tool is provided with two linear motions, one along the *x* direction with cutting speed of V_x=5240 mm/s and other along *y* direction with cutting speed of V_y=1000 mm/s to achieve a tapered/inclined tool path as shown with dotted red lines. Rotational movement of the tool is constrained. Also, the rigid body constraint is applied to the diamond tool at the reference point. No thermal boundary conditions as per the assumptions stated in section 4.4.1.

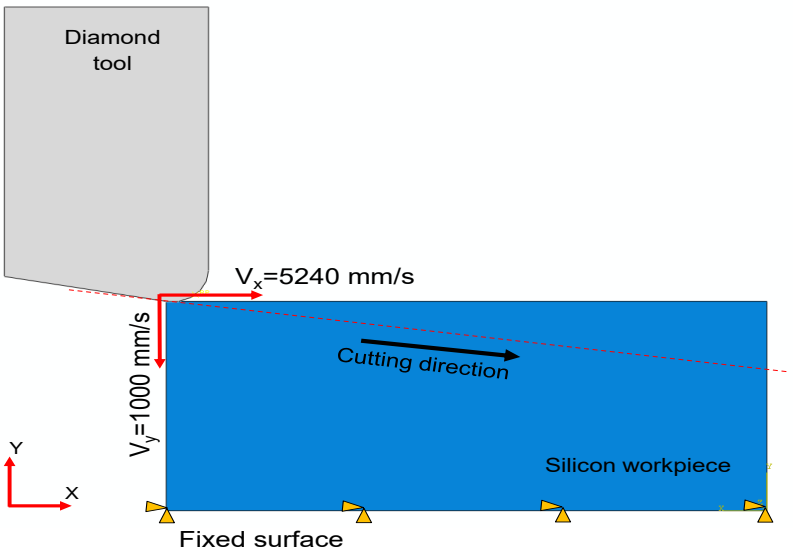

Figure 4.10 Schematic of the boundary conditions applied to the tool and workpiece

4.4.11 Solution Methodology

After the development of geometric models of the workpiece and tool, material properties, material damage law and friction law, the non-linear dynamic-explicit method with automatic (self-adaptive) time step are applied. Automatic time step algorithm maintains the constant time increment in each step. In dynamic explicit automatic time step algorithm, the time increment is adjusted automatically to meet the corresponding convergence rate. The FEM solver utilizes the equations of motion (governing equations), boundary conditions and input process conditions to simulate the plunge cutting process. It considers one element at a time and solves the equations for field outputs (stress, strain, displacement and force) and applies it to next surrounding element. To achieve an economical solution, semi-automatic mass scaling with a scale factor of about 10^6 was employed. Mass scaling was originally developed to solve high-speed dynamic problems those were difficult to simulate using the implicit method.

4.4.12 Post Processing

After the completion of the simulation, the outputs such as surface profile, chips, forces and tool displacement are extracted from the visualization module. During carrying out the simulation, solver stores the results in a neutral binary file which is later used by Abaqus/CAE for post-processing. This file is called Abaqus output database file and has the extension .ODB. To extract the required outputs data such as force, displacement and stress values from the simulation, the ODB field output is selected and these output parameters were extracted by selecting the specified node(s) of interest.

4.5 Results and Discussion

The main objective of this present work is to determine the ductile to brittle transition through the plunge cutting simulation of brittle material. It is believed that the critical depth of cut obtained during the simulation can be utilized to obtain crack free surface by keeping the depth below the critical depth of cut. In the current simulation, surface profile, cutting force and specific cutting energy are analyzed to find out the transition point between ductile and brittle. The approach employed in the present work is to obtain critical depth of cut.

4.5.1 Determination of Critical Depth of Cut

After the study of formation of chips, it was decided to determine the critical depth of cut (CDC). In this work, three different methods were selected for the determination of CDC. These are elaborated one by one in the following sub sections.

4.5.1.1 Visual Inspection of Surface Profile

Figure 4.11 shows the profile generated from the plunge cut simulation using 0º rake angle tool when the depth of cut gradually increases from 0 to 600 nm. The surface profile is carefully observed and it is noted that there is formation of first brittle fracture. This was occurred at 211.4 nm depth in case of 0º rake angle tool, which was considered to be the critical depth of cut for the chosen process condition.

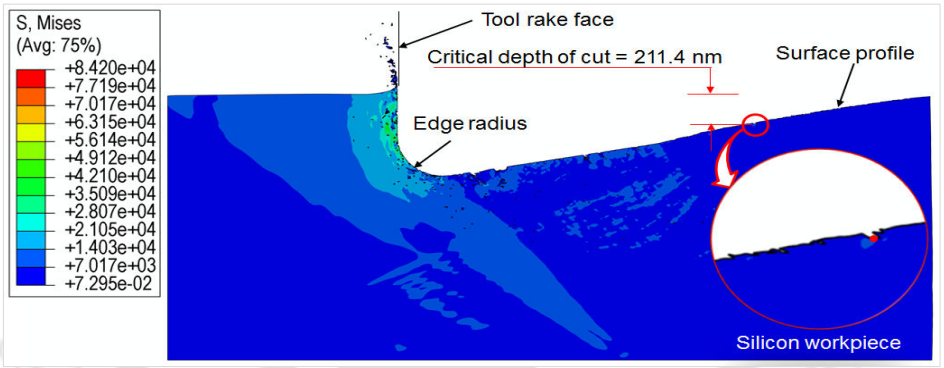

Figure 4.11 Plunge cut with 0° rake angle

Two more sets of simulations of plunge cut were carried out by taking −25º and −30º rake angles to analyze the effect of rake angle on critical depth of cut or DBT. The surface profiles obtained during these simulations are shown in Figure 4.12 and 4.13.

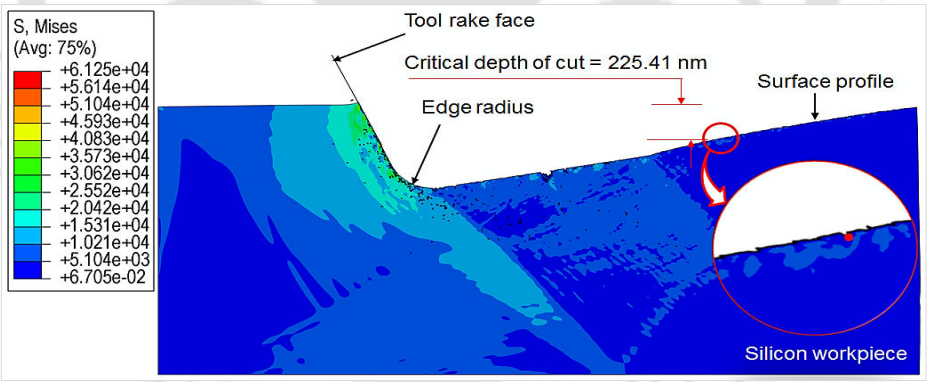

Figure 4.12 Plunge cut with −25° rake angle

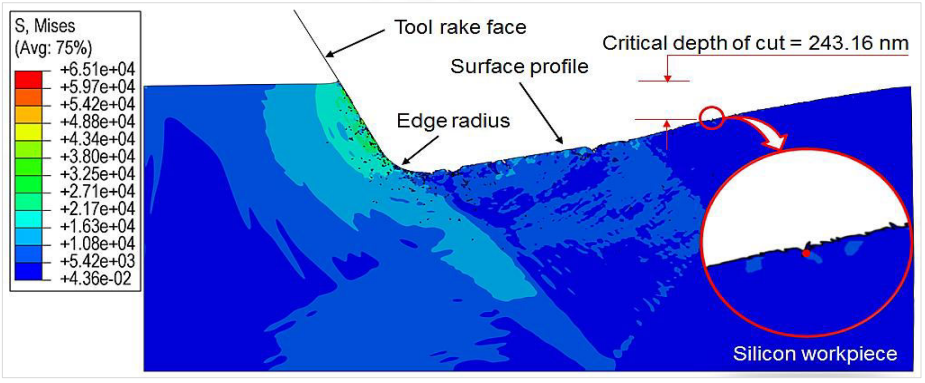

Figure 4.13 Plunge cut with −30° rake angle

The critical depths of cut evaluated from the Figures 4.11, 4.12 and 4.13 using visual inspection method are tabulated in Table 4.1. These are based on the first visible micro cracks on the machined surface.

Table 4.1 Critical depth of cut for 0º, −25º and −30º rake angle from visual inspection

Rake angle (°)	X co-ordinate	Y co-ordinate	Critical thickness (nm)
0°	0.0038453965	0.0017886002	211.40
–25°	0.0037578676	0.0017745867	225.41
–30°	0.0036918412	0.0017568420	243.16

The coordinates of the first visible micro crack were determined using plot digitizer. The plot digitizer takes the original dimension of the workpiece (5 µm × 2 µm) and then displays the coordinates, i.e., *x* and *y* length based on the position of the computer-mouse. After determining the position of the first visible micro crack by clicking the mouse on the crack, the critical depths of cut was calculated by subtracting the *y* coordinate length from the original height of the workpiece. The critical depths of cut obtained from visual inspection are listed in Table 4.1 for 0º, −25º and −30º rake angle tools and *y* direction speed of 1000 mm/s. From the table, it can be seen that, the critical depths of cut are 211.4, 225.41, 243.16 nm for 0º, −25º and −30º rake angle tools respectively. From the table, it can also be observed that, with the increase in rake angle, the critical depth of cut increases. This is due to the fact that, with higher rake angle tool, more material in front of the cutting edge is downward suppressed and the compressive stress component becomes predominant. This provides a stress state similar to the hydrostatic stress field. From the theory of plasticity, hydrostatic pressure determines strain at fracture, which in turn determines material ductility or brittleness. The high hydrostatic pressure induced by the extremely negative rake angle is reported to cause phase transformations to metallic phases, and prevent the initiation or propagation of cracks. Therefore, with increase in negative rake angle tool, the critical depth of cut during plunge cut also increases.

4.5.1.2 Analysis of Machining Forces

In this present work, cutting force, thrust force and coefficient of friction during plunge cutting simulation are extracted and carefully examined to estimate the ductile to brittle transition. Figure 4.14 presents the variation in cutting force and thrust force in a single plunge cut with a 0º rake angle tool.

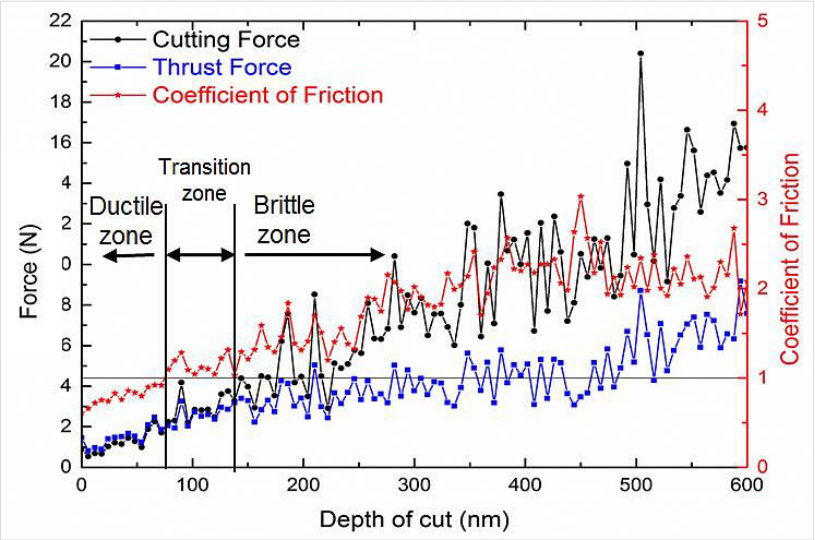

Figure 4.14 Variations of the cutting and thrust forces during a single plunge cut using 0º rake angle tool for continuously varying depth of cut

From the figure 4.14, it can be seen that as the depth of cut increases from 0 to 78 nm, both the cutting force and the thrust force increase smoothly. The fluctuations of the forces are noted to be more prominent when the depth of cut increases beyond 138 nm. These observations can be inferred that, below 78 nm depth of cut, the cutting process is completely in ductile mode similar to metal machining through plastic deformation. When the depth of cut increases beyond 78 nm, micro-fractures began to form at the bottom of the groove. Thus the machining mode switches into a partially brittle mode in which the brittle chips form. Due to the formation of brittle micro-fractures, the force values start fluctuating. Thus the zone of 78 nm to 138 nm can be considered as transition zone. The transition from the ductile to brittle cut can also distinguished from the variation of cutting force and thrust force as suggested by Yan *et al.* (2009b). As per Yan *et al.* (2009b), when the cutting process changes from ductile to brittle, cutting force starts dominating the thrust force. This is due to the fact that, in ductile mode cutting, depth of cut is smaller than cutting edge radius and the effective rake angle is highly negative, whereas, in the brittle region, i.e., beyond 78 nm depth of cut, the cutting force becomes higher than thrust force. This finding is also depicted from the co-efficient of friction (F_c/F_t) curve of Figure 4.14 that shows below 78 nm depth of cut, the cutting force is lower than the thrust force. When the depth of cut reaches the transition point, the cutting force and thrust force becomes equal. Beyond transition point, as the depth of cut increases beyond 78 nm, the cutting force becomes higher than the thrust force and the co-efficient of friction value becomes higher than unity. Thus, the machining force can be classified into three distinct zones, i.e. ductile-mode, transitional-mode and brittle-mode.

These observations were also observed during the simulations with −25º and −30º rake angles. Figures 4.15 and 4.16 show the variation of cutting and thrust forces that generated

during simulations with −25º and −30º rake angles respectively. The transition depths were found to be 84 nm and 108 nm for the rake angles of −25º and −30º respectively. These values are quite closer to the results reported by Yan *et al.* (2009b) and Wang and Liao (2008). Yan *et al.* (2009b) reported 120 nm as the transition depth during the experimental study using −30º rake angle tool. Similarly, Wang and Liao (2008) reported a transition depth between 100 nm to 500 nm. From the present analysis it was noted that the values of transition depths estimated using proposed force analysis approach fairly match with the reported experimental values. However, some of the researchers have used specific cutting energy concept to determine the transition depth. In the next section, determination of ductile to brittle transition depth using specific cutting energy is discussed.

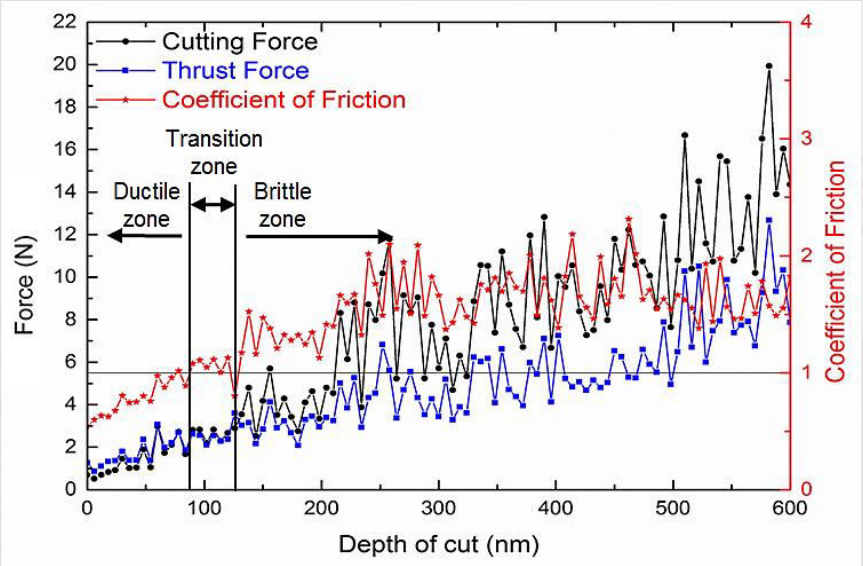

Figure 4.15 Variations of cutting and thrust forces during a single plunge cut using −25º rake angle tool

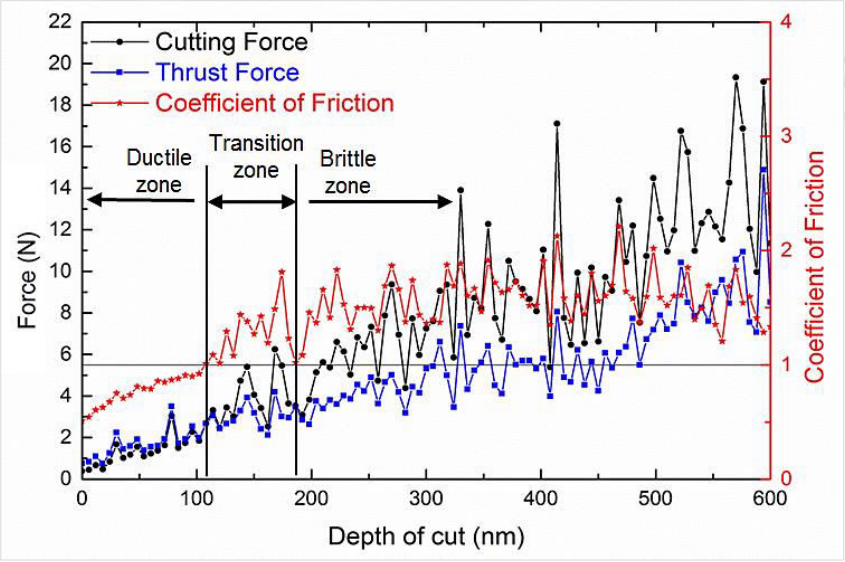

Figure 4.16 Variations of cutting and thrust forces during a single plunge cut using −30º rake angle tool

4.5.1.3 Specific Cutting Energy

Literature reports some important studies on the concept of characterization of the mode of material removal in machining and grinding of brittle material using specific cutting energy approach. According to these studies, the change in the specific cutting energy can be used to determine the ductile to brittle transition phenomenon of the plunge cut process. The term specific cutting energy (SCE) is defined as the energy needed to remove or displace a unit volume of work material [An *et al.* (2015), Wang and Liao (2008)]. It is given by the ratio of energy per unit time to the volume removed per unit time. Thus, specific cutting energy is dependent upon the cutting load and the contact area between the tool rake face and the chip, i.e., SCE changes with change in cutting depth. Therefore, the change of specific cutting energy can be used as a criterion for estimating the critical depth of cut.

In the present work, the specific cutting energy values were computed and based on them the ductile to brittle transition depths were identified. The specific cutting energy can be expressed as:

$$SCE = \frac{F_c}{A} = \frac{F_c}{w \times d} \tag{4.12}$$

where F_c is the cutting force, A is the cross sectional area of the chip, w is the width of cut and d is the depth of cut.

Figure 4.17 shows a schematic of geometry considered in the determination of chip area. The area of a curved segment of a circle (refer Figure 4.17) can be computed as:

$$\text{Chip area, } A_1 = \frac{R^2}{2}\left(\frac{\pi}{180}\theta - \sin\theta\right) \quad \text{where, } \theta = 2\cos^{-1}\left(\frac{R-d}{R}\right) \tag{4.13}$$

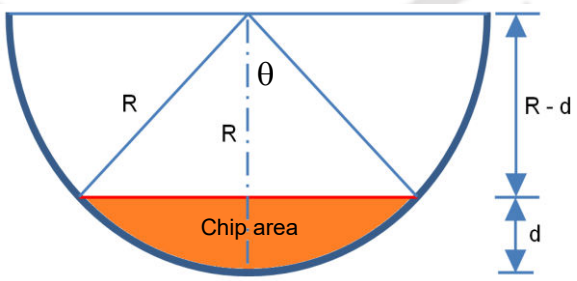

Figure 4.17 Schematic for the determination of chip area

By using the calculated chip area the specific cutting energy was obtained. As the present simulation considers 2D domain, the nose radius could not be incorporated. Therefore, an approximated plane strain thickness of 0.35 mm was used for maximum depth of cut of

about 1 µm corresponding to the given nose radius (1.5 mm). Thus, the chip area was calculated by multiplying the width of cut with the varying depth of cut.

To determine the values of SCE, the values of cutting forces were extracted from the FEM simulation. Then, the corresponding contact areas were calculated as a function of nose radius and depth of cut (equation 4.10). For the current 2D plunge cut simulation, only the product of constant average width of cut and varying depth of cut was used. Figure 4.18 shows the plots of SCEs computed for various values of depth of cut for 0º, −25º and −30º rake angles.

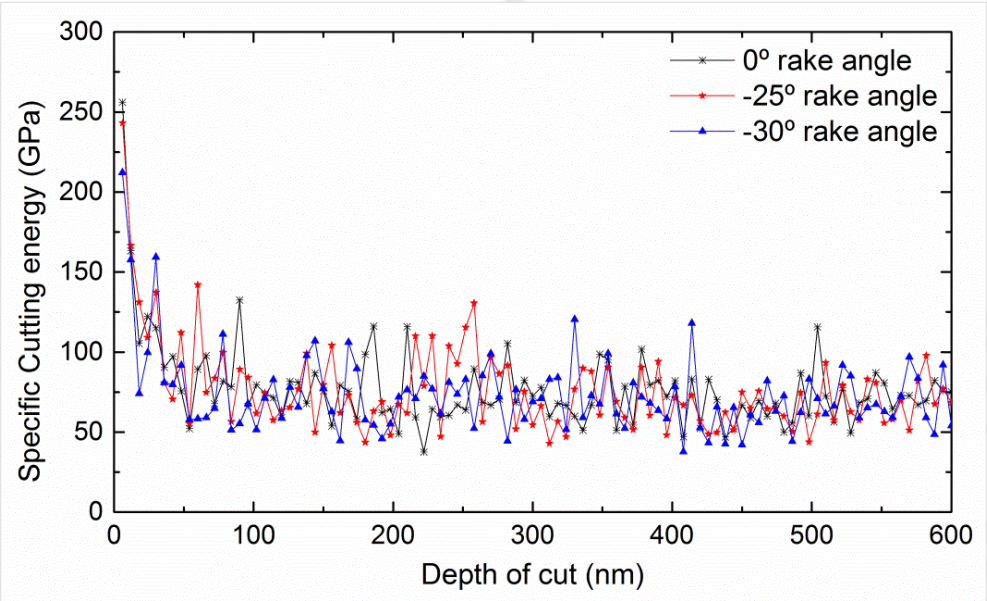

Figure 4.18 Variation of specific cutting energy for 0º, −25º and −30º rake angle tools

As per the analysis of simulated cutting force presented in the previous section, it was revealed that the transition depth lies in between 78 nm to108 nm for silicon when processed with 0º, −25º and −30º rake angle tool. In order to justify and add more emphasis to the results obtained from the observation of surface profile and machining force analysis, it was decided to study the specific cutting energy for better indication of the transition point. According to the study, the transition depth or critical depth of cut has been defined as the intersection point of the high slope at the small cutting depth and the lower slope at the larger depth of cut [Wang and Liao (2008)]. From Figure 4.18, it can be observed that the specific cutting energy is maximum (250–300 GPa) at the start of the plunge cut, i.e., at minimum depth of cut. This is because; at very low depth of cut (near to zero), the workpiece experiences plastic deformation and the cutting force developed is high. At this point, only sliding and plowing actions take place. The material is in the ductile state due to compressive stress exerted by the highly negative effective rake angle tool. When the undeformed chip thickness increases gradually, material starts deforming plastically and SCE decreases suddenly as it enters into

the brittle transition region from the ductile region. The average values of SCEs were noted to be same after the depth of 50 nm to 100 nm. This is because after 50 nm the brittle fracture starts. Thus less energy is needed to remove the material. It can be said that, the sharp sloped portion of the specific cutting energy curve can be considered as the ductile-zone. After 50 to 100 nm of depth of cut, the curve flattens, that can be considered as the brittle-zone. Thus, the transition depth or critical depth of cut can be estimated by the intersection point of the high slope of ductile region and the lower slope of brittle region.

Figure 4.18 shows highly fluctuating SCE just after a few nanometric displacements (10-15 nm) of the tool from the origin. This jerky or highly fluctuating specific cutting energy is due to continuous fluctuations of the machining force compared to small chip area. Because of the high fluctuations of the cutting force in the cutting process, the transition point cannot be easily identified. Therefore, it was decided to fit the curve to minimize the energy fluctuation. In this work, the SCE curves are fitted by using MATLAB tool. Various curve fitting algorithms were tried and found that 9^{th} degree polynomial is best suited to fit the given SCE curve. The fitted curves are shown in Figure 4.19.

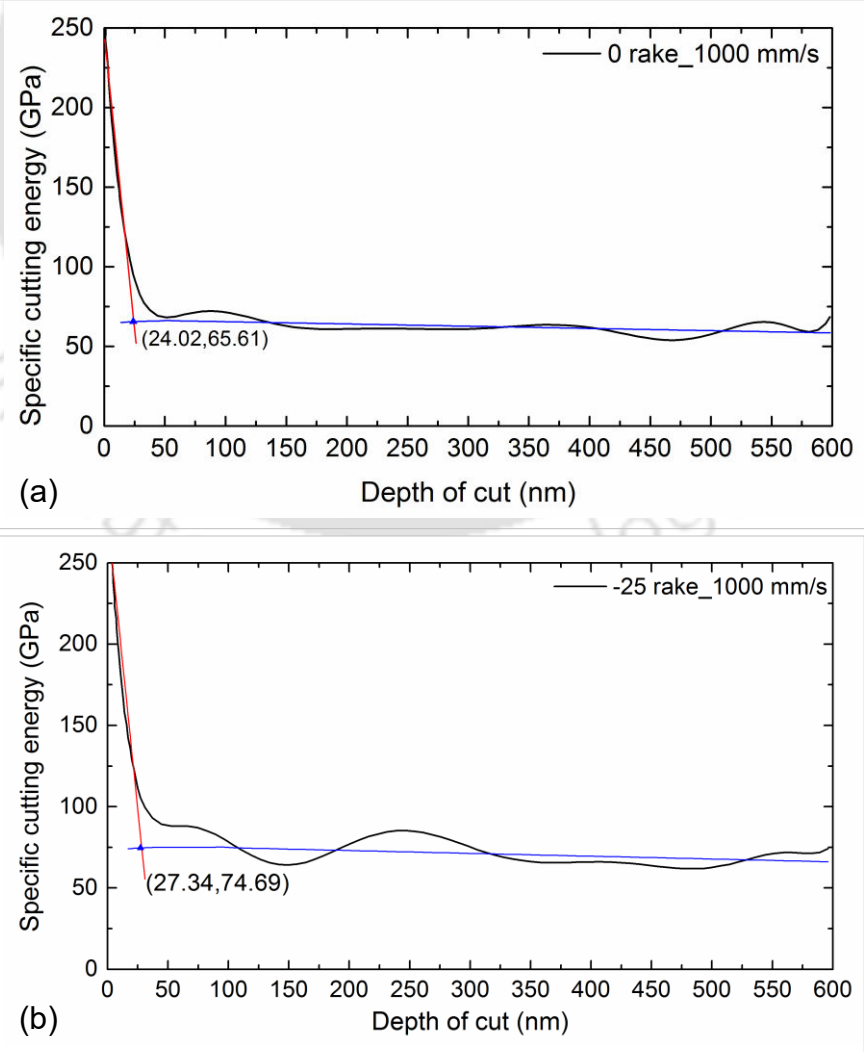

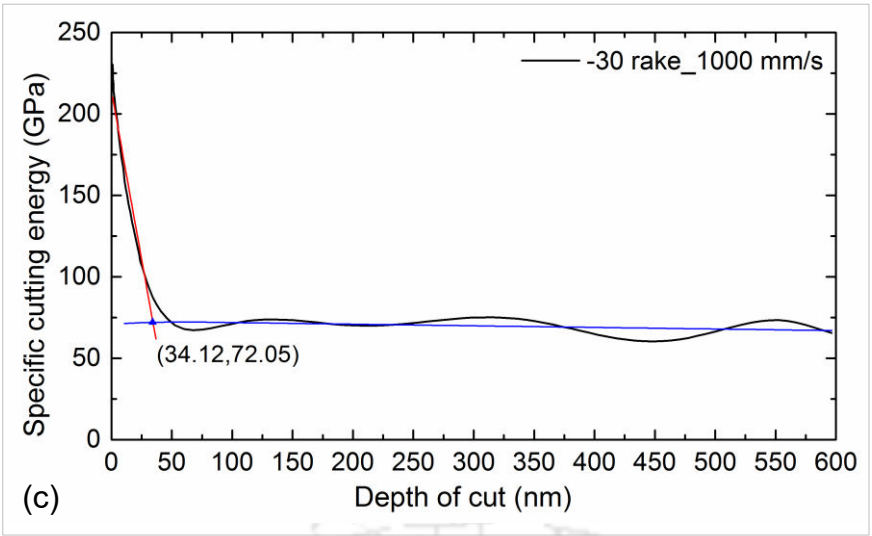

Figure 4.19 Determination of critical depth of cut from simulated specific cutting energy for (a) 0° rake angle, (b) −25° rake angle and (c) −30° rake angle tools

The fitted curves are divided into two parts: high slope at small cutting depth and lower slope at the large cutting depth. Both the slopes are linearly fitted. The intersection point between the two slopes is obtained as shown in Figure 4.19. The estimated transition depths were found to be in the range of 28-54 nm. The ductile to brittle transition depth was found to increase with increase in rake angle. The estimated transition depths from SCE curves were noted to be lower than the transition depths obtained from the cutting force analysis as well as the surface profile analysis. This is because; during the calculation of the specific cutting energy, actual chip area was not considered. The force value was computed by using the depth of cut and constant plane strain thickness, i.e. width of cut. However, in reality, the width of cut increases with the increase in depth of cut. Thus, it can be stated that, SCE cannot be used to determine the transition point if the simulation is carried out in 2D plane strain condition.

4.5.2 Comparison of Methods used to Determine Critical Depth of Cut during Plunge Cutting Simulation

From the above analyses of critical depth of cut, a comparative analysis of all the three methods viz. visual inspection, machining force and specific cutting energy has been carried out. Table 4.2 shows the critical depth of cut obtained from three methods for 0º, −25º and −30° rake angle tools. From the Table, it can be observed that in case of −30° rake angle tool the critical depths of cut obtained from surface profile analysis is higher than the experimental results [Yan *et al.* (2009b)]. This is due the fact that the micro cracks formed at transition zone are difficult to identify via visual inspection. It will require a complicated image processing technique which is time consuming and computationally costly. SCE analysis significantly underestimates the transition depth values. This may be due to the fact that, the

actual chip area could not considered while calculating the specific cutting energy, as only 2D plane strain condition was considered. The critical depth of cut obtained from the force analysis was found to be fairly closer to the experimental values. Moreover, similar trends of variation of transition depths were noted in case of 0º and −25º rake angle tool in all three methods. There are no experimental transition depth values available in the literature for the validation for 0º and −25º rake angle. Therefore use of force analysis based method is recommended for its use in practice.

Table 4.2 Critical depth of cut obtained from three methods for 0º, −25º and −30° rake angle

Rake angle (°)	Critical thickness (nm)			
	Visual	Force	SCE	Experimental
0°	211.40	78.08	24.02	
–25°	225.41	84.03	27.34	
–30°	243.16	108.08	34.12	120

4.6 Numerical Simulation of Plunge Cutting of Silicon Carbide

Similar to the Si material, in the present work, simulations were carried out on silicon carbide workpiece and transition depths were determined. The model development, assumptions, geometric modeling, material model, element and meshing, contact algorithm and boundary condition were similar to those used for the plunge cutting simulation of silicon. The diamond tool considered in this work has cutting edge radius of 50 nm and provided with two linear cutting speeds of 400 mm/s and 50 mm/s along x and y directions respectively. The material properties of silicon carbide have been presented in sections 3.4.2 (D) and 3.4.2 (E) of Chapter 3. Based on the conclusion of previous section, only the force analysis method was adopted to compute the transition depth for silicon carbide.

Figure 4.20 presents the variations in cutting force and thrust force in a single plunge cut with a 0º rake angle tool. It can be observed that below 65 nm depth of cut, the cutting and thrust forces are varying smoothly. When the depth of cut increases beyond 65 nm, the fluctuation of force value increases. It is due to the formation of micro fractures, which indicates the transition from ductile to brittle zone. Similar trend was also noted for the coefficient of friction value. At the depth of cut of 65 nm, the cutting force becomes higher than the thrust force and the coefficient of friction becomes greater than unity which indicates the transition of ductile to the brittle zone (Figure 4.20).

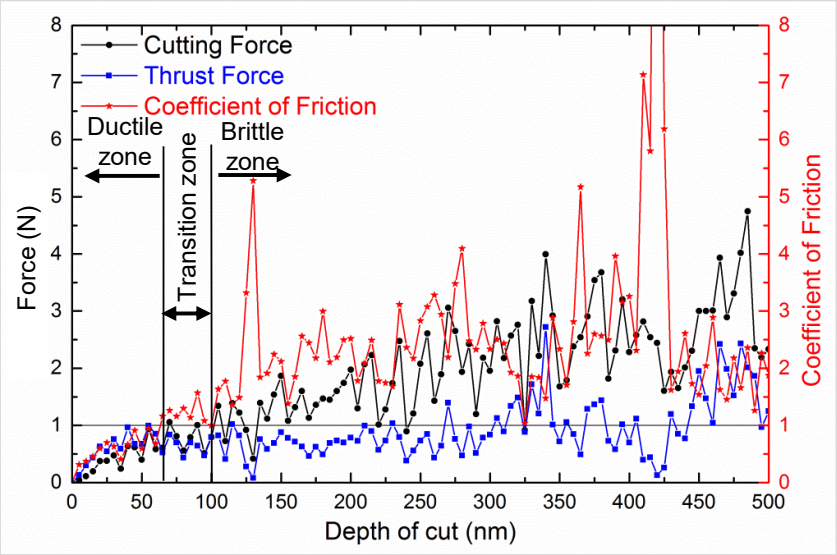

Figure 4.20 Variations of the cutting and thrust forces during a single plunge cut using 0º rake angle tool

In addition to 0º rake angle, simulations were performed for –25º and –30º rake angle tools. Figure 4.21 and 4.22 show the variations of cutting and thrust forces obtained during plunge cutting of SiC for –25º and –30º rake angles. From these figures the transition depths were found to be around 65 nm for both the rake angles. For reference, Jacob *et al.* (2005) reported a transition depth or critical depth of cut of 70 nm for 6H-SiC in fly cutting experiment. Recently, Xiao *et al.* (2018) have also reported a critical undeformed chip thickness of 50 nm during plunge cutting experiment of 6H-SiC using –30° rake angle, 10° clearance angle, 1.507 mm nose radius, 50 nm cutting edge radius, 3 mm/s cutting speed and 0.03° tilting angle.

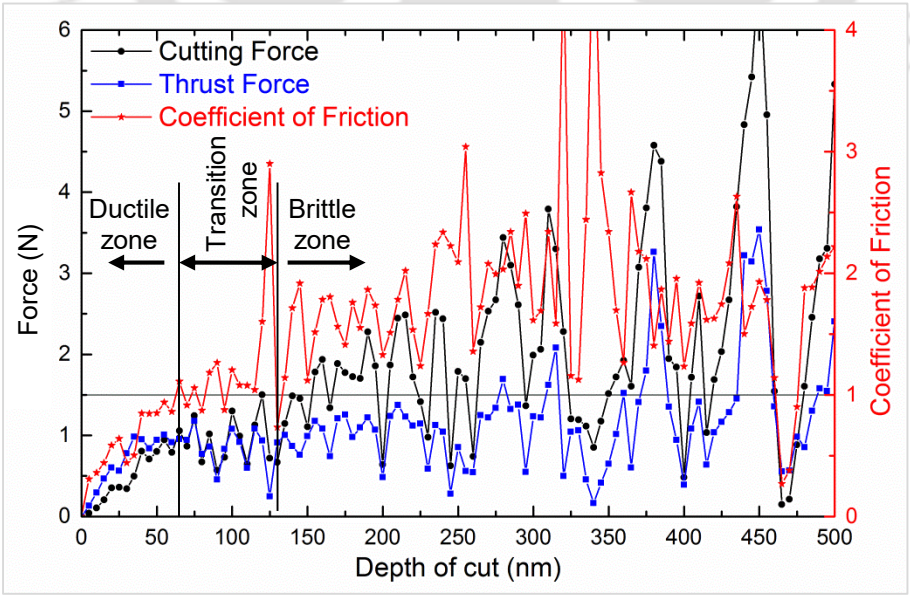

Figure 4.21 Variations of the principal and thrust cutting forces during a single plunge cut using –25º rake angle tool

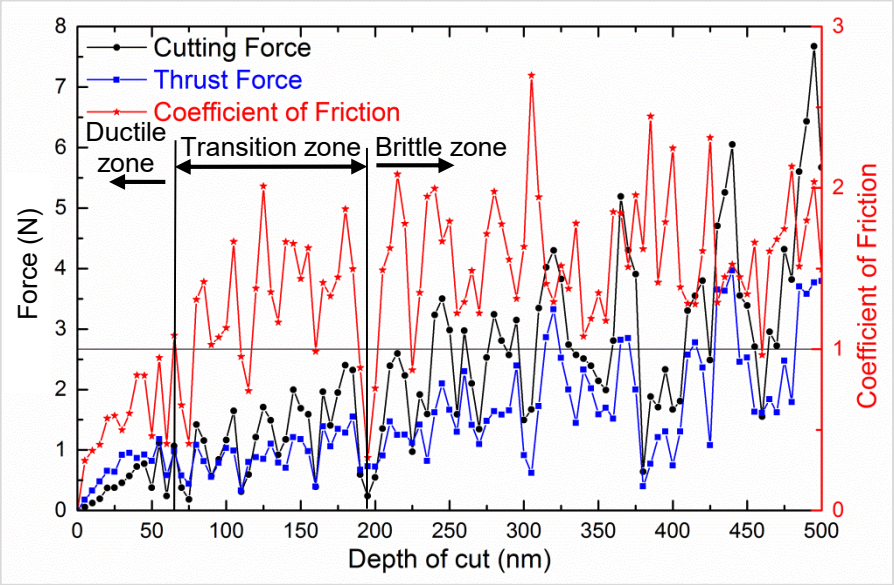

Figure 4.22 Variations of the principal and thrust cutting forces during a single plunge cut using –30º rake angle tool

From the overall analysis, it is observed that study of variation of machining force provides results close to the experimental results for –30º rake angle tool. The predicted results for silicon carbide fairly match with the experimental results of Xiao *et al.* (2018) and Jacob *et al.* (2005). It is also important to mention that the critical undeformed chip thickness obtained from nanoindentation simulation (Chapter 3) gives higher critical depth of cut compared to plunge cutting. This is due to the fact that, in nanoindentation, stress exerted by the indenter is mostly compressive, whereas in plunge cutting, tensile stress also acts on the workpiece along with compressive stress. The tensile stress increases with increase in depth of cut. Therefore, a lower value of critical undeformed chip thicknesses, or, ductile to brittle transition thicknesses are obtained during plunge cut simulation.

4.7 Summary

This chapter presented, in details, the development of a numerical (FEM) model for the simulation of plunge cutting process. Numerical simulations were carried out considering silicon and silicon carbide as work material and diamond as a cutting tool having 0º, –25º and –30º rake angle. FEM based numerical model was developed by incorporating simultaneous speeds along x and y-axis directions to achieve a depth of cut from 0 to 600 nm. Various zones of material removal, viz. ductile zone, transition zone, and brittle zone were studied. To identify the critical depth of cut, i.e., ductile to brittle transition, various output parameters such as machined surface, cutting force and specific cutting energy were thoroughly analyzed. Pressure sensitive Drucker-Prager material model was used to define the material behavior of

silicon and silicon carbide. Material damage law and friction law were used to account for chip separation and contact interaction.

During the study, initially, the surface profiles were studied using the visual method. The criterion of initiation of first brittle fracture was used to determine the critical depth of cut. For 0º rake angle tool with 1000 mm/s speed in the *y*-direction, the initiation of first brittle fracture was noted to occur at a depth of cut of 211.4 nm, which was considered to be the critical depth of cut. Similarly, for –25º and –30º rake angles, critical depths of cut were found to be 225.41 nm and 243.16 nm respectively. These results were found consistent with the fact that with the increase in the rake angle, there will be larger plastic deformation and hydrostatic pressure and ultimately increase in the critical depth of cut.

In the second part, the variation of machining forces as a function of depth of cut was analyzed for the determination of critical depth of cut. It was seen that, with the increase in depth of cut, the fluctuation/frequency of the force becomes more prominent in the brittle region than that in the ductile region. The ductile to brittle transition thicknesses were found to be 78 nm, 84 nm and 108 nm for 0º, –25º and –30º rake angle tools respectively. The transition points or thicknesses are also verified by studying the coefficient of friction (the ratio of cutting force to thrust force). At the transition point, the cutting force becomes higher than the thrust force and the coefficient of friction becomes higher than unity.

In the third section, the criterion of specific cutting energy was used to identify the transition depth. The intersection point of the ductile zone and the brittle zone were obtained and accordingly the values of transition depths were obtained. The curves were fitted using 9^{th} order polynomial curve fitting algorithm and intersection points were calculated by fitting the high slope and flat slope linearly. The estimated CDCs were found to be in the range of 24–34 nm.

Finally, a comparative analysis of the three methods was carried out. From the comparison, it was observed that the CDCs obtained from the visual inspection were the highest and CDCs from the SCE method were the lowest. However, the CDCs obtained from the force analysis were found close to the experimental CDCs obtained from the available literature and earlier nanoindentation simulations described in Chapter 3. However, based on the above discussion, it can be concluded that the visual inspection method and the SCE method have inherent limitations and the force analysis method is found to be realistic.

Further, the work was extended by carrying out a simulation for silicon carbide and the critical depth of cut was determined. For this simulation, only the force analysis was

adopted. From the analysis, it was observed that the evaluated critical depth of cut was found to be around **65 nm** for 0°, –25° and –30° rake angles. The predicted results for silicon carbide fairly match with the experimental results.

It is envisaged that this work provides a quicker prediction of transition depths; which would help in generation of desired surfaces during SPDT operation. After completion of the study on DRM in SPDT, the machining forces generated during SPDT operation were studied. The details about the same are presented in the next chapter.

भारतीय प्रौद्योगिकी संस्थान गुवाहाटी
Indian Institute of Technology Guwahati

NUMERICAL MODELING AND SIMULATION OF CUTTING FORCES DURING SINGLE POINT DIAMOND TURNING PROCESS

5.0 Scope

This chapter presents the development of two-dimensional non-linear plane strain FEM based numerical model of single point diamond turning (SPDT) to simulate the cutting phenomenon and to predict the cutting forces. Initially, the need to carry out the present numerical analysis of SPDT process is defined. An overview of the proposed approach for modeling of SPDT using FEM is presented. Details of the development of a submicron level orthogonal cutting process that captures ductile deformation leading to material separation has been elaborated. A comparative study on the effect of material models for silicon and silicon carbide has also been carried out. The developed models were validated using the measured cutting and thrust forces during the experiments. A systematic study has been presented on the influence of process parameters on the process performance measures (machining forces) using response surface methodology and full factorial analysis. Finally, the predictive models for the process performance were developed.

5.1 The Need

In mechanical material removal process, the forces that act at the tool-workpiece interface are – cutting force, thrust force and feed force. Analysis of machining (cutting and thrust) forces is important in view of the following aspects:

- Computation of power consumption during the machining process.
- Analysis of machinability of the workpiece.
- Determination of optimal levels of process parameters viz. speed, feed, depth of cut, tool geometry and coolant.
- Analysis and prediction of tool failure during the cutting process.
- Improving product quality by minimizing deflection.
- In case of micro and nano machining, it helps in determining the ductile to brittle transition.

Till date, significant experimental works have been reported on understanding of the cutting mechanism and chip formation during machining of silicon and silicon carbide. However, as the machining scale enters from micro to nano regime, it is interesting and challenging to study the force, pressure, stress, and roughness during the cutting process. Many numerical studies on SPDT process using molecular dynamics (MD) have been

reported to study the insight of the machining process by analyzing stress, chips formation, temperature, phase change during the machining process. However, experimental validation is still difficult due to its very small, i.e., atomic level study domain. Very scant literature has been reported on numerical simulations using finite element method. No literature has been reported on the study of the influence of material model during numerical simulation of SPDT process of brittle material. Selection of proper material model is essential in obtaining accurate results. Researchers worldwide used various material models such as Johnson-Cook [Johnson and Cook (1985)], Johnson and Holmquist [Johnson and Holmquist (1994)] and Drucker-Prager [Drucker and Prager (1951)] for modeling of ceramic materials. However, there is no comparative study amongst these material models for machining of Si and SiC is reported till date. Thus, it was thought worthy to carry out FEM based numerical simulation of SPDT process by using two widely used material models viz. Johnson-Cook (JC) and Drucker-Prager (DP). The present work was carried out to assess the capability of the developed numerical model to predict the responses such as machining forces, chip morphology, and stress during nanometric machining process of silicon and silicon carbide using the diamond tool. In addition, the effect of the extreme rake angle on cutting force was also analyzed.

5.2 Overview of the Process Model Development

In this present work, finite element method based numerical simulations for single point diamond turning of brittle materials such as silicon and silicon carbide with two different material models have been carried out to predict the machining forces. The finite element analysis of machining operation has been carried out on 2D continuum. Figure 5.1 shows the difference between 2D and 3D process continuums used in simulation of a typical SPDT process.

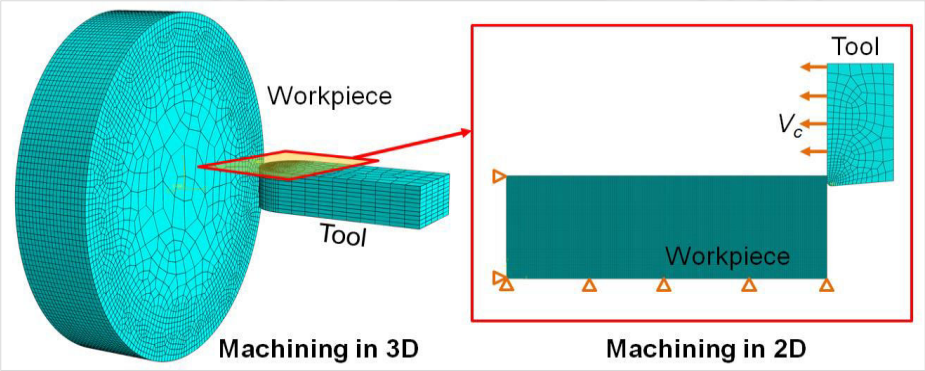

Figure 5.1 3D and 2D process continuums in numerical simulation of SPDT

3D-simulation of cutting process requires huge computation time. The number of elements needed to simulate the plastic deformation and chip formation is high. Patten and Jacob (2008), and Carroll and Strenkowski (1988) justified the comparison of the experimental results with 2D simulation results. According to Patten and Jacob (2008), the radius of curvature of the round-nose tool is much larger (in mm) than the depth of cut (in nm), therefore the tool can be considered as flat tool. Hence, the ratio of mean width of cut to the depth of cut is large enough so that the condition of plane strain deformation (orthogonal cutting) can reasonably be assumed [Carroll and Strenkowski (1988)]. Therefore, in this work, an Arbitrary Lagrangian-Eulerian (ALE) based 2D numerical model has been developed to simulate the SPDT of silicon and silicon carbide using finite element method. The developed model was aimed to predict the machining forces and chip formation for the chosen process condition by considering realistic material behavior, friction model and damage model. The predicted responses from the developed model were validated with the published experimental results. Parametric studies were carried out for obtaining the optimal process conditions to obtain minimum machining force. The details are provided in the following sections. The overview of the work carried out in this chapter is illustrated in the Figure 5.2.

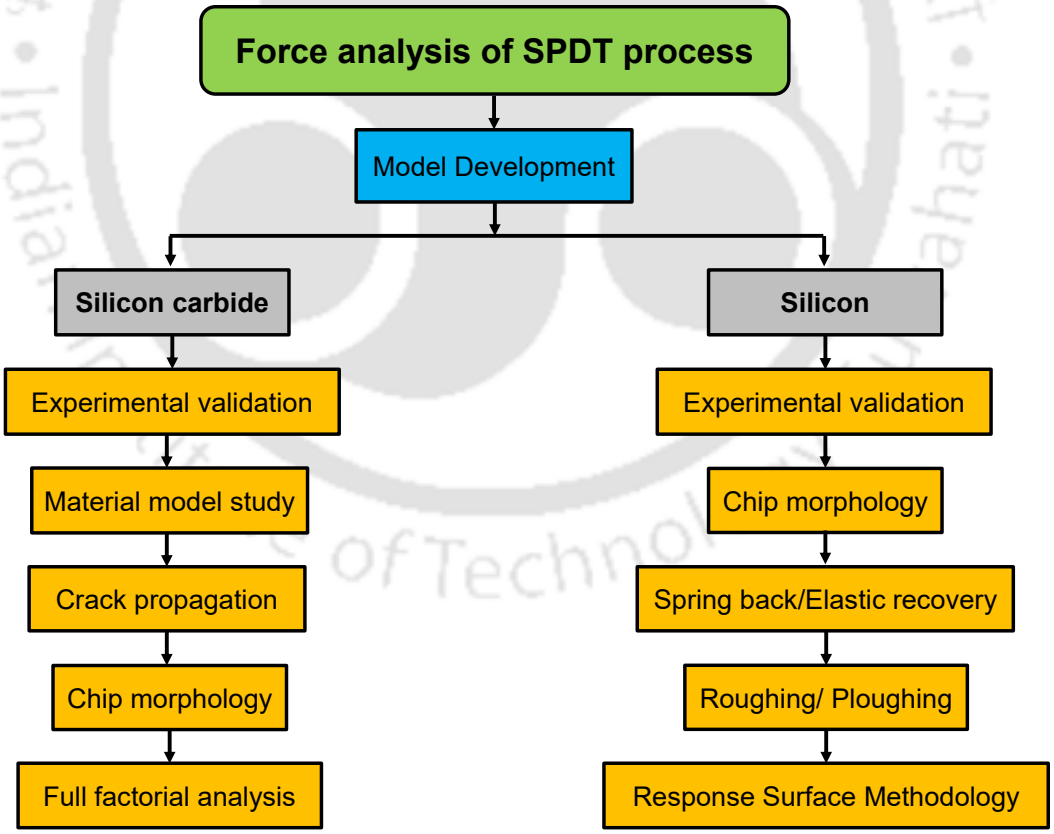

Figure 5.2 Overview of the work carried out in this chapter

The work reported in this chapter is divided in to two stages: first the analysis of machining forces and its experimental validation; and second the study and analysis of

different material models to investigate proper modeling of brittle material while performing nanometric cutting simulation of SPDT. Case studies were carried out to analyze the crack propagation, elastic recovery/spring back effect, roughing/ploughing effect and chip morphology. An integrated analysis using finite element method (FEM) and response surface methodology (RSM) and full factorial analysis (FFA)) were carried out for the prediction of machining forces and optimization of process parameters.

The various stages of the model development are as follows.

- Development of finite element model and simulation of SPDT of hard and brittle materials such as silicon and silicon carbide.
- Experimental validation of computed machining forces with published experimental data (machining force).
- Comparative analysis of formation of chips when two material models employed.
- Case studies using the developed numerical model.
- Parametric study on the machining forces using response surface methodology and full factorial approaches to optimize the process condition for minimum machining force.

The details of above mentioned stages are presented in detail in the following sections.

5.3 Development of Numerical Model for SPDT using Finite Element Method

In this section, finite element method based simulation of 2D orthogonal machining of silicon and silicon carbide is presented. The finite element modeling considered here is identical in many ways to the simulation set up for plunge cutting simulation considered in the previous Chapter 4. However, in metal cutting simulation, no Y-direction movement is provided to the cutting tool. Drucker-Prager material model and Johnson-Cook material model were incorporated to account for the effect of material behavior during machining brittle materials. The finite element model was developed using a commercial FE package Abaqus™. The methodology employed in the current simulation includes the following steps. These steps are schematically depicted in Figure 5.3.

- Selection of proper input process parameters such as cutting speed, feed, depth of cut, tool geometry and machining condition.
- Development of geometric models of cutting tool and workpiece.
- Application of suitable material parameters and material failure criteria for both workpiece and tool.

- Selection of suitable element type based on the problem. Meshing the geometries.
- Selection of suitable solver type (Dynamic Explicit in the present case).
- Application of boundary conditions and contact properties.
- Extraction of data in terms of process performance parameters such as force, surface profile and chip morphology.
- Validation of the computed responses with the experimental results.

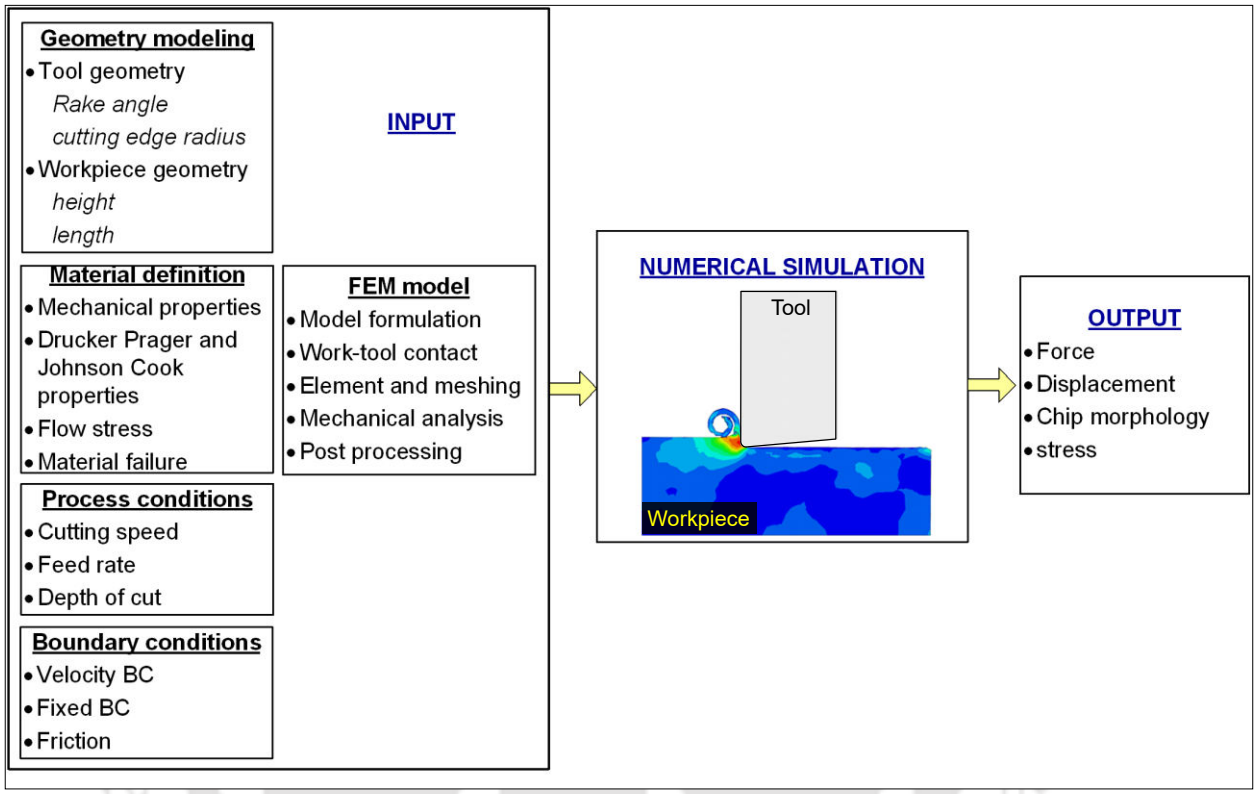

Figure 5.3 Input and output parameters from finite element simulation of machining

5.3.1 Model Definition and Assumptions

The finite element model used in this 2D orthogonal machining simulation is identical to the plunge cutting simulation model described in the previous Chapter 4, Section 4.4. Thus, all the assumptions presented in section 4.4.1 of chapter 4 are considered for the present numerical simulation of SPDT of brittle materials such as silicon and silicon carbide. The basic difference between a plunge (taper) cutting and a SPDT is that in SPDT process, tool is kept fixed and the workpiece is given rotational motion as shown in Figure 5.4 (a). The tool traverses parallel to the surface of the workpiece. In plunge cutting, the workpiece is kept fixed and the tool is given inclined motion to the surface of the workpiece as shown in Figure 5.4 (b).

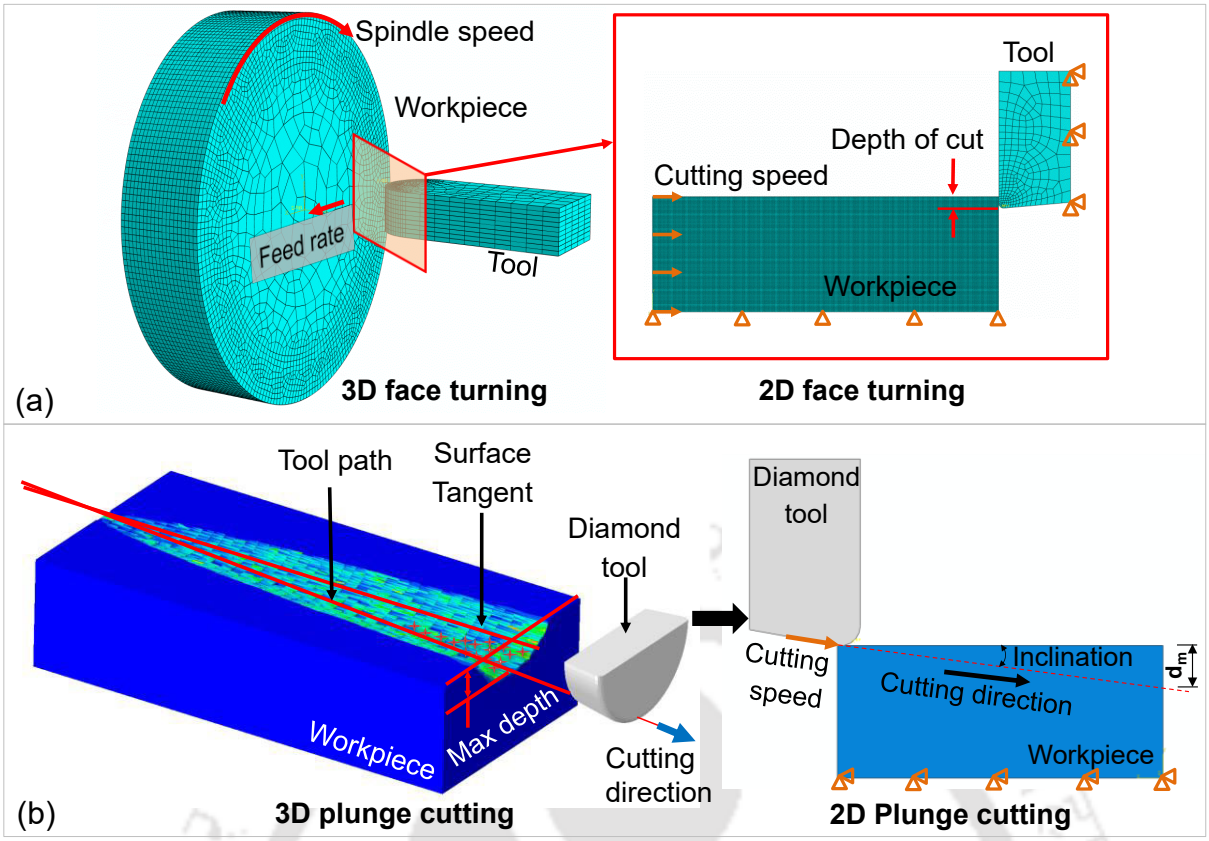

Figure 5.4 Comparison of SPDT machining and plunge cutting

5.3.2 Geometric Modeling

Initially, the geometric models of the cutting tool and the workpiece were modeled. The workpiece geometry was modeled as a rectangular shape with dimensions of 1 µm × 0.5 µm. Simulations were carried out for the machining of silicon and silicon carbide as work material and diamond as the cutting tool. The diamond tools considered for cutting simulation of silicon were having rake angles of −45° and −85° and clearance angles 5° and –45° respectively. For silicon carbide, the tool with rake angles of 0°, −25° and –45° and clearance angle of 5° were used. The cutting edge radius of commercially available diamond tools is in between 30–60 nm. Therefore, in the present analysis, the cutting edge radius has been considered as 40 nm. The depths of cut are taken as 50 nm, 100 nm, 300 nm and 500 nm. The maximum depth of cut was selected to be 500 nm for silicon carbide. This is based on the observations noted in the previous chapters. It was found that the ductile to brittle transition depth is 91 nm for silicon and 375 nm for silicon carbide. Figure 5.5 shows the silicon workpiece, cutting tool, and relevant geometry parameters used.

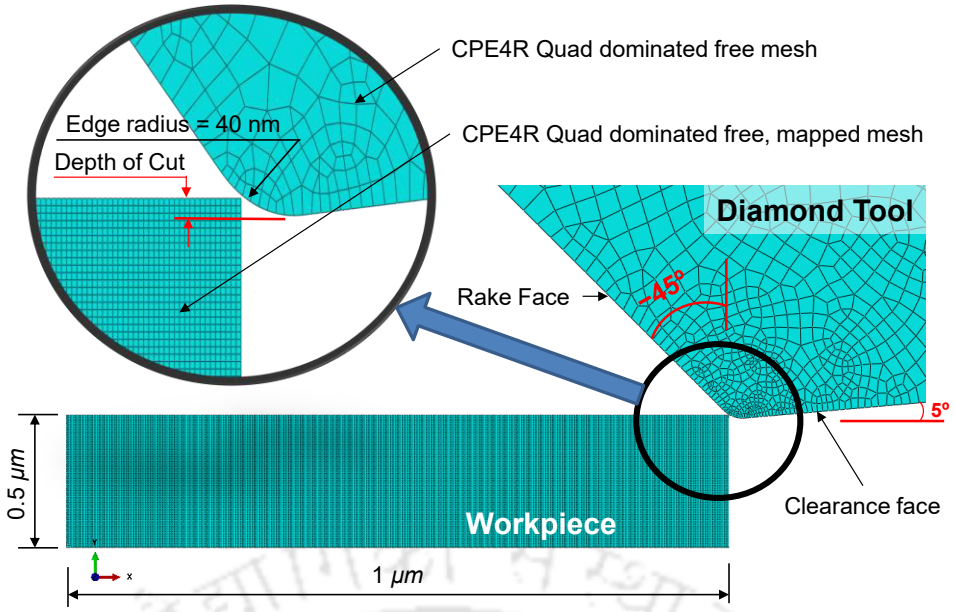

Figure 5.5 Finite element method based numerical model for SPDT of silicon

5.3.3 Material Model and Properties

The diamond tool was defined as rigid and workpieces silicon and silicon carbide in the model were defined as isotropic and homogeneous. The materials properties for diamond, silicon and silicon carbide have already been presented in Table 3.1 in the section 3.4.2 (D) of Chapter 3.

5.3.3.1 Drucker-Prager Material Model

The detail of the Drucker-Prager material model is already described in earlier section 3.4.2 (D) of Chapter 3. The Drucker-Prager materials constants are listed in Table 3.2 in the section 3.4.2 (D) of Chapter 3.

5.3.3.2 Johnson-Cook Material Model

The process of machining of materials is characterized by plastic deformation (more pronounced in metals than in ceramics and other brittle materials) occurring at high values of strain, strain rate and temperature. Initially the material constitutive model adopted in this work was Johnson-Cook's model [Johnson and Cook (1985)] which was used to describe the effect of strain, strain rate and temperature on the material flow stress, especially for metals. The material constants can easily be determined by using the torsion tests, static tensile tests and dynamic Hopkinson bar tests at elevated temperatures [Holmquist and Johnson (1991)].

The reason for using a ductile material model to describe brittle material is that when the undeformed chip thickness is sufficiently small, some amount of tangible plastic flow occurs. There is appreciable material flow during ductile regime machining. Yan *et al.*

(2006a) experimentally demonstrated that brittle materials show significant material flow during ductile regime machining. This was verified from the observations of continuous chip formation and the texture of the surface generated.

The Johnson-Cook constitutive material model is represented by equivalent flow stress σ and is expressed as (equation 5.1):

$$\sigma = (A + B(\varepsilon^{pl})^n)\left(1 + C\ln\left(\frac{\dot{\varepsilon}^{pl}}{\dot{\varepsilon}_0}\right)\right)\left(1 - \left(\frac{\theta-\theta_t}{\theta_m-\theta_t}\right)^m\right) \quad (5.1)$$

where, A (MPa) is the initial yield stress of the material, B (MPa) the hardening modulus, C is the strain rate dependency coefficient, n the work-hardening exponent, m the thermal softening coefficient, ε^{pl} is the equivalent plastic strain, $\dot{\varepsilon}^{pl}$ is the equivalent plastic strain rate and $\dot{\varepsilon}_0$ is the reference plastic strain rate, θ is the room temperature, θ_t is the transition temperature and θ_m is the workpiece melting temperature. Table 5.1 lists the JC material model constants for silicon and silicon carbide [Venkatachalam (2007), Mariayyah (2007)].

Table 5.1 Constants for Johnson-Cook constitutive model

Parameters	A [MPa]	B [MPa]	C	n	m	T_m [K]
Silicon Carbide	1400	2500	0.2	0.6	1	2773
Silicon	896.394	529.273	0.424	0.376	1	1415

5.3.3.3 Chip Separation Criterion and Failure Models

During machining simulations, large deformation of the workpiece material occurs and the material is said to be failed when it loses its load carrying capacity. In order to simulate chip formation, it is essential to simulate the damage and fracture of the material under the action of applied loads. The damage calculated for each element in the finite element model was given by the equation (5.2)

$$D = \sum \frac{\Delta\overline{\varepsilon^p}}{\overline{\varepsilon^p}^f} \quad (5.2)$$

Fracture is allowed to occur when D = 1.0 and the concerned elements are removed from computation. In fact, they still exist, in order to keep the number of nodes and element connectivity between nodes constant, but the deviatoric stress of the corresponding elements was set to zero and remains zero for the rest of the analysis. In Abaqus™, the user can keep the damaged elements either as the part of the analysis or remove from the analysis. The damage models for silicon and silicon carbide material have already been described in the previous sections 3.4.2 (E) and 3.4.2 (F) of Chapter 3. To obtain the material separation in the

cutting zone, element failure models identical to the section 3.4.2 (E) of Chapter 3 and section 4.4.6 of Chapter 4 have been used in the current simulation. For more detail description, refer section 3.4.2 (E) of Chapter 3 and section 4.4.6 of Chapter 4.

5.3.4 Governing Equations

In this present work, SPDT process has been modeled using the explicit dynamic ALE formulation. The explicit dynamic analysis procedure is based on using very small time steps. Thus, the governing equations for the present numerical simulations are also similar to that presented in section 4.4.2 of Chapter 4.

5.3.5 Element and Meshing

SPDT process is a highly non-linear and complex process as it involves large plastic deformation of workpiece material due to the contact of cutting tool with workpiece. Thus, it is necessary to select the right element type for the modelling of SPDT process. The workpiece is meshed with 2D solid elements CPE4R to carry out non-linear mechanical analysis. It is a 2D plane strain 4-noded solid element with reduced integration and hourglass control. This element type provides bilinear displacement, reduced integration with hourglass control and element deletion (for workpiece). The main advantage with the element failure is the deletion of material.

As already shown in Figure 5.4, the entire geometry is discretized into very small finite elements. Mesh sensitivity analysis was also carried out to decide the proper size of the element. Table 5.2 shows the results obtained during various simulations run for a variety of mesh sizes. It was observed that the average error considering both cutting and thrust force reduces when the mesh size is decreased from 10 nm (mesh1) to 2 nm (mesh8). It shows the minimum average error when the global element size was chosen as 2 nm. The average error becomes negative when the mesh size further reduces. Hence, to accommodate nano-metric depth of cut (≥ 50 *nm*), the approximate global element size was taken about 2 *nm*. For this particular case, the tool and the workpiece were discretized into 1212 and 50000 elements respectively. It is to be noted that the element size of the work material is kept uniform whereas the fine mesh is created near the cutting edge region for the cutting tool. The mesh density is kept higher at the cutting region where tool and workpiece interaction takes place. Other regions of the cutting tool were coarsely meshed to increase the computational efficiency of the simulation.

Table 5.2 Mesh convergence simulation

	Global Element size	Nos. of Elements	Cutting force (mN)	Thrust force (mN)	Error		Average error
Mesh1	1.00E-05	2000	96.1	237.6	220.33	296.00	258.17
Mesh2	8.00E-06	3125	88	215.8	193.33	259.67	226.50
Mesh3	6.00E-06	5511	75.25	176.8	150.83	194.67	172.75
Mesh4	4.00E-06	12500	53.44	122.44	78.13	104.07	91.10
Mesh5	3.00E-06	22311	48.65	109.43	62.17	82.38	72.28
Mesh6	2.50E-06	32000	46.13	103.62	53.77	72.70	63.23
Mesh7	2.20E-06	41405	45.96	104.49	53.20	74.15	63.68
Mesh8	**2.00E-06**	**50000**	**45.9**	**68.46**	**53.00**	**14.10**	**33.55**
Mesh9	1.90E-06	55230	20	44.6	−33.33	−25.67	−29.50
Mesh10	1.80E-06	61716	21.82	48.49	−27.27	−19.18	−23.23
Mesh11	1.70E-06	69384	22.96	49.62	−23.47	−17.30	−20.38
Mesh12	1.60E-06	78125	22.35	48.29	−25.50	−19.52	−22.51
Mesh13	1.50E-06	88711	24.76	54.86	−17.47	−8.57	−13.02

5.3.6 Contact Algorithms

The contact algorithm employed is similar to that described for plunge cutting simulation in section 4.4.9 of Chapter 4. Similar to plunge cutting simulation, surface to surface contact with kinematic contact approach was used to define the contact pairs between tool and workpiece.

5.3.7 Boundary Condition

Figure 5.6 depicts a schematic of the boundary conditions applied. The fixed boundary condition is applied at the bottom of the work piece so that the nodes attached to the bottom edge do not move in any direction. The diamond tool is first given rigid body constraint having reference point indicated with 'RP' (Figure 5.6) and provided with linear motion along the *x*-axis, so that it moves from left to right at the specified cutting speed of 20 µm/min. In general, workpiece rotates with a constant speed and tool is kept stationary, however, reverse is also considered valid for the simplicity of the problem. For this purpose, the velocity/angular velocity boundary condition was applied on the reference point of the tool in negative *x*-direction and the other degrees of freedom were set at zero. Thus, the *y*-direction as well as rotational motions of the tool were restrained. The depths of cut were set by moving the tool. Since the cutting speed is very slow (20 µm/min), and length of cut is considered to

be a few micrometers, the effect of tool wear and thermal softening of the material due to temperature rise were neglected. As a result, thermal calculations and vibrations that occur during the machining were not incorporated.

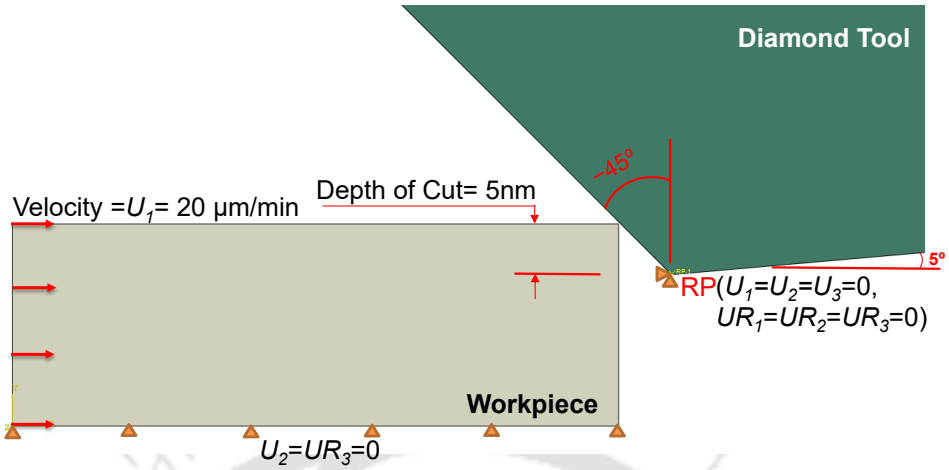

Figure 5.6 Boundary conditions during SPDT of silicon carbide

5.3.8 Solver Selection

After the development of geometric models of workpiece and tool, the material properties, material damage law and friction law, the non-linear mechanical analysis of the 2D orthogonal machining process were applied. In the present analysis, dynamic explicit time integration scheme with ALE formulation was used. ALE formulation controls the severe mesh distortion. The details of ALE are described in the previous Chapter 4, Section 4.4.8. The explicit dynamic analysis procedure uses very small time steps (smaller than the critical time step). This scheme is simple and can handle problems involving high nonlinearity, large deformation, complex friction-contact conditions and thermo-mechanical coupling. 100 frames were generated in the field output module to visualize the whole machining process. To achieve an economical solution, semi-automatic mass scaling with a scale factor of about 10^6 was employed. Mass scaling was originally developed to solve high-speed dynamic problems those were difficult to simulate using the implicit method. The differential equation of motion for determining the nodal acceleration, velocity and displacement vectors described in earlier section 4.4.2.

5.3.9 Post Processing

In order to understand the response behavior of the workpiece and tool during chip formation, it is necessary to determine the variation of output solution variables within chip formation zones as a function of input variables. The output solution variables obtained in FE simulations are node-based quantities (displacement, velocity, reaction force, etc.) or element-

based quantities (stress, strain, etc.). In FE machining studies, the results such as displacement, force, temperature, stress, surface profile, or other fundamental variables can be evaluated from the simulation once the simulation has been completed. To obtain the specified output results, variables must be selected from the field output and history output module prior to the simulation. All the data and results will be stored in a file with .ODB file extension during the simulation and can also be transferred to other system for analysis. The evaluation generally can be done interactively using the Visualization module of Abaqus/CAE. The following sections describe the extraction of force values and contour plots of chips during the machining simulations.

5.4 Results Analysis

Cutting forces are generally investigated to gain a pivotal understanding of mechanics of chip formation, power consumption, machinability and tool wear. High cutting forces can influence surface integrity and cause tool failure. The cutting forces are generally analyzed as a function of cutting force magnitude and its trend during cutting can reveal various process outputs such as tool wear, ductile/brittle fracture etc. To determine the machining forces from the FE simulation, corresponding job file is selected once the simulation is completed and result module is opened. The other method to extract simulation results are to run the .ODB file stored in the project folder using FE package. XY plots of force verses time increment are extracted by selecting the node of interest (i.e., reference point of the tool in the present case) from the field variable output reaction force (RF). The RF is due to the force exerted by the workpiece and chip on the tool as the tool moves towards the workpiece by shearing the workpiece material. The average forces were calculated for all the process conditions after achieving steady state condition. Extracted forces were then validated with the experimental machining force values for the identical process conditions.

5.5 Numerical Simulation and Experimental Validation of SPDT of Silicon Carbide

After the extraction of responses, the experimental validation of the responses predicted by the numerical model was carried out. The experimental validations of the developed numerical model were carried out on silicon carbide. Due to the absence of in-house experimental facility at IIT Guwahati, it was decided to validate the simulated force results with already published experimental results. These are discussed in the following sections.

5.5.1 Selection of Suitable Material Model

Literature reports significant research on modeling of machining (traditional and non-traditional) processes using finite element method based numerical techniques. Though various numerical techniques with different material models have been employed, there are no guidelines exist for selection of suitable material model to a specific material. In view of this, it was thought worthy to carry out an investigation of the effect of material models on the process responses using FEM.

Initially, by using the developed FEM based model and two different material models, force values were computed. Then, the force values were verified with published experimental results by Patten and his team [Patten *et al.* (2005, 2008)]. In this work, two different material models viz. Johnson-Cook (JC) and Drucker-Prager (DP) were employed for SiC material. 6H-Silicon carbide was chosen as workpiece material and polycrystalline diamond tool was chosen as cutting tool. A 3 μm × 1 μm size workpiece was modeled with three sets of tool geometries and a range of depth of cuts. These are as shown in Table 5.3.

The steps involved in the simulations are similar to that described in section 5.3. However, the workpiece and tool geometry, depths of cut, material models and cutting speed (3 m/min) were appropriately chosen. Johnson-Cook and Drucker-Prager material models of silicon carbide material have been applied. Other aspects such as tool nose radius, temperature effect, and friction co-efficient were kept similar to that described in section 5.3. All the process parameters for the simulation were employed exactly similar with experimental conditions.

Table 5.3 Process conditions for simulations

Set	Rake angle (°)	Clearance angle (°)	Depth of cut (nm)	Cutting force (N)	Thrust force (N)
1	0	5	100	0.5	0.6
			300	0.3	1
			500	1	1.9
2	–45	50	50	1.7	
			100	1.45	
			300	1.23	
			500	2.3	
3	–45	5	50	1.5	5
			250	2.3	9

Figures 5.7, 5.8 and 5.9 show the comparison between the cutting forces of JC and DP models with that obtained from the experimental tests [Patten *et al.* (2005, 2008)] for the similar cutting conditions. It can be seen that in case of depth of cut of 100 nm to 500 nm, the predicted cutting forces using DP model are closer to experimental results in comparison to that of JC model. It is because of the behaviour of silicon carbide material. It is to be noted that Johnson-Cook material model considers the effects of high strain, strain rate and temperature of the material during plastic deformation, whilst the Drucker-Prager model works based on the use of hydrostatic pressure. During machining of brittle material (such as SiC) with nano level depth of cut, hydrostatic pressure is generated on the workpiece below the diamond tip. The pressure increases with the increase in negative rake angle. DP model takes care of the pressure generated on the material. In case of very low depth of cut, i.e., below critical depth of cut, brittle material behaves as ductile material, thus the JC model is more appropriate in the case of depth of cut near to 50 nm. From Figures 5.8 and 5.9, it is clear that the predicted cutting force values are closer to the experimental value in case of JC model in comparison to that of DP model.

From Figure 5.7 and 5.8, it can also be observed that the magnitude of cutting forces for set 2 (−45° rake angle) are higher than the cutting forces obtained for set 1 (0° rake angle). This is because the large negative rake angle tool compresses the work material and pushes more material below the tool edge radius. This generates high hydrostatic pressure underneath the cutting tool and material is removed by ploughing process rather than the shearing. The compressive stress are noted to be higher than the tensile stresses in case of −45° rake angle tool in comparison to 0° rake angle tool. Therefore, high negative rake angle increases the cutting forces.

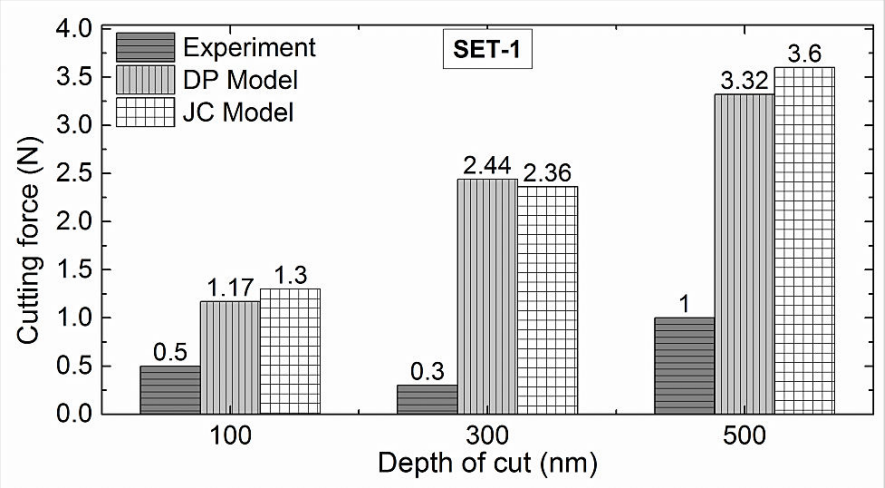

Figure 5.7 Comparison of cutting force for JC and DP model for set 1

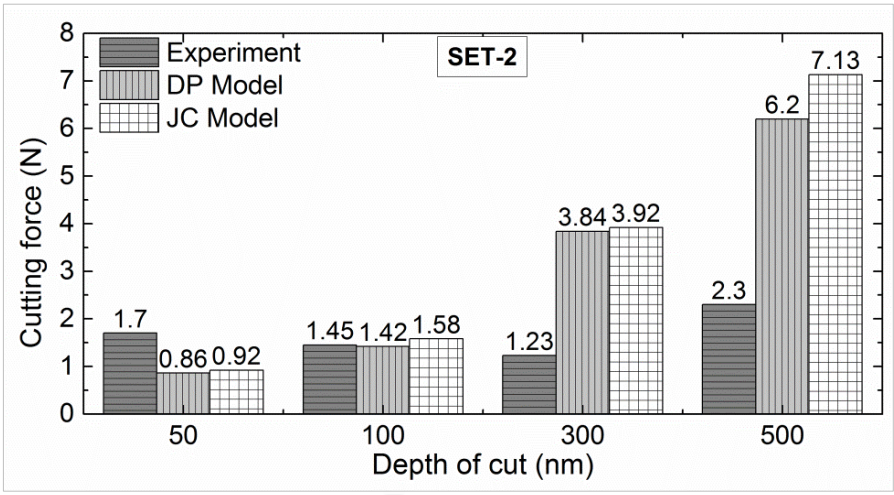

Figure 5.8 Comparison of cutting force for JC and DP model for set 2

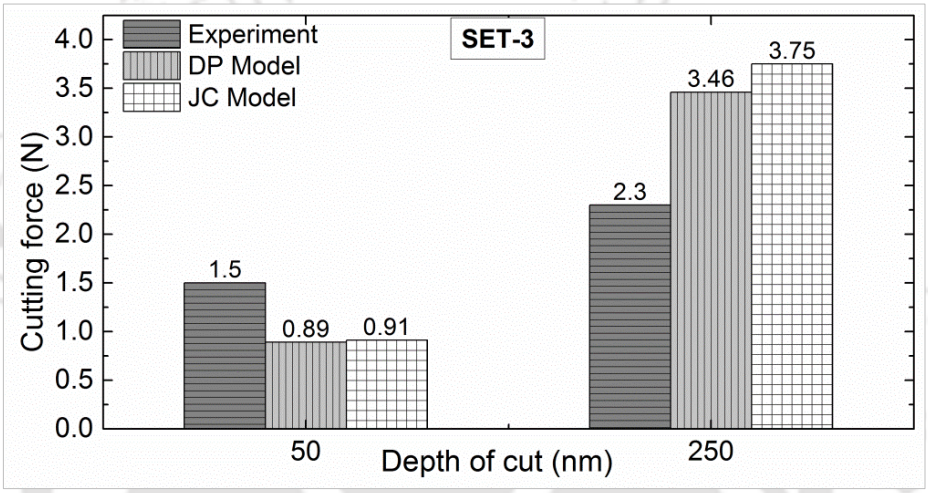

Figure 5.9 Comparison of cutting force for JC and DP model for set 3

From Figures 5.7 to 5.9, it can also be seen that the prediction errors of our numerical model are high in some cases of depths of cut. This is attributed to the consideration of simplifying assumptions and unavailability of all process conditions that to be applied. The simplifying assumptions the responsible are: work material is isotropic and homogeneous; the cutting is considered as perfectly orthogonal. In reality, the work material is anisotropic and the cutting is not perfectly orthogonal. It is also observed that, when the depth of cut is 50 nm, both the models under predicts the experimental cutting force. As the depth of cut increases above 100 nm, the numerical model over predicts the experimental results. This may be due to the fact that in the experimental cutting, material behaviour changes from ductile to brittle as the depth of cut increases. Below 100 nm depth of cut, the cutting occurs in ductile mode, whereas above 100 nm depth of cut, brittle fracture dominates the process. Our model is showing relatively constant material behaviour compared to the physical material. Due to which cutting forces are low at 50 nm depth of cut in which ductile material removal is experienced. When the depth of cut increases above 100 nm, cutting mode changes to brittle

mode. But, our model shows comparatively ductile behaviour than the physical material and thus cutting forces are higher than the experimental results.

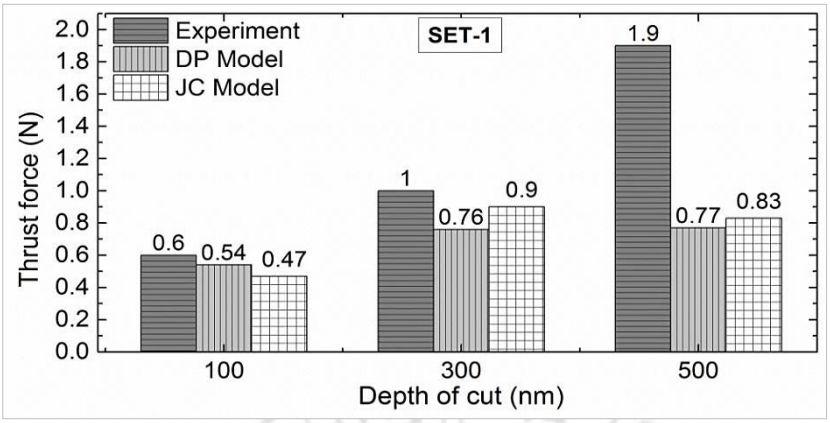

Figure 5.10 Comparison of thrust force for JC and DP model for set 1

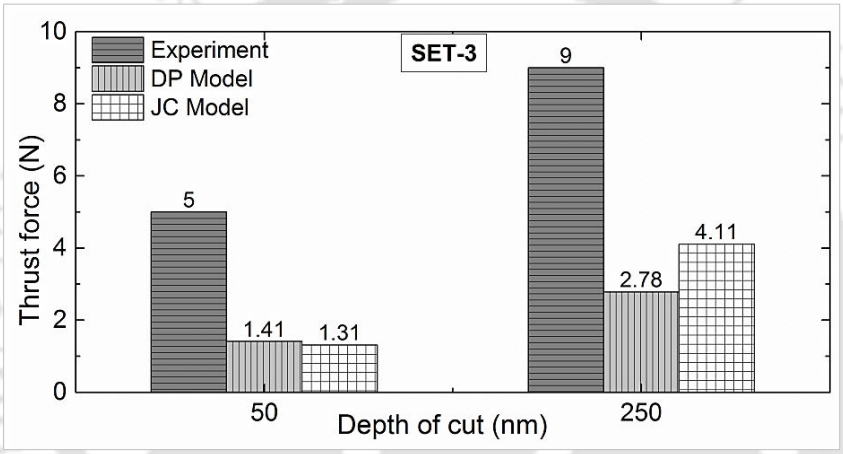

Figure 5.11 Comparison of thrust force for JC and DP model for set 3

Figures 5.10 and 5.11 show the comparison of predicted thrust force values with that of experimental results. It can be noticed that the ductile mode of material removal occurs when depth of cuts are 50 nm to 100 nm. It can also be observed that our model under predicts the thrust force. This is attributed to the consideration of simplifying assumptions. The force values using JC model are noted to be closer to the experimental results. For all process conditions, the predicted results using both the JC and DP models are found to be low in comparison with experimental results. Within the scope of obtained results, it can be seen that JC model predicts well in comparison that of DP model. However, in case of 250 nm to 500 nm depth of cuts, the prediction of thrust force using DP model is better than the JC model. This is because as the depth of cut increases, the silicon carbide starts behaving more brittle as explained earlier. DP model takes care of the pressure generated on the material. The thrust force values for set 2 have not included in the comparison due to unavailability of data.

From the present study, it was concluded that selection of material model plays a crucial role in prediction of the force values. In the context of cutting forces, at low depth of cut, the brittle material behaves like a ductile material; the JC material model can be applied. At higher values of depth of cut, the brittle material behaves like brittle only; then DP model is to be employed. However interestingly, it was seen that when the depth of cut is low, the thrust force is sensitive to high negative rake angle which generates high hydrostatic pressure. Thus, DP model may be useful to predict the thrust force accurately in case of lower depth of cut. At higher depth of cut, the energy required for brittle fracture is comparatively less than that required for plastic deformation.

5.5.2 Study on Quantitative Crack Propagation using JC and DP Material Models

In this section, a quantitative analysis of crack propagation has been carried out to study the crack propagation mechanism and chip morphology during machining of silicon carbide. Figure 5.12 shows the crack initiation and its propagation during machining of silicon carbide using DP material model. It can be observed that the initiation of crack occurs after 1.95 µs (Figure 5.12 (b)). After 0.05 µs, the crack reaches to the top surface and a chip generates. During this process the crack travels a distance of 1.043 µm from point 1 to 2. The shear angle noted to be of 35° (approx.).

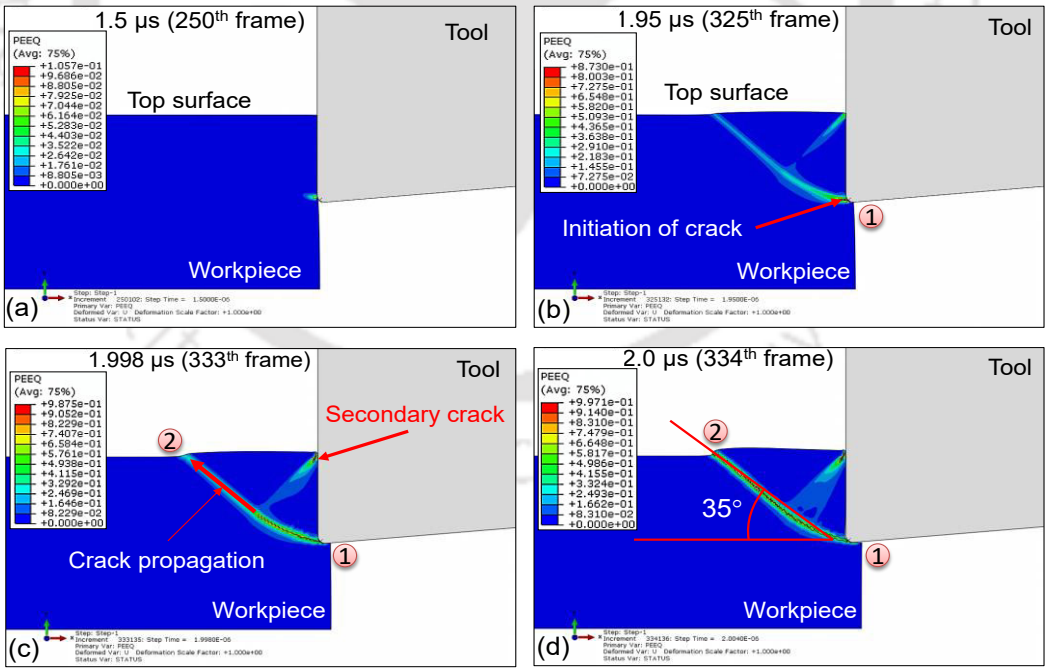

Figure 5.12 Crack propagation of silicon carbide with Drucker-Prager material model at (a) 1.5µs, (b) 1.95 µs, (c) 1.99 µs and (d) 2.0 µs

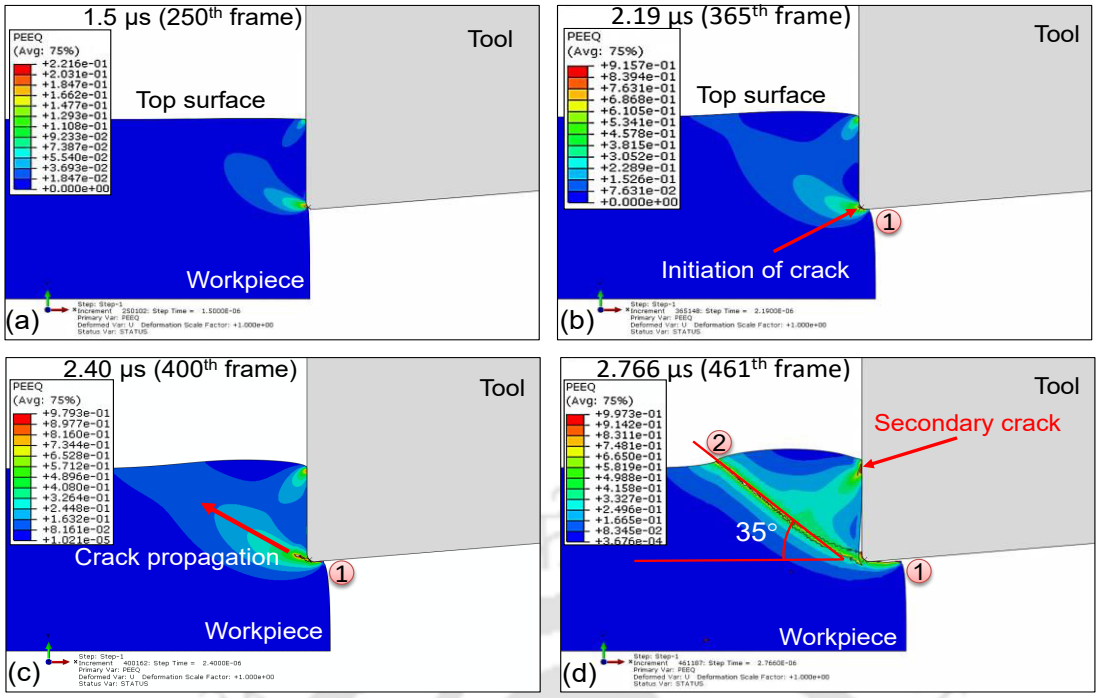

Figure 5.13 Crack propagation of silicon carbide with Johnson-Cook material model at (a) 1.5 μs, (b) 2.19 μs, (c) 2.4 μs and (d) 2.77 μs

Figure 5.13 shows the propagation of crack during simulation of machining of SiC using JC model. It can be seen that the initiation of crack occurs after 2.19 µs (Figure 5.12 (b)). After 0.576 µs, the crack reaches to the top surface and a chip is formed. During this process, the crack travels a distance of 1.052 µm from point 1 to 2 at an angle of 35° (approx.). From above observations, it can be verified that JC material model represents ductile material mode of cutting whereas the DP material model represents brittle behavior. This can be justified by analyzing the time taken to propagate the crack from point 1 to 2. It can be seen that the JC model takes more time (0.576 µs) to propagate the crack as compared to that of DP model (0.05 µs) for same process conditions and tool geometry. The depth of cut and shear angles are same for both the cases, therefore the crack length is found to be same in both cases. The longer crack propagation time indicates that the material is getting deformed plastically. This is very analogous to the tensile test of ductile material; in which the material elongates and takes considerable time till it breaks. While, in case of brittle materials, the material breaks within a short duration without showing any noticeable plastic deformation.

To verify the conclusion that JC model predicts the ductile behavior, the chip morphologies were studied for both the JC and DP models. Figures 5.14 and 5.15 show the progression of workpiece deformation and chip formation for JC and DP material models. It can be seen that, long and connected chips are formed during SPDT of SiC using JC material

model (Figure 5.14). Figure 5.15 shows the chips formed when DP model was employed. It can be seen that brittle chips form during machining using DP model. This is in line with the fact that brittle material break-up into brittle chip (small) during machining above the critical depth of cut.

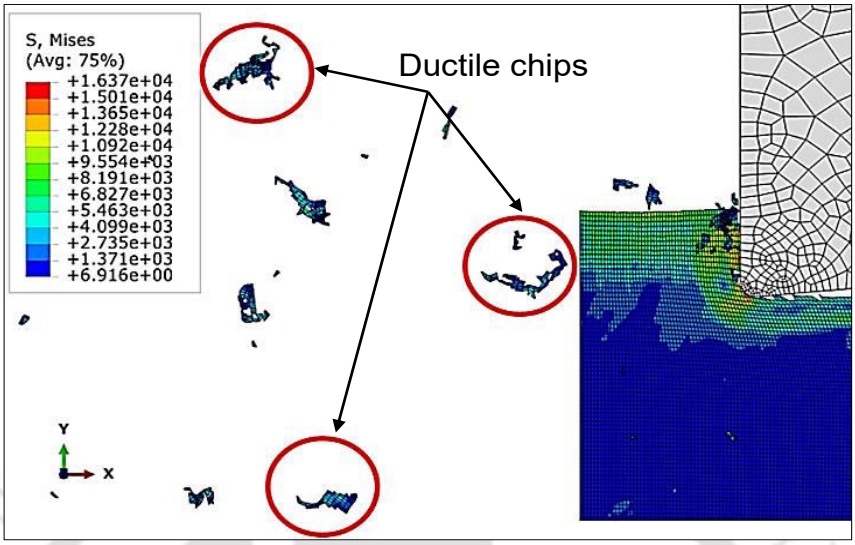

Figure 5.14 Contour plot of equivalent von-Mises stress with the formation of a continuous chip (0° rake angle, 5° clearance angle and 100nm depth of cut)

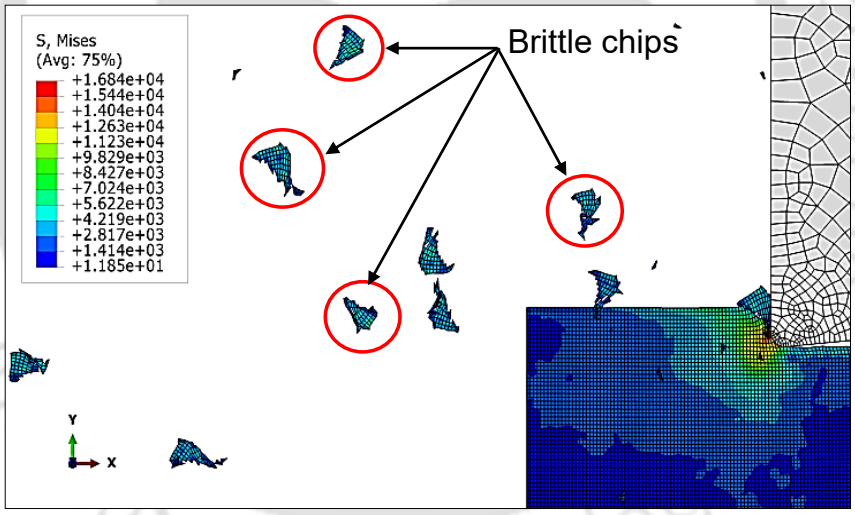

Figure 5.15 Contour plot of equivalent von-Mises stress with the formation of a brittle chip. (0° rake angle, 5° clearance angle and 100 nm depth of cut)

Figure 5.16 shows optical microscopic image of the ductile chip obtained during the experimental cutting of SiC [Mariayyah (2007)]. The process conditions used were cutting speed of 0.8 m/s, depth of cut of 25 nm and feed rate of 25 nm/rev. The diamond tool was having a planar rake angle of −25° and a clearance angle of 10° and cutting edge radius of 50 nm. The formation of chips predicted by our model using JC is similar to the experimental results reported. The experimental results are reported for a very small depth of cut i.e. 25 nm, which can be considered to be less than critical depth of cut.

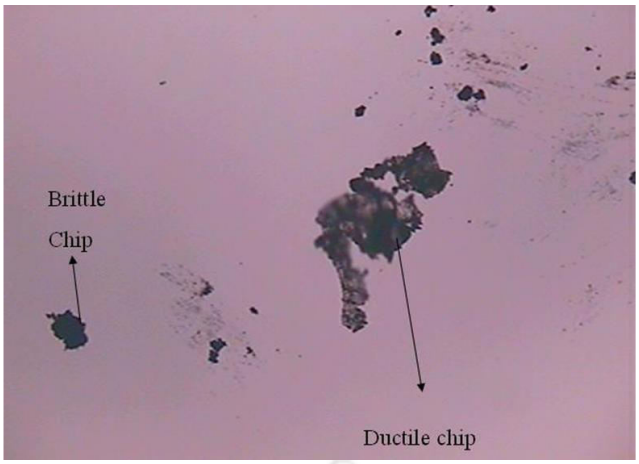

Figure 5.16 Optical microscopic image of the ductile chip during experimental cutting of SiC [Mariayyah (2007)]

The formation of brittle chips during SPDT of SiC can be understood by using basic five stages. These are: (a) dynamic loading, (b) crack initiation, (c) crack propagation, (d) chip formation and (d) Formation of surface and sub-surface damage. Figure 5.17 shows the stages.

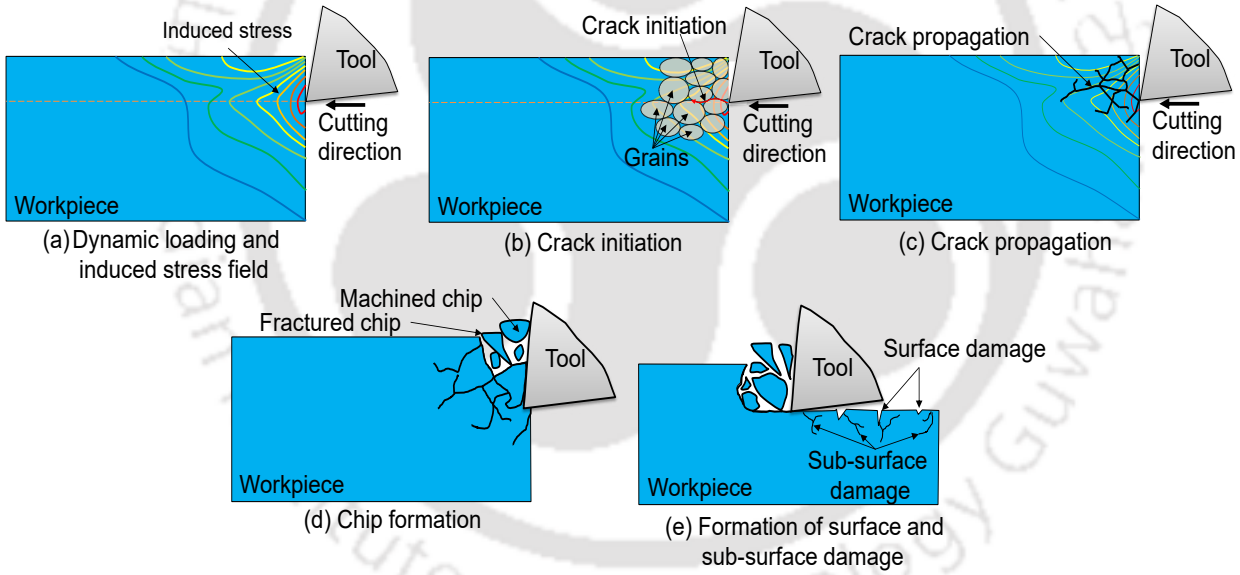

Figure 5.17 Five essential stages in the brittle material removal

Figure 5.17 (a) The tool touches the work piece, the impact between the tool and workpiece induces a stress field.

Figure 5.17 (b) The workpiece starts deforming due the compressive stress exerted by the tool. Due to the induced stress, a crack nucleation begins immediately and propagates as the machining process progresses. Since the deformation is more along the tool side of the chip, a localized plastic deformation zone is first formed in front of the tool and above the cutting edge. Then, an internal

crack initiates along the grain boundaries or crack nucleation after the material reaches the failure strain.

Figure 5.17 (c) The internal crack propagates and reaches the free surface and material is separated by fracture. Sometimes, a free surface crack also initiates during the deformation process and propagates toward the cutting edge to form a chip.

Figure 5.17 (d) The material shears strongly along the crack surface. Sometimes two cracks join together and discontinuous fractured chips are formed subsequently. The chips that formed due to the shearing of material are termed as machined chips. Fragments formed without any direct contact to tool face are called fractured chips.

Figure 5.17 (e) The brittle fracture not only forms the cracks but also creates sub-surface damage to the machined surface.

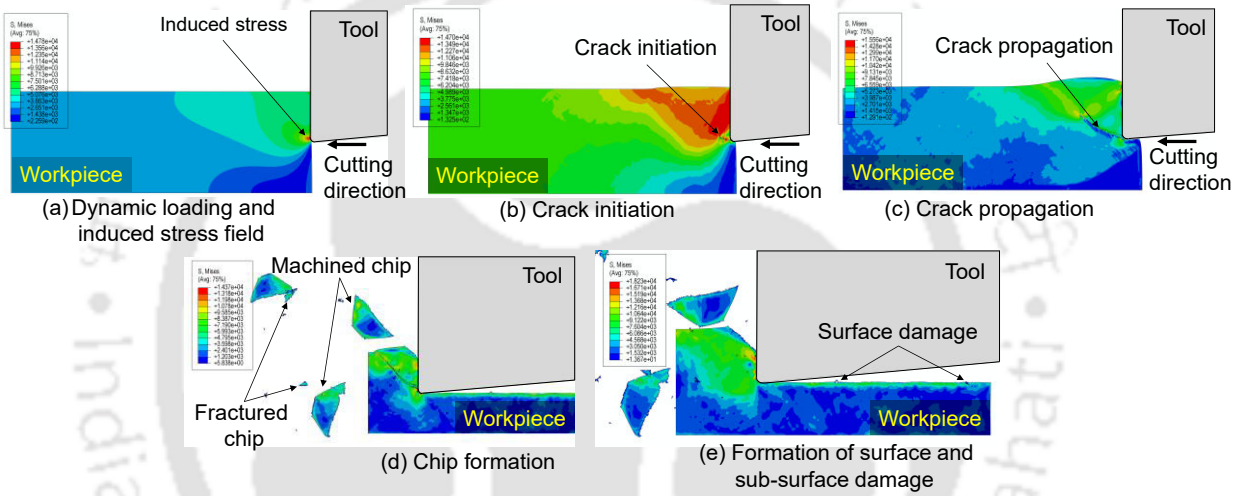

Figure 5.18 Stages of chip formation during SPDT machining of SiC

To verify the above stages, in the present work, a detail analysis has been carried out. Figure 5.18 shows the various stages of chip formation and sub-surface damage. Figure 5.18 (a) shows the contour plots of stresses induced on the workpiece due to the impact of the tool. Crack is initiated at the workpiece near to the tool tip (Figure 5.18(b)) and as the tool proceeds, the stress continues to develop and the crack grows and at last propagates to the free surface. This forms the chips (Figure 5.18 (c)). As a result two types of chips are obtained viz. machined chips of larger size and fractured chips of smaller size (Figure 5.18 (d)). Figure 5.18 (e) shows the formation of machined surface with surface damage that occurred due to brittle fracture. From the above observations, it can be stated that our model is able to successfully simulate the SPDT machining of brittle materials and numerical results are fairly matching with the available published experimental results. After the validation of the developed model, a parametric analysis of machining forces using full factorial design has been carried out. This is presented in the next section.

5.5.3 Parametric Analysis of SPDT of Silicon Carbide using FEM and Full Factorial Analysis

In the present work, a finite element method and full factorial analysis (FEM-FFA) based parametric analysis of SPDT of silicon carbide has been carried out. Total 27 numbers of simulations were performed by varying rake angle, depth of cut and depth to edge radius (d/r) ratio. Full factorial design matrix was prepared for three factors with 3 levels each.

5.5.4 Full Factorial Design

Full factorial design takes all possible combinations of the levels for all the factors. It allows to study the effects of each factor on the response variable, as well as the effects of interactions between factors on the response variable. In the present work, the input parameters considered were rake angle, depth of cut, and depth of cut to cutting edge radius ratio. After collection of the data, the model adequacy check was conducted. Moreover, the test for significance of the regression model, the test for significance on model coefficients and the test for lack of fit [Montgomery *et al.* (2012)] were performed. For this purpose, analysis of variance (ANOVA) was performed.

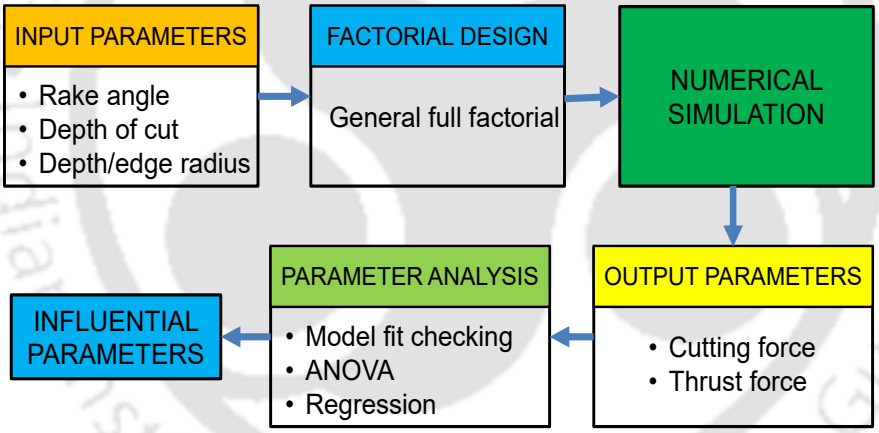

Figure 5.19 Parametric analysis of SPDT of silicon using FEM and full factorial

In the present work, the developed FEM based model is utilized to obtain the machining forces for different process conditions such as rake angle, depth of cut and d/r ratio. Figure 5.19 shows the overall approach of the developed model for the parametric analysis of SPDT of silicon carbide. Rake angle, depth of cut and d/r ratio were the input process parameters that are fed to the numerical model. Developed 2D plane strain dynamic explicit ALE numerical model was utilized to predict the process responses viz. cutting force and thrust forces. Regression and ANOVA analysis were carried out, and results are thoroughly studied and presented in the subsequent sections.

5.5.5 Selection of Machining Parameters and their Importance

In the present study, tool rake angle, depth of cut and d/r ratio have been considered as input process variables. The process variables with their units are listed in Table 5.4. The cutting speed was kept constant at 1 m/s. The ranges of these parameters have been selected based on the research and trade literature [Patten *et al.* (2005, 2008)]

Table 5.4 Process variables and their levels

Parameters	Units	Levels		
Rake angle	(°)	−25	−30	−45
Feed rate	μm/rev	0.1	0.25	0.5
d/r ratio		1	2	5

Importance of each process parameters on SPDT machining of silicon carbide is described below:

Rake angle: Negative rake angle generates hydrostatic pressure which helps in phase transformation from brittle to ductile which further helps in removing brittle material in ductile mode, thus affecting the machining forces. Therefore, it was planned to investigate the effect of negative rake angles (−25°, −30° and −45°) on overall machining forces.

Depth of cut: Increase in depth of cut increases the amount of material to be removed which requires large energy to separate it from the workpiece. Thus machining forces also increase with the increase in depth of cut. The critical depth of cut for silicon carbide was experimentally found to be 50−300 nm, depending on the crystal orientation of the substrate and mode of operation [Patten *et al.* (2005), Ravindra and Patten (2008) and Xiao *et al.* (2018)]. For the present work, the depths of cut were chosen as 100 nm, 250 nm, and 500 nm.

Depth to cutting edge radius (d/r) ratio: For a given rake angle, if the depth of cut is smaller than the edge radius, the effective rake angle becomes negative. In the present study, the d/r ratios of 1 nm, 2 nm and 5 nm were considered. The ratios were chosen kept higher than 1 so that it does not affect the actual rake angle of the tool and at the same time, the effect of edge radius can be studied.

Table 5.5 shows the experimental matrix. Numerical simulations were carried out according to the combinations given in Table 5.5 and corresponding response variables, i.e., cutting force, and thrust force obtained from the simulations were recorded. Then, a systematic analysis of response variables was carried out using ANOVA and regression analysis.

Table 5.5 Numerical matrix and results for the SPDT performance characteristics

RunOrder	Process Parameters			Simulated values	
	Rake angle (°)	depth of cut (nm)	d/r ratio	Cutting Force (N)	Thrust Force (N)
	A	B	C		
1	−25	100	1	0.133	0.097
2	−25	100	2	0.126	0.075
3	−25	100	5	0.120	0.067
4	−25	250	1	0.438	0.314
5	−25	250	2	0.423	0.245
6	−25	250	5	0.407	0.213
7	−25	500	1	1.246	0.892
8	−25	500	2	1.110	0.619
9	−25	500	5	1.082	0.519
10	−30	100	1	0.134	0.103
11	−30	100	2	0.129	0.086
12	−30	100	5	0.125	0.073
13	−30	250	1	0.442	0.330
14	−30	250	2	0.414	0.263
15	−30	250	5	0.412	0.238
16	−30	500	1	1.187	0.865
17	−30	500	2	1.128	0.653
18	−30	500	5	1.105	0.624
19	−45	100	1	0.154	0.133
20	−45	100	2	0.148	0.119
21	−45	100	5	0.157	0.120
22	−45	250	1	0.529	0.446
23	−45	250	2	0.543	0.437
24	−45	250	5	0.548	0.422
25	−45	500	1	1.322	1.068
26	−45	500	2	1.254	0.954
27	−45	500	5	1.173	0.836

The detailed analysis and important observations are described in the following sections.

5.5.6 Analysis of Results and Discussion

For the analysis of the data, the checking of the goodness of the fit of the model is required. The model adequacy checking includes the test for significance of the regression model, test for significance on the coefficients and test for lack of fit [Montgomery *et al.* (2012)]. For this purpose, analysis of variance (ANOVA) was performed.

5.5.6.1 ANOVA Analysis of Cutting Force

The ANOVA was employed to study the effect of input parameters on the machining force. ANOVA is one of the most widely used statistical analysis methods and it is an important analysis tool for scientific experiments. It is often used to examine the significance

of factors in a multi-factor experiment. From the model analysis, it was revealed that the 2 factorial interaction (2FI) model is the appropriate model as quadratic model does not show any relevant result for analysis of variance. Table 5.6 shows ANOVA results from 2FI model for the linear terms rake angle (A), depth of cut (B), and d/r ratio (C) and interactive terms (A ×B), (B×C), and (A×C).

Table 5.6 Analysis of variance (ANOVA) results for cutting force

Source	DF	Adj SS	Adj MS	F-Value	P-Value
Model	18	5.19957	0.28886	783.87	0.000
Linear	6	5.17293	0.86215	2339.57	0.000
Rake angle (°)	2	0.04141	0.02071	56.19	0.000
Depth of cut (nm)	2	5.11942	2.55971	6946.10	0.000
d/r ratio	2	0.01210	0.00605	16.42	0.001
2-Way Interactions	12	0.02664	0.00222	6.02	0.008
Rake angle (°)*Depth of cut (nm)	4	0.01022	0.00256	6.94	0.010
Rake angle (°)*d/r ratio	4	0.00115	0.00029	0.78	0.568
Depth of cut (nm)*d/r ratio	4	0.01526	0.00382	10.35	0.003
Error	8	0.00295	0.00037		
Total	26	5.20252			

S	R-sq	R-sq(adj)	R-sq(pred)
0.0191966	99.94%	99.82%	99.35%

DF: Degree of freedom, SS: Sum of square, MS: Mean square

The test for significance of regression and individual model coefficients were obtained. The sum of squares was used to estimate the square of deviation from the mean. Mean squares were calculated by dividing the sum of squares by degrees of freedom. F-value which is a ratio between the regression mean square and the mean square error was used to measure the significance of the model under investigation with respect to the variance of all the terms including the error term at the desired significance level. Usually, $F > 4$ means that the change of the design parameter has a significant effect on the response variable. P-value (probability value) was also used to determine the statistical significance of results at a confidence level. In this study, the significance level of $\alpha = 0.05$ was used, i.e., the results are valid for a confidence level of 95%. Table 5.6 shows the p-values, the significance levels associated with the F-values for each source of variation. If the P-value < 0.05, then the corresponding factor (source) has a statistically significant contribution to the response variable and if the P-value > 0.05, then it means the effect of factor on the response variable is not statistically significant at 95% confidence level.

From the Table 5.6, only the interaction term of rake angle and d/r ratio was found insignificant because the associated F-value is less than 4 and P-value is higher than 0.05. The other model terms can be considered as significant. The sum of squares was used to estimate the square of deviation from the mean. Mean squares were estimated by dividing the sum of

squares by degrees of freedom. Since, there is only one insignificant model term; no model reduction process was carried out. The other model terms were found to be significant.

The other important term is the coefficient of determination (R-sq), which is defined as the ratio of the explained variation to the total variation and is a measure of the degree of fit. It is the percentage of the response variable variation that is explained by a linear model. R^2 is always between 0 and 100%. 0% indicates that the model explains none of the variability of the response data around its mean. As R^2 approaches unity or 100%, the response model fitness with the actual data improves. This means that regression model provides an excellent explanation of the relationship between the independent variables (factors) and the response (cutting force). The value of R^2 = 99.94% indicates that the model explains 99.94% of the total variations. The adjusted R^2 is a statistic used to adjust the "size" of the model, i.e., the number of factors (machining parameters). The value of adjusted R^2 also gives the idea of how many data points fall within the line of the regression equation. The value of the R^2 (Adj.) = 99.82% indicates that the model explains 99.82% of the total variability after considering the significant factors. R^2 (Pred.) = 99.35% is in good agreement with the R^2 (Adj.) and shows that the model would be expected to explain 99.35% of the variability in new data.

5.5.6.2 Model Fitness Check

The adequacy of the modal has been checked by examining the residuals. The residuals are the differences between the respective observed response and the predicted response. These are examined using normal probability plots of the residuals and the plots of the residuals versus the predicted response. If a model is adequate, the points on the normal probability plots of the residuals form a straight line.

Figure 5.20 shows the normal probability distribution of the residuals for cutting force. It can be noticed that the residuals points are clustered around a straight line, which means that the errors are normally distributed. Figure 5.21 illustrates the relationship between the actual and predicted values of cutting force. It can be noticed that the points are normally distributed along the straight line making an angle of 45° indicating that the factorial model is able to predict the response accurately.

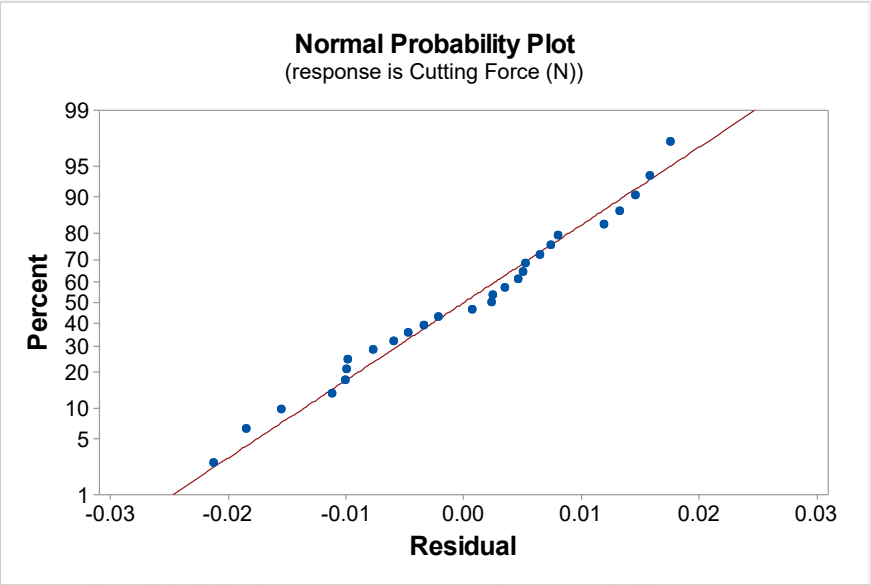

Figure 5.20 Normal plot of residuals for cutting force

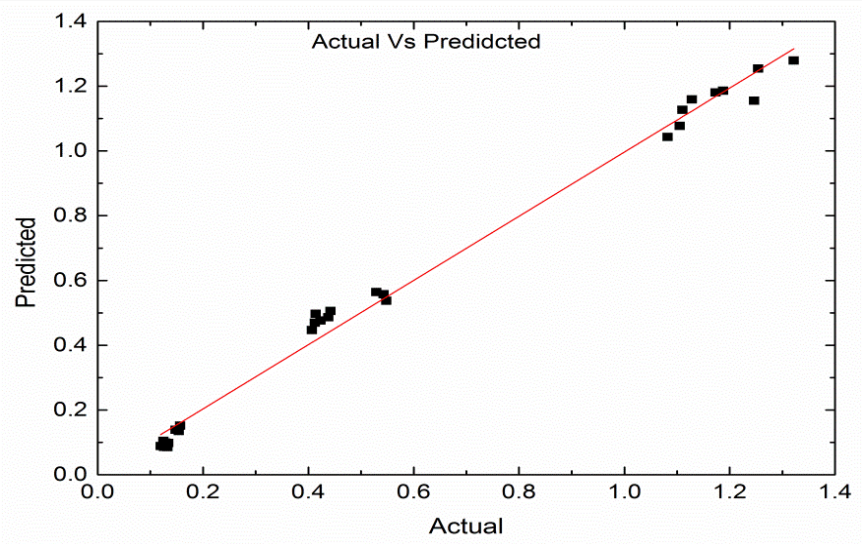

Figure 5.21 Plot of actual vs. predicted response of cutting force

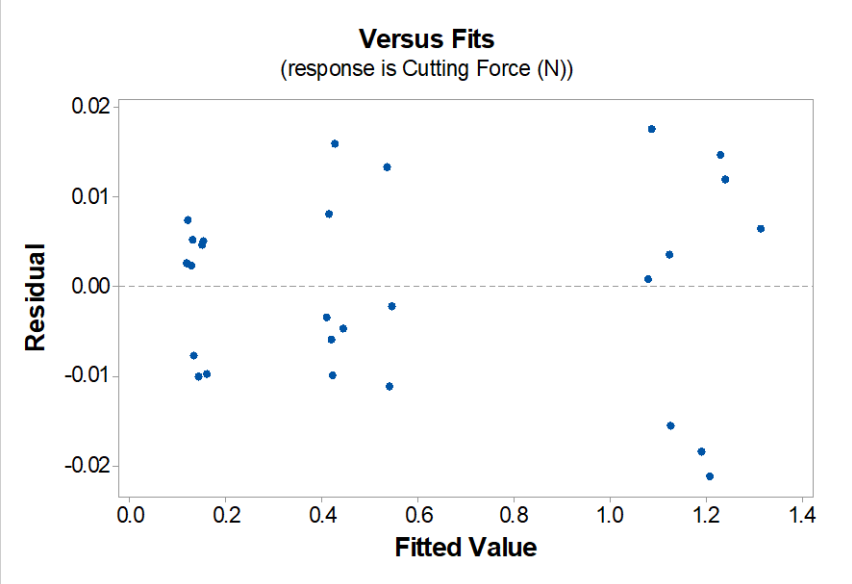

Figure 5.22 Residuals versus fitted value plot of cutting force

Figure 5.22 shows the plots of the residuals versus the fitted value. It is observed that, the points are normally distributed along the horizontal zero line indicating that the general full factorial model is able to predict the response accurately since error terms are having mean zero. These plots indicate that the developed models are adequate and are able to predict the results with good accuracy.

5.5.6.3 Regression Analysis

Using the regression analysis, mathematical expression was developed to predict the cutting force. The response equation for cutting force is given as:

$$\textbf{Cutting Force (N)} = -0.2251 - 0.00139 \times \text{rake angle} + 0.002514 \times \text{depth of cut} + 0.0040 \times \text{d/r ratio} - 0.000009 \times \text{rake angle} \times \text{depth of cut} - 0.000163 \times \text{rake angle} \times \text{d/r ratio} - 0.000072 \times \text{depth of cut} \times \text{d/r ratio} \quad (5.3)$$

The developed mathematical model can be used to predict the cutting force during SPDT of SiC within the scope of applied process conditions.

5.5.6.4 Parametric Influence on Cutting Force

The main effects of machining parameters on mean cutting force are shown in Figure 5.23. It can be observed that, the depth of cut has the significant effect on cutting force than the rake angle and d/r ratio. These findings can also be seen in the Table 5.6.

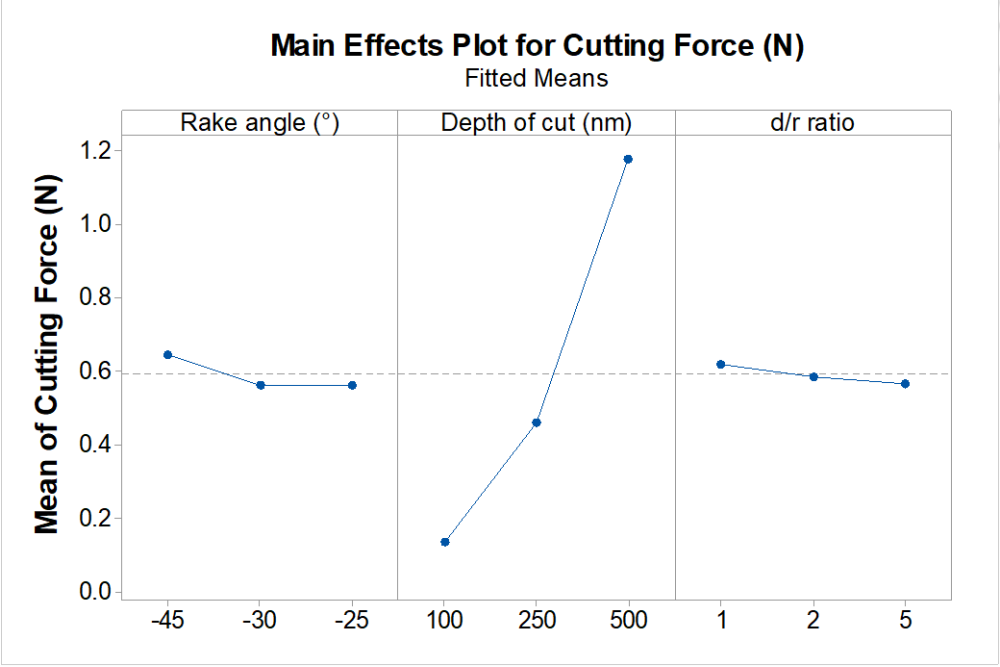

Figure 5.23 Main effect plot of cutting force

From the plots, it can be noted that the depth of cut highly affects the cutting force. This is because with the increase in depth of cut from 100 nm to 500 nm, the volume of the material to be removed increases which leads to increase in cutting force. With the decrease in

negative rake angle from −45° to −30°, the cutting force slightly decreases. This is because, with the increase in negative rake angle, the contact area between the tool and workpiece also increases. This leads to higher frictional force acting at the interface and thus higher cutting force is needed to move the tool along the cutting direction. Finally, with the increase in d/r ratio, the cutting force also decreases. This is due to decrease in cutting edge radius which creates more tensile stress at the cutting zone. Main effect plots clearly show that when the lower value of negative rake angle, depth of cut and higher value of d/r ratio were selected then less cutting force can be obtained.

Interaction effects of tool rake angle and depth of cut on the cutting force are shown in Figure 5.24 (a). It can be inferred that, lesser cutting force can be achieved with a combination of low depth of cut (100 nm) and low negative rake angle tool (−25°). It is obvious that at low depth of cut, the cutting force values are also low. Also, high negative rake angle tool induces more compressive stress compared to low negative tool. Large negative tool also increases the contact surface area. Hence, more cutting force is needed to remove the material.

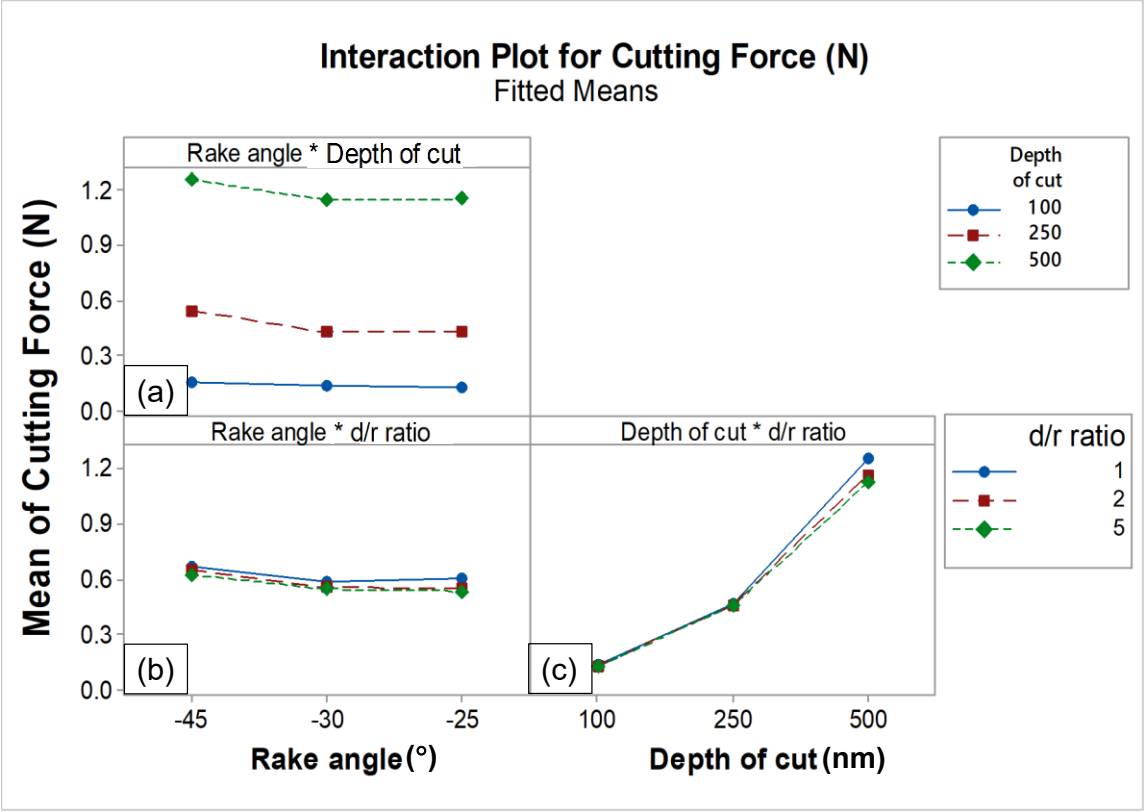

Figure 5.24 Interaction plot for cutting force

Figure 5.24 (b) shows the estimated response plot for cutting force in relation to tool rake angle and d/r ratio. The lower negative rake angle in combination with high d/r ratio is preferred when a low cutting force is desired. Cutting force slightly decreases when the rake angle is reduced from −45° to −25° due to low compressive stress and contact area exerted by

−25º rake angle tool. However, d/r ratio did not show any significant effect on the cutting force. A slight decrease in cutting force was observed with increase in d/r ratio. This is because, for instance, say for a constant rake angle of −45º and depth of cut of 100 nm, d/r ratio of 1, 2 and 5 can be achieved if the cutting edge radius is taken as 100 nm, 50 nm and 20 nm respectively. Higher cutting edge radius increases the effective rake angle more negative, than the nominal rake angle. This increases the cutting force. Figure 5.24 (c) shows the interaction plot of depth of cut and d/r ratio. It can be seen that the cutting force values are low at low depth of cut. It can also be observed that, the d/r ratio has very less significance in determining the cutting force. However, when the depth of cut is high (500 nm), d/r ratio of 1 shows higher cutting force compared to d/r ratio of 5. This is because, at 500 nm depth of cut, the cutting edge radius must be high (~500 nm) to obtain d/r ratio of 1. This creates effective rake angle more negative than the specified rake angle; which increases the cutting force values.

5.5.6.5 ANOVA Analysis of Thrust Force

Similar to the analysis of cutting forces, an analysis of thrust forces has also been carried out. From the model analysis, it was found that the 2-factor interaction (2FI) model is statistically significant for the analysis of thrust force. Table 5.7 presents the ANOVA table for a 2FI model for thrust force. The test for significance of regression and individual model coefficients were obtained. The table also shows the p-values, the significance levels associated with the F-values for each source of variation. It can be observed that, all the model terms are significant except the interaction term of rake angle and d/r ratio. Since, there is only one insignificant model term; no model reduction process was carried out.

Table 5.7 ANOVA table for thrust force

Source	DF	Adj SS	Adj MS	F-Value	P-Value
Model	18	2.52253	0.14014	201.10	0.000
Linear	6	2.40799	0.40133	575.90	0.000
Rake angle (°)	2	0.14635	0.07317	105.00	0.000
Depth of cut (nm)	2	2.18633	1.09316	1568.67	0.000
d/r ratio	2	0.07532	0.03766	54.04	0.000
2-Way Interactions	12	0.11454	0.00954	13.70	0.000
Rake angle (°)*Depth of cut (nm)	4	0.04833	0.01208	17.34	0.001
Rake angle (°)*d/r ratio	4	0.00653	0.00163	2.34	0.142
Depth of cut (nm)*d/r ratio	4	0.05967	0.01492	21.41	0.000
Error	8	0.00557	0.00070		
Total	26	2.52810			

S	R-sq	R-sq(adj)	R-sq(pred)
0.0263984	99.78%	99.28%	97.49%

The value of R^2 and adjusted R^2 were found to be 99.78% and 99.28%, respectively.

5.5.6.6 *Model Fitness Check*

Figure 5.25 shows the normal probability plot of the residuals for thrust force. It can clearly be noted that the residuals are falling on a straight line. The fitted line between predicted and actual values is also falling on a straight line making an angle of 45° with the horizontal axis of observed thrust force (Figure 5.26).

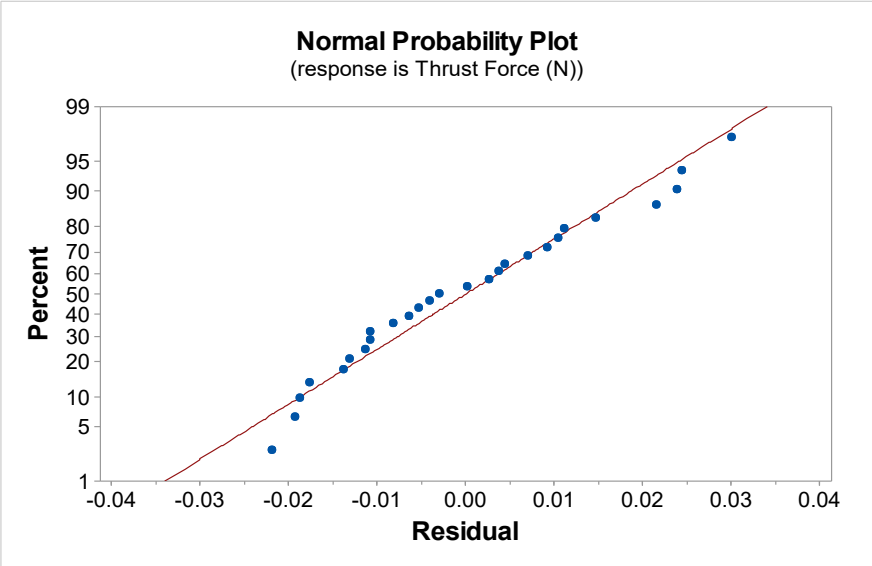

Figure 5.25 Normal plot of residuals for thrust force

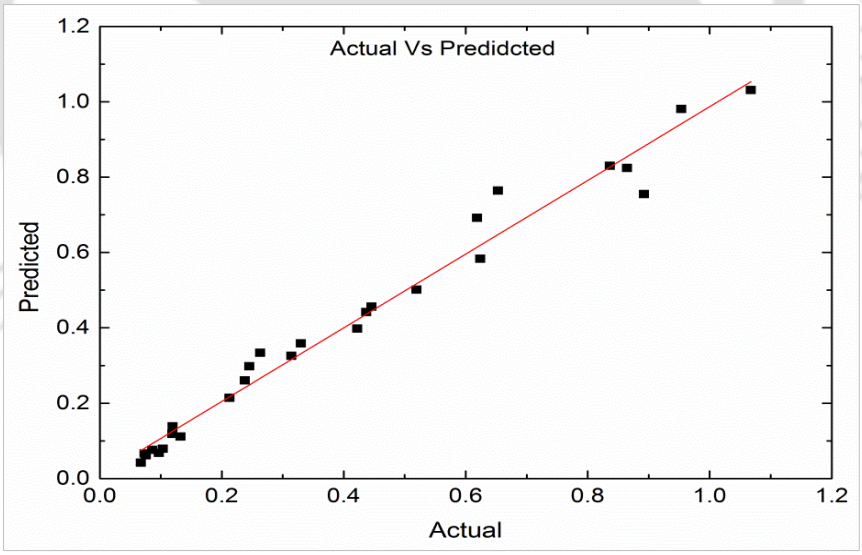

Figure 5.26 Plot of actual vs. predicted response of thrust force

Figure 5.27 shows the plots of the residuals versus the fitted value. It can be seen that, the points are normally distributed along the horizontal zero line indicating that the general full factorial model is able to predict the response accurately since error terms are having mean zero. These plots indicate that the developed models are adequate and are able to predict the results with reasonably good accuracy.

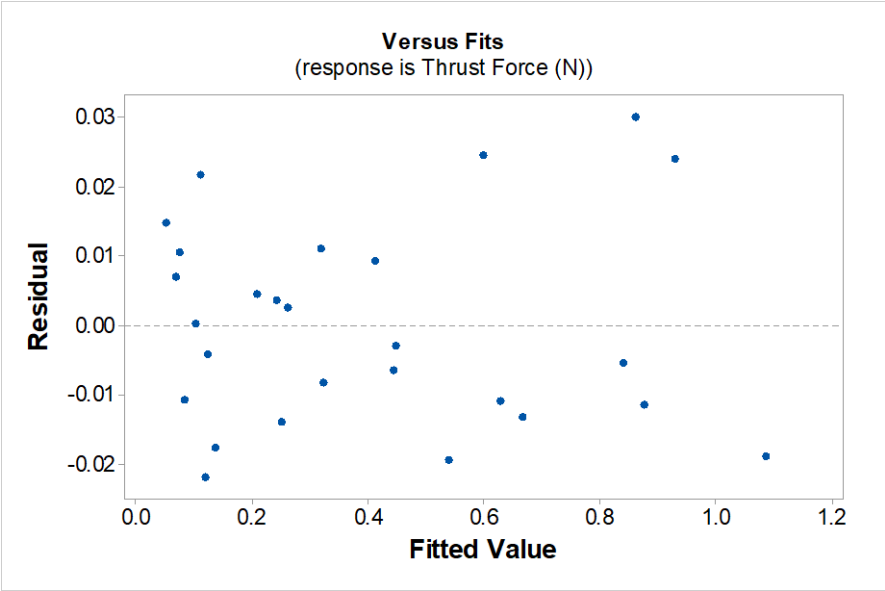

Figure 5.27 Residuals versus fitted value plot of thrust force

5.5.6.7 *Regression Analysis*

Using the regression analysis, a mathematical model was developed in terms of various input parameters and their interactions. This is shown as follows.

$$\begin{aligned} \textit{Thrust Force}\ (N) = {} & -0.076 + 0.00140\times \text{rake angle} + 0.001133 \times \text{depth of cut} - 0.0088\times \text{d/r ratio} \\ & -0.000029 \times \text{rake angle} \times \text{depth of cut} - 0.000660 \times \text{rake angle} \times \text{d/r ratio} \\ & - 0.000142\times \text{depth of cut} \times \text{d/r ratio} \end{aligned} \tag{5.4}$$

5.5.6.8 *Parametric Influence on Thrust Force*

After obtaining the regression equation; a parametric study has been carried out to study the influence of various input process parameters on the thrust force. In view of this, main effect plots are plotted. Figure 5.28 shows the main effects plots for thrust force.

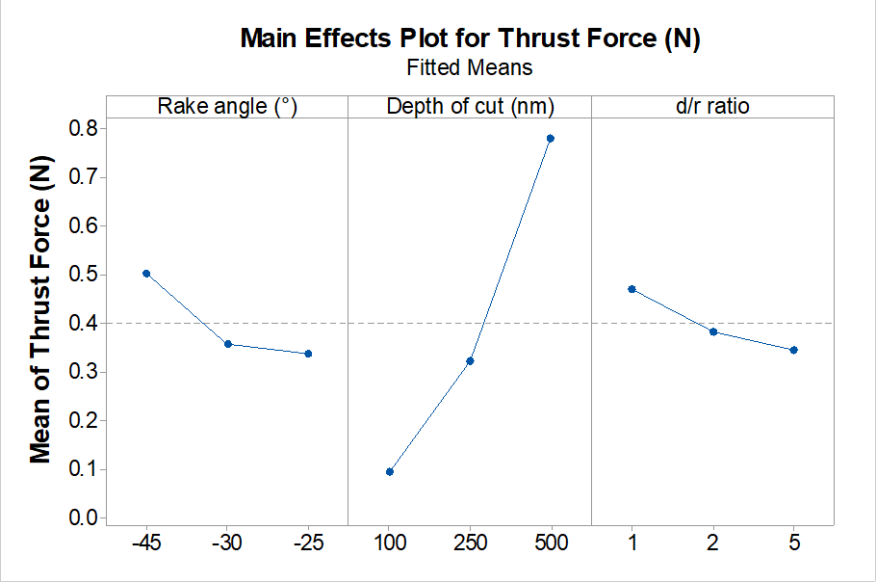

Figure 5.28 Main effect plots of thrust force

It can be seen that the depth of cut has the most significant impact on the thrust force. It is followed by the rake angle and then the d/r ratio. It can also be noted that, increase in the depth of cut increases the thrust force value. It is because as depth of cut increases, the volume of the material to be removed increases. Thrust force increases with the increase in negative rake angle from −25° to −45°. It can be attributed to fact that large negative rake angles increases the contact area between the tool and the workpiece. This leads to higher frictional force acting on to the chip-tool interface; large amount of material to be pushed below the cutting tool; which results in increase in thrust force. For a given depth of cut, the d/r ratio increases if the cutting edge radius decreases. Thus, with the increase in d/r ratio, the thrust force also decreases. This is due to the decrease in cutting edge radius which generates more tensile stress at the cutting zone. It can finally be concluded from the main effect plot that a lower value of negative rake angle, depth of cut and higher value of d/r ratio produce minimum mean thrust force.

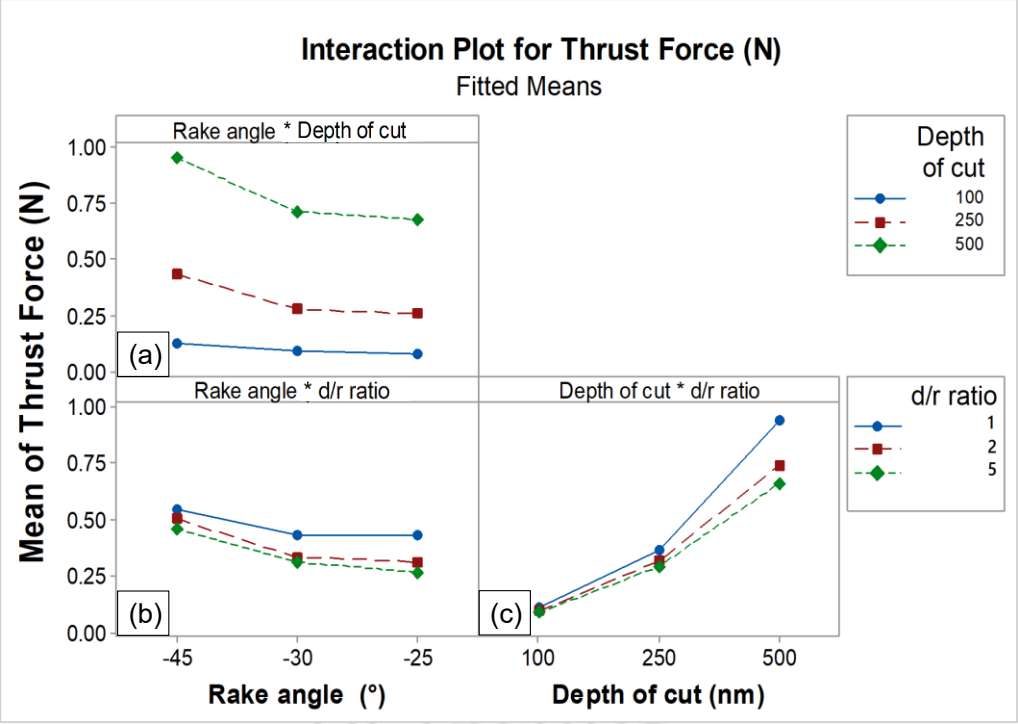

Figure 5.29 Interaction plot for thrust force

Interaction effects of tool rake angle and depth of cut on the thrust force are depicted in Figure 5.29 (a). From the Figure 5.29, it can be inferred that, lesser thrust force can be achieved with a combination of low depth of cut (100 nm) and low negative rake angle tool (−25°). It can also be observed that, at low depth of cut, the rake angle has low effect on the thrust force. Figure 5.29 (b) shows the estimated response plot for thrust force in relation to the tool rake angle and d/r ratio. The low negative rake angle along with high d/r ratio is preferred when lower thrust forces are desired. Figure 5.29 (c) shows the interaction plots for

depth of cut and d/r ratio. From the plots, low depth of cut and high d/r ratio are recommended to achieve low thrust force. It can be seen that, at 100 nm depth of cut, the thrust forces are lowest and almost same for all sets of d/r ratios. With the increase in depth of cut, the cutting edge radius must be increased to achieve the same d/r ratio. Hence, at 500 nm depth of cut, the thrust force slightly increases with the decrease in d/r ratio. This is due to the fact that the cutting edge radius must be decreased to obtain higher value of d/r ratio for a constant depth of cut. However, the amount of decrease in cutting edge radius in the case of lower depth of cut (say 100 nm) is less compared to that of 500 nm depth of cut. To obtain d/r ration from 1 to 2, the cutting edge radius is reduced from 500 nm to 250 nm. This increases the amount of material to be pushed below the cutting tool which results in increase in thrust force.

5.5.7 Confirmation Simulations

After developing the mathematical equations from the regression fits, confirmation tests were carried out. For the tests, the parameters values are chosen from the selected ranges of the parameters (Table 5.4). Three confirmation simulations have been performed. Data obtained from the confirmation simulations and respective computed values of cutting and thrust forces are listed in Table 5.8. It can be observed that full factorial based model predicts the cutting force and thrust force values with maximum percentage error of −17.1% and absolute average error of **8%.**

Table 5.8 Confirmation tests and their comparison with the results

Exp. No.	Machining conditions			Cutting force			Thrust force		
	Rake angle (°)	Depth of cut (*nm*)	d/r ratio (*nm*)	Sim.	Pred.	Error (%)	Sim.	Pred.	Error (%)
1	−40	300	3	0.60	0.66	**−10.0**	0.41	0.48	**−17.1**
2	−35	200	4	0.34	0.37	**−8.8**	0.23	0.25	**−8.7**
3	−25	150	5	0.20	0.21	**−5.0**	0.10	0.10	**0.0**
			Average mean error			**7.93**			**8.57**

After verifying the validity of the regression model, the machining (cutting and thrust) force values for all the 27 simulations were predicted using the regression equation obtained from regression analysis. The comparison of measured and predicted machining forces are shown in Table 5.9 and Figure 5.30. From the Figure 5.30, it is clear that the numerical machining forces and the force values obtained from the derived mathematical expressions are in good agreement. Results show that the average mean percentage error between predicted and numerical computations is about **11.5%** and maximum percentage error is 37%**.**

Table 5.9 FEM simulated and FFA predicted values of cutting and thrust forces

Experiment No.	Cutting force (N)			Thrust force (N)		
	Simulated	Predicted	Mean Error	Simulated	Predicted	Mean Error
1	0.120	0.089	26.17	0.067	0.042	37.28
2	0.125	0.104	16.72	0.073	0.066	9.69
3	0.126	0.086	31.73	0.075	0.062	18.22
4	0.129	0.099	22.92	0.086	0.076	11.85
5	0.133	0.085	35.74	0.097	0.068	29.47
6	0.134	0.098	27.32	0.103	0.079	23.41
7	0.148	0.139	6.21	0.119	0.118	0.64
8	0.154	0.135	12.63	0.120	0.138	−15.63
9	0.157	0.151	3.40	0.133	0.112	15.85
10	0.407	0.447	−9.82	0.213	0.214	−0.77
11	0.412	0.469	−13.81	0.238	0.260	−9.38
12	0.414	0.497	−20.06	0.245	0.298	−21.55
13	0.423	0.477	−12.62	0.263	0.334	−26.89
14	0.438	0.486	−11.04	0.314	0.326	−3.71
15	0.442	0.506	−14.48	0.330	0.358	−8.70
16	0.529	0.564	−6.58	0.422	0.398	5.83
17	0.543	0.557	−2.65	0.437	0.442	−1.10
18	0.548	0.537	1.98	0.446	0.456	−2.45
19	1.082	1.043	3.57	0.519	0.501	3.46
20	1.105	1.078	2.46	0.619	0.692	−11.82
21	1.110	1.127	−1.52	0.624	0.584	6.48
22	1.128	1.159	−2.77	0.653	0.764	−17.05
23	1.173	1.181	−0.61	0.836	0.830	0.76
24	1.187	1.186	0.09	0.865	0.824	4.67
25	1.246	1.155	7.30	0.892	0.755	15.36
26	1.254	1.255	−0.07	0.954	0.981	−2.86
27	1.322	1.279	3.20	1.068	1.031	3.43
	Average mean error		**11.02**			**11.42**

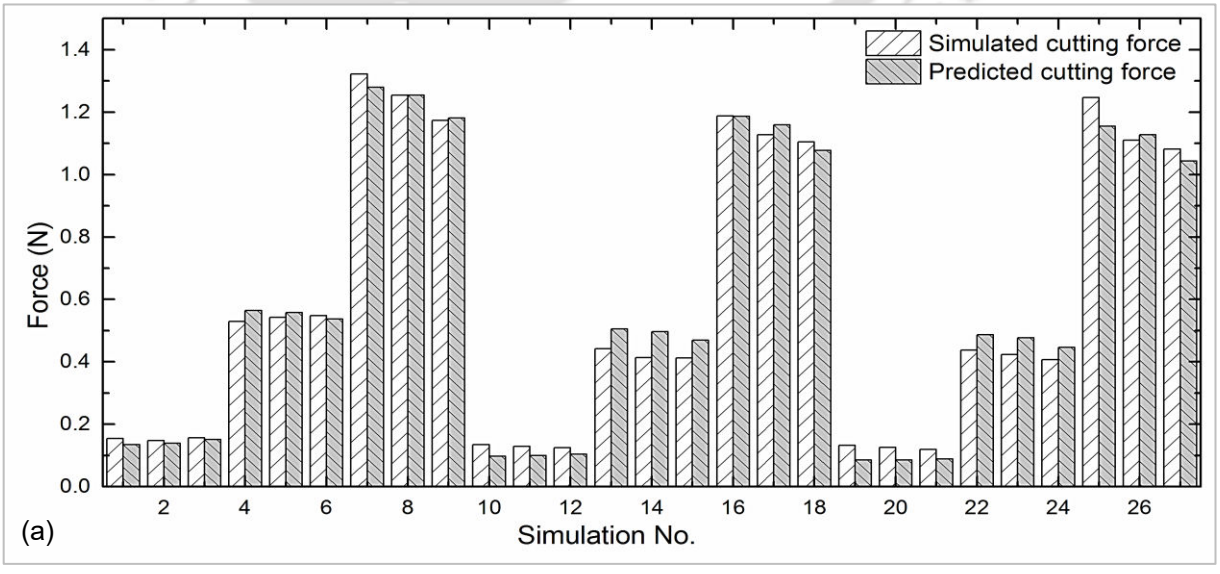

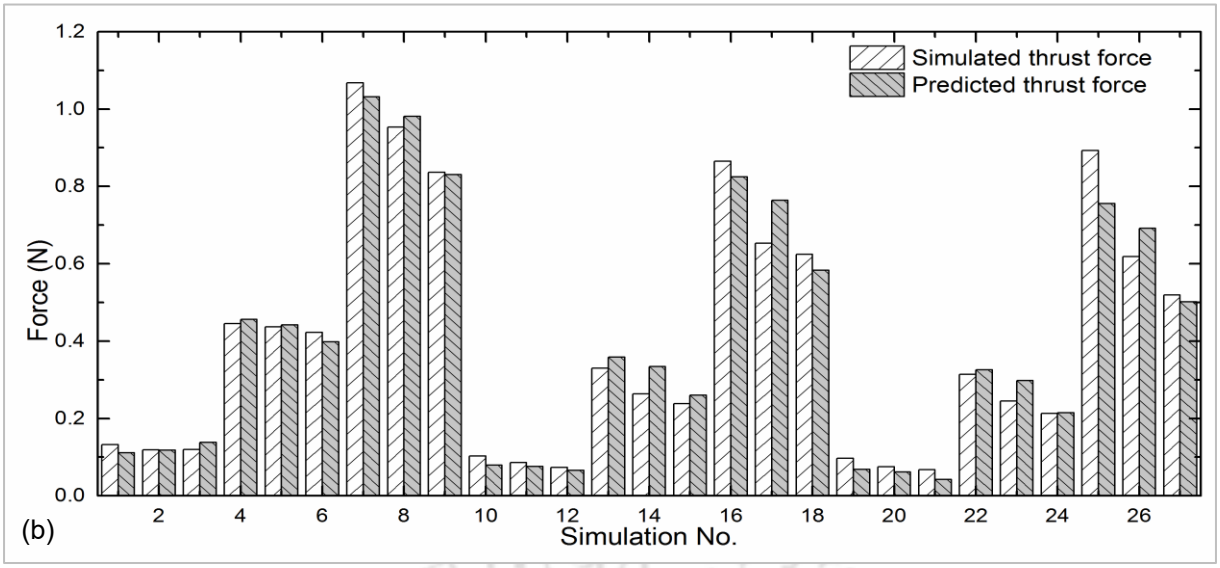

Figure 5.30 Numerically determined and predicted values of (a) cutting force and (b) thrust force

5.5.8 Multi-Objective Optimization of Machining Forces using FFA

After the development of numerical model and regression equations, it was decided to optimize the process conditions to obtain optimum machining forces which will help to reduce the power consumption. Two performance parameters viz. cutting force and thrust force were considered. Though, both of these are preferred to be as low as possible; in nanometric cutting, they are highly conflicting in nature. This confliction arises when the effective rake angle changes from positive to negative or d/r ratio changes. In ductile mode cutting when the depth of cut is below the critical depth of cut, thrust force become higher than the cutting force. However, at higher depth of cut, material removal switches from ductile to brittle mode and thrust force becomes lower than the cutting force. Higher thrust force compared to cutting force is necessary for obtaining ductile mode material removal.

In view of a productive and efficient SPDT operation of silicon carbide, the objective is to minimize the machining forces by determining the optimum values of machining parameters. For obtaining the desired process performance, desirability function (d) analysis associated with FFA was used for obtaining the optimal machining parameters. The desirability function considers that the quality of a product or process is accepted unless and until all of its features are in the "desirable" limit [Candioti *et al.* (2014)]. The scale of the desirability function ranges between 0 and 1. If $d = 0$ or approaches 0, then the response is completely unacceptable and if $d = 1$ or approaches to 1, then the response is perfectly on the target value. There are three types of individual desirability functions: a) the larger the better, b) the smaller the better and c) the nominal the better. In this study, the smaller the better was

considered because minimum machining forces are to be achieved with optimum process parameters.

Table 5.10 shows the optimum process parameters and corresponding performance parameters. Figure 5.31 shows the plots of optimum parameters. It can be recommended that, for minimum machining forces, a set of process conditions, viz. rake angle of −25°, depth of cut of 100 nm and d/r ratio of 5 are to be employed in practice to produce ultra-precision surfaces using SPDT with minimum cutting and thrust forces. The respective cutting force and thrust force values are 0.089 N and 0.0.42 N with desirability values of 1.

Table 5.10 Response optimizations for cutting force and thrust force parameters

Parameters	Goal	Optimum conditions			Target	Upper	Predicted response	Desirability
		Rake angle (°)	Depth of cut (*nm*)	d/r ratio				
Cutting Force	Min	−25	100	5	0.12	1.32	0.089	1
Thrust Force	Min	−25	100	5	0.07	1.07	0.042	1

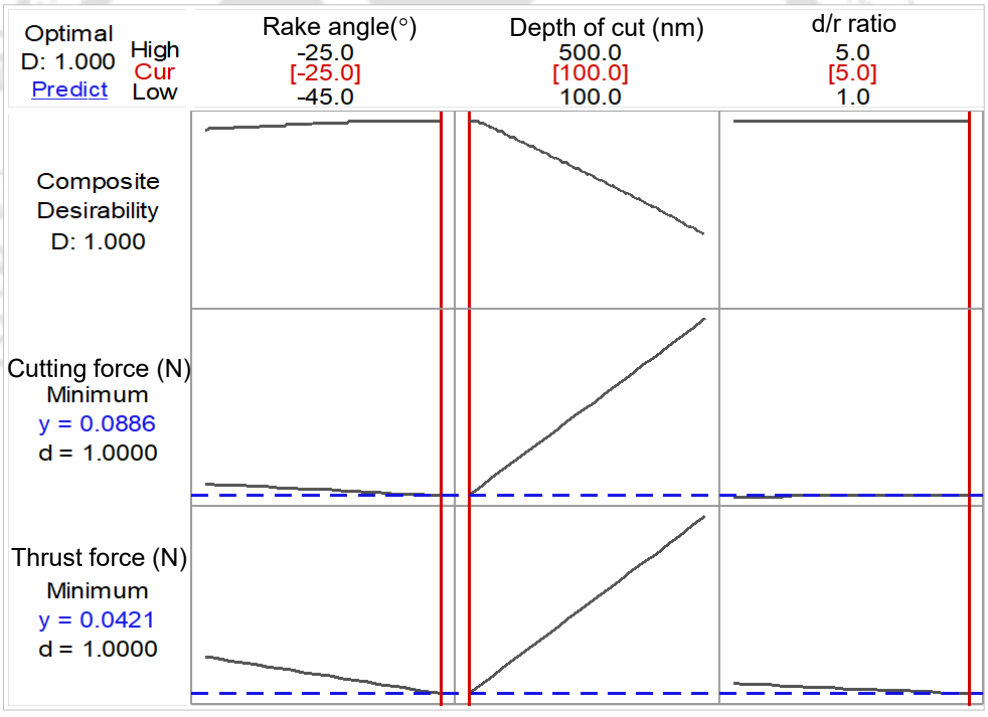

Figure 5.31 Optimization of cutting and thrust forces

Figure 5.31 shows the plots of variation of cutting and thrust forces with the process parameters viz. rake angle, depth of cut and d/r ratio. The columns of the graph correspond to process parameters. The rows of the graph correspond to the responses. Each cell of the graph shows how the response changes as a function of one of the factors, when the other factors remain fixed. The numbers displayed at the top of a column show the current factor level, and high and low levels of the parameters used in the model. The current optimal parameter set

was: rake angle of −25°, depth of cut of 100 nm and d/r ratio of 5 and corresponding minimum cutting force and thrust force are shown. The composite desirability (D) is displayed at the upper left corner of the graph. The label above composite desirability refers to the current setting and changes interactively with the parameter settings. The vertical red lines inside the graph represent current optimal parametric settings and the horizontal dotted blue lines represent the current response values. Moreover, prediction of surface roughness can also be done for any parameters using response optimizer plot in Minitab (Figure 5.31). Here, the plot is interactive and the blue and red lines on the plots can be moved to set any combination of process condition and corresponding machining forces can be predicted.

In addition to SiC, an industrial important material has also been tried and numerical simulations were carried out. In what follows, the numerical simulations carried out for Si are presented in details.

5.6 Numerical Simulation and Experimental Validation of SPDT of Silicon

Numerical simulations on silicon were carried out in similar fashion as of SiC (Section 5.4). Following sections describe the key results obtained from the study.

5.6.1 Experimental Validation of Machining Simulation of Silicon

For the validation of numerical force results of silicon, experimental results from Patten and Gao [Patten and Gao (2001)] were used and simulations were performed according to the process conditions given. Based on the tool geometry, two cutting conditions were considered for the validation. These are listed in Table 5.11.

Table 5.11 Cutting tool geometry during machining of silicon

Set	Rake angle [°]	Clearance angle [°]	Cutting edge radius [nm]
1	−45	5	40
2	−85	45	40

The force values viz. cutting force and thrust force against step time or cutting length are extracted at the reference point of the tool. Figure 5.32 (a) and (b) show the comparison between the predicted cutting and thrust forces with the experimental results reported by Patten and Gao [Patten and Gao (2001)].

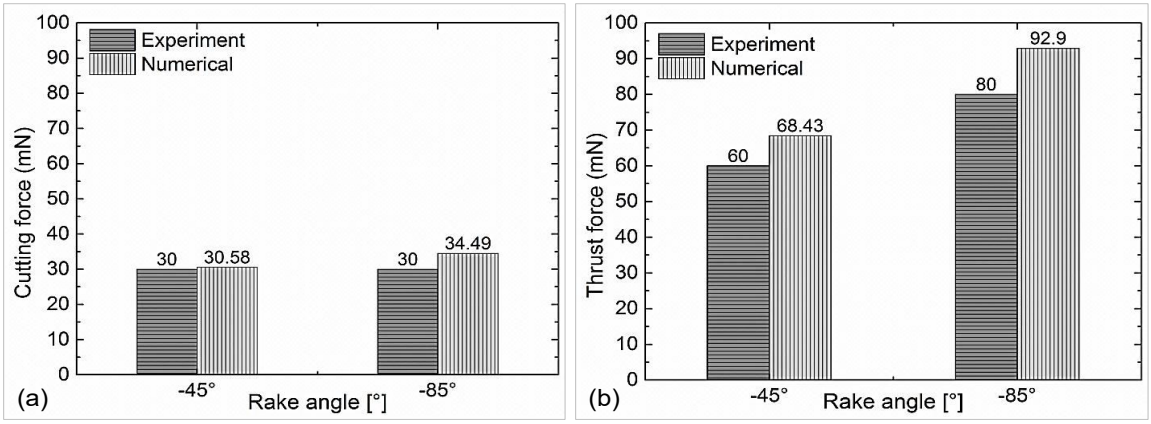

Figure 5.32 Comparison of experimental and numerical results of silicon

From Figure 5.32, it can be observed that our model prediction fairly match with the experimental results, however our numerical model over predicts the forces [Patten and Gao (2001)]. This may be due to various simplifying assumptions such as work piece material is isotropic and homogeneous; cutting is considered as perfectly orthogonal. The absolute percentage errors for cutting force and thrust force with −45° and −85° rake angles are 1.93, 14.96, 14.05 and 16.13% respectively. The mean absolute error was found to be 11.76%. The trend of variation of thrust force with increase in rake angle is noted to match well with the experimental results. The time taken for one simulation was around 5 min by using a quad core processor at 3.6 GHz speed and 8GB RAM.

5.6.2 Formation of Chips during SPDT of Silicon

Figure 5.33 shows a graphical representation of the highly stressed zone that resulted in ductile machining of brittle materials for a typical process condition of rake angle −5°, clearance angle 5°, cutting edge radius 60 nm, cutting speed 1 mm/min, and depth of cut 50 nm.

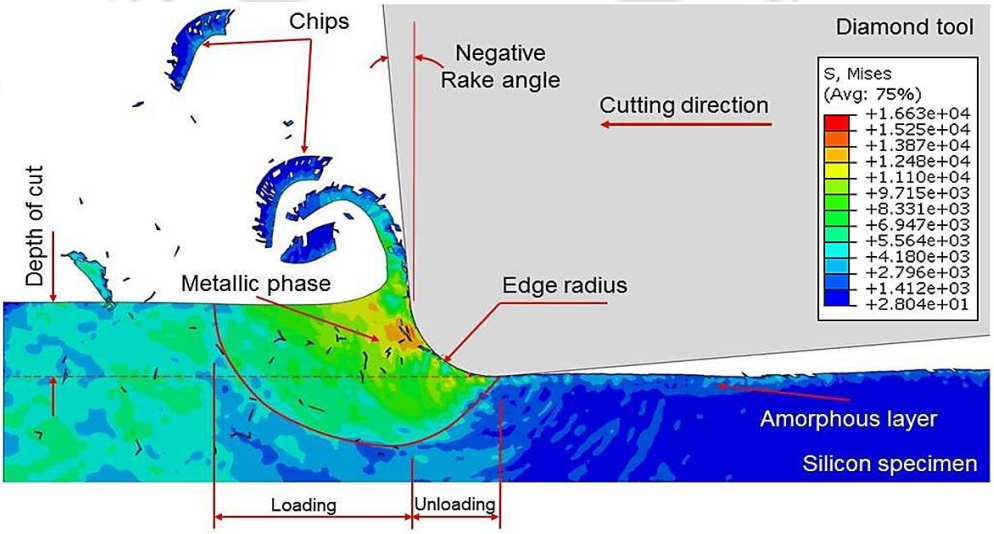

Figure 5.33 Formation of ductile chips with stress zones during SPDT of silicon

From the nanoindentation simulation, it was noted that if the brittle material experiences sufficient compressive stress, i.e., hydrostatic pressure, it undergoes phase change. The hydrostatic stress can be generated by using negative effective rake angle. To obtain this, either the tool with negative rake angle is to be employed or depth of cut should be sufficiently smaller than the cutting edge radius of the tool. Thus, negative rake angle tools are mostly preferred while machining brittle materials as they produce large compressive stress. When this stress exceeds the fracture limit, cracks and brittle fracture occurs. From the previous studies, it was observed that when the undeformed chip thickness is very small (much smaller than the cutting edge radius); effective rake angle is more negative irrespective of the rake angle. Due to which compressive stress acts on the workpiece which changes the crystalline phase of work material to metallic phase. If the compressive stress reaches a threshold value, it is responsible for the ductile mode behavior of brittle material and helps in removing material by plastic deformation instead of brittle fracture. When the tool moves further along the cutting direction, pressure on the workpiece behind the tool drops and amorphous layer is generated. As the depth of cut keep on increasing and becomes larger than the cutting edge radius, tensile stress starts developing in the cutting zone and initiates a crack to propagate. Then the material starts flowing over the rake face of the tool. During the process, the chip thickness reduces compared to undeformed chip thickness as some amount of material is forced to flow below the tool tip. The cracks that formed in front of the cutting tool will be removed along with the chip; however the cracks that penetrate the work surface below the undeformed chip thickness will remain on the machined surface.

5.6.3 Ploughing/Rubbing

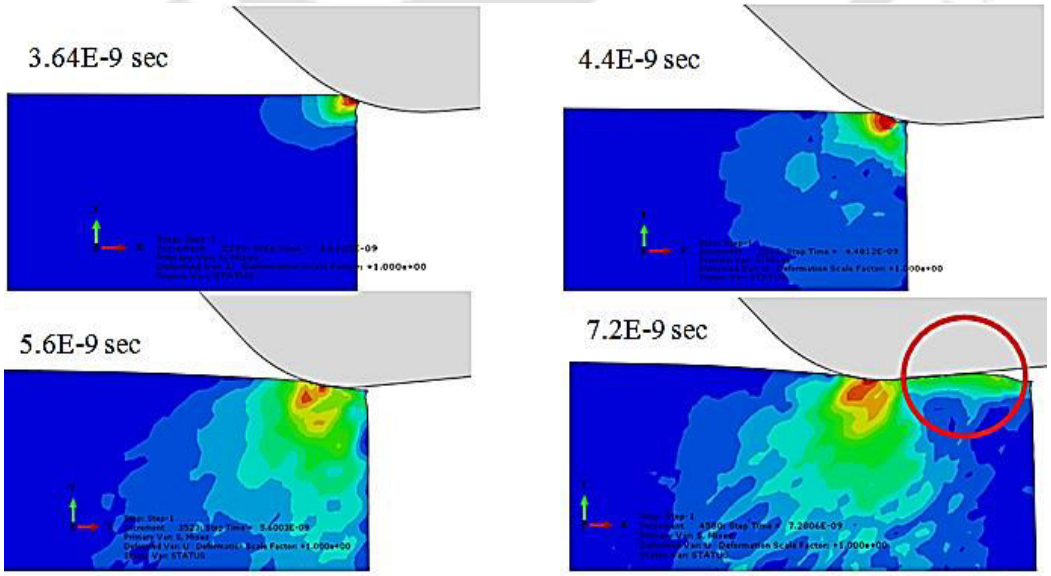

Figure 5.34 Rolling/ploughing action during machining (5nm depth of cut)

Figure 5.34 represents primary von-Mises stresses that present the rolling/ploughing action (encircled in red colour) and spring back effect during machining at a very low depth of cut, higher edge radius and extreme negative rake angle. This effect can be understood with the help of nanoindentation process. Since the depth of cut is very small (5 nm) and cutting edge radius is large (40 nm), the diamond tool acts as an indenter rather than a cutter. The tool compresses the workpiece material due to which elastic and plastic deformation occurs. Elastically deformed material causes expansion and the consequent elastic recovery of the machined surface after the tool passes.

During machining simulation of silicon (40 nm cutting edge radius, 20 µm/min cutting speed and 5 nm depth of cut), it was observed that SPDT becomes rolling/ploughing process due to the application of too small depth of cut and extreme negative rake angle (−45º and −85º). This rolling zone is also called as 'zero cutting zone' within which no chips are produced [Uddin *et al.* (2007)]. In this zone, the tool acts more like a roller than a cutter and continuously slides on and it burnishes the machined silicon surface. A small amount of spring back effect can be seen in Figure 5.34 (red round) which depicts the rolling action. Our numerical findings verify the facts which are already observed by other researchers [Fang *et al.* (2007)]. Thus, the comparative study and observations gave the confidence to employ this numerical model for detailed parametric analysis of SPDT of silicon.

5.6.4 Parametric Analysis of SPDT of Silicon using Response Surface Methodology

After the validation of our developed model for silicon, parametric analysis has been carried out using response surface methodology (RSM). Similar methodologies and procedures have been followed for ANOVA, regression analysis during parametric analysis of silicon as described in section 5.5.3 for silicon carbide. Therefore, only key observations are discussed in the following sections.

5.6.5 Response Surface Methodology

Response surface methodology is a combination of mathematical and statistical techniques that are required for modeling and analysis of real-life problems in which a response of interest that is influenced by several variables [Bradley (2007)]. RSM has been widely applied to various industries, such as chemical engineering, semiconductors, electronics manufacturing, machining, and metal cutting because of its practicability, favorable efficiency, and ease of implementation [Jou *et al.* (2014)]. RSM is developed by Box and Draper in the year 1987 with the objective to predict and optimize the response. It is a sequential experimentation strategy for characterization and optimization of any process. It

creates a model of the response to the independent input variable by applying regression analysis to the experimental results. A near optimal point can then be deduced based on the model of the response. In RSM, the relationship between the response and the independent process parameters in quantitative form can be represented as [Kansal *et al.* (2005)]:

$$R = f(P_1, P_2, P_3, \ldots \ldots P_n) \pm \varepsilon \tag{5.5}$$

where, R is the response, f is the response function, ε is the experimental error, and P_1, P_2, P_3, ……, P_n are independent parameters. R is plotted to get the response surface. Since the form of f is unknown; therefore, RSM approximates the f by a suitable lower ordered polynomial in some region of the independent process variables. The objective of using RSM is not only to investigate the response over the entire factor space, but also to locate the region of interest where the response reaches its optimal or near optimal value. Careful study of the response surface model provides the combination of factors giving best response. For the detailed literature regarding RSM can be referred to Hill and Hunter (1966).

5.6.6 Parametric Analysis of SPDT of Si using FEM and RSM

Figure 5.35 shows the overall approach of the developed integrated FEM-RSM based numerical model for the parametric analysis of SPDT process of silicon. Cutting speed, rake angle, depth of cut and tool edge radius were the input process parameters that were fed to the numerical simulation. A set of numerical simulations were performed using response surface methodology (RSM) and the response variables, viz. cutting and thrust force were recorded. Then, the regression and ANOVA analysis were carried out, and results have been presented.

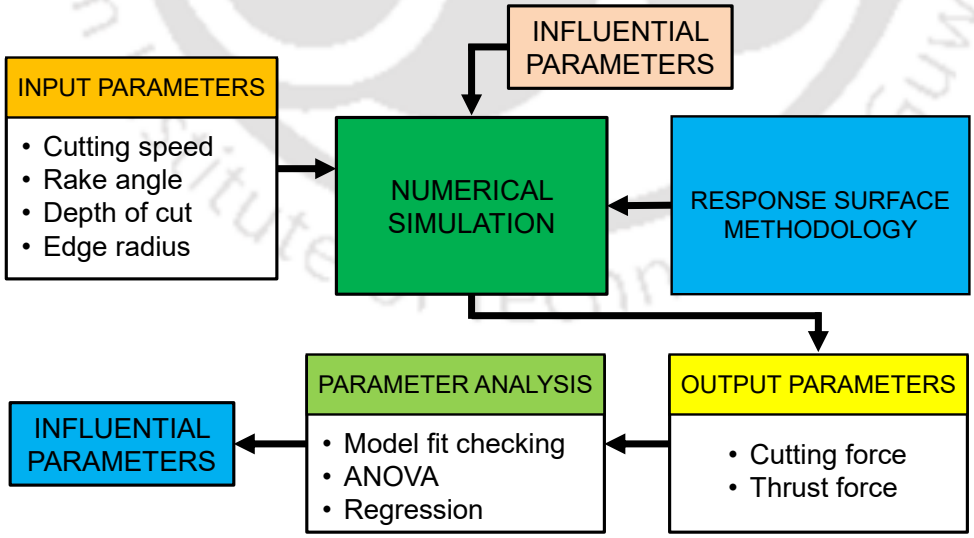

Figure 5.35 Parametric analysis of SPDT of silicon using FEM and RSM

5.6.7 Selection of Machining Parameters and their Importance

In the present study, cutting speed, tool rake angle, depth of cut (sometimes referred to as feed for a 2D analysis [Patten and Jacob (2008)] and tool edge radius have been considered as input process variables. The process variables with their units (and notations) are listed in Table 5.12. The working ranges of these parameters have been selected based on the reported research and trade literature [Patten and Gao (2001), Yan *et al.* (2003), Cardenas *et al.* (2007)].

Table 5.12 Process variables and their levels

Parameters	Units	Code	Low	Central	High
Cutting speed	mm/min	A	0.1	0.5	1.0
Rake angle	(°)	B	−5	−25	−45
Depth of Cut	nm	C	10	30	50
Edge radius	nm	D	20	40	60

FEM-based numerical simulations were carried out using RSM central composite design which consists of 30 combinations of spindle speed, rake angle, depth of cut and edge radius. These 30 runs have 2 blocks and face-centered alpha value. The experimental design is shown in Table 5.13 (all factors are in actual form) with the corresponding response variables, i.e., cutting force, and thrust force obtained from the simulations.

Table 5.13 Experimental matrix and results for the SPDT performance characteristics

Std order	Process parameters				Simulated values	
	Speed (mm/min) A	Rake angle (°) B	Depth of cut (nm) C	Edge radius (nm) D	Cutting force (N)	Thrust Force (N)
1	0.10	−5.00	10.00	20.00	0.25	0.26
2	1.00	−5.00	10.00	20.00	0.16	0.14
3	0.10	−45.00	10.00	20.00	0.25	0.24
4	1.00	−45.00	10.00	20.00	0.17	0.15
5	0.10	−5.00	50.00	20.00	1.02	0.52
6	1.00	−5.00	50.00	20.00	0.92	0.42
7	0.10	−45.00	50.00	20.00	1.18	0.96
8	1.00	−45.00	50.00	20.00	1.02	0.85
9	0.10	−5.00	10.00	60.00	0.26	0.36
10	1.00	−5.00	10.00	60.00	0.28	0.43
11	0.10	−45.00	10.00	60.00	0.27	0.38
12	1.00	−45.00	10.00	60.00	0.29	0.46
13	0.10	−5.00	50.00	60.00	1.05	0.75

14	1.00	−5.00	50.00	60.00	1	0.72
15	0.10	−45.00	50.00	60.00	1.19	1.05
16	1.00	−45.00	50.00	60.00	1.09	1.01
17	0.55	−25.00	30.00	40.00	0.64	0.5
18	0.55	−25.00	30.00	40.00	0.64	0.5
19	0.55	−25.00	30.00	40.00	0.64	0.5
20	0.55	−25.00	30.00	40.00	0.64	0.5
21	0.10	−25.00	30.00	40.00	0.84	0.68
22	1.00	−25.00	30.00	40.00	0.65	0.52
23	0.55	−5.00	30.00	40.00	0.65	0.5
24	0.55	−45.00	30.00	40.00	0.62	0.63
25	0.55	−25.00	10.00	40.00	0.25	0.31
26	0.55	−25.00	50.00	40.00	0.97	0.65
27	0.55	−25.00	30.00	20.00	0.67	0.45
28	0.55	−25.00	30.00	60.00	0.62	0.65
29	0.55	−25.00	30.00	40.00	0.64	0.5
30	0.55	−25.00	30.00	40.00	0.64	0.5

5.6.8 Analysis of Results and Discussion

For analysis of the data, the adequacy of model was checked by using analysis of variance (ANOVA). The ANOVA was employed to study the effect of input parameters on the machining force. Table 5.14 presents the statistical parameters for the model of cutting force. It suggested that both quadratic model and cubic model are appropriate for the parametric analysis because the model has very low standard deviation and the residual-squared (R^2) near to 1. Therefore, the quadratic model was chosen for further investigation.

Table 5.14 Summary of statistical parameters of cutting force (CF)

Source	Std. Dev.	R^2	Adj. R^2	Predicted R^2	PRESS	
Linear	0.054	0.9773	0.9735	0.9635	0.11	
2FI	0.0493	0.9857	0.9777	0.9714	0.0873	
Quadratic	0.0397	0.9928	0.9855	0.9622	0.1153	Suggested
Cubic	0.0085	0.9999	0.9993	0.9533	0.1426	Aliased

5.6.8.1 ANOVA Analysis of Cutting Force

Table 5.15 shows the ANOVA analysis for cutting force. From the table, it can be seen that the factors A (Cutting speed), B (Rake angle), C (Depth of Cut), D (Edge radius), interaction effect of factor B (rake angle) with factor C (Depth of Cut) and second order term of factor A (Cutting speed) are significant. The other model terms can be considered as insignificant. The coefficient of determination (R^2) value of 0.993 indicates that the model

explains 99.3% of the total variations of response while the value of R^2 (Adj.) as 0.986 indicates that the model can predict 98.6% of the total variations of response after considering the significant factors. R^2 (Pred.) of 0.962 is in good agreement with the R^2 (Adj.) and shows that the model would be expected to predict 96.2% of the variability in new data. To fit the quadratic model of cutting force, insignificant terms are eliminated by backward elimination process, and the model terms were recomputed. After this, the reduced model results indicated that the model is significant with R^2 value of 99.18% and adjusted R^2 value of 98.79%.

Table 5.15 ANOVA for cutting force (before elimination)

Source	Sum of Squares	DOF	Mean Square	F Value	p-value (Prob>F)	
Model	3.028	14	0.216	136.990	< 0.0001	significant
A	0.030	1	0.030	18.753	0.0007	
B	0.013	1	0.013	8.449	0.0115	
C	2.928	1	2.928	1854.854	< 0.0001	
D	0.009	1	0.009	5.916	0.029	
AB	0.001	1	0.001	0.396	0.5393	
AC	0.005	1	0.005	3.104	0.0999	
AD	0.006	1	0.006	4.054	0.0637	
BC	0.013	1	0.013	8.377	0.0118	
BD	0.000	1	0.000	0.016	0.9016	
CD	0.000	1	0.000	0.253	0.6225	
A^2	0.020	1	0.020	12.806	0.003	
B^2	0.001	1	0.001	0.693	0.4192	
C^2	0.005	1	0.005	3.367	0.0879	
D^2	0.000	1	0.000	0.186	0.6728	
Residual	0.022	14.00	0.002			
Lack of Fit	0.022	10.00	0.002			
Pure Error	0.000	4.00	0.000			
Cor Total	3.050	29				
Std. Dev.	0.040		R^2	0.993		
Mean	0.650		Adj R^2	0.986		
C.V. %	6.110		Pred R^2	0.962		
PRESS	0.115		Ad eq Prec	34.731		

5.6.8.2 Model Fitness Check

Figure 5.36 shows the normal probability distribution of the residuals for cutting force.

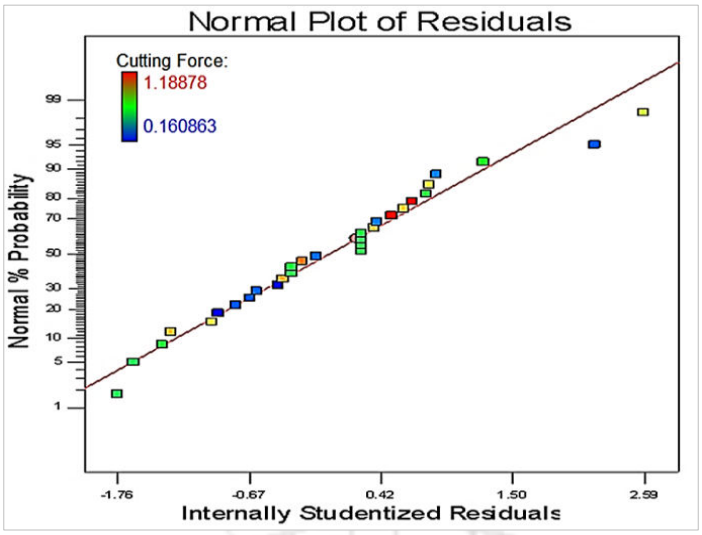

Figure 5.36 Normal plot of residuals for cutting force

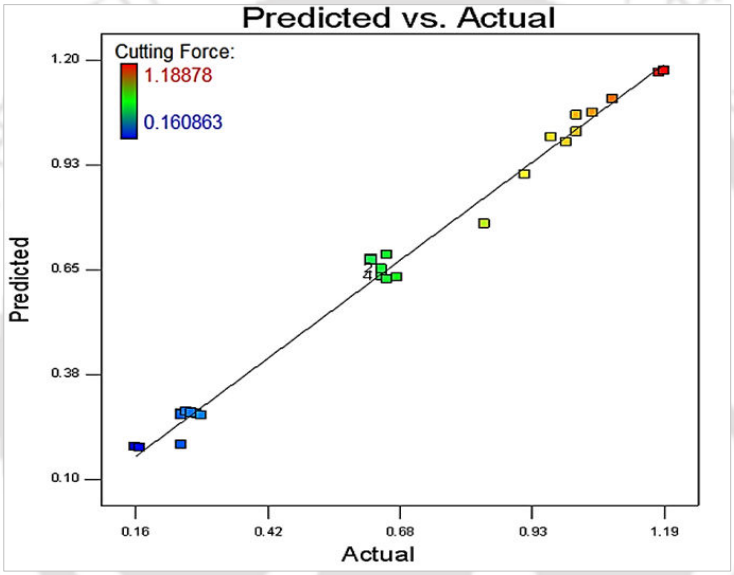

Figure 5.37 Plot of actual vs. predicted response of cutting force

It can be noticed that the residuals are falling on a straight line, which means that the errors are normally distributed. Further, the observed values are compared with the predicted values computed from the developed RSM model. This comparison is shown in Figure 5.37. It can be seen that the points are normally distributed along the straight line indicating that the RSM model is able to predict the response accurately. In other words, the regression model is well fitted with the observed values.

5.6.8.3 Regression Analysis

After eliminating the non-significant terms, the final response equation for cutting force is given as follows (equation 5.4):

$$\textit{Cutting force} = +0.064 - 0.542 \times S - 7.951E\text{-}04 \times R + 0.028 * D - 8.333E\text{-}05 \times E - 1.944E\text{-}03 \times S \times D + 2.222E\text{-}03 \times S \times E + 7.188E\text{-}05 \times R \times D + 0.383 \times S^2 - 1.434E\text{-}04 \times D^2 \quad (5.6)$$

where, *S, R, D, E* are cutting speed, rake angle, depth of cut and cutting edge radius respectively.

5.6.8.4 Parametric Influence on Cutting Force

The main effect plots of machining parameters are shown in Figure 5.38.

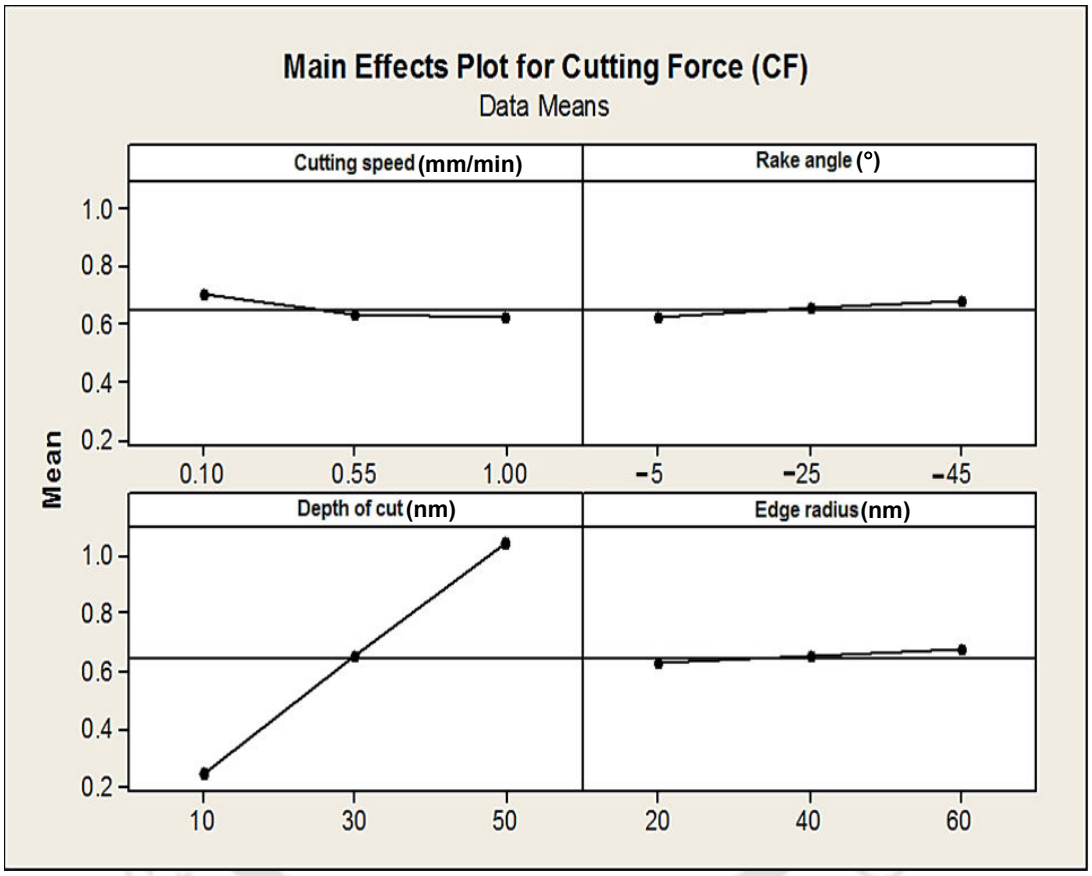

Figure 5.38 Main effect plots for cutting force

Figure 5.39 shows the estimated response contour plots for cutting force with respect to the possible combinations of design parameters. In each graph, *x* and *y* axes represent the combinations of process parameters whereas the shaded green surface/area represents value/range of cutting force. The legend in the right side corner shows the respective ranges of cutting force.

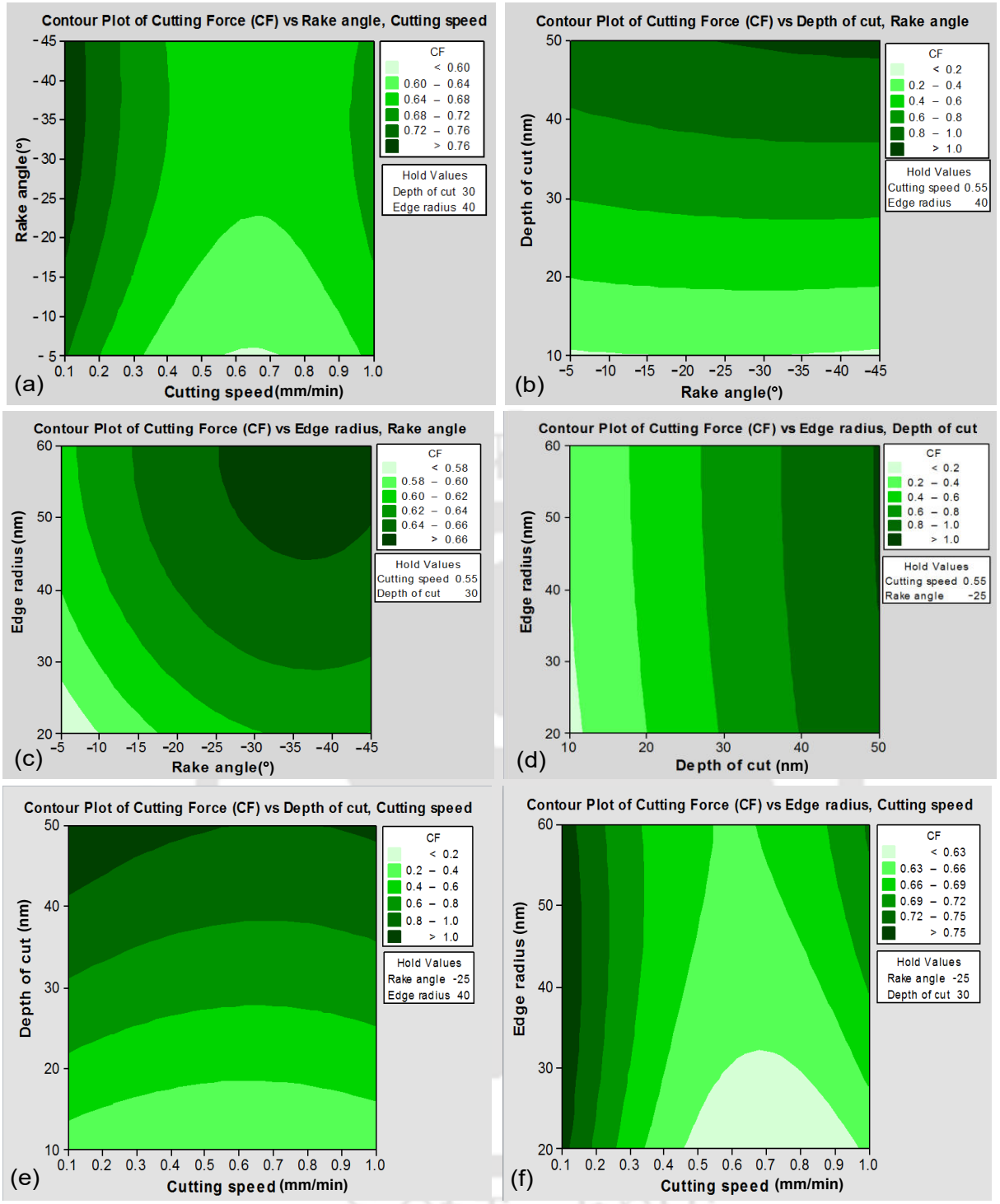

Figure 5.39 Contour plot for cutting force

Based on the above graphs, the observations were noted and tabulated in the Table 5.16.

Table 5.16 Observations on the effect of process parameters on cutting forces

Figure	Observations
5.39 (a)	It can be seen that the cutting force increases with the increase in negative rake angle and decreases with the increase in cutting speed. It can also be noted that cutting force is minimum when rake angle is around −5°, and cutting speed is in between 0.6 to 0.7 mm/min. This may be due to the fact that when negative rake angle is used, the material accumulation rate in front of the rake surface and below the tool tip is more in comparison with the material removal rate of the process.
5.39 (b)	It is observed that the cutting force increases with the increase in depth of cut. However increase in the rake angle up to 30 nm depth of cut does not show any significant effect on the cutting force value. This is because below 30 nm depth of cut, increase in the rake angle does not affect the effective rake angle. But when depth of cut is high (i.e. ≥ 30 nm), there is increase in cutting force with the increase in negative rake angle. This may be due to fact that at higher depth of cut, the chips are formed due to material shearing and the cut work material touches the rake face which increases the cutting forces.
5.39 (c)	It is seen that cutting force increases with the increase in rake angle as well as increase in edge radius. This may be due to the fact that when the edge radius is higher than the depth of cut, the effective rake angle becomes even more negative.
5.39 (d) and (e)	These figures show the well-known fact that increase in depth of cut leads to increase in the cutting force. However, for constant values of depth of cut, no significant effect of increase in edge radius on cutting force is observed (Figure 5.39 (d)).
5.39 (e) and (f)	Increase in the cutting speed decreases the cutting force value for the edge radius value of about 30 nm. Above 30 nm of edge radius, effective rake angle changes and cutting force decreases up to a certain point and then increases. This may be due to the fact that increase in cutting speed reduces the friction between tool and work piece surface. But, as the cutting speed exceeds 0.8 mm/min, the work material accumulates more in-front of rake face and below the tool tip. This leads to increase in the value of cutting force.

5.6.8.5 ANOVA Analysis of Thrust Force

Table 5.17 presents the ANOVA table for a 2FI model for thrust force. For thrust force, the model summary recommends that the 2-factor interaction (2FI) model is statistically significant for the analysis.

Table 5.17 ANOVA table for thrust force (before elimination)

Source	Sum of Squares	DOF	Mean Square	*f*-Value	Prob > *f*	
Model	1.4735	10	0.1473	50.6894	< 0.0001	significant
A	0.0139	1	0.0139	4.7780	0.0423	
B	0.1476	1	0.1476	50.7785	< 0.0001	
C	0.9800	1	0.9800	337.1345	< 0.0001	
D	0.1840	1	0.1840	63.3064	< 0.0001	
AB	0.0000	1	0.0000	0.0086	0.9271	
AC	0.0030	1	0.0030	1.0406	0.3212	
AD	0.0156	1	0.0156	5.3752	0.0324	
BC	0.1260	1	0.1260	43.3545	< 0.0001	
BD	0.0030	1	0.0030	1.0406	0.3212	
CD	0.0002	1	0.0002	0.0774	0.784	
Residual	0.0523	18	0.0029			
Lack of Fit	0.0523	14	0.0037			
Pure Error	0	4	0			
Cor Total	1.5259	29				
Std. Dev.	0.0539		R^2	0.9657		
Mean	0.5363		Adj R^2	0.9467		
C.V. %	10.0526		Pred R^2	0.8941		
PRESS	0.1616		Adeq Prec.	26.5567		

The value of R^2 and adjusted R^2 are found to be 96.57% and 94.67%, respectively. In this case, factors A, B, C, D; interaction effect of factor A with factor D, interaction effect of factor B with factor C are significant model terms. The other model terms are said to be insignificant. In order to fit the 2FI model for thrust force appropriately, the insignificant terms are eliminated by backward elimination process. The reduced model results indicate that the model is significant with R^2 value of 96.16% and adjusted R^2 value of 95.11%.

5.6.8.6 Model Fitness Check

Figure 5.40 shows the normal probability plot of the residuals for thrust force. It can be noted that the residuals are falling on a straight line, which means that the errors are normally distributed. Further, each observed value is compared with the predicted value computed from the model. Figure 5.41 shows the plots of actual vs. predicted responses. It can be obsereved that the regression model fits well with the observed values.

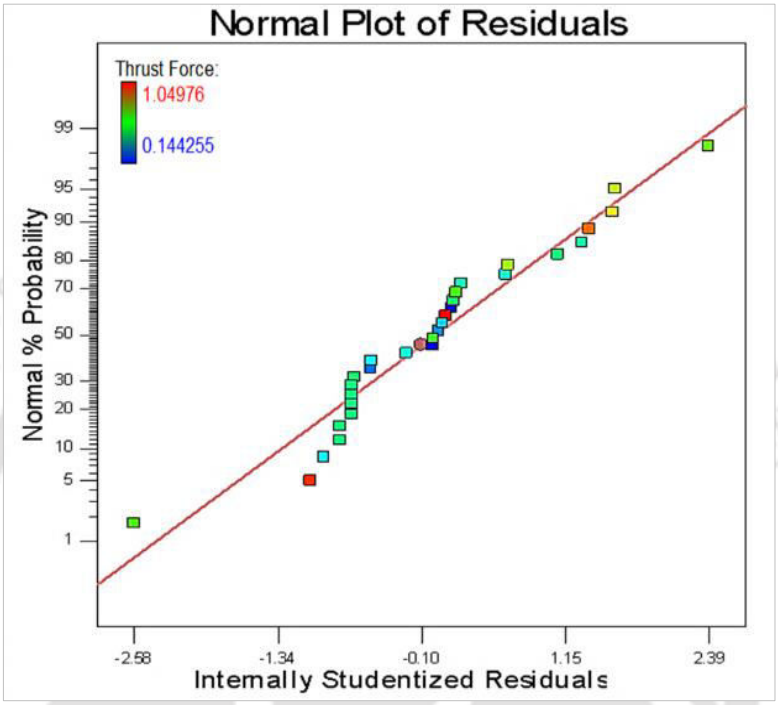

Figure 5.40 Normal plot of residuals for thrust force

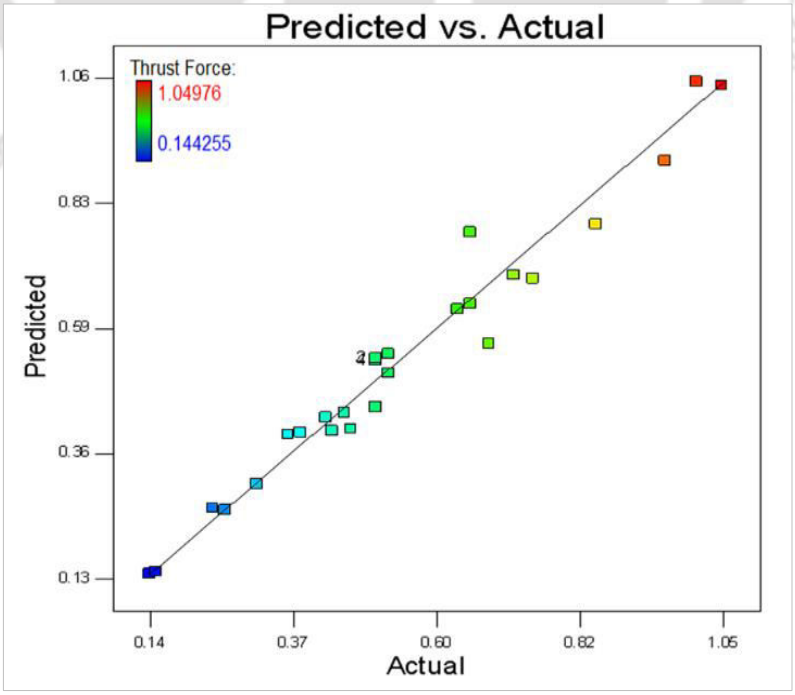

Figure 5.41 Plot of actual vs. predicted response of thrust force

5.6.8.7 Regression Analysis

After eliminating the non-significant terms, the final response equation for thrust force is given as follows (equation 5.5):

$$\textit{Thrust force} = +0.14833 - 0.201 \times S - 2.128E\text{-}03 \times R + 6.1198E\text{-}03 \times D + 3.146E\text{-}03 \times E + 3.472E\text{-}03 \times S \times E + 2.219E\text{-}04 \times R \times D \quad (5.7)$$

5.6.3.1 Parametric Influence on Thrust Force

The main effect plots for thrust force are shown in Figure 5.42. It can be seen that the depth of cut has the most significant impact on thrust force followed by rake angle and cutting edge radius. Cutting speed has the least effect on the thrust force. Increase in the cutting speed slightly decreases the force value. It is because the work material softens and the machining becomes almost steady from 0.55 m/min. With the increase in the depth of cut, the volume of the material to be removed also increases, because of which the thrust force also increases. Thrust force increases with the increase in negative rake angle since the contact area between tool and workpiece increases. It pushes more material below the cutting tool; as a result, the thrust force also increases. The effective rake angle of the cutting tool becomes more negative if the edge radius is higher than the depth of cut. Thus, increase in the cutting edge radius increases the thrust force.

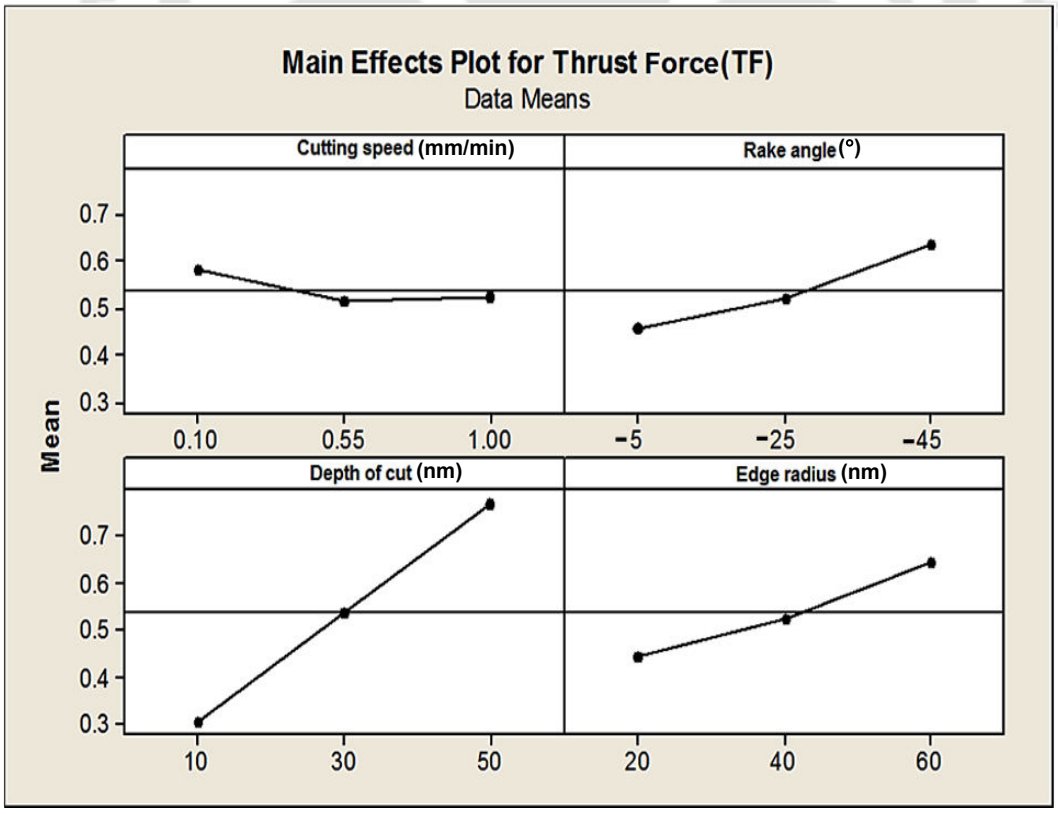

Figure 5.42 Main effect plots of thrust force

Figure 5.43 shows the estimated response contour plots for thrust force in relation to the possible combinations of design parameters. In each graph, x and y axes represent the combination process parameters and shaded blue-green surface/area represents value/range of thrust force. The legend in the right side corner shows the respective range of thrust force.

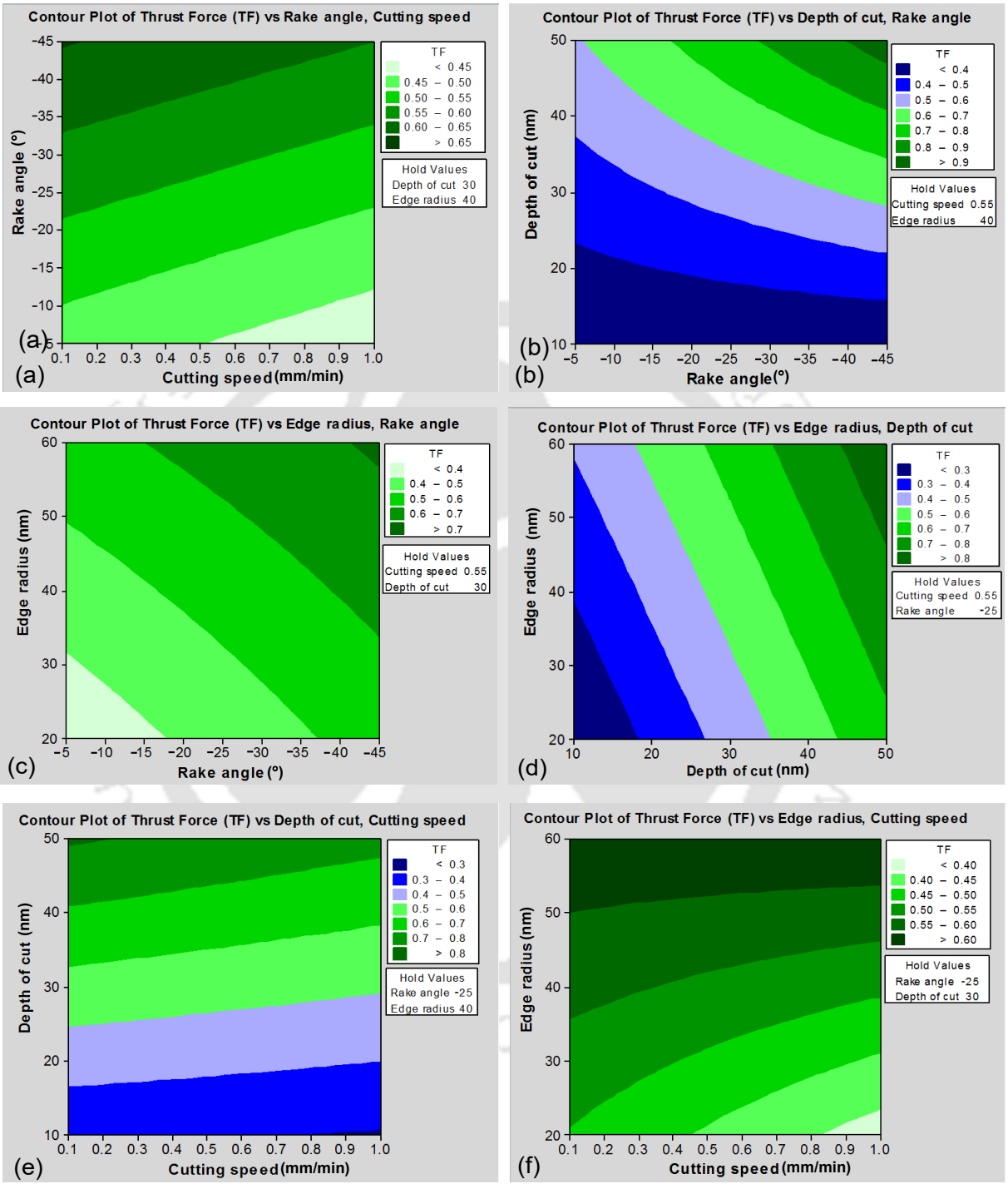

Figure 5.43 Contour plots for thrust force

The key observations of the contour plots are presented in the table 5.18.

Table 5.18 Observations on the effect of process parameters on the thrust force

Figure	Observations
5.43 (a)	Thrust force increases with the increase in rake angle and decreases with the increase in cutting speed. It is because the high negative rake angle pushes more material beneath the tool tip and thus increases the thrust force. Higher cutting speed reduces the friction acting at the chip-tool interface, thus reduces the thrust force.
5.43 (b)	Thrust force increases with the increase in depth of cut. It is because the increase in depth of cut increases the material which is pushed below the tool. This results in higher compressive force and higher thrust force. The effect of variation of rake angle on thrust force can only be seen when depth of cut is higher than 40 nm. This is because below 40 nm depth of cut, increase in the rake angle does not affect the effective rake angle.
5.43 (c)	Increase in the rake angle and edge radius push the undeformed chip material beneath the tool. This generates more compressive stress at the cutting region which leads to increase in the thrust force.
5.43 (d)	Thrust force increases with the increase in edge radius and depth of cut. This may be due to the fact that, for constant value of depth of cut, effective rake angle (negative) increases with the increase in cutting edge radius. However this is applicable only the case wherein the edge radius is greater than depth of cut. In the case of higher depth of cut, with the increase in both edge radius and depth of cut, large volume of work material tries to flow below the tool tip and thus increases the thrust force. However it has been noted that the rate of increase in thrust force is more in the case of increase in depth of cut rather than increase in the edge radius.
5.43 (e)	Thrust force increases with increase in depth of cut. It is observed a slight decrease in the thrust force with the increase in cutting speed. It may be due to reduction in friction between tool and work surface.
5.43 (f)	Thrust force increases with the increase in edge radius because of the increase in effective rake angle (negative) and decreases with the increase in cutting speed.

5.6.3.2 Confirmation Simulations

After the parametric study, the response surface equations were derived from the regression fits. Then the confirmation tests were performed to verify the validity of equations. The independent variable values selected for the confirmation test were chosen from the ranges for which the equations were derived. In this work, three confirmation simulations have been performed. Data obtained from the confirmation runs and their comparison with the

predicted values of cutting and thrust forces are presented in Table 5.19. It can be observed that RSM based model predicts the cutting force and thrust force values with an absolute average error of about 5%.

Table 5.19 Confirmation tests and their comparison with the results

Exp. No.	Machining conditions				Cutting force			Thrust force		
	Speed (mm/min)	Rake angle (°)	Depth of cut (nm)	Edge radius (nm)	Sim.	Pred.	Error (%)	Sim.	Pred.	Error (%)
1	0.2	−5	20	60	0.45	0.49	**−9.21**	0.49	0.47	**3.56**
2	0.5	−25	30	40	0.68	0.65	**4.88**	0.52	0.54	**−3.86**
3	0.8	−45	40	20	0.84	0.83	**0.35**	0.71	0.65	**7.79**
				Average mean error			**4.81**			**5.07**

Predicted values of machining forces from the developed mathematical model and the numerical simulations values are shown in Table 5.20 and Figure 5.43.

Table 5.20 FEM simulated and RSM predicted values of cutting and thrust forces

Experiment No.	Cutting force (N)			Thrust force (N)		
	Simulated	Predicted	Mean Error	Simulated	Predicted	Mean Error
1	0.25	0.27	–8.37	0.26	0.26	–1.54
2	0.16	0.18	–15.51	0.14	0.15	–4.25
3	0.25	0.24	3.79	0.24	0.28	–16.92
4	0.17	0.15	9.17	0.15	0.16	–8.38
5	1.02	1.04	–1.49	0.52	0.52	–0.46
6	0.92	0.88	4.44	0.42	0.40	3.73
7	1.18	1.19	–0.59	0.96	0.93	3.48
8	1.02	1.03	–1.07	0.85	0.81	4.88
9	0.26	0.27	–2.54	0.36	0.40	–12.24
10	0.28	0.26	6.97	0.43	0.41	4.42
11	0.27	0.30	–10.50	0.38	0.40	–4.81
12	0.29	0.29	–0.77	0.46	0.41	11.91
13	1.05	1.08	–2.67	0.75	0.73	2.98
14	1	1.00	–0.20	0.72	0.73	–2.03
15	1.19	1.16	2.72	1.05	1.04	0.55
16	1.09	1.08	0.77	1.01	1.05	–4.08
17	0.64	0.64	0.77	0.5	0.50	–0.44
18	0.64	0.64	0.77	0.5	0.50	–0.44
19	0.64	0.64	0.77	0.5	0.50	–0.44

20	0.64	0.64	0.77	0.5	0.50	–0.44
21	0.84	0.78	7.66	0.68	0.63	7.03
22	0.65	0.69	–6.85	0.52	0.58	–10.89
23	0.65	0.62	4.20	0.5	0.44	12.13
24	0.62	0.65	–4.40	0.63	0.61	3.82
25	0.25	0.25	1.37	0.31	0.30	4.33
26	0.97	1.02	–5.50	0.65	0.75	–15.19
27	0.67	0.66	1.95	0.45	0.44	1.49
28	0.62	0.61	1.13	0.65	0.60	7.38
29	0.64	0.63	0.78	0.5	0.52	–4.53
30	0.64	0.63	0.78	0.5	0.52	–4.53
	Average mean error		**3.64**			**5.32**

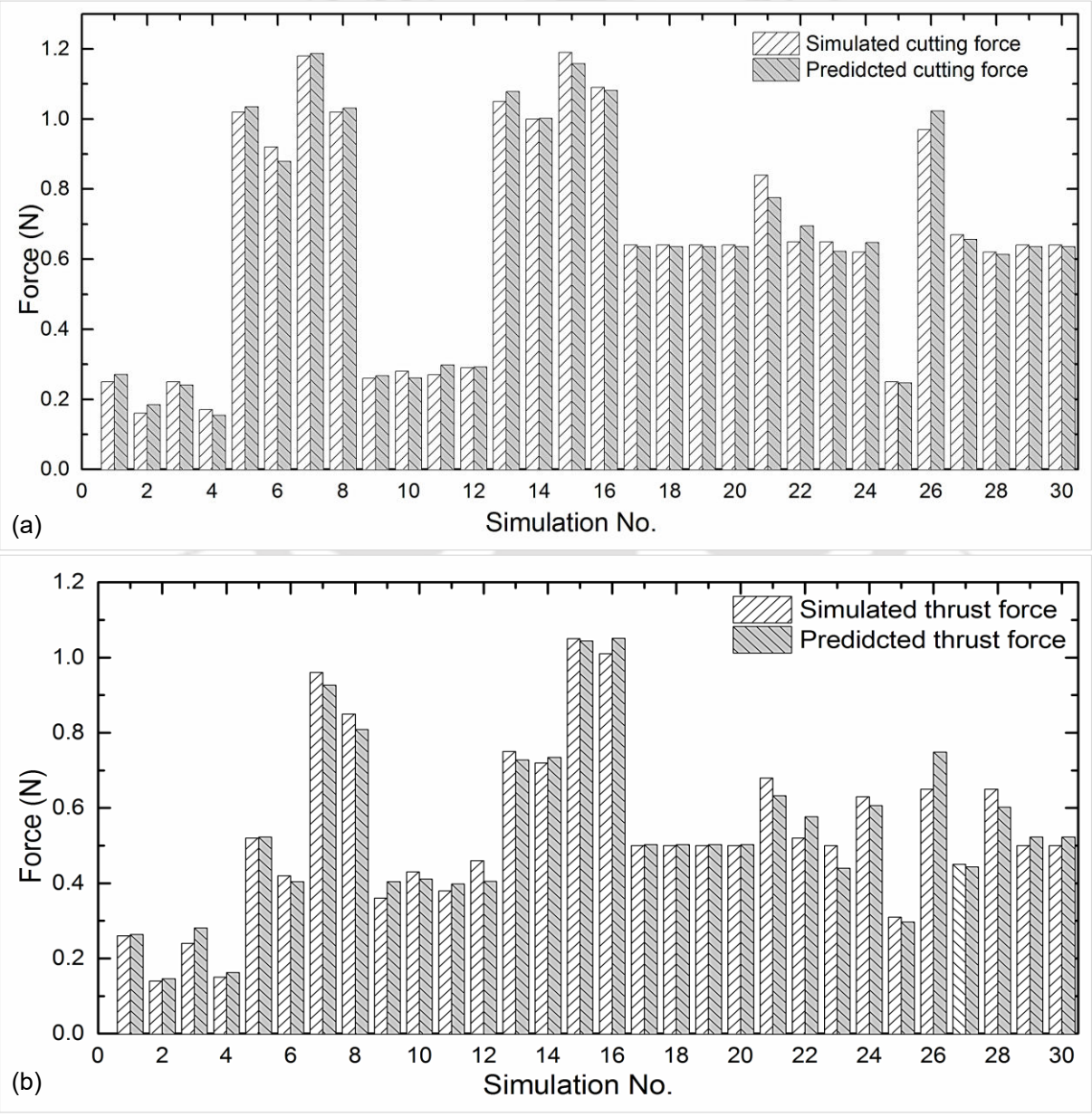

Figure 5.44 Numerically computed and predicted values (a) cutting force and (b) thrust force

5.6.4 Multi-Objective Optimization of Machining Forces using RSM

After the development of predictive models to predict the machining forces, it was decided to optimize the process conditions. The objective was set to minimize the machining forces (cutting and thrust force) by determining the optimum values of process parameters. Based on the RSM methodology, optimization results obtained for minimization of cutting force and thrust force are shown in Table 5.18 and Figure 5.45. Optimum cutting parameters are found to be: cutting speed of 0.68 mm/min, rake angle of −45°, depth of cut of 10 nm and cutting edge radius of 20 nm for production of minimum cutting force of 0.179 N and thrust force of 0.183 N with desirability value of 0.967.

Table 5.18 Response optimizations for cutting force and thrust force parameters

Parameters	Goal	Optimum conditions				Lower	Target	Upper	Predicted response	Desirability
		Speed (mm/min)	Rake angle (°)	Depth of cut (nm)	Edge radius (nm)					
Cutting Force	Min	0.68	–45	10	20		0.14	1.05	0.1799	0.967
Thrust Force	Min	0.68	–45	10	20		0.16	1.19	0.1828	0.967

Thus it can be concluded that suggested machining parameters can be applied in practice with confidence to enhance the productive and energy consumption during SPDT machining of silicon and silicon carbide materials.

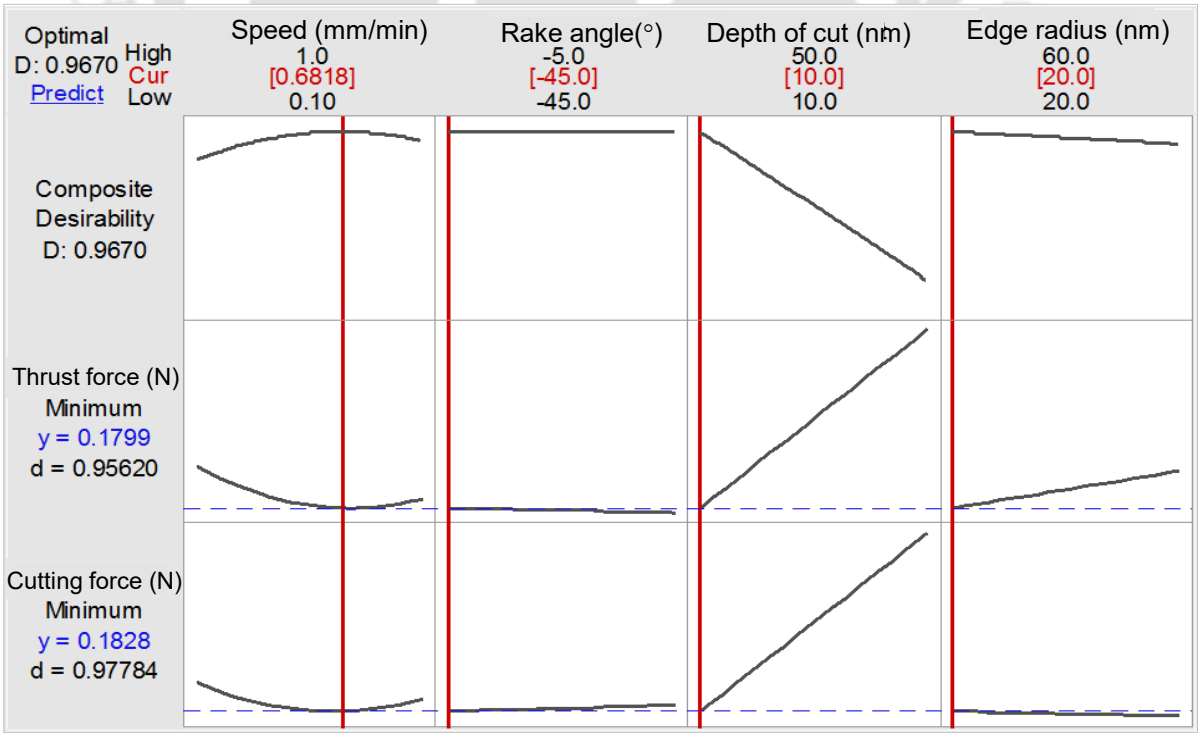

Figure 5.45 Response optimizations for cutting and thrust forces

5.7 Summary

This chapter presents in details, the development of a 2D numerical (FEM) model for the nanometric machining of silicon and silicon carbide. ALE formulation with dynamic explicit solution scheme was employed to simulate the complex interaction between the tool, workpiece, and chips. The behavior of the materials was defined with two material models viz. Johnson-Cook (stress, strain and temperature dependent) and Drucker-Prager (pressure dependent) and their results were compared with already published experimental results. Ductile damage properties, yield stress-strain properties, and friction law were used to model the phenomenon of chip separation and contact interaction. Some of the findings from the simulations are listed below:

- A detailed approach to model the cutting process that captures ductile fracture leading to material separation has been developed by using the FEM. Material separation was modeled via element failure and damage model. The developed numerical model was then validated by using published experimental results. The results predicted by the model were found in good agreement with the experimental results.
- Simulation results show that the selection of the material model plays a significant role in the accurate prediction of machining forces. Based on the present comparative study, it was concluded that JC material model is better than the DP model when analyzed quantitatively. However, in mechanistic point of view, the JC model is not suitable for the simulation of brittle material machining. Moreover, various stages of chip formation during SPDT of SiC has been studied and found close with the experimental results.
- Parametric studies were carried out using a full factorial approach to study the behavior of SPDT of silicon carbide by varying the rake angle, depth of cut and d/r ratio. The study revealed that the depth of cut has the most significant effect on both cutting force and thrust force followed by rake angle and d/r ratio. Both cutting force and thrust force were found to be increased with increase in depth of cut and negative rake angle and decrease with an increase in d/r ratio.
- A predictive model was developed for SPDT of silicon carbide using regression analysis to predict the machining forces. The confirmation simulations showed mean prediction error below 9%.
- The process conditions were optimized with an objective of minimal cutting and thrust forces, FFA optimization approach was employed. The developed FFA approach recommends an optimal process condition of rake angle of −25°, depth of cut of 100 nm and d/r ratio of 5 for generation of minimum cutting force and thrust force.

In addition to the numerical study on SPDT of SiC, a study on Si was also carried out. A two-dimensional nonlinear plane strain FEM model of SPDT of silicon has been developed.

- The developed numerical model was first validated by comparing with the published experimental data from the literature and found in good agreement. Simulated chip morphology study showed that the stress state ahead of the tool is indeed favorable for the ductile fracture to occur.
- Non-cutting plastic work on the material including plowing and flank face rubbing had more impact on the unit energy than the cutting process at lower depths of cut. Spring back effect could also be seen in case of very low depth of cut with high negative rake angle tool.
- Parametric studies were performed to study the behavior of SPDT of silicon by varying cutting speed, rake angle, depth of cut and tool edge radius using response surface methodology.
- ANOVA analysis and main effect plot study revealed that both rake angle and depth of cut have significant effect on cutting force as well as thrust force whereas the cutting speed and tool edge radius have minimal effect. Both the cutting force and thrust force were found to be increased with the increase in depth of cut, negative rake angle and cutting edge radius. Increase in the cutting speed showed a marginal effect on the cutting force and thrust force.
- The predictive mathematical models found to be predicting the machining forces with mean prediction error of about 5%. The optimal process condition obtained by the RSM optimization approach was cutting speed of 0.68 mm/min, rake angle of −45°, depth of cut of 10 nm and cutting edge radius of 20 nm. This process condition was found to generate a minimum cutting force of 0.179 N and thrust force of 0.183 N with a desirability value of 0.967.

Overall, it was felt that the proposed approach provides an efficient alternative to the costly, time consuming and tedious experimental study of SPDT of silicon and silicon carbide materials. Predicted machining forces will be helpful for an approximate estimation of energy requirement during machining. However, this model does not predict the surface quality, which is an important factor to be considered during the SPDT process. Thus, in this work, a finite element based surface roughness prediction model integrated with an image processing technique was developed. The next chapter presents the details of the same.

NUMERICAL PREDICTION OF SURFACE ROUGHNESS DURING SINGLE POINT DIAMOND TURNING

6.0 Scope

This chapter presents a methodology developed to predict the surface roughness obtained during SPDT process using finite element method based numerical model. Initially, the need for this work is defined. Then, an overview of the proposed approach is presented. The details of model development are presented. Then the validation of the model is presented. At the end, the usefulness of the developed model is discussed.

6.1 The Need

Surface roughness is an important criterion to characterize the quality of the product that is manufactured by a machining process. It affects several functional attributes viz. friction, wear, lubrication, light reflection/refraction, corrosion resistant, etc. of the components [Jomaa *et al.* (2014), Naidu and Rao (2013)]. Theoretically, in case of the cutting process (turning or facing), the surface finish mainly depends on the tool nose radius and the feed rate. However, in reality, it depends on various factors such as process parameters, tool geometry, the interaction between the workpiece and cutting tool, workpiece and tool material properties, tool wear, cutting environment and the type of machine tool used.

Surface roughness measurement is a post-process operation, i.e., the roughness is measured after the completion of the machining operation. Thus, it is time-consuming and costly. Moreover, the parts that do not meet the specified surface roughness during machining need re-machining, which may cause additional production cost [Aykut (2011)]. Literature reports that most of the research works in surface quality of SPDT have been used either experimental or theoretical way to describe the surface quality. Very scant literature is available on modeling of surface roughness directly from FEM simulations of SPDT process. Therefore, it was thought worthy to develop an integrated finite element method with image processing technique to predict the surface roughness. The main objective of this work was to demonstrate the feasibility of predicting the surface roughness during nanometric level cutting range. To investigate the behavior of surface finish under the orthogonal cutting which itself allows to study the mechanism of the machining process before carrying out actual machining process. Moreover, it will eliminate the instruments cost for measuring various output parameters such as force, temperature, roughness, residual stress, deformation, etc. Using the

current approach, one can study the surface roughness for different process conditions without having an actual machine and surface measuring instrument.

6.2 Overview of the Present Work

In the present work, a unique model has been proposed by combining the finite element method and image processing technique to predict the surface roughness during SPDT process. It can predict the surface roughness during single point diamond turning of ductile as well as brittle materials. Figure 6.1 shows an overview of the proposed methodology.

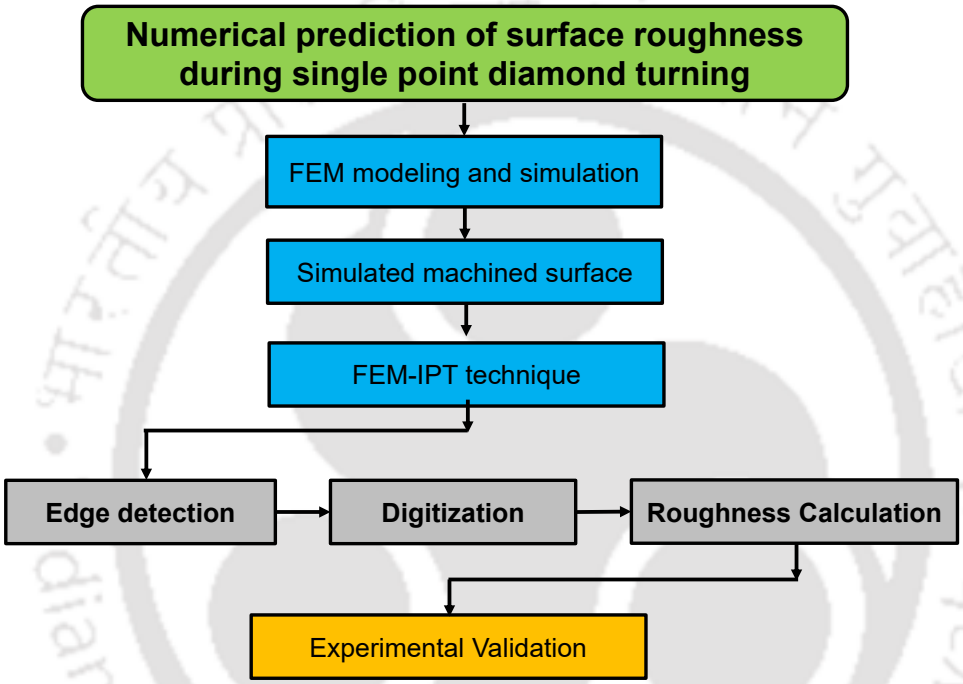

Figure 6.1 Overview of the work carried out in this chapter

The stages of work involved in the present chapter are as follows.

- Development of a finite element based machining simulation model for machining of Al6061 using the diamond tool. It comprises of 2D plane strain orthogonal machining simulation of Al6061 by considering the cutting speed and undeformed chip thickness. This undeformed chip thickness takes into account of feed rate, depth of cut and tool nose radius.
- The snapshots of the workpiece with chips are then extracted from the simulation and then fed into the roughness calculator which computes the surface roughness.
- The simulated surface profiles are processed using image processing technique which comprises of various steps such as edge detection, digitization, and roughness calculation.

- Finally, turning experiments are carried out on Al6061-T6 using diamond tool and the surface roughness values have been measured using 2D profilometer. The computed surface values were validated using experimental results.

The details of above-mentioned stages are presented in detail for the machining of Al6061 in the following sections.

6.3 Selection of Workpiece Material

In this new approach, finite element method based numerical simulation is integrated with image processing technique for the prediction of surface roughness while nanometric machining of Al6061 aluminium alloy using SPDT process. The measurement of surface roughness is carried out on FE simulated machined surface with the help of image processing technique. The experiments for validation of this work have been carried out at Central Scientific Instruments Organisation (CSIO), Chandigarh (India). The experimental facility was allowed to carry out experiments on Al6061-T6 aluminium alloy only. The main objective of this study was to develop FEM-IPT technique to predict the roughness during SPDT process. Therefore, in view of experimental results available, the aluminium 6061-T6 alloy materials were chosen for present work. Al6061-T6 has various applications in engineering and industrial fields such as aerospace, automobile, optical mould inserts for plastic lens and most importantly aluminum mirrors (with aspheric surfaces) required in optical industries [John (2003)].

6.4 Selection of Modeling Domain

Modeling and simulation of macro sized work-parts with nanometric elements is very much time consuming and requires huge computational time. In the current simulation, a two dimensional (2D) finite element based numerical simulation of nanometric orthogonal cutting of Al6061-T6 is presented. In the present 2D simulation, only orthogonal cutting condition is considered, hence, the effect of tool nose radius and feed rate are not incorporated in the model. However, an approximation from 3D to 2D orthogonal cutting is still valid as explained by [Blake and Scattergood (1989), Patten and Jacob (2008)]. This has already been explained in section 5.2 of Chapter 5.

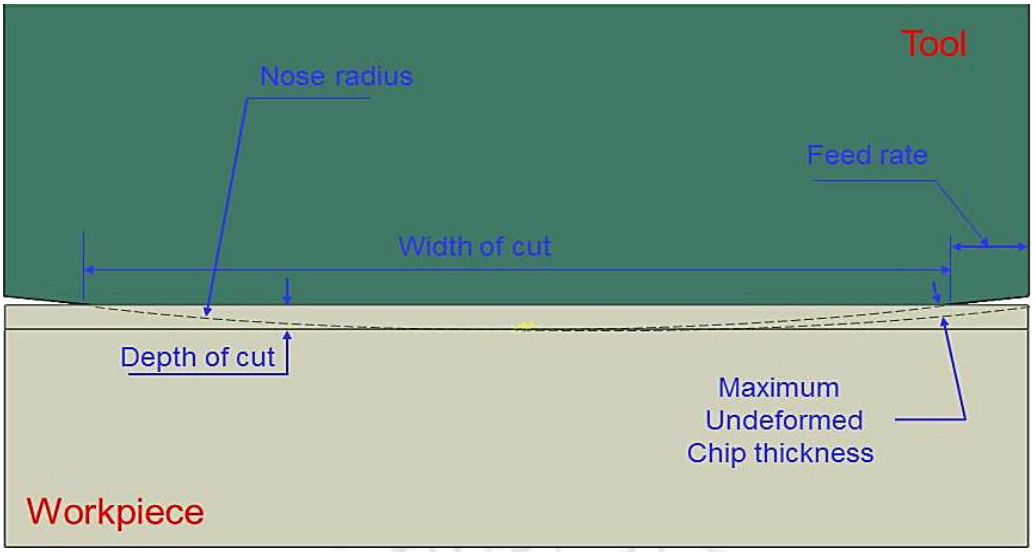

Figure 6.2 Cross section of undeformed chip geometry

Figure 6.2 shows the cutting process with round nose tool. In this case, the width of cut is much higher than the depth of cut. If the tool is moved further by giving feed rate, the maximum undeformed chip thickness further decreases. Thus, the tool can be considered as flat tool and cutting process can be assumed as orthogonal cutting. Figure 6.2 also shows a cross sectional view of the SPDT cutting process along the plane parallel to the 0º rake face. From the figure, it can be seen that the depth of cut is in nanometric range and the tool nose radius is in mm range, because of which it can be considered as orthogonal cutting.

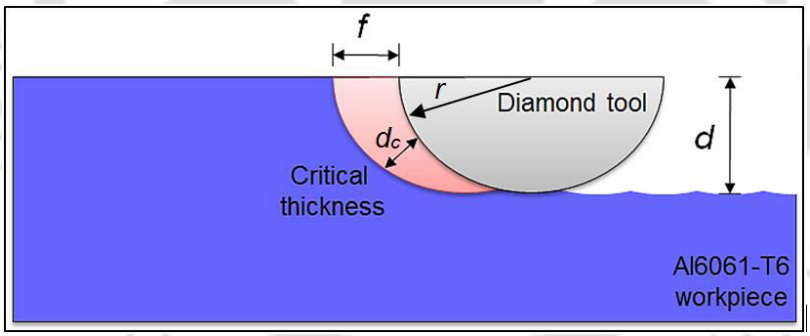

Figure 6.3 Geometries of 3D turning simulation and boundary condition

Moreover, in the current simulation, instead of depth of cut, critical/maximum undeformed chip thickness is considered as depth of cut. It is calculated by considering the feed rate, depth of cut and tool nose radius as described in equation 6.1. The depth of cut employed in actual cutting is not exactly the same as that applied in orthogonal cutting. Figure 6.3 shows the schematic of the geometries and its parameters during actual cutting process. The parameters are nose radius, feed rate and depth of cut. However, the actual depth of cut changes due to round tool. Corresponding to each feed rate and depth of cut, the undeformed critical chip thickness (d_c) can be obtained by using the correlation given in equation (6.1) where R is the tool radius, f is the feed rate and d is the depth of cut.

$$d_c = R - \sqrt{R^2 + f^2 - 2f\sqrt{2Rd - d^2}} \quad (6.1)$$

In the present study, a finite element method based numerical simulation was performed on a simplified 2D rectangular geometry (10 µm × 5 µm) which is considered to be a very small portion of a 25 mm diameter and 10 mm thickness Al6061-T6 disc as shown in Figure 6.4. Surface roughness values were calculated from the numerical simulation by using image processing technique. The calculated roughness is then compared with experimental roughness for validation purpose. Figure 6.4 shows the difference between the process continuums required for 2D and 3D mode of simulation of a typical face turning operation of SPDT process.

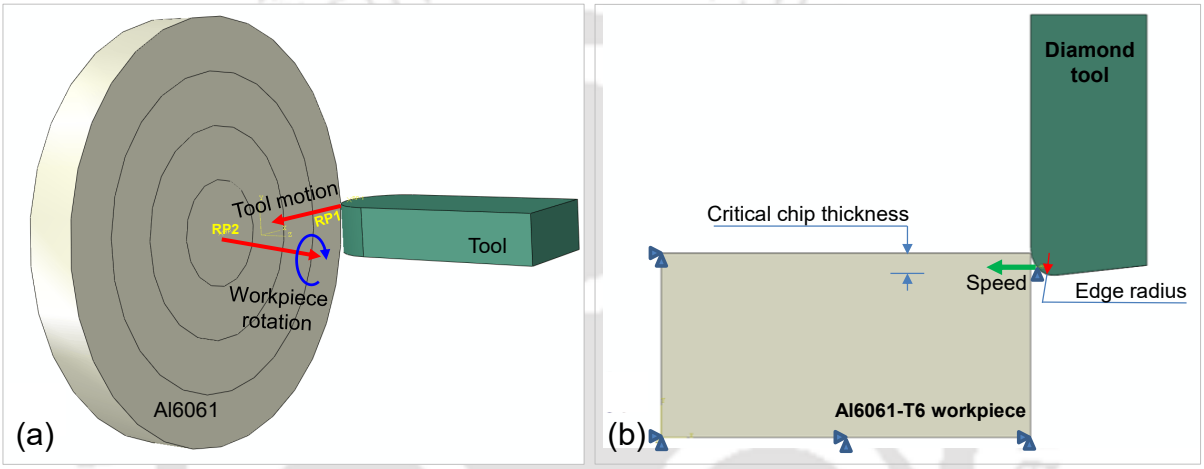

Figure 6.4 Process continuums in numerical simulation of SPDT of Al6061-T6 for (a) 3D and (b) 2D numerical models

6.5 2D Finite Element Simulation of SPDT of Al6061-T6

The finite element modeling and simulation was carried out using finite element software Simulia Abaqus™. The numerical model employed for the simulation of SDPT of Al6061-T6 is identical to the numerical model developed for SiC and Si. The details are provided in Chapter 5.

As presented earlier, a 2D rectangular workpiece was considered. The reason for modeling 2D simulation is to reduce the time constraint for simulating larger 3D circular disc of 25 mm diameter with the elements of nanometric size. The undeformed critical chip thickness was considered as the depth of cut as discussed earlier. The 2D orthogonal cutting process was modelled based on plane strain conditions. The diamond tools used in the present study have rake angle of 0°, clearance angle of 5°, edge radius of 300 nm, and nose radius of 1.628 mm. The depth of cut was varied and simulations were carried out. The Johnson–Cook (JC) constitutive equation was used to model the material behavior of Al6061-T6 alloy. The

JC material model constants for Al6061-T6 are listed in Table 6.1. The physical properties of Al6061-T6 are taken from MetWeb [MatWeb (2013)], an online material information source. These are listed in the Table 6.2.

Table 6.1 JC material parameters values for Al6061-T6 [Johnson and Holmquist (1989)]

A(MPa)	*B(MPa)*	*n*	*C*	*m*	$\dot{\varepsilon}_0$ (s^{-1})
324.1	113.8	0.42	0.002	1.34	1.0

Table 6.2 Material properties of Al6061-T6 [MatWeb (2013)]

Parameters	Value
Density, ρ $\left({}^{kg}/_{m^3}\right)$	2700
Elastic modulus, *E (GPa)*	68.9
Poisson ratio, ν	0.33
Specific heat, C_p $\left({}^{J}/_{kg.\,℃}\right)$	896
Thermal expansion , α *(10e^{-6}/°C)*	25.2
Thermal conductivity, λ $\left({}^{W}/_{m.\,℃}\right)$	167
T_{melt} *(°C)*	582-651
T_{room}*(°C)*	20

In the present study, Johnson-Cook damage model [Johnson and Cook (1985)] has been employed to model the material failure when the tool exceeds the load carrying capacity of the work material. Fracture occurs in the Johnson-Cook model when the damage parameter *D* exceeds 1.0. This model uses a damage parameter *D* which is defined as the accumulated incremental effective plastic strains $\bar{\varepsilon}^p$ divided by the current strain at fracture $\varepsilon_{failure}$ and is given by the equation 6.2.

$$D = \sum \frac{\Delta \bar{\varepsilon}^p}{\varepsilon_{failure}} \tag{6.2}$$

The fracture strain $\varepsilon_{failure}$ is of the form as given in equation 6.3

$$\varepsilon_{failure} = [D_1 + D_2 \exp(D_3 \sigma^*)\,|1 + D_4 \ln(\dot{\varepsilon}^*)|1 + D_5 T^*] \tag{6.3}$$

where D_1- D_5 are the damage constants, σ* is the ratio of the pressure to the effective stress, i.e.

$$\sigma^* = \frac{pressure}{\bar{\sigma}} \tag{6.4}$$

$\dot{\varepsilon}^*$(non-dimensional strain rate) is the ratio of the effective plastic strain rate $\dot{\bar{\varepsilon}}^p$ to the reference strain rate $\dot{\varepsilon}^0$ (usually equal to 1.0), i.e.

$$\dot{\varepsilon}^* = \frac{\dot{\bar{\varepsilon}}^p}{\dot{\varepsilon}^0} \tag{6.5}$$

and the non-dimensional temperature T^*

$$T^* = \frac{T - T_{room}}{T_{melt} - T_{room}} \tag{6.6}$$

where T is the current temperature, T_{room} is the ambient temperature, and T_{melt} is the melt temperature. Johnson-Cook failure parameters for Al6061-T6 alloy materials in this study have taken from previously published data (Table 6.3).

Table 6.3 Johnson– Cook failure parameters for Al6061-T6 [Johnson and Holmquist (1989)]

Parameters	D_1	D_2	D_3	D_4	D_5
Values	−0.77	1.45	−0.47	0.0	1.6

The element deletion criterion was used along with the JC damage law to simulate the chip separation. Both the workpiece and diamond tool were meshed using 4-node plane strain, reduced integration, and hourglass controlled (CPE4R) element as shown in Figure 6.5. The diamond cutting tool was considered to be rigid and undeformable. Modified coulomb friction model was used to define the contact between the cutting tool and the workpiece. The coefficient of friction between tool and workpiece was taken as 0.4 [Soundararajan *et al.* (2005)].

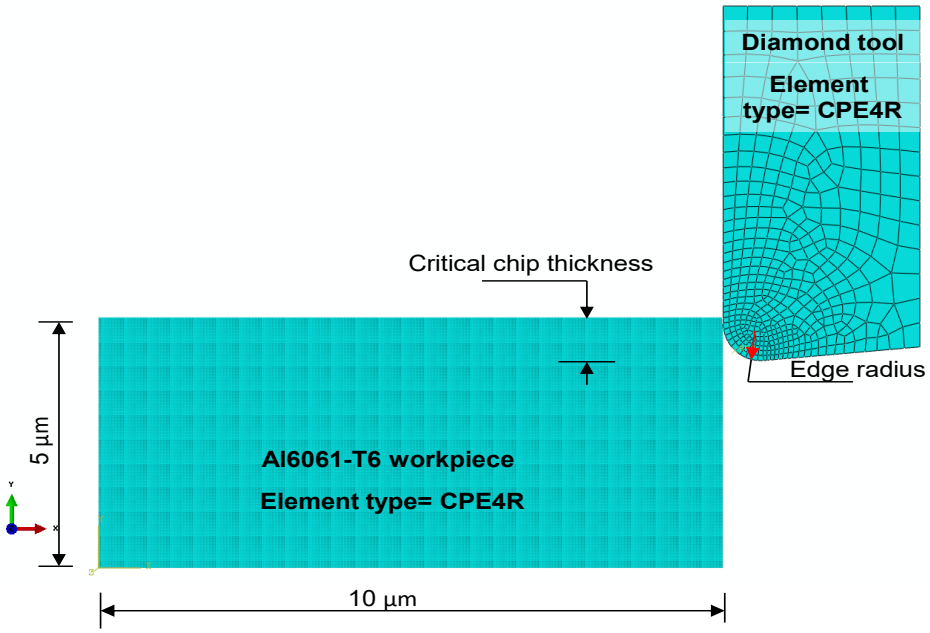

Figure 6.5 Element type and mesh model of 2D orthogonal cutting simulation

Figure 6.6 shows a schematic of the boundary conditions applied. The fixed boundary condition was applied at the bottom of the work piece and the tool was provided with linear motion along the *x*-axis, so that it moves from left to right at the specified cutting speed of 1309 mm/s. The *y*-direction as well as rotational motions of the tool were restrained. In the present analysis as well, dynamic explicit time integration scheme with ALE formulation was used to solve the machining problem.

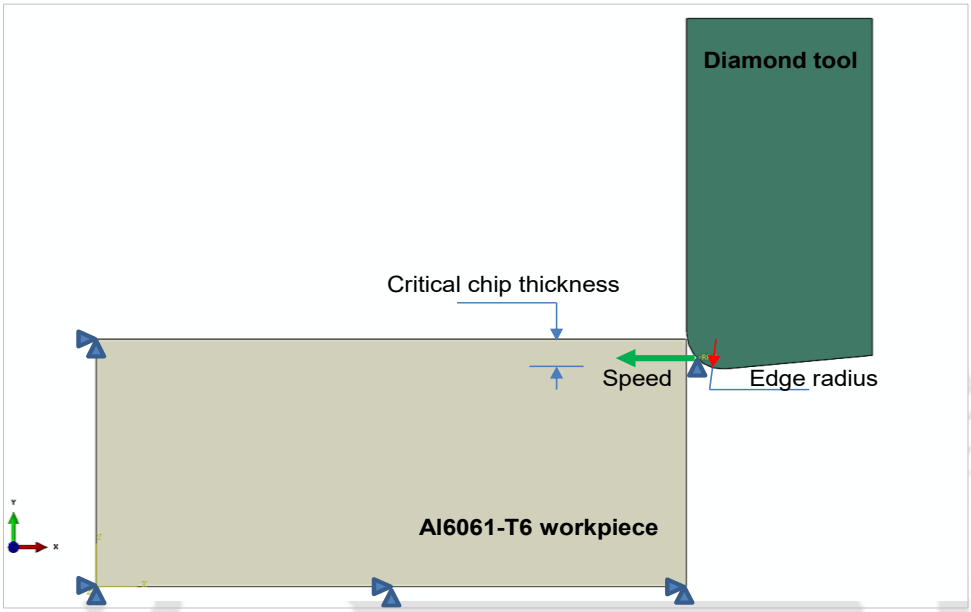

Figure 6.6 Boundary conditions

6.6 Numerical Simulations using the Developed Model

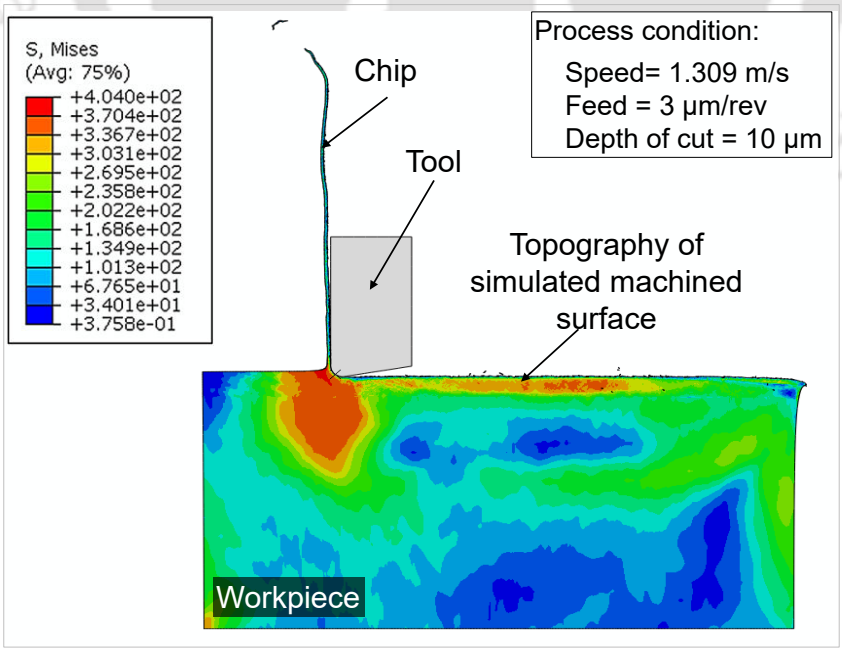

Figure 6.7 2D turning with formation of chips showing von-Mises stress

Figure 6.7 shows the predicted von-Mises stress in the workpiece after steady state chip formation. After the simulations, roughness profiles were generated. These profiles were further used to compute the average roughness value. The methodology used in image processing technique to extract the surface profile and to compute the surface roughness value is explained in the following sections.

6.7 Calculation of Surface Roughness using FEM-IPT Technique

Figure 6.8 shows the overall approach of development of integrated MATLAB code for FEM–IPT technique. It consists of three modules viz. edge detector, digitizer and average surface roughness (Ra) calculator.

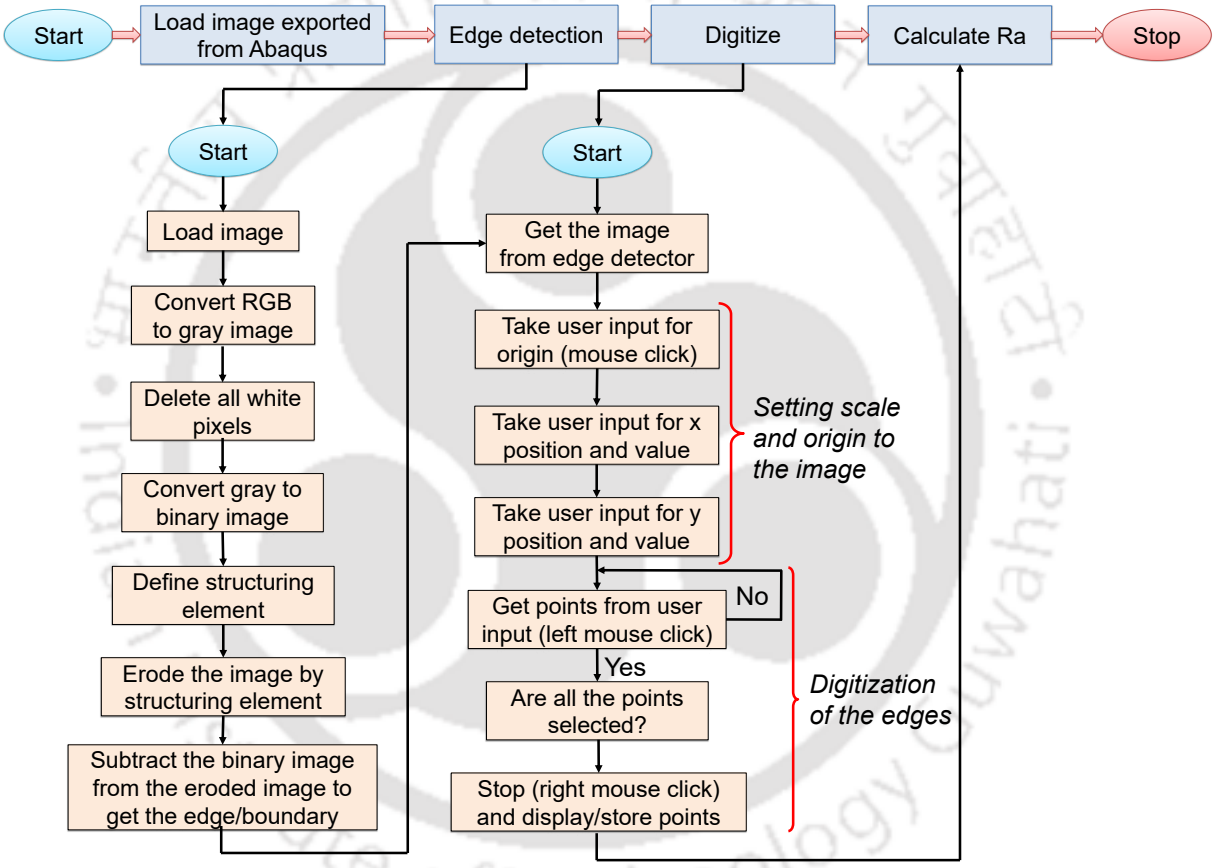

Figure 6.8 Overview of the integrated MATLAB code of FEM-IPT technique

In this technique, the image of the simulated workpiece is exported from Abaqus™ visualization module. Then, by using the edge detector algorithm, the rough surface along and edges/boundaries were detected. Then the image is digitized and surface roughness is computed by using the digitized data, i.e., co-ordinates of the points on the edges. The modules viz. edge detector, digitizer and Ra calculator are explained in detail in the following sub-sections.

6.7.1 Edge Detection

The exported image from Abaqus™ is given as input to the Edge detector algorithm to detect the edge, i.e., boundary. The flow chart for edge detector is shown in Figure 6.8. The image is first converted from RGB to gray and all the white pixels are deleted. Next, it is converted to binary image from the gray image. Structuring element which is an essential part of the dilation and erosion operations is defined to probe the input image. Two-dimensional, or flat, structuring elements consist of a matrix of 0's and 1's, typically much smaller than the image being processed. The center pixel of the structuring element, called the origin, identifies the pixel of interest—the pixel being processed. In the present case, flat disk-shaped structuring element with radius value 4 pixels and no approximation has been used. Erosion of the image is then executed with structuring element. Erosion removes pixels on object boundaries of objects in an image. The number of pixels removed from the objects in an image depends on the size and shape of the structuring element used to process the image. The boundary can be obtained by subtracting binary image from the eroded image. Figure 6.9 (a) shows the image of the simulated machined workpiece and (b) shows the detected edges of the simulated machined workpiece.

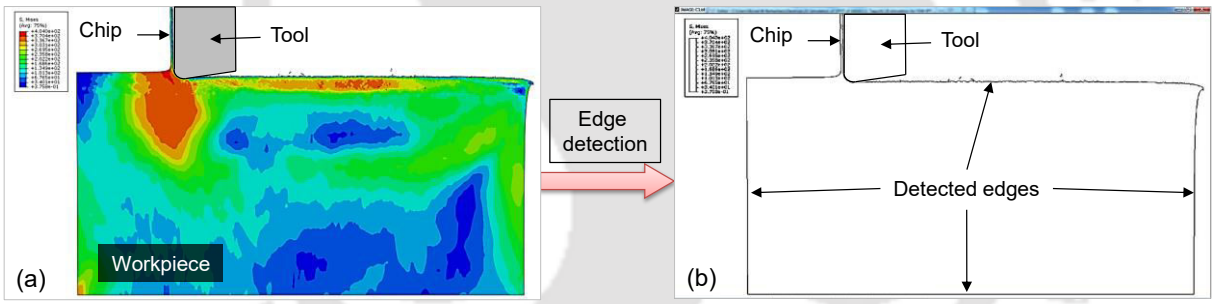

Figure 6.9 (a) Image of the simulated machined workpiece including chip, (b) Edge of the simulated machined workpiece including chip

6.7.2 Digitization

The image from the edge detector will be entered into digitize module. The flow chart for the digitizer module is shown in Figure 6.8. First, the digitizer sets the limits of x and y axis. The MATLAB code will ask the user to select the origin and x-y limits with left mouse click and can set the desired value. In Figure 6.10 (b), green circle shows the origin and square boxes (red and blue) show the limits of x-axis and y-axis respectively. Here, origin is (0, 0), x limit is 0.01 mm and y limit is 0.005 mm for the present case. After setting the scale to the image, a popup window will appear for selecting the points on the line for which the surface roughness is to be calculated. It allows the user to select the points by clicking left mouse button and right mouse button to stop the process. After selecting all the data points, if

the user clicks right mouse button, it closes the digitization process and fed the data points with their coordinates to the roughness calculator.

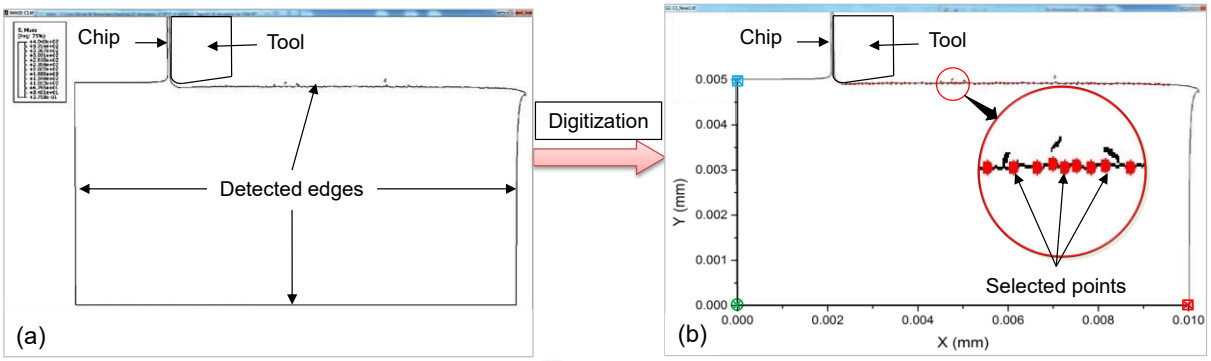

Figure 6.10 (a) Simulated machined workpiece with detected edge, (b) Adding of scale the workpiece and digitization

6.7.3 Roughness Calculation

Digitized data were then entered into the roughness calculator. The Centre Line Average or Arithmetic Average method was used to compute the average roughness.

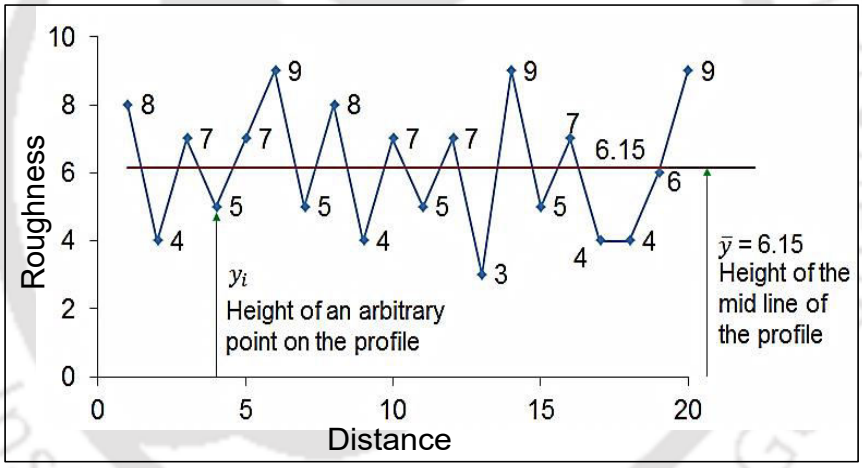

Figure 6.11 Schematic of surface roughness measurement using arithmetic average method

Centre line average is defined as the average values of the ordinates from the mean line, regardless of the arithmetic signs of the ordinates. The height of the mid line ($\bar{y}$) is calculated by summing up all the data points divided by the total number of data points. The modes of arithmetic deviations of the data points are then calculated by subtracting the ordinate values with mid line values. Then average roughness value can be determined by summing all arithmetic deviations above and below the mean line and dividing it by number of data points taken along the sampling length (n) as shown in the equation 6.8.

$$R_a = \frac{1}{n}\sum_{i=1}^{n}|y_i - \bar{y}| \qquad (6.7)$$

where, n = the number of data taken along the sampling length

y_i= height of an arbitrary point i on the profile

$\bar{y}$ = height of the mid line of the profile

The roughness value thus obtained from FEM-IPT technique is 0.000006 mm or 6 nm for the chosen process condition shown in Figure 6.12. Figure 6.13 shows the roughness plot against the sampling length.

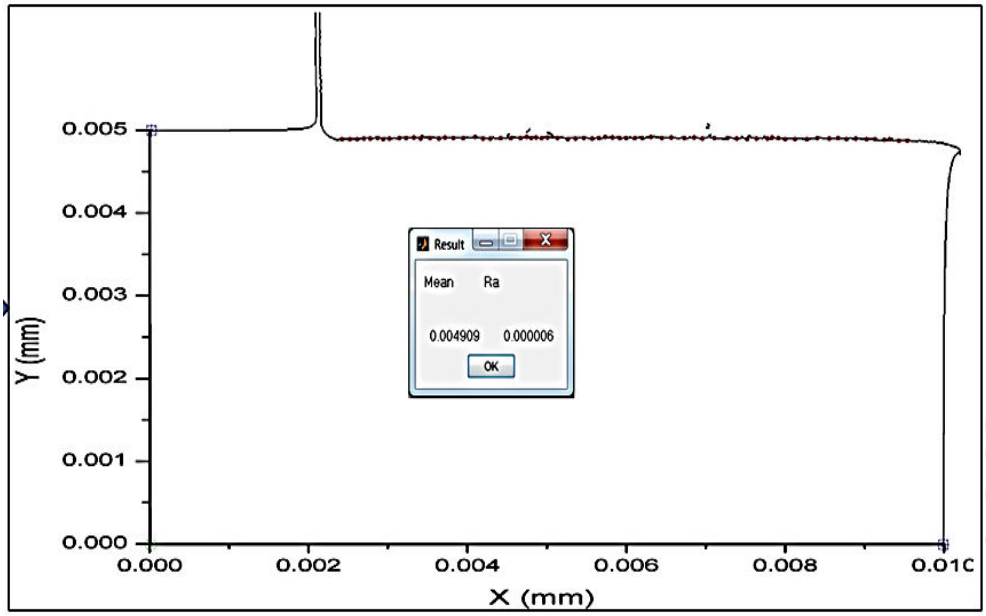

Figure 6.12 Measured surface roughness showing mean and arithmetic average roughness

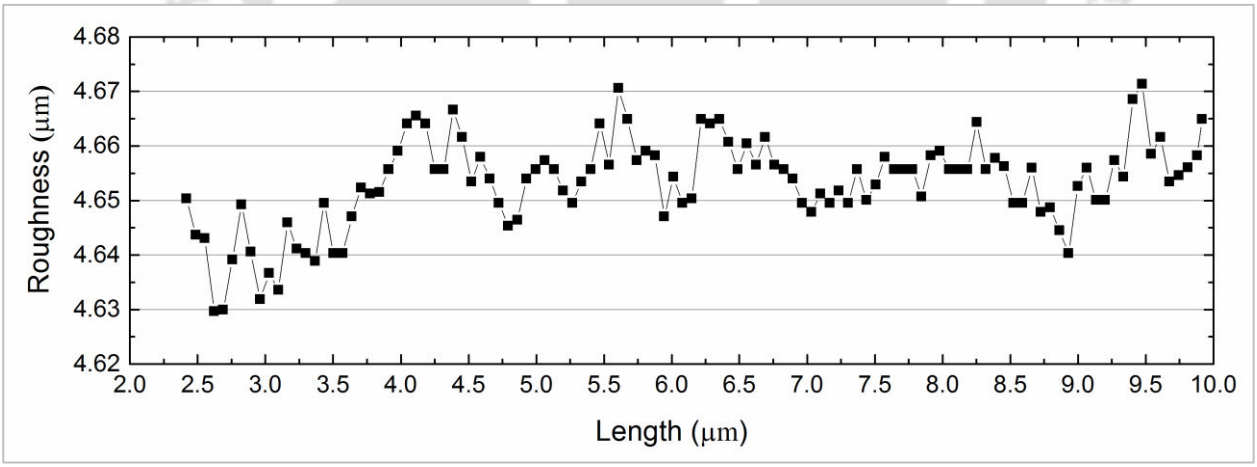

Figure 6.13 Roughness profile from numerical simulation for process conditions of speed 1.309 m/s, feed 3 μm/rev and depth of cut 10 μm

6.8 Experimental Validation of the Developed Integrated FEM-IPT Model

After the development of numerical model and integrated with image processing technique, experimental validation of the responses predicted by the developed integrated

FEM-IPT model was carried out. For this purpose, the various process parameters used: spindle speed of 1309 mm/s, depth of cuts of 1 and 10 µm and feed rates of 3 and 6 µm/rev; diamond tool having 0º rake angle, 5º clearance, 300 nm edge radius and 1.628 mm nose radius. Within the scope of these process conditions, three sets of experiments with low critical undeformed chip thickness were performed. SPDT physical experiments were performed on a Nanoform 250 diamond turning machine and the experimental surface roughness values were measured using contact type surface profilometer (Form Talysurf PGI 120). The details of the experimental setup that has been used for experimental study are elaborated in the Chapter 7. Numerical simulations were carried out with similar process conditions of experiments and the surface roughness values were determined using the developed integrated FEM-IPT model.

Table 6.4 shows the comparison of experimental and numerical surface roughness values obtained against the four combinations of process conditions. The comparison shows that the mean prediction error between experimental roughness and numerically predicted roughness is **2.19%** to **20.41%** and average mean prediction error is found to be **8.71%.** This shows a close correlation between the values of the simulation and the. In nanometric cutting using single point diamond turning, the surface roughness that is generated may not be exactly due to the tool feed and nose radius mark as the case of macro or micro cutting. The roughness may also be due to the subsurface damage or fracture as the material removal is in nanometric scale. Therefore, analytical expression (which is the function of tool nose radius and feed rate) used in macroscopic scale is found to be inappropriate in case of nanometric cutting.

Table 6.4 Comparison of experimental and numerical roughness values

SN	Speed (mm/s)	Feed (µm/rev)	Depth (µm)	Critical thickness (nm)	Experimental roughness (nm)	Numerical roughness (nm)	Mean Error (%)
1	1309	3	1	102	7.3	7.14	2.19
2	1309	3	10	329	6.5	6.27	3.54
3	1309	6	1	199	12.3	9.79	20.41
						Average mean error	**8.71**

6.9 Summary

In this present work, FEM based numerical simulation of SPDT process was integrated with image process technique to predict the surface roughness prior to the actual machining process. The novelty and uniqueness of the present technique is that it is simple, economical

and moreover it can analyze and study the roughness before carrying out the actual experiment with the help of finite element simulation. Preliminary studies have been carried out on Al6061-T6 workpiece material to compare the surface roughness obtained from FEM-IPT technique with that of experimental results. After the completion of the FE simulation, the image of the workpiece is extracted from the FE software for further processing. Extracted image is converted to a grey image and then the outer boundary (edge) is extracted. The surface roughness was calculated by using the extracted image. The experiments were performed and the predictions were validated. The comparison of numerical and experimental results shows that the prediction error varies between is **2.19−20.41%** and the average mean prediction error is about **8.71%.**

Overall, the present numerical works provided a realistic, simple, efficient integrated approach for roughness prediction during SPDT of ductile and brittle materials. Based on the results obtained, it is felt that the developed model can be applied with confidence in practice for quick and accurate computation of *in-situ* force and roughness measurement of SPDT process. Prior estimation of energy required for machining by using the computed cutting forces and quality of the surface produced can also be made using the developed numerical models.

CHAPTER 7

EXPERIMENTAL STUDIES ON SINGLE POINT DIAMOND TURNING PROCESS

7.0 Scope

This chapter presents the experimental study on SPDT of Al6061 material and parametric analysis on surface roughness to find the influencing parameters. First, the need to carry out physical experiments is defined. Details of the experimental study on SPDT of Al6061-T6 are elaborated in stage 1. Total 18 numbers of experiments have been performed on SPDT of Al6061-T6 by varying speed, feed, and depth of cut. Surface roughness values were measured using contact type 2D profilometer for each set of process conditions. A mixed level full factorial analysis of surface roughness was performed. A detailed discussion on the influence of process parameters on surface roughness is presented and finally, optimal parameters are presented.

7.1 The Need

The numerical investigations of SPDT process helped in understanding the mechanism of the process such as complex interaction between cutting tool and workpiece, material behavior (transition), etc. Moreover, based on simulations, the machining forces, ductile to brittle transition thickness, chip morphology and surface roughness were successfully obtained. However, it is difficult to take into account the effect of uncontrollable parameters such as imperfections in machine tool and cutting tool structures, errors in the setting of cutting tools, deformations, and vibrations in the structure of machine tool such as spindle, workpiece fixtures, and material inhomogeneity. In view of this, it was felt worth to carry out systematic and comprehensive experiments to determine proper levels of machining parameters to obtain desired process performance. Also, it was noted from the literature review that, very scant studies have been reported on obtaining optimal values of tool geometry and process parameters that influence the SPDT process. Moreover, the experiments were thought to be essential to validate the surface roughness prediction module.

7.2 Experimental Procedure

In the present work, experimental studies have been carried out to determine the performance characteristics of the SPDT process and to validate the surface roughness calculations. The experiments were carried out at Central Scientific Instruments Organization (CSIO) Lab at Chandigarh, India. In view of limited availability of SPDT machine for experiments and more tool wear of diamond tool in machining of Si and SiC, it was thought

appropriate to work on Al6061-T6 and to validate the developed FEM-IPT model. The experimental study was carried out in three steps.

1. Initially, based on trade and published research literature ranges of process parameters have been selected.
2. Preliminary experiments were carried out to fine tune the ranges of process parameters.
3. Finally, the main experiments were performed, and the influence of selected machining parameters on the performance of the SPDT process was studied. After the experiments, the recorded response data was carefully studied to determine the proper levels of machining parameters.

7.3 Experimental Setup

Experiments were carried out on a Nanoform-250, a precision two-axis computer numerically controlled (CNC) diamond turning machine from Taylor-Hobson, UK. It provides a position feedback resolution of 3.6 nm. Figure 7.1 shows the photograph of the experimental setup used. The facility availed for the current experimental study is located in Central Scientific Instruments Organization (CSIO) under Council of Scientific and Industrial Research (CSIR) at Sector 30C, Chandigarh, India. The Specifications of the SPDT machine are listed in Appendix 7.1. Mono-crystalline diamond tools of rake angle 0˚ having clearance angle of 10˚ supplied by Contour Fine Tooling, UK were used. For all the experiments, deionized water with pH value 7 was used as the coolant.

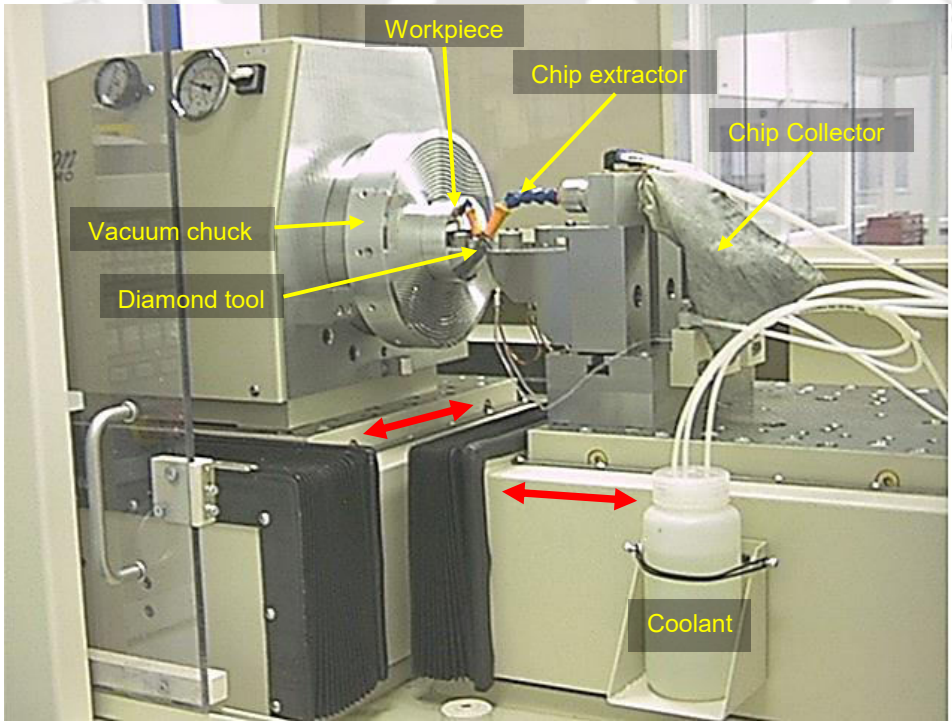

Figure 7.1 Experimental setup of SPDT

7.3.1 Workpiece

In this work, aluminum alloy 6061-T6, an aerospace grade commercial alloy has been used for conducting the experiments. It is a precipitation-hardened aluminum alloy, containing magnesium and silicon as its major alloying elements and it is solutionized, stress-relieved stretched and artificially aged. Al6061 has applications in aircraft fittings, camera lens mounts, brake pistons, hydraulic pistons, appliance fittings and valves. The alloy possesses high strength, good workability, low density and high corrosion resistance with excellent joining characteristics. The chemical composition of the alloy is listed in Table 7.1.

Table 7.1 Chemical composition of Al6061-T6 Al alloy (wt%)

Element	Cu	Fe	Si	Mn	Mg	Zn	Cr	Ti	Others	Al
Composition	0.15-0.4	0.70	0.4-0.8	0.15	0.8-1.2	0.25	0.04-0.35	0.15	0.15	Balance

The specimens were prepared by cutting 25 mm diameter and 12 feet long bar using a general center lathe machine (Make: Panther) as shown in Figure 7.2 (a). From the specimen, 18 samples were made (Figure 7.2 (c)).

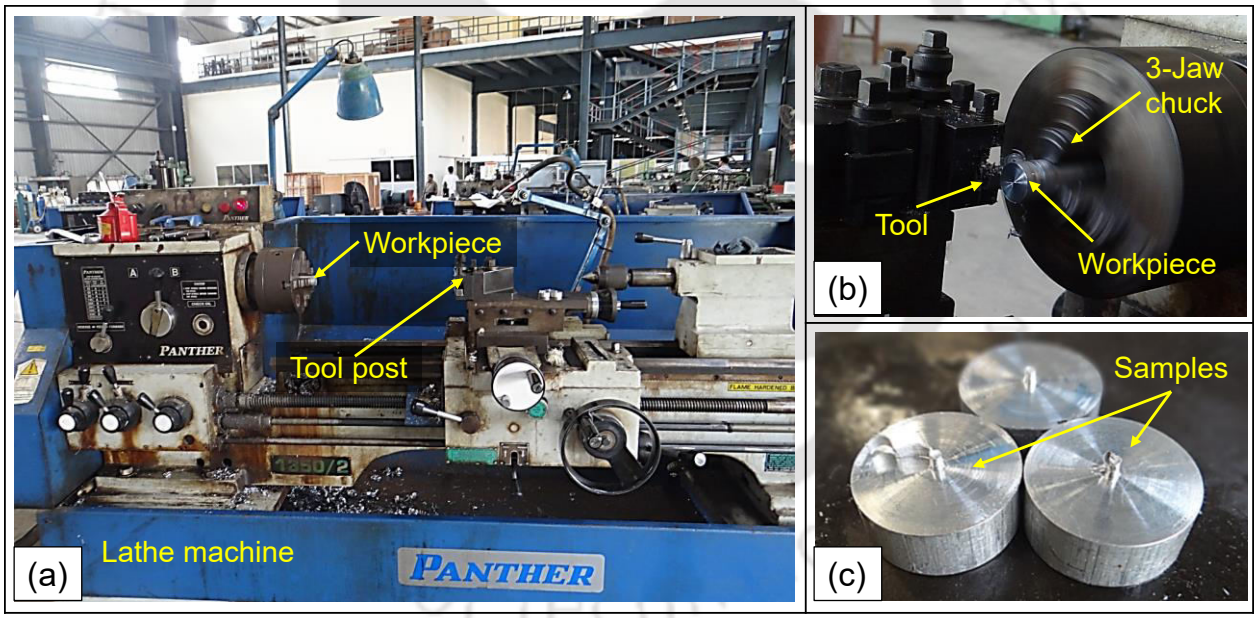

Figure 7.2 Preparation of sample for facing operation on SPDT

The samples thus obtained were highly rough and the surface was not completely flat. This is termed as wedge. It is difficult to fix the sample on the vacuum chuck if wedge is present on the surface. Because, air escapes through the gaps and holding cannot be done properly. To remove the wedge from the surface of specimen and to make the surface flat, all the samples were then fixed on a large aluminium plate using special water soluble wax as shown in Figure 7.3 (a). Rough cuts were made on SPDT machine. CBN tool was used to remove the wedges from the samples (Figure 7.3 (b)). After removing the wedge, all the

samples were taken out from large aluminium plat. During SPDT, a sample was fixed on the vacuum chuck. However, due to small diameter workpiece, sufficient vacuum could not be generated on the vacuum chuck due to small diameter workpiece. Therefore, a specialized fixture was made from an aluminium 6061 work material to mount the workpiece onto the vacuum chuck. The fixture is shown in Figure 7.3 (c). The samples were fixed one by one on to the fixture with double sided cello tap as shown in Figure 7.3 (d) for each cutting operation.

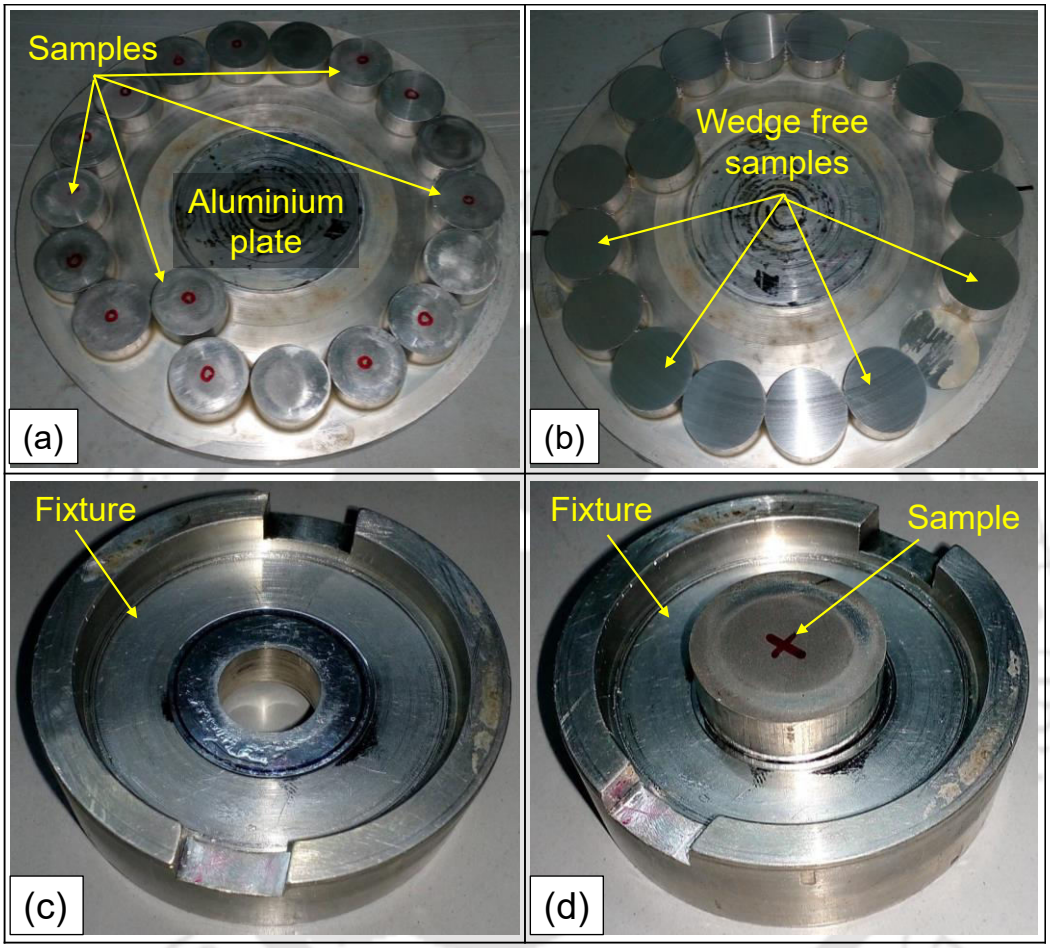

Figure 7.3 (a) Fixing of the samples to a large aluminum plate, (b) Samples after removing the wedge, (c) Fixture to hold the sample and (d) Sample with fixture

7.3.2 Cutting Tool

The experiments were conducted using monocrystalline diamond tool (Figure 7.4). These tools were having rake angle of 0˚, clearance angle of 10˚ supplied. These tools were of Contour Fine Tooling, UK make. It is resistant to abrasion, erosion, wear, compression, and heat; and it exhibits high hardness, thermal conductivity and longevity and nanometric sharpness.

Figure 7.4 Single point diamond tool from Contour Fine Tooling [Contour Fine Tooling, UK]

7.4 Measurement of Process Responses

The available SPDT machine was not equipped with the cutting force measurement facility (force dynamometer), therefore in this work, only the surface roughness parameter was measured. A contact type surface profilometer (Form Talysurf Series 2 (PGI) 120 Model from Taylor Hobson) was used for measuring the surface roughness. Figure 7.5 shows the surface profilometer. The specifications of the surface roughness equipment are given in the Appendix 7.2. The measurement was carried out by precise manoeuvring of a conical shaped diamond tip of radius 2 μm and 10 mm vertical range on to the machined surface to record the variation in the height along the length of measurement. The measurements considered a bandwidth of 300:1 (ISO 11562:1996 and ISO 3274:1996). The high filter cut-off (L_c) was fixed at 0.8 mm while the low filter cut-off (L_s) was fixed at 0.0025 mm.

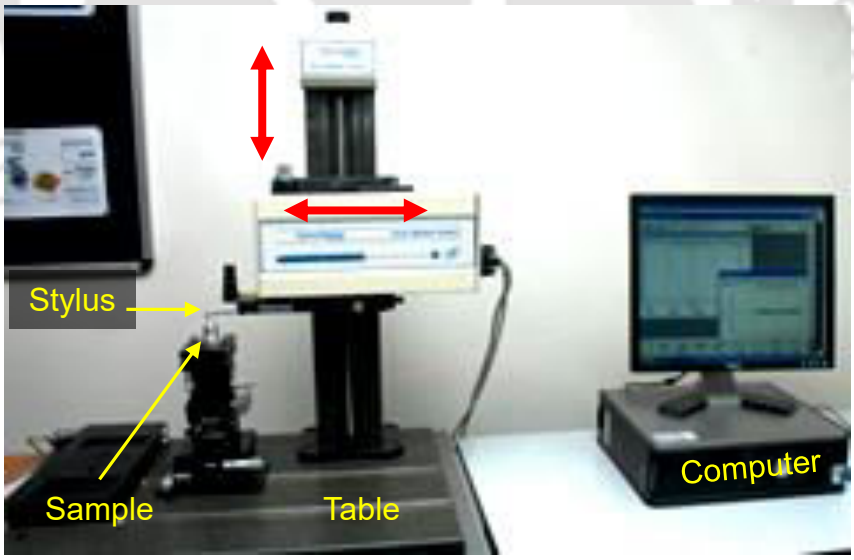

Figure 7.5 Taylor Hobson 2D Profilometer

7.5 Selection of Machining Parameters and their Levels

Selection of proper process parameters and their respective appropriate levels is important in view of an efficient and accurate machining process. The machining parameters were chosen by taking into account the capacity/limiting cutting conditions of the available

SPDT machine. Moreover the ranges of parameters suggested by the researchers in the literature [Khan *et al.* (2003), Mishra *et al.* (2014)] also have been considered. Cutting speed (v), feed rate (f) and depth of cut (d) were varied and their influence on the performance measure viz. surface roughness (Ra) was studied keeping other process parameter constant. The constant parameters are tool geometry, coolant, tool overhang. Table 7.2 lists the machining parameters and their levels.

Table 7.2 Machining parameters and their levels

Factors	Symbols	Levels		
Cutting speed (m/s)	s	1.309		2.356
Feed rate (µm/rev)	f	3	6	10
Depth of cut (µm)	d	1	10	20

7.6 Experimental Study based on Mixed Level Full Factorial Design

After the selection of parameters, experiments were carried out based on mixed level full factorial design of SPDT of Al6061-T6 rod of 25 mm diameter. Total 18 experiments were carried out and surface roughness was measured. Table 7.3 shows the experimental design and the corresponding measured surface roughness. The workpiece size was 25 mm of diameter and 10 mm of thickness. The specimens were then diamond turned by varying the tool feed rates (3, 6 and 10 µm/rev), cutting speeds (1.309 and 2.356 m/s) and depth of cuts (1, 10 and 20 µm) keeping all the other machining parameters constant. Repetition of the experiments was not done due the availability of the machine for a very limited period of time. The experimental surface roughness values were measured using a 2D profilometer (Taylor Hobson). Figure 7.6 shows the schematic of roughness measurement using 2D profilometer. The diamond stylus touches the roughness profile of the workpiece surface along the scan length.

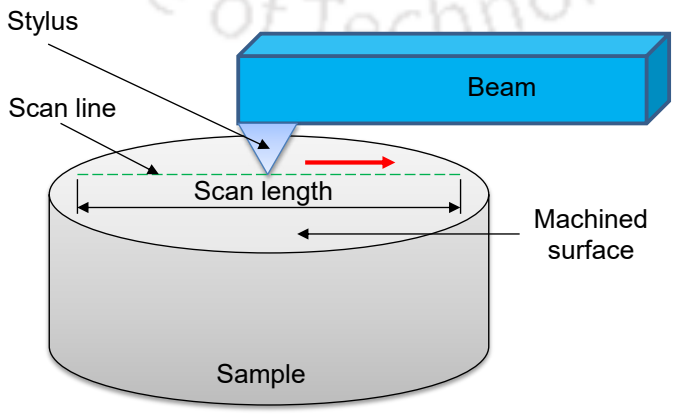

Figure 7.6 Measurement of surface roughness using 2D profilometer

Three sets of reading were made for each sample. The respective average values are listed in Table 7.3. After obtaining the response data (Ra), the significant factors were determined by using analysis of variance (ANOVA) method.

Table 7.3 Measured surface roughness for all the set of process combinations

Expt. No	Speed m/s	Feed µm/rev	Depth of Cut µm	Measured Ra nm
1	1.309	3	1	7.3
2	1.309	3	10	6.5
3	1.309	3	20	6.8
4	1.309	6	1	12.3
5	1.309	6	10	10.67
6	1.309	6	20	8.67
7	1.309	10	1	12.47
8	1.309	10	10	11.6
9	1.309	10	20	12.1
10	2.356	3	1	8.93
11	2.356	3	10	8.33
12	2.356	3	20	8.07
13	2.356	6	1	8.9
14	2.356	6	10	8.83
15	2.356	6	20	8.93
16	2.356	10	1	12.5
17	2.356	10	10	12.23
18	2.356	10	20	13.03

7.7 Results and Discussion

From the Table 7.3, it can be seen that minimum surface roughness value of Ra = 6.5 nm can be obtained for a combination of speed 1.309 m/s, feed 3 µm/rev and depth of cut 10 µm whereas the maximum surface roughness value (Ra) of 13.03 nm was noted at the speed of 2.356 m/s, feed rate of 10 µm/rev and depth of cut of 20 µm. Figure 7.7 and Figure 7.8 show the results obtained from profilometer measurement.

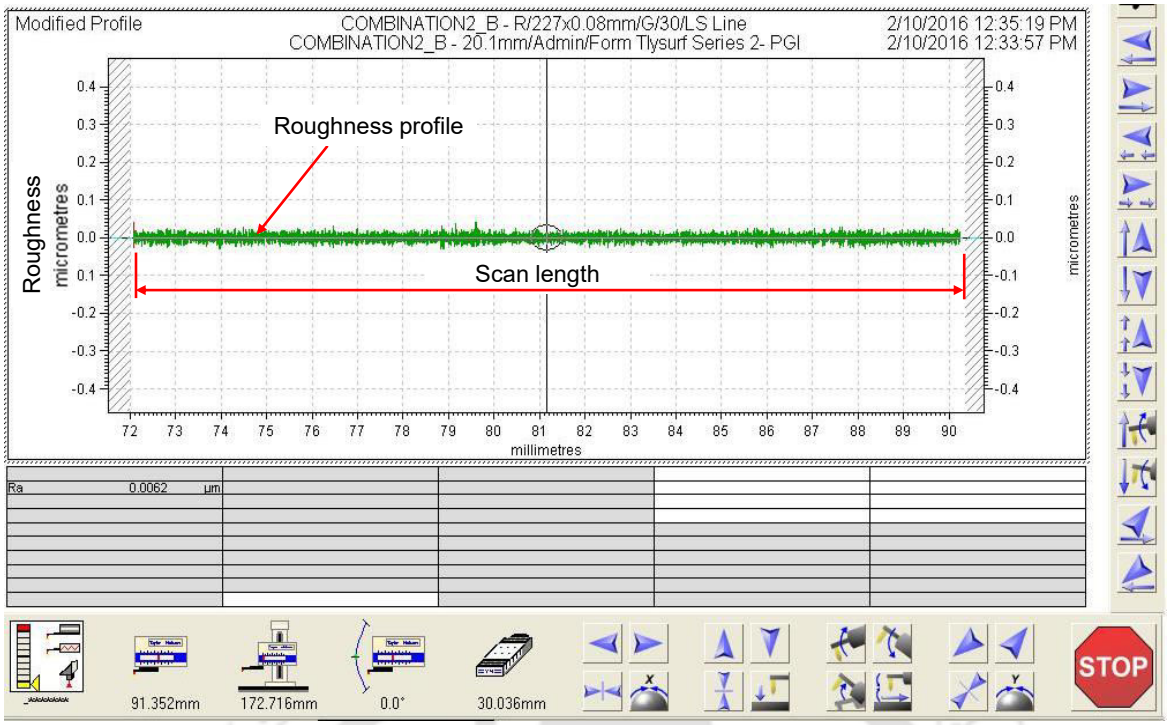

Figure 7.7 Roughness profile for least Ra = 6.5 nm (Process condition: Cutting speed=1.309 m/s, feed rate=3 µm/rev and depth of cut=10 µm)

Figure 7.8 Roughness profile for largest Ra =13.03 nm (Process condition: Cutting speed=2.356 m/s, feed rate=10 µm/rev and depth of cut=20 µm

The surface roughness values were plotted against the depth of cut and shown in Figure 7.9. It can be seen that at lower feed rate (3 µm/rev); a very good surface finish can be achieved for all the depths of cut (1, 10 and 20 µm). It is because of known fact that at lower feed rate, the feed marks are low. This also verifies the analytical expression ($R_t = f^2/8R$).

Here, R_t is the highest peak-to-lowest valley difference in sample length, f is the feed rate and R is the tool nose radius. It can also be observed that, depth of cut shows minimal effect on surface roughness as there are very less variation on roughness values with change in depth of cut. In ductile material machining, material removal takes place through plastic deformation. This reduces the chances of formation of surface damage during large depth of cut. However, it is observed that at feed rate of 6 μm/rev, increase in depth of cut decreases the roughness value. Large depth of cut removes more volume of work, thus the heat generation is substantial. This increases the heat at the cutting zone which leads to easy removal of material and improves the surface roughness.

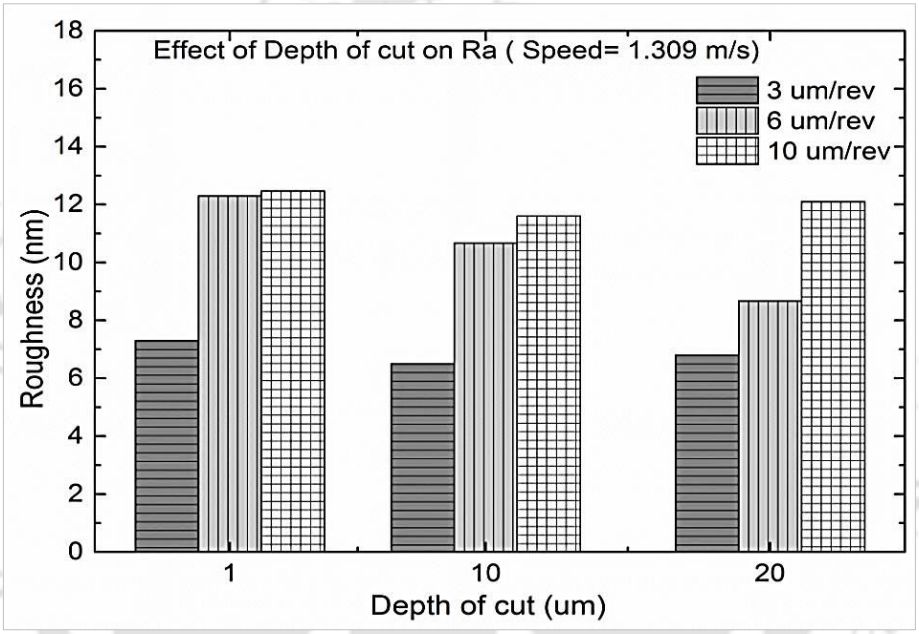

Figure 7.9 Effect of depth of cut on surface roughness (speed =1.309 m/s)

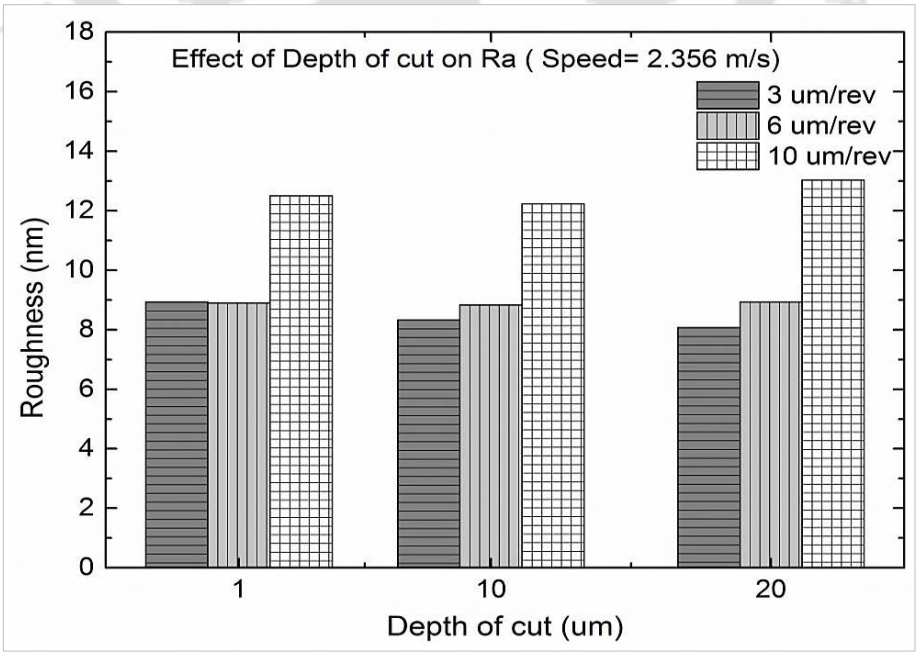

Figure 7.10 Effect of depth of cut on surface roughness (speed = 2.356 m/s)

Figure 7.10 shows the effect of depth of cut and feed rate on surface roughness at cutting speed of 2.356 m/s. It can be seen that the surface roughness value decreases with the increase in cutting speed. It is because, with the increase in cutting speed, more heat is generated that softens the material and the friction between the tool and workpiece decreases. Figure 7.11 shows the surface finish obtained from our experimental study. The figures show the mirror finishes that occur at the workpieces for the chosen process conditions.

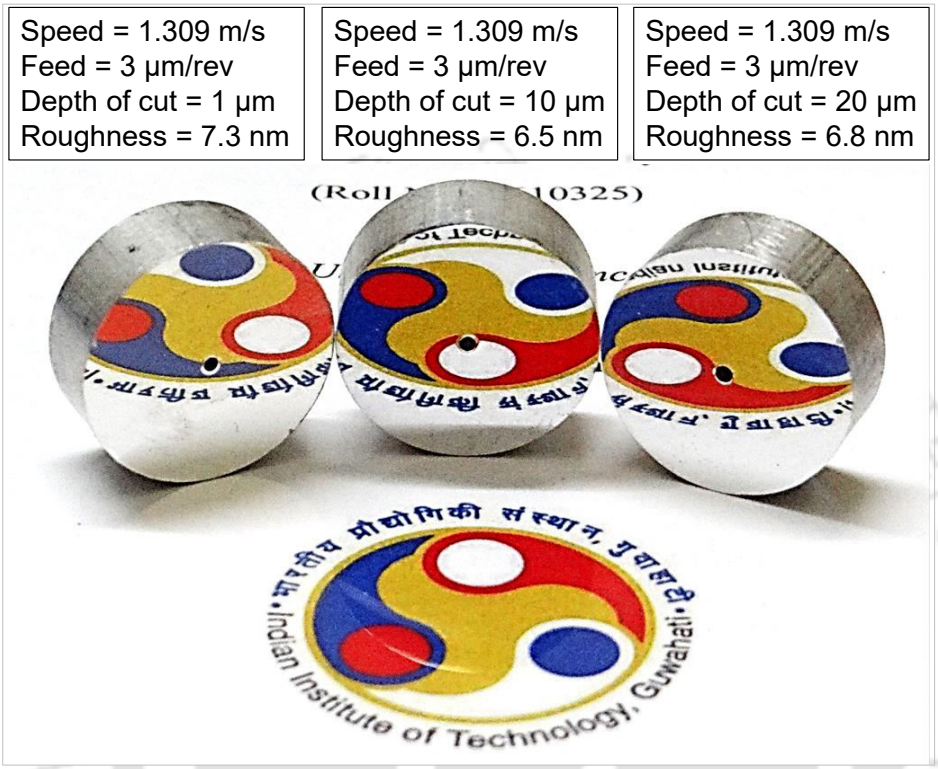

Figure 7.11 Mirror like surface obtained from SPDT of Al6061 alloy

The primary objective of the present the experimental study was to validate the developed integrated FEM-IPT model presented in Chapter 6 to predict the surface roughness using SPDT. After the successful validation of the developed model, it was planned to carry out a statistical analysis of the data that were generated during the full factorial experimental study. Following sections discusses the parametric analysis of surface roughness to determine the influential parameters.

7.8 Parametric Study

After the experiments, the ANOVA and regression analysis were carried out. The details are presented as below.

7.8.1 ANOVA Analysis

Table 7.4 shows ANOVA results for the linear factors such as speed (v), feed (f) and depth of cut (d) and their interactions ($v \times f$), ($v \times d$), and ($f \times d$). From the model analysis, 2 factorial interaction (2FI) model was found appropriate.

Table 7.4 Analysis of variance (ANOVA) results

Source	DF	Adj SS	Adj MS	F-Value	P-Value
Model	13	79.7707	6.1362	11.23	0.016
Linear	5	68.0245	13.6049	24.89	0.004
Speed	1	0.0998	0.0998	0.18	0.691
Feed	2	65.6285	32.8143	60.04	0.001
Depth of cut	2	2.2962	1.1481	2.10	0.238
2-Way Interactions	8	11.7462	1.4683	2.69	0.178
Speed*Feed	2	8.1838	4.0919	7.49	0.044
Speed*Depth of cut	2	1.4775	0.7388	1.35	0.356
Feed*Depth of cut	4	2.0849	0.5212	0.95	0.518
Error	4	2.1862	0.5466		
Total	17	81.9569			

S	R-sq	R-sq(adj)	R-sq(pred)
0.739294	97.33%	88.66%	45.98%

DF: Degree of freedom, SS: Sum of square, MS: Mean square

From the Table 7.4, it was noted that the factors: feed rate and interaction of speed and feed rate can be considered as significant model terms, because the associated p-values for these model terms are lower than 0.05, i.e., with 95% confidence level. The other model terms can be considered as insignificant. The value of R^2 as 97.33% indicates that the model explains 97.33% of the total variations. The value of R^2 (Adj.) as 88.66% represents that the model explains 88.66% of the total variability after considering the significant factors. However, R^2 (Pred.) value of 45.98 is considerably lesser than the R^2 (Adj.) and shows that the model would be expected to explain only 45.98% of the variability in new data. As there are many insignificant model terms, model reduction was carried out by backward elimination process to improve the model. The default backward elimination procedure ends when none of the variables included in the model have a p-value greater than the value specified in Alpha (α) to remove. In the present case, $\alpha = 0.2$ is chosen so that it does not eliminate important model terms. Table 7.5 shows the ANOVA table after eliminating insignificant. The reduced model results indicate that the model is significant with R^2 of 92.99% and adjusted R^2 of 88.08%, respectively. It is seen that, due to the elimination of insignificant model terms, R^2 (Pred.) has improved to 77.27%, and shows that the model would be expected to explain 77.27% of the variability in new data.

Table 7.5 Analysis of variance (ANOVA) results after eliminating insignificant terms

Source	DF	Adj SS	Adj MS	F-Value	P-Value
Model	7	76.2083	10.8869	18.94	0.000
Linear	5	68.0245	13.6049	23.67	0.000
Speed	1	0.0998	0.0998	0.17	0.686
Feed	2	65.6285	32.8143	57.08	0.000
Depth of cut	2	2.2962	1.1481	2.00	0.186
2-Way Interactions	2	8.1838	4.0919	7.12	0.012
Speed*Feed	2	8.1838	4.0919	7.12	0.012
Error	10	5.7486	0.5749		
Total	17	81.9569			

S	R-sq	R-sq(adj)	R-sq(pred)
0.758197	92.99%	88.08%	77.27%

7.8.2 Model Fitness Check

The adequacy of the modal has been investigated by the examination of residuals. The residuals, which are the differences between the respective observed response and the predicted response, are examined using normal probability plots of the residuals and the plots of the residuals versus the predicted response. If a model is adequate, the points on the normal probability plots of the residuals form a straight line.

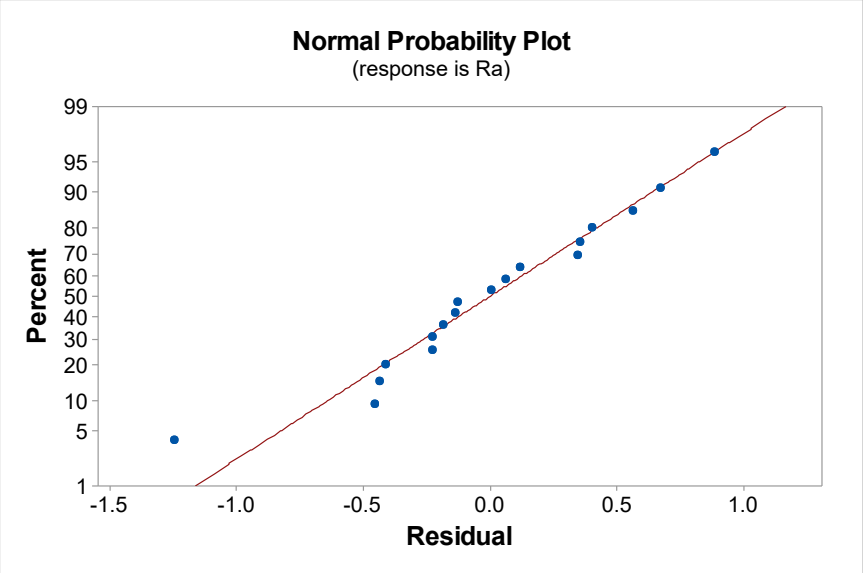

Figure 7.12 Normal plot of residuals for surface roughness

Figure 7.12 shows the normal probability distribution of the residuals for surface roughness. It can be noticed that the residuals points are clustered around a straight line, which means that the errors are normally distributed. Further, the observed values are compared with the predicted (fitted) values computed from the developed mixed level factorial model. This comparison is shown in Figure 7.13. It can be seen that the points are normally distributed along the horizontal zero line which indicates that the mixed level

factorial model is able to predict the response accurately since the error terms are having mean zero (Figure 7.14). In other words, the regression model is well fitted with the observed values.

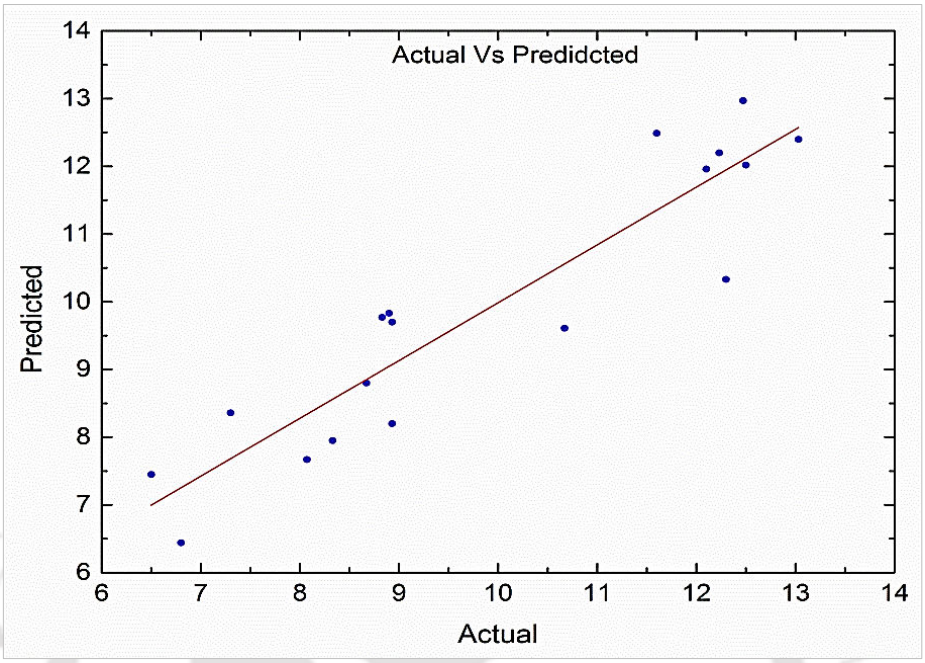

Figure 7.13 Plot of actual vs. predicted response of surface roughness

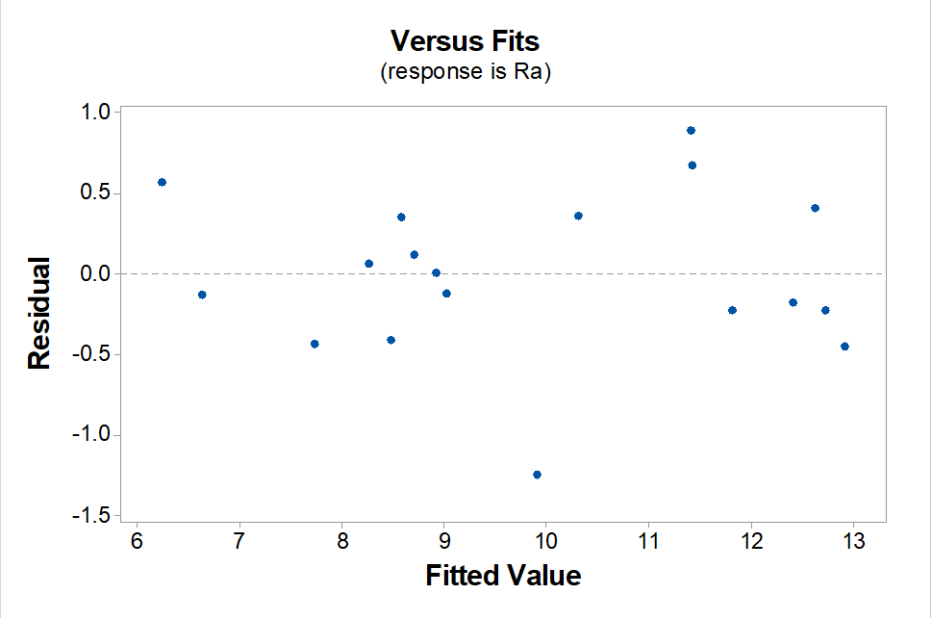

Figure 7.14 Residuals versus fitted value plot of surface roughness

7.8.3 Regression Analysis

Using regression analysis, mathematical expression was formulated for prediction of the surface roughness. By using this expression, the roughness values were predicted for all 18 sets of process conditions.

Regression Equation: After eliminating insignificant terms

$$Ra = 6.38 + 0.09\,v + 0.791\,f - 0.213\,d - 0.107\,v \times f + 0.0702\,v \times d + 0.0068\,f \times d \quad (7.1)$$

where, v is speed, f is feed rate and d is depth of cut.

7.8.4 Parametric Influence on Surface Roughness

The main effects of machining parameters on mean surface roughness are shown in Figure 7.15.

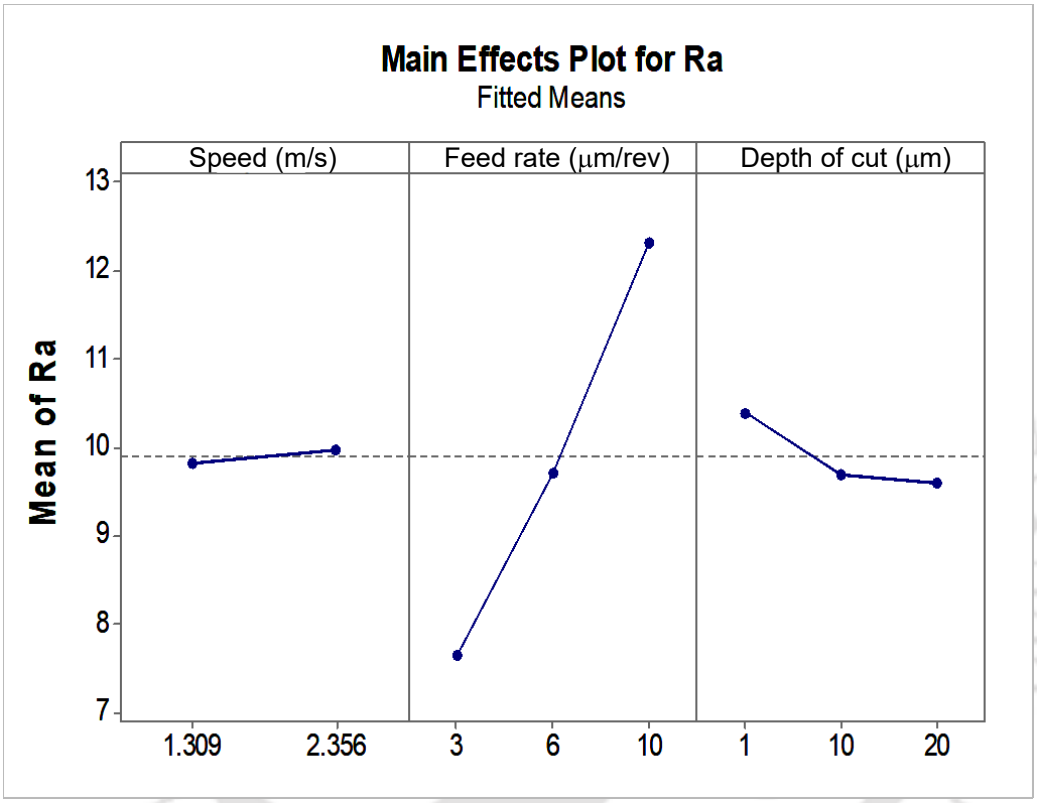

Figure 7.15 Main effect plot of surface roughness

It is found that the feed has the most significant effect on surface roughness followed by depth of cut and speed. The results also match with the ANOVA results shown in Table 7.5. This is due to the well-known fact that with increase in feed rate, the feed marks due to feed rate and tool nose radius increases. This can also be demonstrated with a schematic shown in Figure 7.16. For tools having same tool nose radius and same process conditions, increase in the feed rate from f_1 to f_2 increases the peak-to-valley roughness from R_{t_1} to R_{t_2}. Increase in the cutting speed improves the surface roughness. It is because at low spindle speed, the friction between the work-piece and the cutting tool is high due to the deposition of cut chips at the workpiece–tool interface. This causes interruptions during cutting operations leading to a poor surface quality. As the spindle speed increases, the coefficient of friction between the workpiece and tool interface decreases, and continuous chips are formed. This

leads to better surface quality. However, present main effect analysis shows almost same surface roughness with the increase in cutting speed from 1.309 m/s to 2.356 m/s. This could be the effect of chatter or vibration which occurs at the higher cutting speed. At 2.356 m/s cutting speed, the spindle was rotated at 2000 RPM. Similar observation was reported by Mishra *et al.* (2014) during study on the effect of machining parameters and tool overhang in SPDT of aluminium-6061.

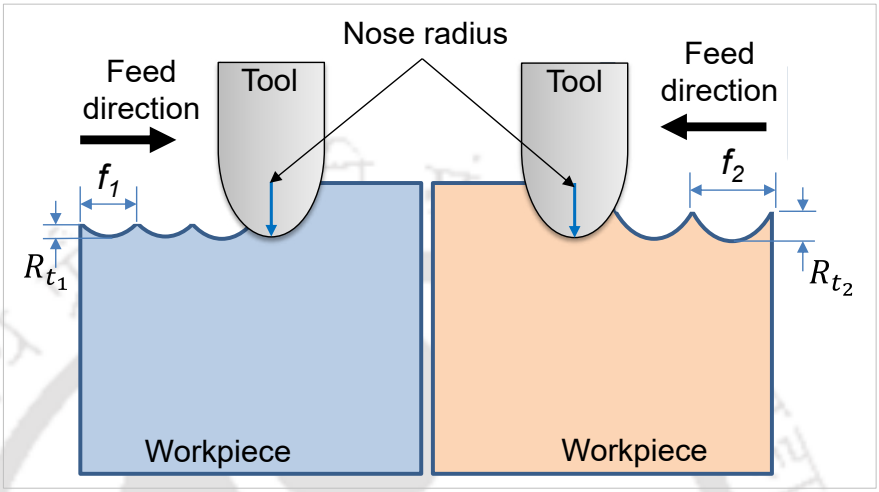

Figure 7.16 Schematic of effect of feed rate on surface roughness

From Figure 7.15, it can also be seen that surface roughness improves with the increase in the depth of cut. This contradicts with the theory that increase in depth of cut deteriorates the surface roughness. This may be due to fact that, at lower depth of cut, i.e., 1 µm, the critical undeformed chip thickness is smaller than the cutting edge radius (200-300 nm) of the diamond tool. This results in roughing/ploughing instead of machining of workpiece. This leads to swelling and elastic recovery effect and thus deteriorate the surface roughness. This phenomenon can be understood with the help of a schematic shown in Figure 7.17. Due to large tool edge radius, some part of the material from the undeformed chip thickness pushed below the tool. Tool does not remove the extra material, instead, it indents onto the machined surface and the material gets embedded in to the machined surface. Residual stresses are generated on indented material due to which some part of it recovers back when the tool leaves the region. This elastic recovery depends on material properties and tool geometry [Kong *et al.* (2006)]. At higher depth of cut, the cutting edge radius becomes smaller than the critical undeformed chip thickness and thus the ploughing process vanishes slowly and the cutting occurs smoothly. The main effect plot clearly shows that the mean surface roughness is minimum, when the smaller values of cutting speed, feed rate and higher value of depth of cut are employed.

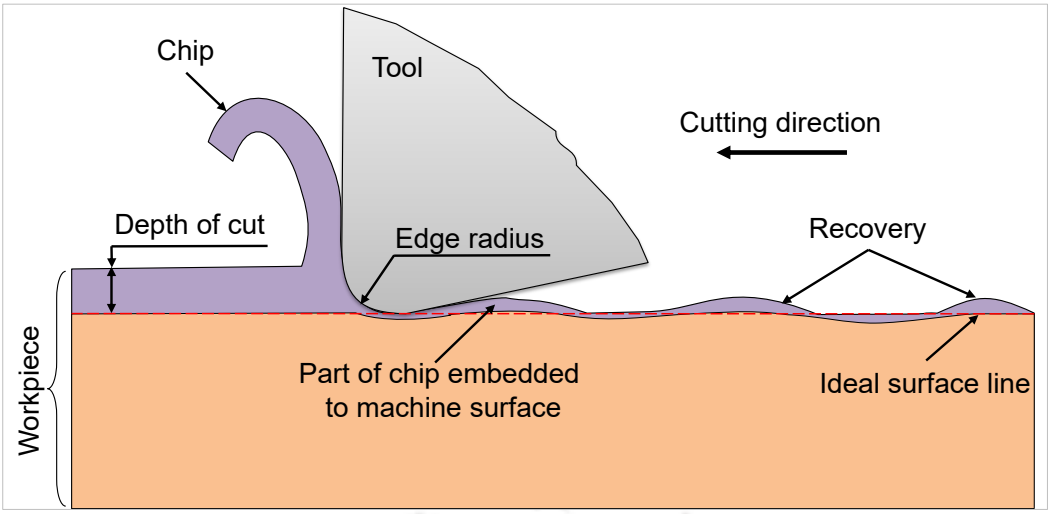

Figure 7.17 Schematic of material recovery and swelling during ductile material cutting

Interaction effects of speed and feed rate on the surface roughness are shown in Figure 7.18 (a). It can be observed that, minimum surface roughness can be achieved with a combination of low feed rate (3 µm/rev) and speed (1.309 m/s). It is also seen that with the increase in cutting speed, the surface roughness increases. This could be due to the increase in machine vibration at higher speed. However, at feed rate of 6 µm/rev, increase in depth of cut decreases the roughness value. This is possibly due to elastic recovery and material swelling at lower depth of cut as explained earlier. Higher feed rate leaves tool mark on the surface machined. Thus, higher feed rate increases the surface roughness.

Figure 7.18 (b) shows the estimated response plot for surface roughness for variation in the cutting speed and depth of cut. It can be seen that increase in the cutting speed increases the surface roughness for depth of cut of 10 and 20 µm. However, at depth of cut of 1 µm, roughness value slightly decreases as the speed increases. This could be due to the burnishing phenomenon occurring at this depth of cut because the critical undeformed chip thickness is very small. With an increase in the cutting speed, the friction between the workpiece-tool interfaces reduces. Hence, surface roughness reduces with an increase in the cutting speed. The interaction plot of feed rate and depth of cut and its effect on surface roughness is shown in Figure 7.18 (c). It can be observed that the low feed rate and high depth of cut produce fine surface quality. It is also observed that the increase in feed rate and a decrease in depth of cut deteriorate the surface quality.

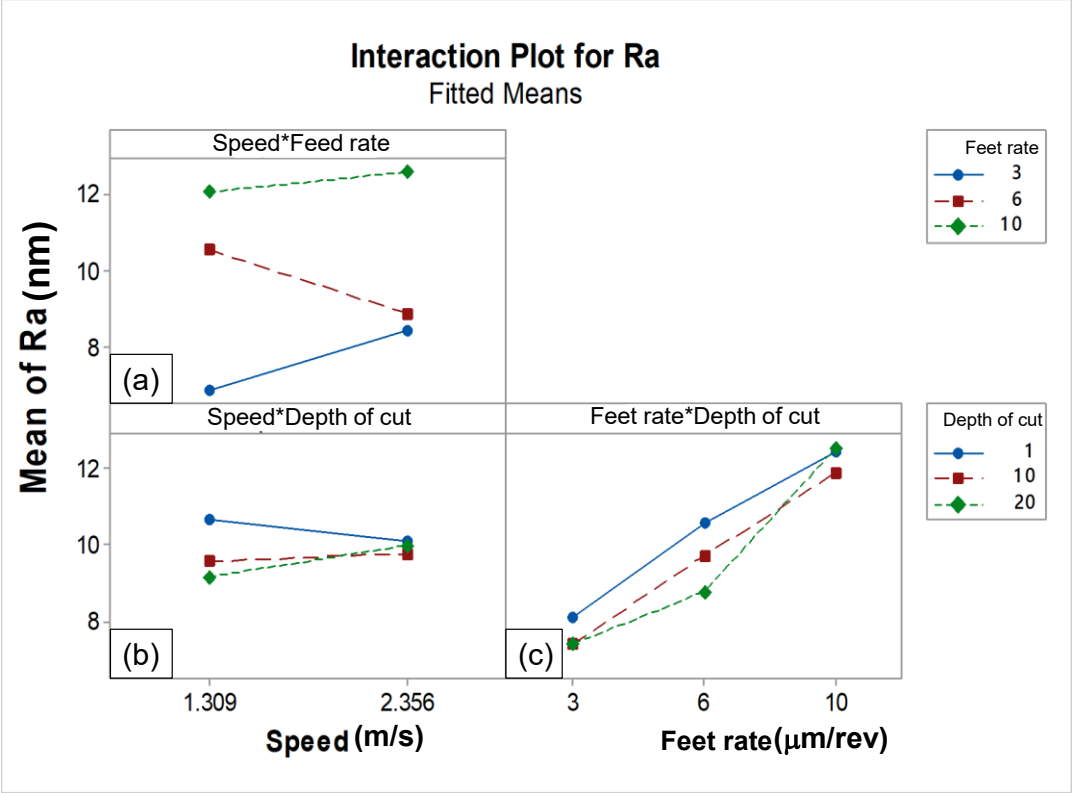

Figure 7.18 Interaction plot for surface roughness

7.8.5 Regression Modeling of Surface Roughness using Factorial Analysis

After the experiments, regression equation was derived based on the generated data. By using the equation, the surface roughness values were predicted. The comparison of measured and predicted roughness values are shown in Figure 7.19 and Table 7.6.

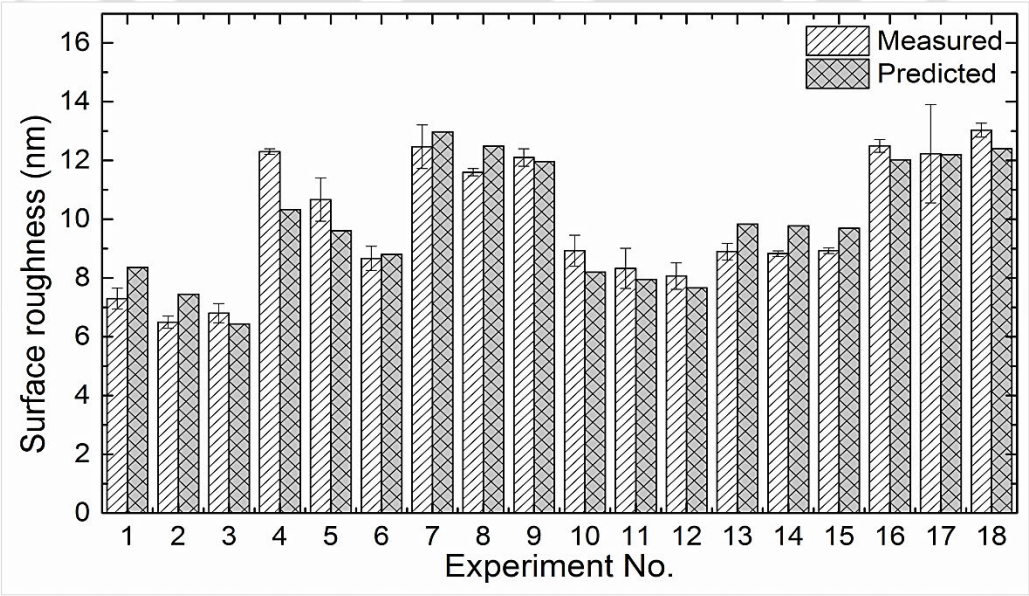

Figure 7.19 Measured vs. Predicted surface roughness plot

From the Figure 7.19 it is clear that the experimental roughness and the roughness from the derived mathematical expressions are in good agreement. Results show that the

average mean percentage error between measured and predicted surface roughness is about 7.3%. Based on the Table 7.6, it can also be observed that the superior surface can be achieved at a process condition of cutting speed of 1.309 m/s, feed rate of 3 μm/rev and depth of cut of 10 μm (Experiment number 2). Therefore, these parameters are recommended for their application in practice.

Table 7.6 Measured and predicted surface roughness for all the set of process combinations

Expt. No	Cutting speed m/s	Feed μm/rev	Depth of Cut μm	Measured Ra nm	Predicted Ra nm	Mean error
1	1.309	3	1	7.3	8.36	14.52
2	1.309	3	10	6.5	7.45	14.62
3	1.309	3	20	6.8	6.44	−5.29
4	1.309	6	1	12.3	10.33	−16.02
5	1.309	6	10	10.67	9.61	−9.93
6	1.309	6	20	8.67	8.8	1.50
7	1.309	10	1	12.47	12.97	4.01
8	1.309	10	10	11.6	12.49	7.67
9	1.309	10	20	12.1	11.96	−1.16
10	2.356	3	1	8.93	8.2	−8.17
11	2.356	3	10	8.33	7.95	−4.56
12	2.356	3	20	8.07	7.67	−4.96
13	2.356	6	1	8.9	9.83	10.45
14	2.356	6	10	8.83	9.77	10.65
15	2.356	6	20	8.93	9.7	8.62
16	2.356	10	1	12.5	12.02	−3.84
17	2.356	10	10	12.23	12.2	−0.25
18	2.356	10	20	13.03	12.4	−4.83
					Absolute error	**7.28**

7.9 Summary

This chapter presented a systematic experimental study on SPDT of aluminum alloy 6061-T6. Full factorial experiments were carried out by varying cutting speed at two levels, feed rate at three levels and depth of cut at three levels. Total 18 experiments were performed and the process performance in terms of surface roughness was recorded for each experiment. Results were studied and the findings were presented with suitable scientific justification. Then, a mathematical model for the prediction of surface roughness has been developed using mixed-level factorial analysis. Optimum values of machining parameters producing minimum surface roughness were found out. The following are some of the conclusions drawn from the study:

- The feed has the most significant effect on surface roughness followed by depth of cut. Speed has minimal effect on surface roughness.

- The mathematical model developed using factorial analysis predicts the surface roughness with 7.3% prediction error.
- The surface roughness varied between 6.5 to 13.03 nm within the scope of experiments.
- Low cutting speed and feed rate and high depth of cut were found to provide better surface finish within the scope of present process conditions.
- The minimum surface roughness of 6.5 nm was found at a cutting speed of 1.309 m/s, feed rate of 3 µm/rev and depth of cut 10 µm.

Chapter 8 summarizes the research carried out in the present work. It also presents the conclusions and research contributions.

CHAPTER 8

CONCLUSIONS AND FUTURE WORK

8.0 Overview

The primary objective of the present research work was to improve the surface quality and process efficiency by conducting systematic numerical and experimental studies on single point diamond turning of the brittle and ductile materials. The work reported herein was carried out in the following stages:

- Development of a finite element based two-dimensional plane strain non-linear dynamic explicit numerical model of nanoindentation and plunge cutting process to determine the ductile to brittle transition (DBT) thickness and to understand the ductile regime machining (DRM) of brittle materials.
- Development of a two-dimensional numerical model of SPDT process of silicon and silicon carbide using FEM followed by experimental validation of the developed numerical model in terms of machining force values.
- Development of an integrated finite element method-image processing technique (FEM-IPT) based model for the prediction of surface roughness during SPDT of Al6061-T6 and silicon.
- Experimental studies of SPDT of Al6061-T6 to validate the developed FEM-IPT model and to investigate the influencing parameters such as speed, feed, and depth of cut on surface roughness.

Important observations and research contributions from the present work are summarized in the section to follow.

8.1 Conclusions and Research Contributions

Specific contributions of the current research work are presented below.

8.1.1 A Study on Ductile Regime Machining using Numerical Simulations of Nanoindentation

In this work, a study on ductile regime machining of brittle materials such as silicon (Si) and silicon carbide (SiC) has been carried out using finite element method based nanoindentation simulation. The displacement controlled quasi-static 2D-axisymmetric nanoindentation simulations were carried out by following the non-linear dynamic explicit

solution step method. Pressure sensitive Drucker-Prager material model has been employed to define the material behavior.

- During the FEM model development, sensitivity analysis was carried out for selecting suitable FEM parameters. It was found that the 2D axisymmetric model with spherical shaped indenter of radius 300 nm and loading speed 0.1 mm/s and coefficient of friction μ = 0.1 with an element size of 0.00001 mm gives good results. The P-h plot closely matches with the experimental results.
- The numerical simulations of nanoindentation of SiC and Si were found to be predicting well with an overall prediction error of 15.4% respectively.
- Developed numerical model predicted Young's modulus and hardness of SiC as 347-459 GPa and 13-35 GPa. For silicon, our model predicts Young's modulus and hardness as 153-197 GPa and 16-28 GPa respectively. These values fairly match well with the established Young's modulus and hardness values reported by Saddow and Agarwal (2004), Goel (2014), and Reddy (2008). The reported values of Young's modulus and hardness for SIC are 424 GPa and 20-30 GPa respectively, and for silicon are 190 GPa and 12 GPa respectively. This indicated that the FEM based numerical model can be used to compute Young's modulus and hardness without conducting experiments.
- von-Mises stresses were noted to be 16 GPa and 38 GPa when the indenter's depth was around 91 nm and 375 nm for Si and SiC respectively. At these depths, cracks/fractures have seen to be initiated. These pressures are higher than the hardness of the workpieces (12 GPa for silicon and 26 GPa for SiC) that felicitate the phase change of silicon and silicon carbide.
- The critical depth of indentation, i.e., ductile to brittle transition was studied carefully. The depths of indentation before the initiation of fracture were found to be around 91 nm for Si and 375 nm for SiC. These values match well with the already published results where the ductile to brittle transition thickness of silicon was reported to be 50–200 nm and SiC of 300-500 nm.
- During 3D spherical indentation simulation, irregular stress (compressive) fields were observed. This is due to the presence of dislocations below the amorphous layer just underneath the indenter tip. When the indentation process begins, stress is developed in the workpiece as the indenter is forced into the workpiece surface. However, due to the presence of dislocations, nucleation of fracture is initiated. Due to these micro fractures, stresses field of lesser stress were found during the simulation. This triggers the plastic deformation and permanent shape change of the workpiece during the nanoindentation

process. These observations are found in line with previously reported literature by Jasinevicius *et al.* (2005) and Nix and Gao (1998).

- Further, the average stress was calculated along the contact surface between indenter and SiC specimen and plotted against the indentation depth. It was noted that the stress increases linearly up to certain depth (~120 nm) and when it reaches the threshold, the dislocation initiates in the form of small microcracks. Due to the movement of dislocations, some of the stresses get absorbed; this leads to irregular stress plots. After the completion of dislocation movements, linear stress of 30–35 GPa was obtained which is near to the phase changing pressure. Similar plots and observations can also be seen in the literature [Szlufarska *et al.* (2004, 2005)] from molecular dynamics simulations. Hence, it can be concluded that the ductile to brittle transition thickness is 120 nm.
- During the study of the effect of residual stress using multiple indentation process, it was found that Young's modulus and hardness values of multiple nanoindentations were lesser than the stress-free indentation. This may be due to the fact that in the first 10 nm loading, silicon undergoes a phase change as the indentation stress exceeds the hardness of silicon. An amorphous layer of silicon forms when the indenter is removed and pressure is reduced to below 4 GPa. Because of the amorphous layer, hardness and Young's modulus value decreases.
- Displacement controlled quasi-static 2D-axisymmetric nanoindentation simulations were performed on Si and SiC specimen using a spherical indenter. Quasi-static nanoindentation simulation in particular permits systematic examination to enable a better understanding of deformation mechanisms, evaluation of mechanical properties, and aspects of the plasticity of brittle materials such as Si and SiC.
- Overall, the present work provided a realistic, simple, efficient integrated approach for the prediction of load-displacement, mechanical properties and ductile to brittle transition during nanoindentation of brittle materials. Based on the results obtained, it is felt that the developed FEM model can be applied with confidence in practice for quick and accurate computation of mechanical properties and ductile to brittle transition.

8.1.2 A Study on Ductile Regime Machining using Numerical Simulations of Plunge Cutting

The nanoindentation study could able to provide useful information such as mechanical properties and ductile to brittle transition thickness of brittle materials. However, the proposed model does not provide the clear information about the machining, quality of surface machined and chip morphology which is vital in deciding the machining parameters to obtain the desired process performance during SPDT process. Hence, in the present work, numerical

simulations of plunge cut or taper cut were carried out on silicon and silicon carbide using a diamond tool to study the ductile to brittle transition zone. During the study, various output parameters such as machined surface, cutting force and specific cutting energy were thoroughly observed and analyzed. Plunge cutting simulations were carried out by using a diamond tool having rake angles of 0º, −25º and −30º, clearance angle of 10º. To achieve an inclined motion of the tool, i.e., continuously varying depth of cut from 0 to 600 nm, tool has been given simultaneous speeds along *x* and *y*-axis directions.

- During the first step, it was found that, for 0º rake angle tool, the first brittle fracture occurs at the depth of cut of 211.4 nm, which can be considered to be the critical depth of cut. Similarly, for –25º and –30º rake angles, the critical depths of cut were found to be 225.41 nm and 243.16 nm respectively.
- In the second step of the study, the variation of machining forces as a function of depth of cut was analyzed to determine the critical depth of cut. It was seen that the variations in machining forces were uniform up to a depth of cut of 78 nm in case of 0º rake angle tool. Beyond this depth, high fluctuation of force value was noted. A similar observation was noted at plunge cutting with –25º and –30º rake angle. The corresponding transition depths were found to be around 84 and 108 nm respectively.
- In the third step, specific cutting energy was calculated using the cutting force, chip area and then the critical depth of cut (CDC) was identified. Intersection points of linearly fitted lines of high slopes and flat slopes were calculated. The estimated CDCs were found to be in the range of 24.02, 27.34 and 34.12 nm corresponding to rake angles 0º, −25º and −30º.
- Overall it was noted that the CDCs obtained from the visual inspection were the highest and CDCs from the SCE method were the lowest. Similar trends of variation of transition depths were noted in case of 0º and −25º rake angle tool for all three methods. However, the CDCs obtained from the force analysis were found close to the experimental CDCs reported in the available literature and the nanoindentation simulations described in Chapter 3.
- From the comparison of three methods, it was observed that the critical depths of cut obtained from surface profile analysis (visual inspection) are higher than the experimental results. This is due to the fact that the micro-cracks formed at the transition zone are difficult to identify via visual inspection. It will require a complicated image processing technique which is time-consuming and computationally costly. SCE analysis significantly underestimates the transition depth values. This may be due to the fact that the actual chip area could not be considered while calculating the specific cutting energy,

as only 2D plane strain condition was considered. The critical depth of cut obtained from the force analysis was found to be fairly close to the experimental values.

- In addition, simulations were carried out for silicon carbide and the critical depth of cut was determined by using only the force analysis. It was found that the critical depths of cut were found to be around 65 nm for 0°, –25° and –30° rake angles.

8.1.3 Numerical Modeling and Simulation of Cutting Forces during Single Point Diamond Turning Process

In this research work, a two-dimensional non-linear dynamic-explicit numerical model was developed for machining of silicon and silicon carbide using finite element method. A detailed approach to model the cutting process that captures ductile fracture leading to material separation has been presented.

- Machining forces were calculated from the simulations and validated with the published experimental results. Results show that the results of the developed numerical model matches well with experiments. However, the model over-predicts the forces in comparison with those obtained from the experiments reported by Patten *et al.* (2005, 2008). It is due to various simplifying assumptions such as workpiece material is isotropic and homogeneous; cutting was considered as perfectly orthogonal. However, the results predicted by the model were found in good agreement with the reported experimental results.
- In the present work, the effect of the application of two different material models viz. Johnson-Cook (JC) and Drucker-Prager (DP) on the chip formation during nanometric cutting simulation of SPDT of SiC was carried out. Results showed that the selection of the material model plays an important role in the accurate prediction of force. Based on the present study, it can be concluded that JC material model is better than the DP model when analyzed quantitatively. However, in the mechanistic point of view, the JC model was found not suitable for the simulation of SPDT of brittle material.
- The present study verified that JC material model represents the ductile material model whereas DP material model represents brittle behavior. This has been carried out with the help of quantitative analysis of crack propagation mechanism and chip morphology study during machining of silicon carbide. It was noticed that the JC model takes more time to propagate the crack from the initial point to the free surface.
- During the simulation of SPDT of SiC, five different stages of chip formation were noted. These are: loading and stress field, crack initiation, crack propagation, chip formation, and surface and sub-surface damage.

- Parametric studies were carried out using full factorial approach to study the behavior of SPDT of silicon carbide by varying the rake angle, depth of cut and depth to cutting edge radius (d/r) ratio. The study revealed that the depth of cut has the most significant effect on both cutting force and thrust force followed by rake angle and d/r ratio. Both the cutting force and thrust force were found to increase with the increase in depth of cut and negative rake angle. However, they decrease with the increase in d/r ratio. A mathematical model was developed for SPDT of silicon carbide using regression analysis to predict the machining forces. The confirmation simulations showed that the regression model predicts the process response with good accuracy (prediction error of below 9%).
- The process conditions were optimized for obtaining minimum machining forces. Based on the present investigation, an optimal process condition of rake angle of −25°, depth of cut of 100 nm and d/r ratio of 5 is recommended to obtain minimum cutting force and thrust force. On employing the optimal process conditions, the cutting force and thrust force obtained were 0.087 N and 0.042 N respectively for desirability value of 1.
- Numerical analysis of SPDT of silicon has also been carried out. The predicted results were validated by comparing with the published experimental data and found in good agreement. The absolute prediction percentage errors for cutting force and thrust force with –45° and –85° rake angles were 1.93, 14.96, 14.05 and 16.13 respectively. The mean absolute error was calculated and was about 11.76%.
- Simulation of chips formation and the morphology study revealed that the hydrostatic pressure developed at the cutting zone is indeed favorable for the ductile fracture to occur. It was observed that to produce necessary compressive stress for ductile regime machining of brittle materials, the tool with negative rake angle is to be employed or depth of cut should be sufficiently smaller than the cutting edge radius of the tool.
- During the simulation of SPDT of silicon with 40 nm cutting edge radius, 20 µm/min cutting speed and 5 nm depth of cut, it was observed that SPDT becomes rolling/ploughing process. It is due to the application of very small depth of cut in comparison with the edge radius, and the subsequent occurrence of extreme negative rake angle (–45º and –85º). This is called ‘zero cutting zone’ within which no chips are produced. In this zone, the tool acts more like a roller than a cutter and continuously slides on and burnishes the machined silicon surface. A small amount of spring back effect was also observed in case of very low depth of cut with high negative rake angle tool which adds more emphasis on rolling action rather than metal shearing.
- Parametric studies were carried out to study the behavior of SPDT of silicon by varying cutting speed, rake angle, depth of cut and tool edge radius using response surface

methodology. ANOVA analysis and main effect plot study revealed that both rake angle and depth of cut have most significant effect on cutting force as well as thrust force, whereas the cutting speed and tool edge radius have minimal influence. Both cutting force and thrust force were found to be increased with the increase in depth of cut, negative rake angle and cutting edge radius. Increase in the cutting speed showed a marginal effect on the cutting force and thrust force. Both the forces decrease slightly with the increase in cutting speed.

- The regression model was found to be predicting the machining forces with mean prediction error of about 5% during the confirmation experiments. The optimal process conditions obtained were found to be as cutting speed of 0.68 mm/min, rake angle of −45°, depth of cut of 10 nm and cutting edge radius of 20 nm for generation of minimum cutting force and thrust force with desirability value of 0.967. The predicted values of forces were 0.179N and 0.183N. It can be stated that these optimum levels of process conditions can be employed in practice with confidence.

8.1.4 Numerical Prediction of Surface Roughness during Single Point Diamond Turning

In the present work, FEM based numerical model of SPDT process was integrated with image process technique to predict the surface roughness. The developed technique is simple and efficient. It can be used to analyze and study the roughness before carrying out actual experiments. This numerical model was successfully employed for the prediction of surface roughness during the nanometric cutting of Al6061. This eliminates the need to carry out costly, time-consuming and tedious experiments.

- The comparison of predicted results with actual shows that the mean prediction error between experimental roughness and numerically predicted roughness during SPDT of Al601-T6 is between 2.19−20.41% and the overall mean prediction error is found to be 8.41%.
- The present study indicates that the developed integrated FEM-IPT technique predicts roughness value well during the FEM simulation of the precision machining operation. Based on the results obtained, it is felt that the developed model can be applied with confidence in practice for quick and accurate computation of *in-situ* force and roughness measurement of SPDT process.

8.1.5 Experimental Studies on Single Point Diamond Turning Process

In this work, a systematic experimental study on SPDT of Al6061 material has been carried out and parametric analysis on surface roughness was performed to determine the influencing parameters. Total 18 numbers of experiments based on mixed level full factorial design were performed. The effect of variation in speed, feed, and depth of cut on the surface roughness was studied.

- Experimental results showed that a very good quality surface with surface roughness value of 6.5 nm can be obtained for a combination of speed 1.309 m/s, feed 3 μm/rev and depth of cut 10 μm. Maximum surface roughness value of 13.03 nm was noted at the speed 2.356 m/s, feed 10 μm/rev and depth of cut 20 μm.
- From the ANOVA and main effect plots, it was found that the feed has the most significant effect on the surface roughness followed by depth of cut. The cutting speed has minimal effect on the surface roughness. Low levels of cutting speed and feed rate, while high depth of cut were found to provide better surface finish within the scope of present experiments.
- The mathematical model developed using factorial analysis predicts the surface roughness with 7.3% prediction error.

8.2 Recommendations for Future Work

The present research work can be extended on the following fronts.

- To carry out numerical (FEM) simulations of micro-cutting by SPDT process using Modified- J C model.
- Carrying out the thermo-mechanical (FEM) analysis for SPDT of other industrial important materials such as germanium, glass, titanium, etc.
- Numerical modeling and simulations of diamond tool wear and tool deflection using FEM.
- Investigations on the influence of tool path strategies on the product quality.
- Comprehensive 3D numerical analysis of SPDT process using parallel computing techniques.

References

- ABAQUS 6.11, (2011) Documentation and user's manual, Simulia, DASSAULT, Version 6.11
- Abdulkadir, L. N., Abou-El-Hossein, K., Jumare, A. I., Liman, M. M., Olaniyan, T. A., & Odedeyi, P. B. (2018). Review of molecular dynamics/experimental study of diamond-silicon behavior in nanoscale machining. *The International Journal of Advanced Manufacturing Technology*, 1-55.
- Ajjarapu, S. K., Patten, J. A., Cherukuri, H., & Brand, C. (2004). Numerical simulations of ductile regime machining of silicon nitride using the Drucker-Prager material model. *Proceedings of the Institution of Mechanical Engineers, Part C: Journal of Mechanical Engineering Science*, *218*(6), 577-582.
- Akram, S., Jaffery, S. H. I., Khan, M., Mubashar, A., & Ali, L. A Numerical Investigation of Effects of Cutting Velocity and Feed Rate on Residual Stresses in Aluminum Alloy Al-6061.
- Alder, B. J., & Wainwright, T. (1957). Phase transition for a hard sphere system. *The Journal of chemical physics*, *27*(5), 1208-1209.
- Alexander, H., & Haasen, P. (1969). Dislocations and plastic flow in the diamond structure. In *Solid state physics* (Vol. 22, pp. 27-158). Academic Press.
- Ali, S. H. (2012). Advanced nanomeasuring techniques for surface characterization. *ISRN optics*, *2012*.
- An, Q., Ming, W., & Chen, M. (2015). Experimental investigation on cutting characteristics in nanometric Plunge-Cutting of BK7 and fused silica glasses. *Materials*, *8*(4), 1428-1441.
- Arefin, S., Li, X. P., Rahman, M., & Liu, K. (2007). The upper bound of tool edge radius for nanoscale ductile mode cutting of silicon wafer. *The International Journal of Advanced Manufacturing Technology*, *31*(7-8), 655.
- Arif, M., Xinquan, Z., Rahman, M., & Kumar, S. (2013). A predictive model of the critical undeformed chip thickness for ductile–brittle transition in nano-machining of brittle materials. *International Journal of Machine Tools and Manufacture*, *64*, 114-122.
- Asai, S., & Kobayashi, A. (1990). Observations of chip producing behaviour in ultra-precision diamond machining and study on mirror-like surface generating mechanism. *Precision Engineering*, *12*(3), 137-143.
- Aykut, Ş. (2011). Surface roughness prediction in machining castamide material using ANN. *Acta Polytechnica Hungarica*, *8*(2), 21-32.
- Bakkal, M., Shih, A. J., & Scattergood, R. O. (2004). Chip formation, cutting forces, and tool wear in turning of Zr-based bulk metallic glass. *International Journal of Machine Tools and Manufacture*, *44*(9), 915-925.
- Belak, J. F., & Stowers, I. F. (1990). *A molecular dynamics model of the orthogonal cutting process* (No. UCRL-102697; CONF-9009241--1). Lawrence Livermore National Lab., CA (USA).
- Beltrão, P. A., Gee, A. E., Corbett, J., Whatmore, R. W., Goat, C. A., & Impey, S. A. (1999). Single point diamond machining of ferroelectric materials. *Journal of the European Ceramic Society*, *19*(6-7), 1325-1328.
- Bhagwat Vishal, B., Manu, R., & Sreenath, A. M. (2012). Ductile Mode Machining Simulation of Glass Material Using MATLAB. *2*(4).
- Bhattacharya, A. K., & Nix, W. D. (1988). Analysis of elastic and plastic deformation associated with indentation testing of thin films on substrates. *International Journal of Solids and Structures*, *24*(12), 1287-1298.
- Bhattacharya, A. K., & Nix, W. D. (1988). Finite element simulation of indentation experiments. *International Journal of Solids and Structures*, *24*(9), 881-891.
- Bhattacharya, B., Patten, J. A., & Jacob, J. (2006, January). Single point diamond turning of CVD coated silicon carbide. In *ASME 2006 International Manufacturing Science and Engineering Conference* (pp. 1153-1158). American Society of Mechanical Engineers.
- Bhattacharya, B., Patten, J. A., Jacob, J., Blau, P. J., Howe, J., & Braden, J. D. (2005). Ductile regime nano-machining of polycrystalline silicon carbide (6H). *American Society of Precision Engineers*.

- Bifano, T. G., Dow, T. A., & Scattergood, R. O. (1991). Ductile-regime grinding: a new technology for machining brittle materials. *Journal of engineering for industry*, *113*(2), 184-189.
- Blackley, W. S., & Scattergood, R. O. (1989). Diamond Turning of Brittle Materials. In *5th International Precision Engineering Seminar* (Vol. 18, No. 22, p. 9).
- Blackley, W. S., & Scattergood, R. O. (1991). Ductile-regime machining model for diamond turning of brittle materials. *Precision engineering*, *13*(2), 95-103.
- Blackley, W. S., & Scattergood, R. O. (1994). Chip topography for ductile-regime machining of germanium. *Journal of Engineering for Industry*, *116*(2), 263-266.
- Blake, P. N., & Scattergood, R. O. (1989). Ductile-regime turning of germanium and silicon.
- Blake, P. N., & Scattergood, R. O. (1990). Ductile-regime machining of germanium and silicon. *Journal of the American ceramic society*, *73*(4), 949-957.
- Born, D. K., & Goodman, W. A. (2001). An empirical survey on the influence of machining parameters on tool wear in diamond turning of large single-crystal silicon optics. *Precision Engineering*, *25*(4), 247-257.
- Bradley, N. (2007). *The response surface methodology* (Doctoral dissertation, Indiana University South Bend).
- Bridgman, P. W., & Šimon, I. (1953). Effects of very high pressures on glass. *Journal of applied physics*, *24*(4), 405-413.
- Brinksmeier, E. (1995). From Friction to Chip Removal. An Experimental Investigation of the Microcutting Process. In *Proc. 8th Int. Precision Engineering Seminar, May 15-19, Compiegne, France* (Vol. 335).
- Bulychev, S. I., Alekhin, V. P., Shorshorov, M. H., Ternovskii, A. P., & Shnyrev, G. D. (1975). Determining Young's modulus from the indentor penetration diagram. *Ind. Lab.*, *41*(9), 1409-1412.
- Cai, M. B., Li, X. P., & Rahman, M. (2007). High-pressure phase transformation as the mechanism of ductile chip formation in nanoscale cutting of silicon wafer. *Proceedings of the Institution of Mechanical Engineers, Part B: Journal of Engineering Manufacture*, *221*(10), 1511-1519.
- Cai, M. B., Li, X. P., Rahman, M., & Tay, A. A. O. (2007). Crack initiation in relation to the tool edge radius and cutting conditions in nanoscale cutting of silicon. *International Journal of Machine Tools and Manufacture*, *47*(3-4), 562-569.
- Candioti, L. V., De Zan, M. M., Camara, M. S., & Goicoechea, H. C. (2014). Experimental design and multiple response optimization. Using the desirability function in analytical methods development. *Talanta*, *124*, 123-138.
- Carroll III, J. T., & Strenkowski, J. S. (1988). Finite element models of orthogonal cutting with application to single point diamond turning. *International Journal of Mechanical Sciences*, *30*(12), 899-920.
- Chan, K. C., Cheung, C. F., Ramesh, M. V., Lee, W. B., & To, S. (2001). A theoretical and experimental investigation of surface generation in diamond turning of an Al6061/SiCp metal matrix composite. *International journal of mechanical sciences*, *43*(9), 2047-2068.
- Chang, K. J., & Cohen, M. L. (1987). Ab initio pseudopotential study of structural and high-pressure properties of SiC. *Physical Review B*, *35*(15), 8196.
- Chao, C. L., Ma, K. J., Liu, D. S., Bai, C. Y., & Shy, T. L. (2002). Ductile behaviour in single-point diamond-turning of single-crystal silicon. *Journal of Materials Processing Technology*, *127*(2), 187-190.
- Chen, J., & Zhao, Q. (2015). A model for predicting surface roughness in single-point diamond turning. *Measurement*, *69*, 20-30.
- Chen, W. F., & Han, D. J. (1988). *Plasticity for structural engineers*. Springer-Verlag, New York.
- Cheong, W. C. D., & Zhang, L. C. (2000). Molecular dynamics simulation of phase transformations in silicon monocrystals due to nano-indentation. *Nanotechnology*, *11*(3), 173.

- Cheung, C. F., & Lee, W. B. (2000). A theoretical and experimental investigation of surface roughness formation in ultra-precision diamond turning. *International Journal of Machine Tools and Manufacture*, *40*(7), 979-1002.
- Cheung, C. F., & Lee, W. B. (2001). Characterisation of nanosurface generation in single-point diamond turning. *International Journal of Machine Tools and Manufacture*, *41*(6), 851-875.
- Chiu, W. M., & Lee, W. B. (1997). Development of ultra-precision machining technology.
- Clarke, D. R., Kroll, M. C., Kirchner, P. D., Cook, R. F., & Hockey, B. J. (1988). Amorphization and conductivity of silicon and germanium induced by indentation. *Physical review letters*, *60*(21), 2156.
- Dashwood, R. J., & Grimes, R. (2010). Structural Materials: Aluminum and Its Alloys–Properties. *Encyclopedia of Aerospace Engineering*.
- Davies, M. A., Evans, C. J., Vohra, R. R., Bergner, B. C., & Patterson, S. R. (2003, November). Application of precision diamond machining to the manufacture of microphotonics components. In *Lithographic and micromachining techniques for optical component fabrication II* (Vol. 5183, pp. 94-109). International Society for Optics and Photonics.
- Davim, J. P., Maranhao, C., Jackson, M. J., Cabral, G., & Gracio, J. (2008). FEM analysis in high speed machining of aluminium alloy (Al7075-0) using polycrystalline diamond (PCD) and cemented carbide (K10) cutting tools. *The International Journal of Advanced Manufacturing Technology*, *39*(11-12), 1093-1100.
- Davim, J. P., Reis, P., Maranhao, C., Jackson, M. J., Cabral, G., & Gracio, J. (2009). Finite element simulation and experimental analysis of orthogonal cutting of an aluminium alloy using polycrystalline diamond tools. *International Journal of Materials and Product Technology*, *37*(1-2), 46-59.
- Davis, G. E., Roblee, J. W., & Hedges, A. R. (2009, August). Comparison of freeform manufacturing techniques in the production of monolithic lens arrays. In *Optical Manufacturing and Testing VIII* (Vol. 7426, p. 742605). International Society for Optics and Photonics.
- Davis, J. R., ed. *Alloying: understanding the basics*. ASM international, 2001.
- Ding, X., & Rahman, M. (2012). A study of the performance of cutting polycrystalline Al 6061 T6 with single crystalline diamond micro-tools. *Precision Engineering*, *36*(4), 593-603.
- Dixit, U. S. (2009). *Finite element methods for engineers*. Delmar Learning.
- Doerner, M. F., & Nix, W. D. (1986). A method for interpreting the data from depth-sensing indentation instruments. *Journal of Materials research*, *1*(4), 601-609.
- Domnich, V., & Gogotsi, Y. (2001). 5. High-pressure surface science. In *Experimental Methods in the Physical Sciences* (Vol. 38, pp. 355-445). Academic Press.
- Domnich, V., Gogotsi, Y., & Dub, S. (2000). Effect of phase transformations on the shape of the unloading curve in the nanoindentation of silicon. *Applied Physics Letters*, *76*(16), 2214-2216.
- Drucker, D. C., & Prager, W. (1952). Soil mechanics and plastic analysis or limit design. *Quarterly of applied mathematics*, *10*(2), 157-165.
- Durazo-Cardenas, I., Shore, P., Luo, X., Jacklin, T., Impey, S. A., & Cox, A. (2007). 3D characterisation of tool wear whilst diamond turning silicon. *Wear*, *262*(3-4), 340-349.
- Dursun, T., & Soutis, C. (2014). Recent developments in advanced aircraft aluminium alloys. *Materials & Design (1980-2015)*, *56*, 862-871.
- Fang, F. Z. (1998). Nano-turning of single crystal silicon. *Journal of Materials Processing Technology*, *82*(1-3), 95-101.
- Fang, F. Z., & Venkatesh, V. C. (1998). Diamond cutting of silicon with nanometric finish. *CIRP annals*, *47*(1), 45-49.
- Fang, F. Z., & Zhang, G. X. (2003). An experimental study of edge radius effect on cutting single crystal silicon. *The International Journal of Advanced Manufacturing Technology*, *22*(9-10), 703-707.

- Fang, F. Z., & Zhang, G. X. (2004). An experimental study of optical glass machining. *The International Journal of Advanced Manufacturing Technology*, *23*(3-4), 155-160.
- Fang, F. Z., Huang, K. T., Gong, H., & Li, Z. J. (2014). Study on the optical reflection characteristics of surface micro-morphology generated by ultra-precision diamond turning. *Optics and Lasers in Engineering*, *62*, 46-56.
- Fang, F. Z., Liu, X. D., & Lee, L. C. (2003). Micro-machining of optical glasses—A review of diamond-cutting glasses. *Sadhana*, *28*(5), 945-955.
- Fang, F. Z., Wu, H., & Liu, Y. C. (2005). Modelling and experimental investigation on nanometric cutting of monocrystalline silicon. *International Journal of Machine Tools and Manufacture*, *45*(15), 1681-1686.
- Fang, F. Z., Wu, H., Zhou, W., & Hu, X. T. (2007). A study on mechanism of nano-cutting single crystal silicon. *Journal of Materials Processing Technology*, *184*(1-3), 407-410.
- Fang, F. Z., Zhang, X. D., Weckenmann, A., Zhang, G. X., & Evans, C. (2013). Manufacturing and measurement of freeform optics. *CIRP Annals*, *62*(2), 823-846.
- Field, J. S., & Swain, M. V. (1993). A simple predictive model for spherical indentation. *Journal of Materials Research*, *8*(2), 297-306.
- Gao, W., Hocken, R. J., Patten, J. A., & Lovingood, J. (2000). Experiments using a nano-machining instrument for nano-cutting brittle materials. *CIRP Annals-Manufacturing Technology*, *49*(1), 439-442.
- Goel, S. (2013). *An atomistic investigation on the nanometric cutting mechanism of hard, brittle materials* (Doctoral dissertation, Heriot-Watt University).
- Goel, S. (2014). The current understanding on the diamond machining of silicon carbide. *Journal of Physics D: Applied Physics*, *47*(24), 243001.
- Goel, S., Chavoshi, S. Z., & Murphy, A. (2017). Molecular dynamics simulation (MDS) to study nanoscale machining processes. In V. K. Jain (Ed.), Nanofinishing Science and Technology: Basic and Advanced Finishing and Polishing Processes (Micro and Nanomanufacturing Series). Taylor and Francis.
- Goel, S., Faisal, N. H., Luo, X., Yan, J., & Agrawal, A. (2014). Nanoindentation of polysilicon and single crystal silicon: Molecular dynamics simulation and experimental validation. *Journal of physics D: applied physics*, *47*(27), 275304.
- Goel, S., Kovalchenko, A., Stukowski, A., & Cross, G. (2016). Influence of microstructure on the cutting behaviour of silicon. *Acta Materialia*, *105*, 464-478.
- Goel, S., Luo, X., Reuben, R. L., & Rashid, W. B. (2011). Atomistic aspects of ductile responses of cubic silicon carbide during nanometric cutting. *Nanoscale research letters*, *6*(1), 589.
- Goel, S., Luo, X., & Reuben, R. L. (2012). Molecular dynamics simulation model for the quantitative assessment of tool wear during single point diamond turning of cubic silicon carbide. *Computational Materials Science*, *51*(1), 402-408.
- Goel, S., Luo, X., Reuben, R. L., & Pen, H. (2012). Influence of temperature and crystal orientation on tool wear during single point diamond turning of silicon. *Wear*, *284*, 65-72.
- Goel, S., Luo, X., & Reuben, R. L. (2013). Wear mechanism of diamond tools against single crystal silicon in single point diamond turning process. *Tribology International*, *57*, 272-281.
- Goel, S., Luo, X., Comley, P., Reuben, R. L., & Cox, A. (2013). Brittle–ductile transition during diamond turning of single crystal silicon carbide. *International Journal of Machine Tools and Manufacture*, *65*, 15-21.
- Goel, S., Stukowski, A., Luo, X., Agrawal, A., & Reuben, R. L. (2013). Anisotropy of single-crystal 3C–SiC during nanometric cutting. *Modelling and Simulation in Materials Science and Engineering*, *21*(6), 065004.
- Goel, S., Yan, J., Luo, X., & Agrawal, A. (2014). Incipient plasticity in 4H-SiC during quasistatic nanoindentation. *journal of the mechanical behavior of biomedical materials*, *34*, 330-337.

- Goel, S., Luo, X., Agrawal, A., & Reuben, R. L. (2015). Diamond machining of silicon: a review of advances in molecular dynamics simulation. *International Journal of Machine Tools and Manufacture*, *88*, 131-164.
- Guo, X., Li, Q., Liu, T., Kang, R., Jin, Z., & Guo, D. (2017). Advances in molecular dynamics simulation of ultra-precision machining of hard and brittle materials. *Frontiers of Mechanical Engineering*, *12*(1), 89-98.
- Gupta, S., Khatri, N., Karar, V., & Dhami, S. S. (2016, September). Investigation of Surface Roughness of Single Point Diamond Turned Germanium Substrate by Coherence Correlation Interferometry and Image Processing. In *IOP Conference Series: Materials Science and Engineering* (Vol. 149, No. 1, p. 012032). IOP Publishing.
- He, C. L., Zong, W. J., Cao, Z. M., & Sun, T. (2015). Theoretical and empirical coupled modeling on the surface roughness in diamond turning. *Materials & Design*, *82*, 216-222.
- Hill, W. J., & Hunter, W. G. (1966). A review of response surface methodology: a literature survey. *Technometrics*, *8*(4), 571-590.
- Holmquist, T. J., & Johnson, G. R. (1991). Determination of constants and comparison of results for various constitutive models. Le Journal de Physique IV, 1(C3), C3-853.
- Hu, J. Z., & Spain, I. L. (1984). Phases of silicon at high pressure. *Solid state communications*, *51*(5), 263-266.
- Huerta, M., & Malkin, S. (1976). Grinding of glass: the mechanics of the process. *Journal of Engineering for Industry*, *98*(2), 459-467.
- Ikawa, N., R. R. Donaldson, R. Komanduri, W. König, P. A. McKeown, T. Moriwaki, and I. F. Stowers. "Ultraprecision metal cutting—the past, the present and the future." *CIRP Annals-Manufacturing Technology* 40, no. 2 (1991): 587-594.
- Inamura, T., Shimada, S., Takezawa, N., & Nakahara, N. (1997). Brittle/ductile transition phenomena observed in computer simulations of machining defect-free monocrystalline silicon. *CIRP Annals*, *46*(1), 31-34.
- Jacob, J., Patten, J. A., Bhattacharya, B., Couey, J. A., & Marsh, E. R. (2005, October). Determination of the ductile to brittle transition and critical depth of cut in 6H-silicon carbide through fly cutting. In *Proceedings of the ASPE Annual Meeting*.
- Jagadesh, T., & Samuel, G. L. (2015). Mechanistic and finite element model for prediction of cutting forces during micro-turning of titanium alloy. *Machining Science and Technology*, *19*(4), 593-629.
- Jagadesh, T., & Samuel, G. L. (2017). Finite Element Simulations of Micro Turning of Ti-6Al-4V using PCD and Coated Carbide tools. *Journal of The Institution of Engineers (India): Series C*, *98*(1), 5-15.
- Jasinevicius, R. G., Porto, A. J. V., Duduch, J. G., Pizani, P. S., Lanciotti Jr, F., & Dos Santos, F. J. (2005). Multiple phase silicon in submicrometer chips removed by diamond turning. *Journal of the Brazilian Society of Mechanical Sciences and Engineering*, *27*(4), 440-448.
- Jasinevicius, R. G., Duduch, J. G., Montanari, L., & Pizani, P. S. (2012). Dependence of brittle-to-ductile transition on crystallographic direction in diamond turning of single-crystal silicon. *Proceedings of the Institution of Mechanical Engineers, Part B: Journal of Engineering Manufacture*, *226*(3), 445-458.
- John, B. P. (2003). *Scaling Down of Manufacturing Systems: Meso and Nano Level Machining: an Analysis* (Doctoral dissertation, Pennsylvania State University).
- Johnson, G. R., & Cook, W. H. (1985). Fracture characteristics of three metals subjected to various strains, strain rates, temperatures and pressures. *Engineering fracture mechanics*, *21*(1), 31-48.
- Johnson, G. R., & Holmquist, T. J. (1989). Test data and computational strength and fracture model constants for 23 materials subjected to large strains, high strain rates, and high temperatures. *Los Alamos National Laboratory, Los Alamos, NM, Report No. LA-11463-MS*.
- Johnson, G. R., & Holmquist, T. J. (1994, July). An improved computational constitutive model for brittle materials. In *AIP Conference Proceedings* (Vol. 309, No. 1, pp. 981-984). AIP.

- Jomaa, W., Songmene, V., & Bocher, P. (2014). Surface finish and residual stresses induced by orthogonal dry machining of AA7075-T651. *Materials*, *7*(3), 1603-1624.
- Jou, Y. T., Lin, W. T., Lee, W. C., & Yeh, T. M. (2014). Integrating the Taguchi method and response surface methodology for process parameter optimization of the injection molding. *Applied Mathematics & Information Sciences*, *8*(3), 1277.
- Juliano, T., & Penrose, D. (2002). Nano-Indentation Simulation on Silicon Using ABAQUS.
- Kansal, H. K., Singh, S., & Kumar, P. (2005). Parametric optimization of powder mixed electrical discharge machining by response surface methodology. *Journal of materials processing technology*, *169*(3), 427-436.
- Khan, G. S., Sarepaka, R. G. V., Chattopadhyay, K. D., Jain, P. K., & Narasimham, V. M. L. (2003). Effects of tool feed rate in single point diamond turning of aluminium-6061 alloy.
- Khatri, N., Sharma, R., Mishra, V., Kumar, M., Karar, V., & Sarepaka, R. V. (2015, June). An experimental investigation on the influence of machining parameters on surface finish in diamond turning of silicon optics. In *International Conference on Optics and Photonics 2015* (Vol. 9654, p. 96540M). International Society for Optics and Photonics.
- King, R. F., & Tabor, D. (1954). The strength properties and frictional behaviour of brittle solids. *Proc. R. Soc. Lond. A*, *223*(1153), 225-238.
- King, R. F., & Tabor, D. (1954). The strength properties and frictional behaviour of brittle solids. *Proc. R. Soc. Lond. A*, *223*(1153), 225-238.
- Komanduri, R., & Raff, L. M. (2001). A review on the molecular dynamics simulation of machining at the atomic scale. *Proceedings of the Institution of Mechanical Engineers, Part B: Journal of Engineering Manufacture*, *215*(12), 1639-1672.
- Komanduri, R., Chandrasekaran, N., & Raff, L. M. (1998). Effect of tool geometry in nanometric cutting: a molecular dynamics simulation approach. *Wear*, *219*(1), 84-97.
- Komanduri, R., Chandrasekaran, N., & Raff, L. M. (2000). MD Simulation of nanometric cutting of single crystal aluminum–effect of crystal orientation and direction of cutting. *Wear*, *242*(1-2), 60-88.
- Komanduri, R., Chandrasekaran, N., & Raff, L. M. (2001). Molecular dynamics simulation of the nanometric cutting of silicon. *Philosophical Magazine B*, *81*(12), 1989-2019.
- Kong, M. C., Lee, W. B., Cheung, C. F., & To, S. (2006). A study of materials swelling and recovery in single-point diamond turning of ductile materials. *Journal of materials processing technology*, *180*(1-3), 210-215.
- Kovalchenko, A. M. (2013). Studies of the ductile mode of cutting brittle materials (A review). *Journal of Superhard Materials*, *35*(5), 259-276.
- Králík, V., & Němeček, J. (2014). Comparison of nanoindentation techniques for local mechanical quantification of aluminium alloy. *Materials Science and Engineering: A*, *618*, 118-128.
- Krauskopf, B. (1984). Diamond turning: reflecting demands for precision. *Manuf. Eng.*, *92*(5), 90-100.
- Krulewich, D. A. (1996). *Experimental design for single point diamond turning of silicon optics*. UCRL-ID-127385.
- Kushendarsyah, S., & Sathyan, S. (2013). Orthogonal Microcutting of Thin Workpieces. *Journal of Manufacturing Science and Engineering*, *135*(3), 031004.
- Lai, M., Zhang, X. D., & Fang, F. Z. (2012). Study on critical rake angle in nanometric cutting. *Applied Physics A*, *108*(4), 809-818.
- Lakhdari, F., Belkhir, N., Bouzid, D., & Herold, V. (2019). Relationship between subsurface damage depth and breaking strength for brittle materials. *The International Journal of Advanced Manufacturing Technology*, 1-11.

- Lawn, B. R., & Evans, A. G. (1977). A model for crack initiation in elastic/plastic indentation fields. *Journal of Materials Science*, *12*(11), 2195-2199.
- Lawn, B. R., & Wilshaw, R. (1975). Indentation fracture: principles and applications. *Journal of materials science*, *10*(6), 1049-1081.
- Lawn, B. R., Evans, A. G., & Marshall, D. B. (1980). Elastic/plastic indentation damage in ceramics: the median/radial crack system. *Journal of the American Ceramic Society*, *63*(9-10), 574-581.
- Lawn, B. R., Padture, N. P., Cait, H., & Guiberteau, F. (1994). Making ceramics" ductile". *Science*, *263*(5150), 1114-1116.
- Lee, W. B., Cheung, C. F., & To, S. (2007). Multi-scale modelling of surface topography in single-point diamond turning. *J Achiev Mater Manuf Eng*, *24*(1), 260-266.
- Leung, T. P., Lee, W. B., & Lu, X. M. (1998). Diamond turning of silicon substrates in ductile-regime. *Journal of materials processing technology*, *73*(1-3), 42-48.
- Li, X. P., He, T., & Rahman, M. (2005). Tool wear characteristics and their effects on nanoscale ductile mode cutting of silicon wafer. *Wear*, *259*(7-12), 1207-1214.
- Lin, Z. C., Huang, J. C., & Jeng, Y. R. (2007). 3D nano-scale cutting model for nickel material. *Journal of materials processing technology*, *192*, 27-36.
- Liu, X., DeVor, R. E., Kapoor, S. G., & Ehmann, K. F. (2004). The mechanics of machining at the microscale: assessment of the current state of the science. *Journal of manufacturing science and engineering*, *126*(4), 666-678.
- Liu, K., Li, X. P., Rahman, M., Neo, K. S., & Liu, X. D. (2007). A study of the effect of tool cutting edge radius on ductile cutting of silicon wafers. *The International Journal of Advanced Manufacturing Technology*, *32*(7-8), 631.
- Lo-A-Foe, T. C. G., Dautzenberg, J. H., & Van Der Wolf, A. C. H. (1988). Cutting forces and their influences upon the surface integrity in single-point diamond turning. In *Ultra-precision Manufacturing Engineering, Proceedings of the International Congress for Ultraprecision Technology, Springer-Verlag* (pp. 110-125).
- Lu, C. J., & Bogy, D. B. (1995). The effect of tip radius on nano-indentation hardness tests. *International journal of solids and structures*, *32*(12), 1759-1770.
- Lu, Y. P., He, D. W., Zhu, J., & Yang, X. D. (2008). First-principles study of pressure-induced phase transition in silicon carbide. *Physica B: Condensed Matter*, *403*(19-20), 3543-3546.
- Lucca, D. A., Rhorer, R. L., & Komanduri, R. (1991). Energy dissipation in the ultraprecision machining of copper. *CIRP Annals-Manufacturing Technology*, *40*(1), 69-72.
- Lucca, D. A., Seo, Y. W., Rhorer, R. L., & Donaldson, R. R. (1994). Aspects of surface generation in orthogonal ultraprecision machining. *CIRP Annals-Manufacturing Technology*, *43*(1), 43-46.
- Luo, X., Goel, S., & Reuben, R. L. (2012). A quantitative assessment of nanometric machinability of major polytypes of single crystal silicon carbide. *Journal of the European Ceramic Society*, *32*(12), 3423-3434.
- Luo, X., Tong, Z., & Liang, Y. (2014). Investigation of the shape transferability of nanoscale multi-tip diamond tools in the diamond turning of nanostructures. *Applied Surface Science*, *321*, 495-502.
- Mabrouki, T., Girardin, F., Asad, M., & Rigal, J. F. (2008). Numerical and experimental study of dry cutting for an aeronautic aluminium alloy (A2024-T351). *International Journal of Machine Tools and Manufacture*, *48*(11), 1187-1197.
- Mahajan, K. A., Sadaiah, M., & Gawande, S. H. (2010). Experimental investigations of surface roughness on OFHC copper by diamond turning machine. *International Journal of Engineering Science and Technology*, *2*(10), 5215-5220.
- Mariayyah, R. (2007). *Experimental and numerical studies on ductile regime machining of silicon carbide and silicon nitride* (Doctoral dissertation, The University of North Carolina at Charlotte).

- Markopoulos, A. P. (2012). *Finite element method in machining processes*. Springer Science & Business Media.
- Marshall, D. B., & Lawn, B. R. (1985). Indentation of brittle materials. In *Microindentation techniques in materials science and engineering*. ASTM International.
- MatWeb, L. L. C. (2013). MatWeb: Material Property Data. *línea]. Available: http://www. matweb. com/search/DataSheet. aspx*.
- Meng, B., Zhang, F., & Li, Z. (2015). Deformation and removal characteristics in nanoscratching of 6H-SiC with Berkovich indenter. *Materials Science in Semiconductor Processing*, *31*, 160-165.
- Merchant, M. E. (1945). Mechanics of the metal cutting process. I. Orthogonal cutting and a type 2 chip. *Journal of applied physics*, *16*(5), 267-275.
- Merchant, M. E. (1945). Mechanics of the metal cutting process. II. Plasticity conditions in orthogonal cutting. *Journal of applied physics*, *16*(6), 318-324.
- Minomura, S., & Drickamer, H. G. (1962). Pressure induced phase transitions in silicon, germanium and some III–V compounds. *Journal of Physics and Chemistry of Solids*, *23*(5), 451-456.
- Minor §, A. M., Lilleodden, E. T., Jin, M., Stach, E. A., Chrzan, D. C., & Morris, J. W. (2005). Room temperature dislocation plasticity in silicon. *Philosophical Magazine*, *85*(2-3), 323-330.
- Mir, A. (2016). *Investigation of cutting mechanics in single point diamond turning of silicon* (Doctoral dissertation, University of Strathclyde).
- Mir, A., Luo, X., & Sun, J. (2016). The investigation of influence of tool wear on ductile to brittle transition in single point diamond turning of silicon. *Wear*, *364*, 233-243.
- Mir, A., Luo, X., & Siddiq, A. (2017). Smooth particle hydrodynamics study of surface defect machining for diamond turning of silicon. *The International Journal of Advanced Manufacturing Technology*, *88*(9-12), 2461-2476.
- Mishra, M., & Szlufarska, I. (2009). Possibility of high-pressure transformation during nanoindentation of SiC. *Acta Materialia*, *57*(20), 6156-6165.
- Mishra, V., Garg, H., Karar, V., & Khan, G.S. (2018). Ultra-precision Diamond Turning Process, "Micro and Nano Machining of Engineering Materials.", pp. 65-97.
- Mishra, V., Khan, G. S., Chattopadhyay, K. D., Nand, K., & Sarepaka, R. V. (2014). Effects of tool overhang on selection of machining parameters and surface finish during diamond turning. *Measurement*, *55*, 353-361.
- Mohammadi, H., Ravindra, D., Kode, S. K., & Patten, J. A. (2015). Experimental work on micro laser-assisted diamond turning of silicon (111). *Journal of Manufacturing Processes*, *19*, 125-128.
- Montgomery, D. C., Peck, E. A., & Vining, G. G. (2012). *Introduction to linear regression analysis* (Vol. 821). John Wiley & Sons.
- Moore, M. A., & King, F. S. (1980). Abrasive wear of brittle solids. *Wear*, *60*(1), 123-140.
- Moriwaki, T., Shamoto, E., & Inoue, K. (1992). Ultraprecision ductile cutting of glass by applying ultrasonic vibration. *CIRP annals*, *41*(1), 141-144.
- Morris, J. C., Callahan, D. L., Kulik, J., Patten, J. A., & Scattergood, R. O. (1995). Origins of the ductile regime in single-point diamond turning of semiconductors. *Journal of the American Ceramic Society*, *78*(8), 2015-2020.
- Naidu, K. M., & Rao, S. R. (2013). ANN based surface roughness prediction in turning of AA 6351. *International Journal of Engineering Research and Applications*, *3*(4), 1455-1459.
- Nair, R. (2014). Measuring Hardness and More through Nanoindentation. *Archived on May*, *14*.
- Nakasuji, T., Kodera, S., Hara, S., Matsunaga, H., Ikawa, N., & Shimada, S. (1990). Diamond turning of brittle materials for optical components. *CIRP Annals-Manufacturing Technology*, *39*(1), 89-92.

- Nawaz, A., Mao, W. G., Lu, C., & Shen, Y. G. (2017). Nano-scale elastic-plastic properties and indentation-induced deformation of single crystal 4H-SiC. *Journal of the mechanical behavior of biomedical materials*, *66*, 172-180.
- Needs, R. J., & Mujica, A. (1995). First-principles pseudopotential study of the structural phases of silicon. *Physical Review B*, *51*(15), 9652.
- Ngoi, B. K. A., & Sreejith, P. S. (2000). Ductile regime finish machining-a review. *The International Journal of Advanced Manufacturing Technology*, *16*(8), 547-550.
- Nix, W. D., & Gao, H. (1998). Indentation size effects in crystalline materials: a law for strain gradient plasticity. *Journal of the Mechanics and Physics of Solids*, *46*(3), 411-425.
- Noreyan, A., Amar, J. G., & Marinescu, I. (2005). Molecular dynamics simulations of nanoindentation of β-SiC with diamond indenter. *Materials Science and Engineering: B*, *117*(3), 235-240.
- Numerical Simulation and Experimental Test of Nanoindentation Analysis on Metal Thin Film, Department of Mechanical and Mechanical Engineering, National Sun Yat-Sen University.
- O'Connor, B. P., Marsh, E. R., & Couey, J. A. (2005). On the effect of crystallographic orientation on ductile material removal in silicon. *Precision Engineering*, *29*(1), 124-132.
- Ohta, T., Yan, J., Kuriyagawa, T., Kodera, S., & Nakasuji, T. (2007). Prediction of subsurface damage depth of ground brittle materials by surface profiling. *International Journal of Machining and Machinability of Materials*, *2*(1), 108.
- Oliver, W. C., & Pharr, G. M. (1992). An improved technique for determining hardness and elastic modulus using load and displacement sensing indentation experiments. *Journal of materials research*, *7*(6), 1564-1583.
- Oliver, W. C., & Pharr, G. M. (2004). Measurement of hardness and elastic modulus by instrumented indentation: Advances in understanding and refinements to methodology. *Journal of materials research*, *19*(1), 3-20.
- Oluwajobi, A. (2012). Molecular Dynamics Simulation of Nanoscale Machining. In *Molecular Dynamics-Studies of Synthetic and Biological Macromolecules*. InTech.
- Optics & Allied Engineering Pvt. Ltd., http://www.opticsindia.com/products/ir-optics-and-spdt/spdt-applications-areas/, as seen on 10-1-2019.
- Oxley, P.L.B. (1989) "The mechanics of machining: an analytical approach to assessing machinability." Chichester, England: Ellis Horwood Publisher.
- Pandey, K. K., Garg, N., Shanavas, K. V., Sharma, S. M., & Sikka, S. K. (2011). Pressure induced crystallization in amorphous silicon. *Journal of Applied Physics*, *109*(11), 113511.
- Panich, N. (2004). Nanoindentation of silicon (100) studied by experimental and finite element method. *KMUTT Research and Development Journal*, *27*(3), 273-284.
- Patten, J. A. (1996). High Pressure Phase Transformation Analysis and Molecular Dynamics Simulations of Single Point Diamond Turning of Germanium.
- Patten, J. A., & Gao, W. (2001). Extreme negative rake angle technique for single point diamond nano-cutting of silicon. *Precision Engineering*, *25*(2), 165-167.
- Patten, J. A., & Jacob, J. (2008). Comparison between numerical simulations and experiments for single-point diamond turning of single-crystal silicon carbide. *Journal of Manufacturing Processes*, *10*(1), 28-33.
- Patten, J., Gao, W., & Yasuto, K. (2005). Ductile regime nanomachining of single-crystal silicon carbide. *Journal of manufacturing science and engineering*, *127*(3), 522-532.
- Patten, J. A., Jacob, J., Bhattacharya, B., Grevstad, A., Fang, N., & Marsh, E. R. (2007). Numerical simulations and cutting experiments on single point diamond machining of semiconductors and ceramics. Semiconductor Machining at the Micro-Nano Scale. *Transw Res Netw Kerala India*, *2*, 1-36.

- Pawase, P., Brahmankar, P. K., Pawade, R. S., & Balasubramanium, R. (2014). Analysis of machining mechanism in diamond turning of germanium lenses. *Procedia Materials Science*, *5*, 2363-2368.
- Pulliam, W. J., Russler, P. M., Mlcak, R., Murphy, K. A., & Kozikowski, C. L. (2000, December). Micromachined SiC fiber optic pressure sensors for high-temperature aerospace applications. In *Industrial Sensing Systems* (Vol. 4202, pp. 21-31). International Society for Optics and Photonics.
- Puttick, K. E., Rudman, M. R., Smith, K. J., Franks, A., & Lindsey, K. (1989). Single-point diamond machining of glasses. *Proc. R. Soc. Lond. A*, *426*(1870), 19-30.
- Qian, S., & Takacs, P. (2012). Nano-accuracy surface figure metrology of precision optics. In *Modern Metrology Concerns*. InTech.
- Rao, R., Bradby, J. E., Ruffell, S., & Williams, J. S. (2007). Nanoindentation-induced phase transformation in crystalline silicon and relaxed amorphous silicon. *Microelectronics journal*, *38*(6-7), 722-726.
- Ravindra, D., & Patten, J. (2007, September). Determining the ductile to brittle transition (DBT) of a single-crystal 4H-SiC wafer by performing nanometric cutting. In *Proceedings of ISAAT 2007 on Precision Grinding and Abrasive Technology at SME International Grinding Conference* (pp. 26-28).
- Ravindra, D., & Patten, J. (2008, January). Improving the surface roughness of a CVD coated silicon carbide disk by performing ductile regime single point diamond turning. In *ASME 2008 International Manufacturing Science and Engineering Conference collocated with the 3rd JSME/ASME International Conference on Materials and Processing* (pp. 155-161). American Society of Mechanical Engineers.
- Ravindra, D., Patten, J. A., & Qu, J. (2009, January). Single point diamond turning effects on surface quality and subsurface damage in ceramics. In *ASME 2009 International Manufacturing Science and Engineering Conference* (pp. 707-713). American Society of Mechanical Engineers.
- Ray, I. L. F., & Cockayne, D. J. H. (1971). The dissociation of dislocations in silicon. *Proc. R. Soc. Lond. A*, *325*(1563), 543-554.
- Reddy, J. D. (2008). *Mechanical Properties of Silicon Carbide (SiC) Thin Films* (Doctoral dissertation, University of South Florida).
- Robichaud, J., Green, J., Catropa, D., Rider, B., & Ullathorne, C. (2008). Silicon carbide optics for space situational awareness and responsive space needs. In *Proc. Adv. Maui Optical and Space Surveillance Tech. Conf., E67-E71*.
- Saddow, S. E., & Agarwal, A. (2004). *Advances in silicon carbide processing and applications*. Artech House.
- Schaefer, John. "Single point diamond turning: progress in precision." In *International Optical Design Conference*, p. ThB1. Optical Society of America, 2006.
- Sekine, T., & Kobayashi, T. (1997). Shock compression of 6H polytype SiC to 160 GPa. *Physical Review B*, *55*(13), 8034.
- Shaffer, P. T. (1964). Effect of crystal orientation on hardness of silicon carbide. *Journal of the American Ceramic Society*, *47*(9), 466-466.
- Shibata, T., Fujii, S., Makino, E., & Ikeda, M. (1996). Ductile-regime turning mechanism of single-crystal silicon. *Precision Engineering*, *18*(2-3), 129-137.
- Shimada, S., Ikawa, N., Inamura, T., Takezawa, N., Ohmori, H., & Sata, T. (1995). Brittle-ductile transition phenomena in microindentation and micromachining. *CIRP Annals-Manufacturing Technology*, *44*(1), 523-526.
- Singh, K., Vaishya, R. O., Singh, H., Mishra, V., & Ramagopal, S. (2013). Investigation of tool life & surface roughness during single point diamond turning of silicon. *Int J Sci Res*, *2*(6), 265-267.
- Sneddon, I. N. (1948, October). Boussinesq's problem for a rigid cone. In *Mathematical Proceedings of the Cambridge Philosophical Society* (Vol. 44, No. 4, pp. 492-507). Cambridge University Press.

- Sneddon, I. N. (1965). The relation between load and penetration in the axisymmetric Boussinesq problem for a punch of arbitrary profile. *International journal of engineering science*, *3*(1), 47-57.
- Soundararajan, V., Zekovic, S., & Kovacevic, R. (2005). Thermo-mechanical model with adaptive boundary conditions for friction stir welding of Al 6061. *International Journal of Machine Tools and Manufacture*, *45*(14), 1577-1587.
- Strössner, K., Cardona, M., & Choyke, W. J. (1987). High pressure X-ray investigations on 3C-SiC. *Solid state communications*, *63*(2), 113-114.
- Sumipro, https://www.sumipro.nl/technicaloptics/, as seen on 12, June 2018.
- Sun, X., Li, L., Guo, Y., Zhao, H., Zhang, S., Yu, Y., Wu, D., Liu, H., Yu, M., Shi, D., Liu, S., Zhou, M., Ren, L. & Liu, Z. (2018). Influences of organic component on mechanical property of cortical bone with different water content by nanoindentation. *AIP Advances*, *8*(3), 035003.
- Szlufarska, I., Kalia, R. K., Nakano, A., & Vashishta, P. (2004). Nanoindentation-induced amorphization in silicon carbide. *Applied Physics Letters*, *85*(3), 378-380.
- Szlufarska, I., Kalia, R. K., Nakano, A., & Vashishta, P. (2005). Atomistic processes during nanoindentation of amorphous silicon carbide. *Applied Physics Letters*, *86*(2), 021915.
- Toh, S. B., and R. McPherson. "Fine scale abrasive wear of ceramics by a plastic cutting process." In *Science of Hard Materials. Proc. 2 nd Int. Conf. on Science of Hard Materials held at Rhodes 23-28 Sept. 1984. Edited by E. A. Almond, C. A. Brookes and R. Warren. Bristol, Adam Hilger, 1986.*, p. 865. 1984.
- Tohme, Y. (2008, October). Trends in ultra-precision machining of freeform optical surfaces. In *Optical fabrication and testing* (p. OThC6). Optical Society of America.
- Tong, L., Mehregany, M., & Matus, L. G. (1992). Mechanical properties of 3C silicon carbide. *Applied physics letters*, *60*(24), 2992-2994.
- Uddin, M. S., Seah, K. H. W., Rahman, M., Li, X. P., & Liu, K. (2007). Performance of single crystal diamond tools in ductile mode cutting of silicon. *Journal of materials processing technology*, *185*(1-3), 24-30.
- Vaz, M., Owen, D. R. J., Kalhori, V., Lundblad, M., & Lindgren, L. E. (2007). Modelling and simulation of machining processes. *Archives of computational methods in engineering*, *14*(2), 173-204.
- Venkatachalam, S. (2007). *Predictive modeling for ductile machining of brittle materials* (Doctoral dissertation, Georgia Institute of Technology).
- Venkatachalam, S., Fergani, O., Li, X., Yang, J. G., Chiang, K. N., & Liang, S. Y. (2015). Microstructure effects on cutting forces and flow stress in ultra-precision machining of polycrystalline brittle materials. *Journal of Manufacturing Science and Engineering*, *137*(2), 021020.
- Venkatachalam, S., Li, X., & Liang, S. Y. (2009). Predictive modeling of transition undeformed chip thickness in ductile-regime micro-machining of single crystal brittle materials. *Journal of materials processing technology*, *209*(7), 3306-3319.
- Wang, H., & To, S. (2011). A study on tool wear in ultra-precision diamond turning with finite element modelling. *International journal of nanomanufacturing*, *7*(5-6), 500-516.
- Wang, J. J. J., & Liao, Y. Y. (2008). Critical depth of cut and specific cutting energy of a microscribing process for hard and brittle materials. *Journal of Engineering Materials and Technology*, *130*(1), 011002.
- Wedberg, D. (2013). *Modelling of high strain rate plasticity and metal cutting* (Doctoral dissertation, Luleå tekniska universitet).
- Wu, H. B., & Zhang, S. J. (2014). 3D FEM simulation of milling process for titanium alloy Ti6Al4V. *The International Journal of Advanced Manufacturing Technology*, *71*(5-8), 1319-1326.
- Xi, X. K., Zhao, D. Q., Pan, M. X., Wang, W. H., Wu, Y., & Lewandowski, J. J. (2005). Fracture of brittle metallic glasses: Brittleness or plasticity. *Physical review letters*, *94*(12), 125510.

- Xiao, G., Ren, M., & To, S. (2018). A Study of Mechanics in Brittle–Ductile Cutting Mode Transition. *Micromachines*, *9*(2), 49.
- Xiao, G., To, S., & Zhang, G. (2015). Molecular dynamics modelling of brittle–ductile cutting mode transition: case study on silicon carbide. *International journal of machine tools and manufacture*, *88*, 214-222.
- Xiao, G., To, S., & Zhang, G. (2015). The mechanism of ductile deformation in ductile regime machining of 6H SiC. *Computational materials science*, *98*, 178-188.
- Yan, J. (2004). Laser micro-Raman spectroscopy of single-point diamond machined silicon substrates. *Journal of Applied Physics*, *95*(4), 2094-2101.
- Yan, J., Asami, T., Harada, H., & Kuriyagawa, T. (2009). Fundamental investigation of subsurface damage in single crystalline silicon caused by diamond machining. *Precision Engineering*, *33*(4), 378-386.
- Yan, J., Asami, T., Harada, H., & Kuriyagawa, T. (2012). Crystallographic effect on subsurface damage formation in silicon microcutting. *CIRP Annals-Manufacturing Technology*, *61*(1), 131-134.
- Yan, J., Gai, X., & Harada, H. (2010). Subsurface damage of single crystalline silicon carbide in nanoindentation tests. *Journal of nanoscience and nanotechnology*, *10*(11), 7808-7811.
- Yan, J., Syoji, K., & Tamaki, J. I. (2003). Some observations on the wear of diamond tools in ultra-precision cutting of single-crystal silicon. *Wear*, *255*(7-12), 1380-1387.
- Yan, J., Syoji, K., Kuriyagawa, T., & Suzuki, H. (2002). Ductile regime turning at large tool feed. *Journal of Materials Processing Technology*, *121*(2-3), 363-372.
- Yan, J., Takahashi, H., Gai, X., Harada, H., Tamaki, J. I., & Kuriyagawa, T. (2006). Load effects on the phase transformation of single-crystal silicon during nanoindentation tests. *Materials Science and Engineering: A*, *423*(1-2), 19-23.
- Yan, J., Takahashi, H., Tamaki, J. I., Gai, X., & Kuriyagawa, T. (2005). Transmission electron microscopic observation of nanoindentations made on ductile-machined silicon wafers. *Applied Physics Letters*, *87*(21), 211901.
- Yan, J., Takahashi, H., Tamaki, J. I., Gai, X., Harada, H., & Patten, J. (2005). Nanoindentation tests on diamond-machined silicon wafers. *Applied physics letters*, *86*(18), 181913.
- Yan, J., Takahashi, Y., TAMAKI, J. I., Kubo, A., Kuriyagawa, T., & Sato, Y. (2006). Ultraprecision machining characteristics of poly-crystalline germanium. *JSME International Journal Series C Mechanical Systems, Machine Elements and Manufacturing*, *49*(1), 63-69.
- Yan, J., Yoshino, M., Kuriagawa, T., Shirakashi, T., Syoji, K., & Komanduri, R. (2001). On the ductile machining of silicon for micro electro-mechanical systems (MEMS), opto-electronic and optical applications. *Materials Science and Engineering: A*, *297*(1-2), 230-234.
- Yan, J., Zhang, Z., & Kuriyagawa, T. (2009). Mechanism for material removal in diamond turning of reaction-bonded silicon carbide. *International Journal of Machine Tools and Manufacture*, *49*(5), 366-374.
- Yan, J., Zhao, H., & Kuriyagawa, T. (2007). Finite Element Analysis of the Hydrostatic Pressure and Temperature in Ductile Machining of Silicon. *Advances in Abrasive Technology*, *10*, 185.
- Yan, J., Zhao, H., & Kuriyagawa, T. (2009). Effects of tool edge radius on ductile machining of silicon: an investigation by FEM. *Semiconductor Science and Technology*, *24*(7), 075018.
- Yin, L., Vancoille, E. Y. J., Lee, L. C., Liu, Y. C., Huang, H., & Ramesh, K. (2003). High-precision low-damage grinding of polycrystalline SiC. In *Key Engineering Materials* (Vol. 238, pp. 59-64). Trans Tech Publications.
- Yoshida, M., Onodera, A., Ueno, M., Takemura, K., & Shimomura, O. (1993). Pressure-induced phase transition in SiC. *Physical Review B*, *48*(14), 10587.

- Yoshino, M., Aoki, T., Shirakashi, T., & Komanduri, R. (2001). Some experiments on the scratching of silicon: In situ scratching inside an SEM and scratching under high external hydrostatic pressures. *International journal of mechanical sciences*, *43*(2), 335-347.
- Young, H. T., Liao, H. T., & Huang, H. Y. (2007). Novel method to investigate the critical depth of cut of ground silicon wafer. *Journal of materials processing technology*, *182*(1-3), 157-162.
- Yu, D. P., San Wong, Y., & Hong, G. S. (2011). A novel method for determination of the subsurface damage depth in diamond turning of brittle materials. *International Journal of Machine Tools and Manufacture*, *51*(12), 918-927.
- Yu, D. P., Hong, G. S., & San Wong, Y. (2012). Profile error compensation in fast tool servo diamond turning of micro-structured surfaces. *International Journal of Machine Tools and Manufacture*, *52*(1), 13-23.
- Yu, N., Polycarpou, A. A., & Conry, T. F. (2003). *Experimental, Analytical and Finite Element Studies of the Nanoindentation Technique to Investigate Material Properties of Surface Layers Less Than 100 Nanometers Thick*. Air Conditioning and Refrigeration Center. College of Engineering. University of Illinois at Urbana-Champaign.
- Yuan, Y. C., Li, B. Z., Zhou, Z. X., & Zhang, Q. (2012). Study on the simulation model and characteristics of high-speed grinding for ceramics. In *Applied Mechanics and Materials*(Vol. 138, pp. 662-667). Trans Tech Publications.
- Zetterberg, M. (2014). A critical overview of machining simulations in ABAQUS. KTH Royal Institute Of Technology, Sweden
- Zhang, L. C., & Tanaka, H. (1999). On the mechanics and physics in the nano-indentation of silicon monocrystals. *JSME International Journal Series A Solid Mechanics and Material Engineering*, *42*(4), 546-559.
- Zhang, G. M., Anand, D. K., Ghosh, S., & Ko, W. F. (1993). *Study of the Formation of Macro-and-Micro-Cracks during Machining of Ceramics*
- Zhang, L., & Mahdi, M. (1996). The plastic behaviour of silicon subjected to micro-indentation. *Journal of materials science*, *31*(21), 5671-5676.
- Zhao, Y. X., Buehler, F., Sites, J. R., & Spain, I. L. (1986). New metastable phases of silicon. *Solid state communications*, *59*(10), 679-682.
- Zhou, M., Zhang, H. J., & Chen, S. J. (2010). Study on diamond cutting of nonrationally symmetric microstructured surfaces with fast tool servo. *Materials and Manufacturing Processes*, *25*(6), 488-494.
- Zhu, D., Yan, S., & Li, B. (2014). Single-grit modeling and simulation of crack initiation and propagation in SiC grinding using maximum undeformed chip thickness. *Computational Materials Science*, *92*, 13-21.
- Zienkiewicz, O. C., Taylor, R. L., Zienkiewicz, O. C., & Taylor, R. L. (1977). *The finite element method* (Vol. 36). London: McGraw-hill.
- Zong, W. J., Huang, Y. H., Zhang, Y. L., & Sun, T. (2014). Conservation law of surface roughness in single point diamond turning. *International Journal of Machine Tools and Manufacture*, *84*, 58-63.

Appendix 1.1

Permission for Figure 1.2

SPRINGER NATURE LICENSE
TERMS AND CONDITIONS

Jan 09, 2019

This Agreement between Mr. Borad Barkachary ("You") and Springer Nature ("Springer Nature") consists of your license details and the terms and conditions provided by Springer Nature and Copyright Clearance Center.

License Number	4504630756979
License date	Jan 09, 2019
Licensed Content Publisher	Springer Nature
Licensed Content Publication	The International Journal of Advanced Manufacturing Technology
Licensed Content Title	A review on the current research trends in ductile regime machining
Licensed Content Author	Wee Keong Neo, A. Senthil Kumar, Mustafizur Rahman
Licensed Content Date	Jan 1, 2012
Licensed Content Volume	63
Licensed Content Issue	5
Type of Use	Thesis/Dissertation
Requestor type	academic/university or research institute
Format	print and electronic
Portion	figures/tables/illustrations
Number of figures/tables /illustrations	1
Will you be translating?	no
Circulation/distribution	<501
Author of this Springer Nature content	no
Title	Numerical and experimental studies on single point diamond turning process of ductile and brittle material
Institution name	Indian Institute of Technology Guwahati
Expected presentation date	May 2019
Portions	Figure 4
Requestor Location	Mr. Borad Barkachary Department of Mechanical Engineering Indian Institute of Technology Guwahati Guwahati, Assam 781039 India Attn: Mr. Borad Barkachary
Billing Type	Invoice
Billing Address	Mr. Borad Barkachary Department of Mechanical Engineering Indian Institute of Technology Guwahati Guwahati, India 781039 Attn: Mr. Borad Barkachary

Appendix 2.1

Permission for Figure 2.7 (a)

JOHN WILEY AND SONS LICENSE TERMS AND CONDITIONS

Feb 07, 2019

This Agreement between Mr. Borad Barkachary ("You") and John Wiley and Sons ("John Wiley and Sons") consists of your license details and the terms and conditions provided by John Wiley and Sons and Copyright Clearance Center.

License Number	4523640764727
License date	Feb 07, 2019
Licensed Content Publisher	John Wiley and Sons
Licensed Content Publication	Journal of the American Ceramic Society
Licensed Content Title	Ductile-Regime Machining of Germanium and Silicon
Licensed Content Author	Peter N. Blake, Ronald O. Scattergood
Licensed Content Date	Mar 8, 2005
Licensed Content Volume	73
Licensed Content Issue	4
Licensed Content Pages	9
Type of use	Dissertation/Thesis
Requestor type	University/Academic
Format	Print and electronic
Portion	Figure/table
Number of figures/tables	1
Original Wiley figure/table number(s)	3
Will you be translating?	No
Title of your thesis / dissertation	Numerical and experimental studies on single point diamond turning of brittle and ductile materials
Expected completion date	Jun 2019
Expected size (number of pages)	250
Requestor Location	Mr. Borad Barkachary Department of Mechanical Engineering Indian Institute of Technology Guwahati Guwahati, Assam 781039 India Attn: Mr. Borad Barkachary
Publisher Tax ID	EU826007151
Total	0.00 USD
Terms and Conditions	

TERMS AND CONDITIONS

This copyrighted material is owned by or exclusively licensed to John Wiley & Sons, Inc. or one of its group companies (each a"Wiley Company") or handled on behalf of a society with which a Wiley Company has exclusive publishing rights in relation to a particular work (collectively "WILEY"). By clicking "accept" in connection with completing this licensing transaction, you agree that the following terms and conditions apply to this transaction (along with the billing and payment terms and conditions established by the Copyright Clearance Center Inc., ("CCC's Billing and Payment terms and conditions"), at the time that

Permission for Figure 2.7 (b)

ELSEVIER LICENSE
TERMS AND CONDITIONS

Feb 07, 2019

This Agreement between Mr. Borad Barkachary ("You") and Elsevier ("Elsevier") consists of your license details and the terms and conditions provided by Elsevier and Copyright Clearance Center.

License Number	4523641264212
License date	Feb 07, 2019
Licensed Content Publisher	Elsevier
Licensed Content Publication	Precision Engineering
Licensed Content Title	Ductile-regime machining model for diamond turning of brittle materials
Licensed Content Author	W.S. Blackley,R.O. Scattergood
Licensed Content Date	Apr 1, 1991
Licensed Content Volume	13
Licensed Content Issue	2
Licensed Content Pages	9
Start Page	95
End Page	103
Type of Use	reuse in a thesis/dissertation
Intended publisher of new work	other
Portion	figures/tables/illustrations
Number of figures/tables/illustrations	1
Format	both print and electronic
Are you the author of this Elsevier article?	No
Will you be translating?	No
Original figure numbers	3
Title of your thesis/dissertation	Numerical and experimental studies on single point diamond turning of brittle and ductile materials
Expected completion date	Jun 2019
Estimated size (number of pages)	250
Requestor Location	Mr. Borad Barkachary Department of Mechanical Engineering Indian Institute of Technology Guwahati Guwahati, Assam 781039 India Attn: Mr. Borad Barkachary
Publisher Tax ID	GB 494 6272 12
Total	0.00 USD
Terms and Conditions	

INTRODUCTION

Permission for Figure 2.10

JOHN WILEY AND SONS LICENSE
TERMS AND CONDITIONS

Feb 07, 2019

This Agreement between Mr. Borad Barkachary ("You") and John Wiley and Sons ("John Wiley and Sons") consists of your license details and the terms and conditions provided by John Wiley and Sons and Copyright Clearance Center.

License Number	4523650205073
License date	Feb 07, 2019
Licensed Content Publisher	John Wiley and Sons
Licensed Content Publication	Wiley Books
Licensed Content Title	Micro-Cutting: Fundamentals and Applications
Licensed Content Author	Dehong Huo Kai Cheng
Licensed Content Date	Oct 1, 2013
Licensed Content Pages	1
Type of use	Dissertation/Thesis
Requestor type	University/Academic
Format	Print and electronic
Portion	Figure/table
Number of figures/tables	1
Original Wiley figure/table number(s)	Figure 5.15
Will you be translating?	No
Title of your thesis / dissertation	Numerical and experimental studies on single point diamond turning of brittle and ductile materials
Expected completion date	Jun 2019
Expected size (number of pages)	250
Requestor Location	Mr. Borad Barkachary Department of Mechanical Engineering Indian Institute of Technology Guwahati Guwahati, Assam 781039 India Attn: Mr. Borad Barkachary
Publisher Tax ID	EU826007151
Total	0.00 USD
Terms and Conditions	

TERMS AND CONDITIONS

This copyrighted material is owned by or exclusively licensed to John Wiley & Sons, Inc. or one of its group companies (each a"Wiley Company") or handled on behalf of a society with which a Wiley Company has exclusive publishing rights in relation to a particular work (collectively "WILEY"). By clicking "accept" in connection with completing this licensing transaction, you agree that the following terms and conditions apply to this transaction (along with the billing and payment terms and conditions established by the Copyright Clearance Center Inc., ("CCC's Billing and Payment terms and conditions"), at the time that you opened your RightsLink account (these are available at any time at http://myaccount.copyright.com).

Permission for Figure 2.11

ELSEVIER LICENSE
TERMS AND CONDITIONS

Feb 07, 2019

This Agreement between Mr. Borad Barkachary ("You") and Elsevier ("Elsevier") consists of your license details and the terms and conditions provided by Elsevier and Copyright Clearance Center.

License Number	4523650356765
License date	Feb 07, 2019
Licensed Content Publisher	Elsevier
Licensed Content Publication	Journal of Materials Processing Technology
Licensed Content Title	Diamond turning of silicon substrates in ductile-regime
Licensed Content Author	T.P Leung,W.B Lee,X.M Lu
Licensed Content Date	Jan 1, 1998
Licensed Content Volume	73
Licensed Content Issue	1-3
Licensed Content Pages	7
Start Page	42
End Page	48
Type of Use	reuse in a thesis/dissertation
Intended publisher of new work	other
Portion	figures/tables/illustrations
Number of figures/tables/illustrations	1
Format	both print and electronic
Are you the author of this Elsevier article?	No
Will you be translating?	No
Original figure numbers	Fig. 4
Title of your thesis/dissertation	Numerical and experimental studies on single point diamond turning of brittle and ductile materials
Expected completion date	Jun 2019
Estimated size (number of pages)	250
Requestor Location	Mr. Borad Barkachary Department of Mechanical Engineering Indian Institute of Technology Guwahati Guwahati, Assam 781039 India Attn: Mr. Borad Barkachary
Publisher Tax ID	GB 494 6272 12
Total	0.00 USD
Terms and Conditions	

INTRODUCTION

Permission for Figure 2.12

ELSEVIER LICENSE
TERMS AND CONDITIONS

Feb 07, 2019

This Agreement between Mr. Borad Barkachary ("You") and Elsevier ("Elsevier") consists of your license details and the terms and conditions provided by Elsevier and Copyright Clearance Center.

License Number	4523650471270
License date	Feb 07, 2019
Licensed Content Publisher	Elsevier
Licensed Content Publication	CIRP Annals - Manufacturing Technology
Licensed Content Title	Diamond Cutting of Silicon with Nanometric Finish
Licensed Content Author	F.Z. Fang,V.C. Venkatesh
Licensed Content Date	Jan 1, 1998
Licensed Content Volume	47
Licensed Content Issue	1
Licensed Content Pages	5
Start Page	45
End Page	49
Type of Use	reuse in a thesis/dissertation
Intended publisher of new work	other
Portion	figures/tables/illustrations
Number of figures/tables/illustrations	1
Format	both print and electronic
Are you the author of this Elsevier article?	No
Will you be translating?	No
Original figure numbers	Fig. 4
Title of your thesis/dissertation	Numerical and experimental studies on single point diamond turning of brittle and ductile materials
Expected completion date	Jun 2019
Estimated size (number of pages)	250
Requestor Location	Mr. Borad Barkachary Department of Mechanical Engineering Indian Institute of Technology Guwahati Guwahati, Assam 781039 India Attn: Mr. Borad Barkachary
Publisher Tax ID	GB 494 6272 12
Total	0.00 USD
Terms and Conditions	

INTRODUCTION

Permission for Figure 2.14

ELSEVIER LICENSE
TERMS AND CONDITIONS

Feb 07, 2019

This Agreement between Mr. Borad Barkachary ("You") and Elsevier ("Elsevier") consists of your license details and the terms and conditions provided by Elsevier and Copyright Clearance Center.

License Number	4523650612867
License date	Feb 07, 2019
Licensed Content Publisher	Elsevier
Licensed Content Publication	Wear
Licensed Content Title	M.D. Simulation of nanometric cutting of single crystal aluminum–effect of crystal orientation and direction of cutting
Licensed Content Author	R Komanduri,N Chandrasekaran,L.M Raff
Licensed Content Date	Jul 10, 2000
Licensed Content Volume	242
Licensed Content Issue	1-2
Licensed Content Pages	29
Start Page	60
End Page	88
Type of Use	reuse in a thesis/dissertation
Intended publisher of new work	other
Portion	figures/tables/illustrations
Number of figures/tables/illustrations	1
Format	both print and electronic
Are you the author of this Elsevier article?	No
Will you be translating?	No
Original figure numbers	Fig. 1
Title of your thesis/dissertation	Numerical and experimental studies on single point diamond turning of brittle and ductile materials
Expected completion date	Jun 2019
Estimated size (number of pages)	250
Requestor Location	Mr. Borad Barkachary Department of Mechanical Engineering Indian Institute of Technology Guwahati Guwahati, Assam 781039 India Attn: Mr. Borad Barkachary
Publisher Tax ID	GB 494 6272 12
Total	0.00 USD
Terms and Conditions	

INTRODUCTION

Permission for Figure 2.15

Nanoscale Res Lett. 2011; 6(1): 589.
Published online 2011 Nov 11. doi: 10.1186/1556-276X-6-589
PMCID: PMC3224798
PMID: 22078069

Atomistic aspects of ductile responses of cubic silicon carbide during nanometric cutting

Saurav Goel,[1] Xichun Luo,[✉1] Robert L Reuben,[1] and Waleed Bin Rashid[1]

[1]School of Engineering and Physical Sciences, Heriot Watt University, Edinburgh, EH144AS, Scotland, UK
[✉]Corresponding author.
Saurav Goel: sg258@hw.ac.uk; Xichun Luo: x.luo@hw.ac.uk; Robert L Reuben: R.reuben@hw.ac.uk; Waleed Bin Rashid: wb31@hw.ac.uk

Received 2011 Aug 2; Accepted 2011 Nov 11.

Abstract

Cubic silicon carbide (SiC) is an extremely hard and brittle material having unique blend of material properties which makes it suitable candidate for microelectromechanical systems and nanoelectromechanical systems applications. Although, SiC can be machined in ductile regime at nanoscale through single-point diamond turning process, the root cause of the ductile response of SiC has not been understood yet which impedes significant exploitation of this ceramic material. In this paper, molecular dynamics simulation has been carried out to investigate the atomistic aspects of ductile response of SiC during nanometric cutting process. Simulation results show that cubic SiC undergoes sp^3-sp^2 order-disorder transition resulting in the formation of SiC-graphene-like substance with a growth rate dependent on the cutting conditions. The disorder transition of SiC causes the ductile response during its nanometric cutting operations. It was further found out that the continuous abrasive action between the diamond tool and SiC causes simultaneous sp^3-sp^2 order-disorder transition of diamond tool which results in graphitization of diamond and consequent tool wear.

Keywords: ductile regime nanometric cutting, silicon carbide, diamond tool, tool wear

Introduction

Silicon carbide (SiC) is a promising ceramic material suited for advanced neural interfaces, packaging for long-term implantation, microfabricated neural probe as well as for semiconductor devices used in severe environments, such as in military aircraft, combat vehicles, power generation, and petrochemical industries [1]. SiC is a very hard substance (9 to 9.5 on Mohs scale) having comparable hardness to the hardest material known as diamond (10 on Mohs scale). The unique blend of properties possessed by SiC which makes it suitable for various MEMS, bio-medical, and other applications can be summarised in the form of Table 1[2].

Permission for Figure 2.16

ELSEVIER LICENSE
TERMS AND CONDITIONS

Feb 07, 2019

This Agreement between Mr. Borad Barkachary ("You") and Elsevier ("Elsevier") consists of your license details and the terms and conditions provided by Elsevier and Copyright Clearance Center.

License Number	4523650755467
License date	Feb 07, 2019
Licensed Content Publisher	Elsevier
Licensed Content Publication	Journal of Manufacturing Processes
Licensed Content Title	Comparison between numerical simulations and experiments for single-point diamond turning of single-crystal silicon carbide
Licensed Content Author	John A. Patten,Jerry Jacob
Licensed Content Date	Jan 1, 2008
Licensed Content Volume	10
Licensed Content Issue	1
Licensed Content Pages	6
Start Page	28
End Page	33
Type of Use	reuse in a thesis/dissertation
Intended publisher of new work	other
Portion	figures/tables/illustrations
Number of figures/tables/illustrations	1
Format	both print and electronic
Are you the author of this Elsevier article?	No
Will you be translating?	No
Original figure numbers	Fig. 3
Title of your thesis/dissertation	Numerical and experimental studies on single point diamond turning of brittle and ductile materials
Expected completion date	Jun 2019
Estimated size (number of pages)	250
Requestor Location	Mr. Borad Barkachary Department of Mechanical Engineering Indian Institute of Technology Guwahati Guwahati, Assam 781039 India Attn: Mr. Borad Barkachary
Publisher Tax ID	GB 494 6272 12
Total	0.00 USD
Terms and Conditions	

INTRODUCTION

Permission for Figure 2.16

SPRINGER NATURE

Title:	Smooth particle hydrodynamics study of surface defect machining for diamond turning of silicon
Author:	Amir Mir, Xichun Luo, Amir Siddiq
Publication:	The International Journal of Advanced Manufacturing Technology
Publisher:	Springer Nature
Date:	Jan 1, 2016

Creative Commons

Appendix 3.1

True stress-strain graph for strain rate of 1800 s^{-1} from SHPB test [Mir (2016)]

Compressive Stress (MPa)	Strain
307.08	0.000
1030.34	0.003
1638.06	0.006
2311.93	0.011
2751.46	0.018
2880.64	0.025
2729.29	0.035
2419.43	0.044
2129.29	0.052

Appendix 4.1

Mesh sensitivity analysis

Table 4.4 shows the various sizes of the element used to discretize the workpiece geometry. The mesh sensitivity analysis was carried out for a typical process condition: rake angle −45°, clearance angle 5°, cutting edge radius 40 nm, cutting speed 50 mm/s, and depth of cut 5 nm. It was observed that the average error considering both cutting and thrust force is lowest when the mesh size is 25 nm (mesh2); however, this produces very coarse mesh. The reduction in mesh size to 10 nm (mesh3) from 25 nm increases the average error. Further reduction in mesh size to 5 nm (mesh8) decreases the error. However, corresponding computation time is also increases to 9276 s. Hence, for this particular case, the tool and the workpiece were discretized into 902 and 204204 elements respectively to keep the computation time low. It is to be noted that the element size of the work material is kept uniform whereas the fine mesh is created near the cutting edge region for the cutting tool. The mesh density is kept higher at the cutting region where tool and workpiece interaction takes place. Other regions of the cutting tool were coarsely meshed to increase the computational efficiency of the simulation.

Mesh no.	Global Element size	Nos. of Elements	Time (s)	Cutting force (mN)	Thrust force (mN)	Error		Average error
Mesh1	5.00E-05	4000	30	24.83	57.35	−17.22	−4.41	−10.82
Mesh2	2.50E-05	16000	102	28.77	72.28	−4.08	20.47	8.19
Mesh3	1.00E-05	100000	1183	36.25	81.84	20.82	36.39	28.61
Mesh4	9.00E-06	123432	1512	33.58	81.60	11.92	36.00	23.96
Mesh5	8.00E-06	156250	2113	31.83	77.92	6.10	29.86	17.98
Mesh6	**7.00E-06**	**204204**	**3443**	**31.33**	**76.87**	**4.43**	**28.12**	**16.28**
Mesh7	6.00E-06	277389	5410	31.04	75.79	3.48	26.32	14.90
Mesh8	5.00E-06	400000	9276	30.92	73.02	3.06	21.70	12.38

Appendix 5.1

Permission for Figure 5.16

Re: Permission to reuse a figure in my thesis/dissertation from your thesis

MARIAYYAH Ravishankar <Ravishankar.MARIAYYAH@3ds.com>
Fri 08/02/2019 09:30
To: Borad M Barkachary <b.borad@iitg.ac.in>

Hi
Yes you can use it

Regards
Ravi

On 07-Feb-2019, at 9:05 PM, Borad M Barkachary <b.borad@iitg.ac.in> wrote:

> Respected sir,
>
> Greetings to you.
> I, Borad M Barkachary, PhD scholar at Indian Institute of Technology Guwahati, seeking your permission to reuse a figure in my thesis/dissertation from your thesis in both print and electronic format.
> The title of my thesis is "Numerical and experimental studies on single point diamond turning of brittle and ductile materials".
>
> Below are the details for which permission is required.
>
> Topic of PhD research: EXPERIMENTAL AND NUMERICAL STUDIES OF DUCTILE REGIME MACHINING OF SILICON CARBIDE AND SILICON NITRIDE.
> Name: Ravishankar Mariayyah
> Advisors: Dr. Harish P. Cherukuri and Dr. John A. Patten
> Date : 10/25/2007
> Original Figure No. : Fig. 4.3
>
> Regards and sincerely
> Borad M Barkachary
> PhD Scholar
> Department of Mechanical Engineering
> Indian Institute of Technology Guwhati
> Guwahati, Assam-781039, India

Appendix 7.1

Specification of SPDT Machine (NANOFORM-250)

Some of the features of the machine are listed below:

- Capable of diamond turning optical quality form and finish in a wide range of non-ferrous, crystals and polymers**.**
- Optional high speed grinding attachment for direct grinding of small lens molds in non diamond machinable materials such as metals and ceramics.
- Software assisted aspheric tool path with online diagnosis and analysis.
- Hydrostatic slides for job and tool axis (250 mm travel on each axis).
- Centering accessory to align job tool within 0.1 µm.
- Safety devices meeting international safety standards for safe and efficient operation.

Technical Specifications of Nanoform-250	
X-axis move	350 mm
z-axis move	250 mm
Horizontal straightness in X-axis	0.5µm full travel (350 mm)
Horizontal straightness in y axis	0.3µm full travel (250 mm)
Side ways	Hydrostatic oil bearings
Feedback resolution	3.60 nm
Radial motion error	<0.05µm
Axial motion error	<0.05 µm
Maximum spindle speed	5000 rev/min
Fabrication Capabilities of Nanoform-250	
Max. Job diameter	450 mm
Surface figure error	<0.1-0.3 µm PV
Surface finish	<10nm Ra

Appendix 7.2

Specification of Contact Type Surface Profilometer (Form Talysurf PGI 120)

The Form Talysurf PGI 120 is a contact type mechanical profiler, uses conical stylus diamond tip which record height variation of surface along a straight line at a time being in contact with surface. The profile meter is mounted on epoxy granite construction on anti-vibration mounts and provides a firm support for the column and work piece. The stylus moves over the surface at a constant speed, and an electrical signal is produced by the transducer. The stylus is provided with a diamond tip with a cone angle of 60˚ or 90˚ and a tip radius in the range of 1-10µm. These electrical signals are amplified and undergo analog-to-digital conversion. The resulting digital profile is stored in the computer and can be analyzed subsequently for roughness or waviness parameter.

Technical specifications of PGI -120 mechanical profiler	
Traverse length	120 mm
Measuring speed	1mm and 0.5 mm/s
Traverse speed	Up to 5 mm/s
Gauge type	Phase grating interferometer
Measuring range	10 mm
Resolution	12.8 nm at 10 mm range
Range to resolution ratio	780,000:1
Straightness accuracy	0.5 µm over 120 mm traverse
Data resolution	0.25µm
Dimensions(LxDxH)	396x127x195 mm
Measurement capabilities Of PGI-120	
Compatible	With aspheric surface generator and polisher
Analysis	Form, figure and finish
Job diameter	120mm
Roughness accuracy	~10-15 nm at 10 mm
Figure accuracy	~0.1 µm/ 20 mm and ~0.5 µm/120mm

Journal Papers

- Barkachary B. M. and Joshi S. N. 2015. Integrated finite element method (FEM) and response surface methodology (RSM) based modeling and simulation of single point diamond turning (SPDT) of silicon. International Journal of Machining and Machinability of Materials 17 (3/4). pp. 330-354.
- Goel S., Khatri N., Barkachary B.M., Giusca C., Joshi S.N. and Karar V., "Are the high negative rake diamond tools conducive to cut silicon or it's a lore?" International Journal of Adv. Mfg. Tech. [To be communicated]

Conference papers

- Barkachary B. M. and Joshi S. N., "Finite element simulation of single point diamond turining (SPDT) of silicon, In: Proceedings of the 8th International Conference COPEN 2013, NIT Calicut, December 13-15, 2013, pp. 1022 – 1026.
- Barkachary B. M. and Joshi S. N., Comparison of Johnson-Cook and Drucker-Prager material models during finite element simulation of single point diamond turning (SPDT) of silicon carbide, 9th International conference on micro-manufacturing (ICoMM) held at Nanyang Technological Institute, Singapore, March, 25-28, 2014.
- Barkachary B.M., Joshi S.N., Goel S. and Agrawal A., Finite element modeling and simulation of spherical tip nano-indentation of nanocrystalline silicon carbide, Manchester, UK, MATADOR, 5^{th}-7^{th} July 2017.
- Barkachary B.M. and Joshi S.N., Numerical modeling and simulation of plunge cutting of silicon using finite element method, International Conference on Recent Innovations and Developments in Mechanical Engineering (IC-RIDME), *NIT Meghalaya, Shillong, India, November 8 – 10, 2018.*
- Barkachary B.M. and Joshi S.N., Numerical Simulation and Experimental Validation of Nanoindentation of Silicon using Finite Element Method, 2nd International Conference on Computational Methods in Manufacturing (ICCMM 2019), 8th-9th March 2019, IIT Guwahati, Guwahati, India.